

Dartmouth College

## Dartmouth Digital Commons

---

Dartmouth College Ph.D Dissertations

Theses and Dissertations

---

Winter 1-31-2023

### The immune modulation on innate immunity, from pathogen recognition to fungal clearance.

Ko-Wei Liu

*Dartmouth College*, [ken77920@gmail.com](mailto:ken77920@gmail.com)

Follow this and additional works at: <https://digitalcommons.dartmouth.edu/dissertations>



Part of the [Immunology of Infectious Disease Commons](#), [Pathogenic Microbiology Commons](#), and the [Virology Commons](#)

---

#### Recommended Citation

Liu, Ko-Wei, "The immune modulation on innate immunity, from pathogen recognition to fungal clearance." (2023). *Dartmouth College Ph.D Dissertations*. 135.  
<https://digitalcommons.dartmouth.edu/dissertations/135>

This Thesis (Ph.D.) is brought to you for free and open access by the Theses and Dissertations at Dartmouth Digital Commons. It has been accepted for inclusion in Dartmouth College Ph.D Dissertations by an authorized administrator of Dartmouth Digital Commons. For more information, please contact [dartmouthdigitalcommons@groups.dartmouth.edu](mailto:dartmouthdigitalcommons@groups.dartmouth.edu).

# **The immune modulation on innate immunity, from pathogen recognition to fungal clearance.**

A Thesis  
Submitted to the Faculty  
in partial fulfillment of the requirements for the  
degree of  
Doctor of Philosophy

In

Microbiology and Immunology

by Ko-Wei Liu

Guarani School of Graduate and Advanced Studies  
DARTMOUTH COLLEGE  
Hanover, New Hampshire

December 2022

Examining Committee:

---

**Chair, Robert A. Cramer, Ph.D.**

---

Joshua J. Obar, Ph.D.

---

James B Bliska, Ph.D.

---

Stuart M. Levitz, M.D.

---

F. Jon Kull, Ph.D.

Dean of Guarani School of Graduate and Advanced Studies





# Abstract

The human lung is not sterile but a complex environment with various microorganisms. Besides commensals in the lung, hundreds to thousands of individual microbiomes enter the lung every day but without causing the symptom. Host innate immunity plays an important role in maintaining homeostasis of the lung environment and as the first defense line against pathogens. *Aspergillus fumigatus* (*A. fumigatus*) is a saprophytic filamentous fungus that can cause human disease in immune compromised patients. However, with functional innate immunity, immune cells can quickly recognize pathogen associated molecular patterns (PAMPs) from *A. fumigatus* through pattern recognition receptors (PRRs). The activation of PRRs can activate innate immunity and facilitate inflammatory responses through cytokine and chemokine production. As the initiation of inflammation, the recruited innate immune cells can eliminate *A. fumigatus* through phagocytosis and kill them in the mature phagolysosome with ROS-dependent and independent mechanisms.

In this dissertation, we will cover the regulation of antifungal immunity in two specific directions: (1) investigate the immune modulation on innate immunity in the post-viral environment and the cause of viral-fungal superinfection. (2) characterize a potential fungal binding receptor and examine its role in antifungal immunity. In the first project, we demonstrated a novel mechanism within specific cell types that can contribute to defective fungal clearance and lead to high mortality in Influenza A Virus-*A. fumigatus* superinfection. For the second part, we used our newly generated mutant mice line and biochemistry approach to study the potential role of fungal surface binding protein in host immunity. These results further demonstrate the importance of antifungal immunity and upstream immune modulation in preventing the initiation of invasive aspergillosis.

## Acknowledgments

Ph.D. journey is a long trip that I won't be able to get done without helps from my mentors, lab colleagues, collaborators, friends and family. Even though I have been on this path for many years before joining the Dartmouth MCB program, I indeed learned a lot and hopefully become a better scientist through the training here. I really like the environment and resources that our program provided, which gave me an incredible experience as a Ph.D. student in the past couple of years.

Among all the people that I am very grateful to have around, I would like to give my special thanks to Dr. Robert Cramer, as an awesome mentor for both my science and life. In addition to the inputs for my scientific career, your attitude to our contribution to the scientific field and nourishing young scientists like us are the most valuable things I learned through my Ph.D. The freedom of letting me explore the science of my interest and fully supports our scientific adventure mean a lot to me. To my committee Dr. Joshua Obar and Dr. James Bliska, many thanks for your support and guidance to the projects as those truly move the projects forward. To Dr. Stuart Levitz, thanks for being my outside examiner for the thesis defense and for your input for the dissertation. If I can do any Flow cytometry experiment and contribute to our research, I must thank all the training I got from Dr. Nan-Shih Liao and Dr. Yae-Huei Liou, which give me a solid ground to move forward with my projects.

People in Cramer lab, you guys are the best! Thank you for all the helps in the lab and life. I had a fabulous life here in the past couple of years because of you. For people in the Obar lab, thanks for your contributions to our viral-fungal superinfection project. It is a fun project and I am glad that we are able to have some scientific contributions to the field. Also, thanks to all of my friends for your accompany and supports during my Ph.D., and hope we cross path again in the future.

Last but not the least, I would like to thank my family. You might not fully understand what my works are about, but our weekly family talks were the strength to push me to move the projects forward. I am so lucky to have your support so that I can fully concentrate on my science. Finally, we made it and now I can move on!

## Table of Content

<b>Title page</b>	i
<b>Abstract</b>	ii
<b>Acknowledgements</b>	iii
<b>Table of Content</b>	iv
<b>List of Figures and Tables</b>	vi
<b>Chapter 1: Introduction</b>	1
Innate immunity and host-pathogen interaction	2
<i>Healthy environment and immune surveillance</i>	2
<i>Immune environment during Invasive aspergillosis in the immune competent host</i>	9
<i>Immune suppression and Invasive aspergillosis</i>	13
<i>Innate immunity against bacterial infection</i>	16
<i>Innate immunity against viral infection</i>	18
Complexity of host environment during infection	22
<i>Airway commensals and their role in pathogen protection</i>	22
<i>Multi-microorganisms' infections and host immune modulation</i>	23
<b>Thesis overview</b>	28
<b>Chapter 2: Postinfluenza Environment Reduces Aspergillus fumigatus Conidium Clearance and Facilitates Invasive Aspergillosis <i>In Vivo</i></b>	51
Abstract	52
Importance	52
Introduction	53
Results	54
Discussion	62
Materials and methods	65
Acknowledgements	67
References	67
<b>Chapter 3: LysMD3, a potential mammalian PRR, binds to fungal cell wall and partially contributes to anti-fungal immunity</b>	80
Abstract	81
Introduction	82
Results	85
Discussion	103
Materials and methods	108
References	113

<b>Chapter 4: Discussion and Perspectives</b>	123
Host innate immunity, from antifungal immunity to multiplex superinfection	124
Future directions for the IAV-Af superinfection model	133
LysMD3 protein – does it actually bind to chitin?	137
The potential role of LysMD3 in host adaptive immunity	140
The redundancy of other PPRs for antifungal immunity	142
Host immunity of antifungal responses	144
References	146
<b>Appendix I: Biochemical properties of LysMD3 proteins</b>	149
<b>Appendix II: Additional animal models of LysMD3/LysMD4 KO mice</b>	163
<b>Appendix III: Aspergillus fumigatus Strain-Specific Conidia Lung Persistence Causes an Allergic Broncho-Pulmonary Aspergillosis-Like Disease Phenotype</b>	179
<b>Appendix IV: Fungal Biofilm Morphology Impacts Hypoxia Fitness and Disease Progression</b>	199
<b>Appendix V: MDA5 is an essential sensor of a pathogen-associated molecular pattern associated with vitality that is necessary for host resistance against Aspergillus fumigatus</b>	215

## List of Figures and Tables

### Chapter 1

<b>Figure 1</b>	Immune defense under homeostasis condition	3
<b>Figure 2</b>	Pathogen associated molecular patterns and corresponding pattern recognition receptors	6
<b>Figure 3</b>	Disease progression of <i>A. fumigatus</i> and fungal clearance by innate immunity	14
<b>Figure 4</b>	Commensal and pathogenic bacteria and innate immunity	19
<b>Figure 5</b>	Viral infection and innate immune responses	21
<b>Figure 6</b>	Comparison between viral-bacterial and viral-fungal superinfections	27

### Chapter 2

<b>Figure 1</b>	Influenza A virus infection aggravates invasive aspergillosis disease progression	55
<b>Figure 2</b>	Influenza A virus infection does not affect lung cellularity during <i>A. fumigatus</i> infection	57
<b>Figure 3</b>	Defects in leukocyte-mediated fungal killing post-influenza A virus infection	58
<b>Figure 4</b>	Postinfluenza immunity does not hinder neutrophil or monocyte ROS production	59
<b>Figure 5</b>	Reduced phagolysosome maturation can be detected in neutrophils and monocytes during early viral infection	60
<b>Figure 6</b>	Functional neutrophils from the post-IAV environment show decreasing phagolysosome maturation and conidial killing	61
<b>Figure 7</b>	Influenza A virus infection increases transcripts of genes associated with an inflammatory response but reduces transcript levels of known fungal pattern recognition receptors	62
<b>Figure S1</b>	Gating strategy for Neutrophils	70

<b>Figure S2</b>	Gating strategy for Macrophages/Monocytes	71
<b>Figure S3</b>	Gating strategy for DCs	72
<b>Figure S4</b>	Influenza A virus infection does not affect immune cell composition during IA	73
<b>Figure S5</b>	FLARE results of lung phagocytes	74
<b>Figure S6</b>	Gating strategy for pHrodo/ROS experiments	75
<b>Figure S7</b>	Post influenza environment does not reduce ROS productive Neutrophils and Monocytes	76
<b>Figure S8</b>	Post influenza environment hinders the phagocytosis of Monocytes	77
<b>Table S1</b>	Staining panels and cellular markers for Flow Cytometry	78
<b>Table S2</b>	Gene list of antifungal RT2 Profiler PCR Arrays	79

### Chapter 3

<b>Figure 1</b>	LysMD3 is a transmembrane protein with predicted LysM domain and GlcNAcs binding site	86
<b>Figure 2</b>	LysMD3 expression is induced in the immune cells during early fungal infection	88
<b>Figure 3</b>	Generation of LysMD3 deficiency mice through CRISPR targeting method	90
<b>Figure 4</b>	LysMD3 KO mice showed similar cellularity during early fungal infection	93
<b>Figure 5</b>	LysMD3 KO mice showed minor defect in fungal killing during early fungal infection	94
<b>Figure 6</b>	LysMD3 deficiency is not sufficient to contribute to mice mortality during fungal infection	96
<b>Figure 7</b>	LysMD3 binds to both fungal conidia and hyphae	98
<b>Figure 8</b>	LysMD3 does not have similar binding pattern correlated to $\beta$ -glucan and chitin exposure on the fungal surface	100
<b>Figure 9</b>	GAG on the fungal surface regulates LysMD3 binding pattern	102
<b>Figure S1</b>	Gating strategy for Neutrophils	119

<b>Figure S2</b>	Gating strategy for Macrophages/Monocytes	120
<b>Figure S3</b>	Gating strategy for DCs	121
<b>Figure S4</b>	FLARE results of lung phagocytes	122

#### **Chapter 4**

---

<b>Figure 1</b>	Potential signaling pathway related to immune modulation of antifungal responses in post-viral environment	128
<b>Figure 2</b>	Neutrophils and monocytes in the post-viral environment revealed decreased bacterial uptake	130
<b>Figure 3</b>	Neutrophils and monocytes in the post-viral environment revealed decreased endocytosis	132



# **Chapter 1**

## **Introduction**

Ko-Wei Liu

# Innate immunity and host-pathogen interaction

## Healthy environment and immune surveillance

Mammals constantly interact with unique microorganisms in the environment, which can be commensal or pathogenic. The sources of microbiomes can come from air, liquid or food, which can colonize in our organs and expand its population. Airborne microbiomes, including bacteria, fungal spores and viruses, can enter our airway system routinely through respiration. Hundreds to thousands of individual microbes populate the lung, but whether they survive and propagate in the new environment depends on their adaptation to the environmental change and escape from the host immune system. The environmental changes include temperature, pH, oxygen and nutrient availability, which require dramatic transcriptional change from the microbe. Even if the microbe is able to adapt to the new environment, it will encounter multiple host immune defense mechanisms to prevent colonization. Even under healthy condition, multiple host cell types that encounter the microbiome can sense and respond to the microbe invasion (Fig. 1).

Airway epithelial cells (AECs), as the immune system's first line of defense, encounter numerous microbiomes in multiple organs, most notably the lung and skin. The conducting lung airways are composed by ciliated cells, goblet cells, basal cells, club and secretory cells (1, 2). AECs and secreted mucus, specifically by goblet cells, set up the physical barrier between host and environmental stimuli, preventing pathogens and their secreted factors from directly affecting host cells and maintain a threshold of immune activation. At the same time, respiratory cilia constantly move the microbiomes out from the air way to prevent accumulation of microbiome in the lung. AECs also express pattern recognition receptors (PRRs) to recognize encountered pathogens and induce immune responses. Various pathogen associated molecular patterns (PAMPs) as well as damage associated molecular patterns (DAMPs) recognized by PRRs can stimulate downstream NF- $\kappa$ B activation and drive type I immune responses (3). As part

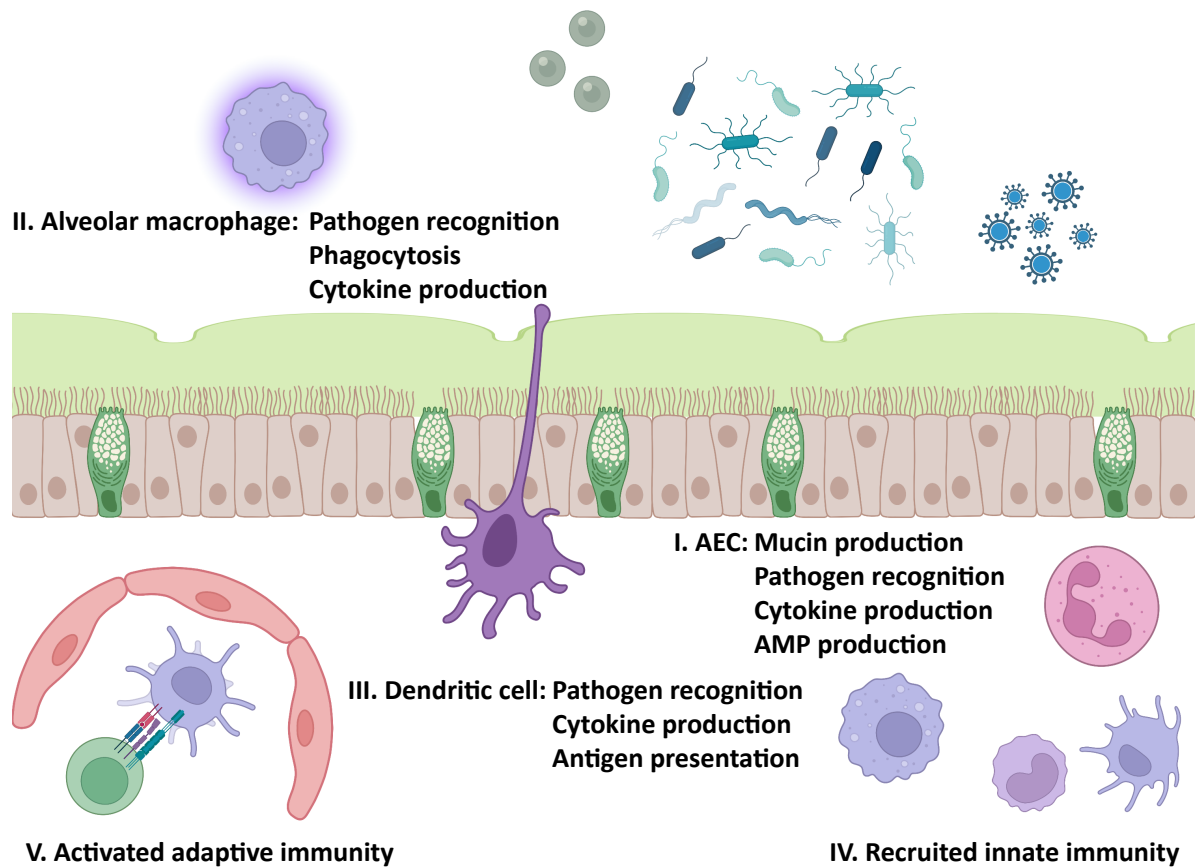


**Fig. 1 Immune defense under homeostasis condition.**

In the health condition, the host immune system has several layers of innate immunity to prevent pathogenesis from evaded pathogens (Bacteria, fungi, and viruses). I. Airway epithelial cells (AECs) and their secreted mucin provide a physical barrier to prevent contact with pathogens. Upon pathogen recognition, AECs secrete cytokines for recruitment and activation of innate immunity and antimicrobial peptides (AMPs) for pathogen killing. II. Tissue-resident alveolar macrophages are the major cell type for pathogen recognition. Activated macrophages can eliminate pathogens through phagocytosis and secrete cytokines for immune responses to the pathogens. Alveolar macrophages also involve immune suppression under homeostasis condition and the immune resolving phase. Tissue repair during and after infection can also be mediated by cytokine production from alveolar macrophages. III. Tissue-resident dendritic cells (DCs) under epithelium and in the alveolar interstitium are also involved in pathogen recognition and initiation of inflammatory responses. At the same time, microbial sampling and antigen presentation by the DCs in the lymph node can connect innate immunity to adaptive immunity. IV. Upon cytokines and chemokines stimulation, recruited neutrophils, monocytes, interstitial macrophages, and DCs can further enhance inflammatory responses for pathogen clearance. V. Pathogen antigen carried by the transferred DCs in the lymph node can perform their antigen presentation to the T cells and initiate Th1 responses.

of the immune surveillance system, the activated AECs secrete first-order cytokines (Interleukin-1 (IL-1), Interferon (IFN), IL-12, IL-23, IL-25, IL-33, Thymic stromal lymphopoietin (TSLP) and Transforming Growth Factor (TGF)) and initiate immune cell recruitment and activation (4). On the other hand, AECs also serve as negative regulators of alveolar macrophages (aMacs) through clustering of cytokines differentiation 200 (CD200), TGF $\beta$  and IL-10 (5). Another role of AECs in microbiome control is through their antimicrobial peptide production. The production of  $\beta$ -Defensins and Cathelicidins by the AECs maintain the microbiome homeostasis in the airway (6, 7)

Besides AECs, immune surveillance by multiple tissue-resident immune cells also play important role in pathogen detection. Tissue-resident aMacs (TR-AMs) and dendritic cells (DCs) sense environmental changes, including pathogen evasion and tissue damage, and trigger the first-order cytokine response (IL-1, TGF, IL-6 and tumor necrosis factor (TNF)) production (8, 9). TR-AMs are a long-lived cell type originating from fetal yolk sac-derived erythromyeloid progenitors and fetal monocytes (10, 11). These TR-AMs can maintain their population through self-renewal and without supplements by the circulating monocytes (12). The TR-AMs can recognize PAMPs and DAMPs, perform phagocytosis and produce cytokines (13). The depletion experiments showed that TR-AMs are essential for early cytokine production and initiation of immune responses (14, 15). TR-AMs also participate in the immune resolving phase through their TGF $\beta$  secretion and initiate tissue repair through TNF $\alpha$  secretion (16, 17). The immune suppression function of TR-AMs also maintains the homeostasis of DC and T cells against environmental stimuli through TGF $\beta$  (18–20). However, in the post viral or bacterial infection environment, the trained long-lasting TR-AMs could be detrimental to the host due to the loss of function against secondary infection (21, 22). The DC populations include CD103<sup>(+)</sup> conventional DC1 (cDC1), CD11b<sup>(+)</sup> cDC2 and plasmacytoid dendritic cells (pDC). The tissue-resident DCs, including cDCs lining the epithelium and pDCs in the alveolar interstitial space, sample pathogens, transport into lymph node,

and present antigens (23). The antigens presenting by DC populations linked between innate immunity and adapt immunity as they stimulating both Th1 and Th2 cells (24).

Recognition of invaded pathogens is the critical step to transition from a healthy homeostasis environment to an inflammatory response. The conserved pathogen components, including their genetic materials (DNA/RNA) or part of cell wall/cell membrane, can often be the PAMPs for recognition (Fig. 2). AECs, TR-AMs and DCs express multiple PRRs, including Toll-like receptors (TLRs), RIG-I-like receptors (RLRs), NOD-like receptors (NLRs), AIM-like receptors (ALRs) and C type lectin receptors, for recognition of both PAMPs and DAMPs from pathogen infection or tissue damage (25, 26). The PRR signaling leads to acute inflammation, cytokine production, cell recruitment and initiation of immune cell response. In the following section, we will discuss individual PRR and their contribution to the innate immunity.

Toll-like receptors (TLRs) are conserved receptors in both insects and animals. The name of TLR came from its similarity to *Drosophila* toll protein as a membrane receptor (27). The TLRs contain the N terminal domain for PAMP recognition, transmembrane domain and C terminal toll-IL-1 receptor (TIR) homologous domain for adaptor binding and signal transduction (28). The TLR family are further divided into cell membrane TLRs and intracellular TLRs, depending on their localization at the cell membrane or lysosomal membrane. Forming of homo- or heterodimers, TLRs form a binding pocket for PAMPs from pathogen surface components (lipids, lipoproteins and proteins) as well as their genetic materials (DNA and RNA). Through PAMP binding, the TLRs are able to recognize diverse types of infection, including bacteria, fungi and viruses. TLR2 binds to peptidoglycan from gram-positive bacteria as well as zymosan from fungi (29, 30). TLR3 recognizes double strand RNA (dsRNA) from virus (31). TLR4 binds to lipopolysaccharide (LPS) from gram-negative bacteria (32) and TLR5 binds to flagellin from bacteria (33). TLR6 binds to both lipoteichoic acid from gram-positive bacteria and zymosan from fungi (34). TLR7 and 8 recognize single strand RNA (ssRNA)

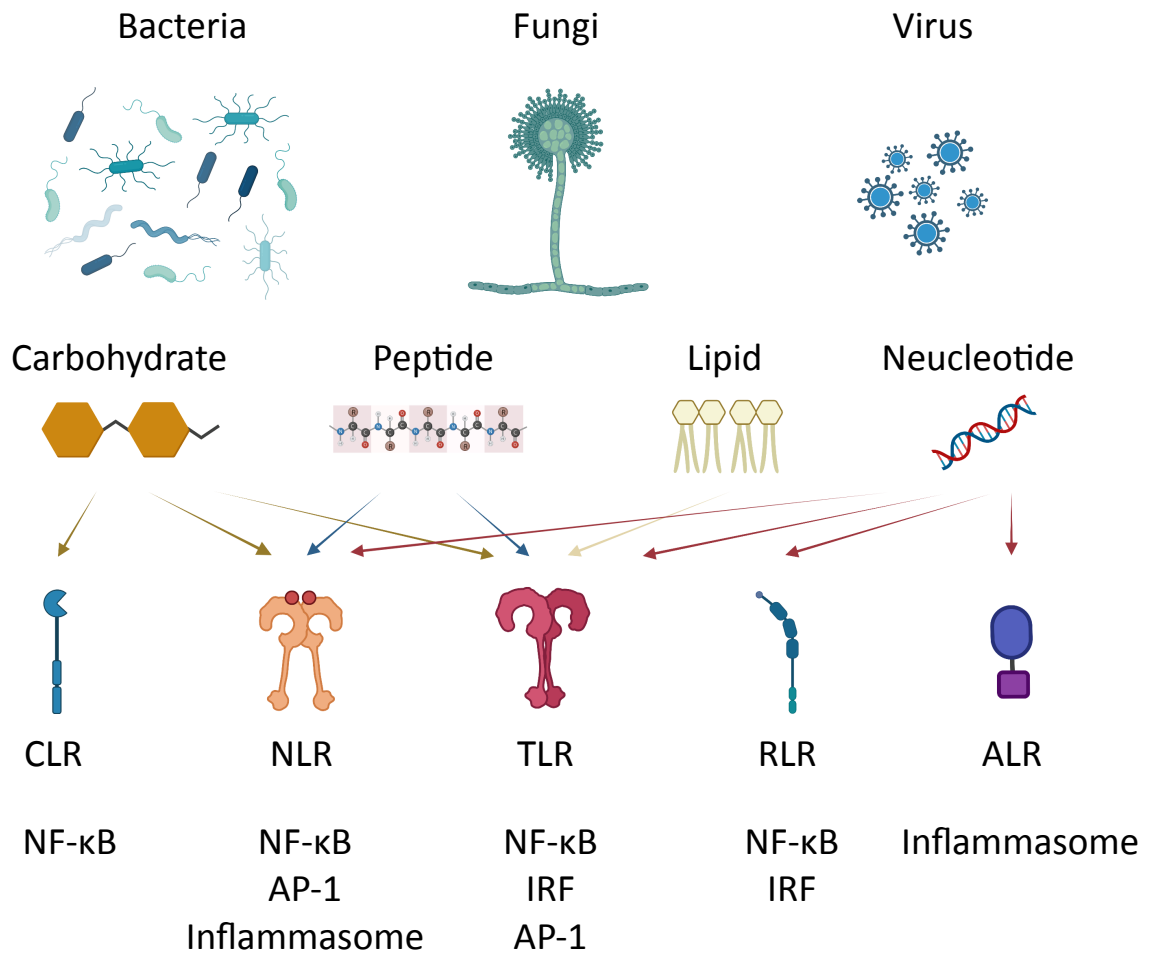


**Fig. 2 Pathogen associated molecular patterns and corresponding pattern recognition receptors.**

Cell wall/membrane blocks, as well as genetic materials from bacteria, fungi and virus can be the pathogen associated molecular patterns (PAMPs). These PAMPs can be recognized by the pattern recognition receptors (PRRs) from the host cells. C-type lectin receptors (CLRs) bind to the carbohydrates in the cell wall of bacteria and fungi as well as viral surfaces. NOD-like receptors (NLRs) bind to peptidoglycan of bacterial and fungal structure as well as viral RNA. Toll-like receptors (TLRs) binds to carbohydrates, peptidoglycan, lipopolysaccharide, lipoteichoic acid, RNA, and DNA from bacteria, fungi and virus. RIG-1-like receptors (RLRs) bind to double-strand RNA from viruses. AIM-like receptors (ALRs) bind to double-strand DNA from bacteria, fungi, and viruses. The stimulation of these PRRs leads to the activation of transcriptional factors as well as inflammasome activation. CLRs, NLRs, TLRs, and RLRs can activate NF-κB signaling for proinflammatory cytokine production. Alternatively, the adaptor of NLRs and TLRs can initiate transcriptions mediated by AP-1. TLRs and RLRs can also turn on IRF-mediated transcriptions. Both NLRs and ALRs can induce inflammasome formation and produce mature IL-1 through downstream caspase-1. The crosstalk between NF-κB, AP-1, and IRF will decide whether it meets the threshold for the production of proinflammatory cytokines. These proinflammatory cytokines together with mature IL-1 from activated inflammasome can initiate immune responses against bacterial, fungal, and viral infections.

from viruses (34, 35). TLR9 recognizes CpG containing DNA from both bacteria and virus (36). The C terminal TIR domain of TLRs can bind to adaptor protein as MyD88 or TRIF for downstream signaling cascades and both pathways can turn on NF- $\kappa$ B or IRF mediated gene transcription (37, 38). The activation of TLR signaling contributes to cell maturation, cytokine/chemokine production, antimicrobial activity, antigen presentation (39). The induced cytokines are involved in inflammatory responses, cell growth and survival as well as anti-inflammatory responses (40).

Similar to viral RNA detection through TLRs, RIG-1-like receptors (RLRs) are RNA helicases that recognize cytoplasmic viral RNA and induce type I IFN and downstream IFN-stimulated genes (ISGs) (41). The RLR family contains retinoic acid-inducible gene I (RIG-I), melanoma differentiation associated factor 5 (MDA5), and laboratory of genetics and physiology 2 (LGP2). These RLRs also are expressed in most cell types, including immune cells and epithelial cells. The resting cells maintain low expression of RLRs but significant enhanced expression can be found upon viral infection in IFN dependent and independent manners (42, 43). RIG-1 and MDA5 recognize various virus double stranded RNA (dsRNA) (44). Recent work from our collaborators also showed that MDA5 can recognize dsRNA from live fungus. Upon viral detection, the activated RLRs can induce type I IFN and downstream interferon-stimulated genes (ISGs) (45).

In addition to viral RNA recognition by TLRs and RLRs, NOD-like receptors, (NLRs) as another category of intracellular PRRs, can recognize microbial PAMPs (peptidoglycan, flagellin, viral RNA and fungal hyphae) and DAMPs from host cells (ATPs, cholesterol crystals and uric acid) (46). NLRs are also expressed in multiple tissues by both immune cells and epithelial cells (46). NLRs are composed of an N-terminal effector domain, central NOD domain for activation, and C-terminal leucine-rich repeat (LRR) domain for PAMPs/DAMPs recognition. The N-terminal effector domain of caspase recruitment domain (CARD), pyrin domain (PYD), acidic transactivating domain (AD), or baculovirus inhibitor repeats (BIRs) can control the interaction of downstream factors,

which lead to activation of NF- $\kappa$ B and MAPKs for autophagy, signal transduction, transcription activation, and inflammasome formation (47, 48).

In addition to RNA from pathogens, host immunity can also sense DNA from the pathogen through cyclic GMP-AMP synthase (cGAS)/stimulator of IFN genes (STING) pathway and AIM-like receptors (ALRs). cGAS/STING pathway is the major dsDNA sensing pathway recognizing dsDNA but with different size binding between human and mice (mice: <45 bp; human: >45 bp) (49). Membrane bound cGAS binds to dsDNA and has the conformational change to induce its enzymatic activity for cyclic GMP (cGMP) production. The STING protein binds to cGMP and can initiate the type I IFN, NF- $\kappa$ B signaling and non-canonical autophagy (50). cGAS recognizes dsDNA from bacteria, viral DNA, and retrovirus and activates STING protein for initiation of IFN pathway for anti-bacterial and anti-viral responses (51). AIM-like receptors (ALRs), including AIM2 and IFI16, are accounted for dsDNA recognition and induction of inflammasome formation (52). ALR protein contains hematopoietic IFN-inducible nuclear protein (HIN) domain for dsDNA binding and pyrin domain (PYD) for the binding of adapter protein apoptosis-associated speck-like protein containing a caspase recruitment team (ASC) (49). Assembly of ALR, ASC and caspase-1 into inflammasome formation can activate enzymatic activity of caspase-1 for cleavage of pro-IL-1 to mature IL-1 as a proinflammatory cytokine and contributes to pyroptosis (53). IFI16 cooperates with cGAS for STING activation to initiate type I IFN signaling (54). Thus, ALRs can recognize dsDNA from pathogens and initiate inflammation through proinflammatory cytokine production.

C-type leptin receptors (CLRs) are widely expressed in myeloid cells (DCs, monocytes, macrophages and neutrophils) and AECs (55). CLRs bind to various carbohydrates on the surface of fungi, bacteria and virus. The activation of CLRs is mediated through Syk/CARD9 induction to activate NF- $\kappa$ B signaling (55). NF- $\kappa$ B-induced transcription can produce pro-inflammatory cytokines and inflammatory responses.



CLRs bind to multiple cell wall components ( $\beta$ -glucan and mannans) on the fungal surface and are involved in multiple anti-fungal responses, including cytokine production, ROS generation and phagocytosis (55). Binding to bacterial glycan, CLRs can initiate cytokine production for immune cell recruitment and activation for bacterial clearance as well as connection to adaptive immunity for antibody and memory generation (56). Upon viral recognition by macrophages and DCs, CLRs are involved in antigen presentation, antiviral innate immunity (type I IFN) as well as T helper cell differentiation (57).

In order to maintain homeostasis in a healthy lung environment, AECs create a barrier to prevent the excessive contact with microbiomes and microbiome-related immune responses. At the same time, TR-AMs set up the threshold of immune activation through their immune suppression function and maintain the homeostasis of AECs. However, upon pathogen invasion and tissue damage, PAMPs and DAMPs can be recognized by PRRs and initiate immune responses. The initiation of immune responses converts the lung environment to an inflammatory environment and the recruitment of effector cells to the lung facilitates pathogen clearance.

#### Immune environment during Invasive aspergillosis in the immune competent host

Many fungal species are opportunistic pathogens and can attempt to colonize the mammalian lung. Due to an efficient immune system, most hosts can encounter hundreds to thousands of spores from individual species without causing symptoms. However, due to poor diagnosis, limited antifungal drug availability and efficacy, lack of vaccine, and immune-compromised hosts, fungal infections are becoming a major issue. Major fungal infections, including *Aspergillus fumigatus* (*A. fumigatus*), *Candida albicans* (*C. albicans*), *Cryptococcus neoformans* and *Pneumocystis jirovecii*, can cause over two million life-threatening infections with up to 95% mortality annually (58). Currently, patients with invasive fungal infections were usually under immune suppression conditions, such as HIV/AIDS, corticosteroid treatments, solid-

organ/hematopoietic stem cell transplants or neutropenic patients (59–61). Fungal infections can happen in various organs, and the lungs are the most common sites of infections with *Aspergillus* and *Cryptococcus* species (62). As we mentioned previously, our innate immunity does a great job preventing the initiation of fungal infections. In this section, we will focus on the progression of *A. fumigatus* infection and host responses to prevent Invasive Aspergillosis (IA).

*A. fumigatus* are filamentous fungi that initiate infection through asexual sporulation, termed conidia. The inhaled conidia encounter the airway and alveoli will initiate the spore to break its dormancy via the raised temperature in the host. Resting conidia break dormancy by hydrolyzing their surface hydrophobin rodlet and uptake water from the environment to initiate germination (63). During the germination, the exposure of PAMPs in the cell wall are recognized by the AECs, tissue-resident aMacs and DC populations in the lung (64). *Aspergillus*-related TLRs, including TLR2, TLR4 and TLR9, trigger NF- $\kappa$ B signaling, cytokine/chemokine production and fungicidal activity (65, 66). In addition to TLRs, the  $\beta$ -glucan receptor, dectin-1, has been shown to contribute to cytokine/chemokine production, which is correlated with neutrophil recruitment as well as ROS production (67). Upon the immune activation, the first wave of cytokines and chemokines will recruit other phagocytes to eliminate the fungal infection. Human studies using *in vitro* culture and examining patient BAL showed that *A. fumigatus* infection can induce proinflammatory cytokines (IL-1, IL-6, IL-12, IL-17, TNF) and chemokines (IL-8, CCL-20 and CXCL10) (68). These cytokines and chemokines will recruit and activate other cell types to the lung and initiate antifungal responses.

Macrophage lineages are essential for antifungal immunity. As TR-AMs keep the homeostasis of lung environment in a healthy condition, the initiation of antifungal responses upon fungal recognition can recruit other immune cell types, including neutrophils, DC populations and other macrophages lineages (69, 70). During *A. fumigatus* infection, aMacs, as one of the professional phagocytes, can recognize

conidia through PRRs (TLRs and CLRs) and engulf the conidia that have entered the lung alveolus (71). Following engulfment, phagosome-containing conidia will acquire endosome markers following the endosome maturation steps and eventually fuse with the lysosome to form a mature phagolysosome (72). During phagocytosis, the killing of conidia in the mature phagolysosome rely on phagolysosome acidification and reactive oxidant intermediate production (72, 73). Upon the first wave of cytokine/chemokine production, circulating monocytes in the blood are recruited to lung environment. Based on the expression of surface markers, the monocytes can further divide into classical inflammatory monocytes (CCR2<sup>(+)</sup> Ly6C<sup>(hi)</sup> in mice and CD14<sup>(+)</sup> CD16<sup>(-)</sup> in humans) and non-classical patrolling monocytes (CCR2<sup>(low)</sup> Ly6C<sup>(low)</sup> in mice and CD14<sup>(low)</sup> CD16<sup>(+)</sup> in humans). The classical monocytes can further differentiate into non-classical monocytes, macrophages and monocyte-derived DCs (moDCs) (74). Monocytes populations in the lung also express multiple PRRs, phagocytize and kill conidia, and induce cytokine production (75). The cytokines produced by monocytes and monocyte-derived cells can facilitate neutrophil function in fungal clearance (75). Thus, macrophage lineages are not only involved in fungal sensing and initiating an immune response, but also contribute to fungal killing.

Neutrophils are the most critical innate immune cell type for fungal clearance. Upon *A. fumigatus* infection, recruited neutrophils will become the most prominent cell type in the lung, accounting for 60-70% of total immune cells. Neutrophils can produce chemoattractants for monocyte and DC recruitment as well as macrophage polarization (76–78). As one of the professional phagocytes, neutrophils recognize and uptake the swollen conidia and small germlings through phagocytosis and kill the fungi through ROS dependent and independent mechanisms similar to aMacs (79). Even though aMacs are considered the major cell type for phagocytosis and pathogen clearance, the large quantity of recruited neutrophils during *A. fumigatus* infection makes them critical to conidial clearance. Additionally, ROS production from neutrophils is essential for antifungal immunity. Chronic granulomatous disease

patients, which is a genetic disease with defective components of the nicotinamide adenine dinucleotide phosphate (NAPDH) oxidase complex, are not able to eliminate invade fungal infection and lead to IA (80). The ROS production from neutrophils not only contribute to conidial clearance through phagocytosis but also as the major source for fungal hyphae clearance (81). However, the conidial clearance in the mature phagolysosome can be contributed by both ROS dependent and independent mechanisms, as neutrophils also contain granules with microbicidal peptides and proteolytic enzymes (82). At the later stage of IA, the fungal clearance is mediated by ROS and nonoxidative neutrophil granular contents because the size of fungal hyphae prevents the killing mediate phagocytosis (83). Neutrophils also perform NETosis, which is the expulsion of DNA and fungicidal proteins. NETosis can be stimulated by swollen conidia, but the NET formation is more correlated with preventing fungi spreading from the infection foci instead of serving as major fungal killing mechanism (84). In summary, neutrophils are the major cell type involved in *A. fumigatus* clearance at both conidial and hyphal stages in the immune competent host.

Airway DC populations (cDC1, cDC2 and pDC) contribute to immune surveillance and sampling pathogens in the airway lumen. At the same time, activated neutrophils recruit inflammatory DCs (CD64<sup>(+)</sup> CD11c<sup>(+)</sup> MHCII<sup>(+)</sup> DCs) to the site of infection through chemokines CCL2 and CCL20 (85). These inflammatory DCs can be further distinguished by their origin from cDCs or monocytes (86). DC populations express TLRs and CLRs as the PRRs that recognize *A. fumigatus* and contribute to cytokine production (87–89). pDCs produce IFN through TLR9 signaling and contribute to clearance of *A. fumigatus* hyphae (90). DCs are able to phagocytose conidia and it has been shown that the fungi can be transported to the lymph node for Th cell differentiation (91). While the progression of IA might lead to Th1/Th2 dysregulation (92), the cytokine production by the DC population can support the Th1/Th17 responses, which are essential for maintaining antifungal immunity (93–95). Overall, DC populations contribute to antifungal immunity through fungal recognition, phagocytosis,

and cytokine production. The cytokine environment regulated by the DC populations not only induces proinflammatory responses but also connect between innate and adaptive immunity.

Overall, innate immunity cells in the immune competent hosts effectively contribute to antifungal immunity through fungal recognition, initiation of inflammatory responses and fungal clearance (Fig. 3).

#### Immune suppression and Invasive aspergillosis

As previously mentioned, our innate immunity acts as an immune surveillance and promotes antifungal responses against *A. fumigatus* to prevent IA development. However, patients with corticosteroid treatment, chemotherapy or neutropenic conditions, which completely or partially compromise the immune response, can significantly increase the risk of occurrence of IA. The mortality of immune compromised patients with IA can be up to 95% (58). Furthermore, loss of immune cells due to acute leukemia and bone marrow transplantation can lead to IA (96, 97). Patients undergoing chemotherapy often become neutropenic, with airway barrier disruption, and therefore greatly increase their chance of developing IA (98, 99). Thus, lack of immune cell infiltration or proper antifungal responses in immune compromised creates a favorable environment for *A. fumigatus* conidia to germinate, grow into biofilms, and develop into IA. We will next focus on the effects of immune suppression on the host immune system and how it contributes to IA development.

Patients with long-term glucocorticoid (GC) treatment or allogeneic transplant patients with immune suppression are also the high risk populations for IA development. GCs and their receptors can reduce inflammation through three

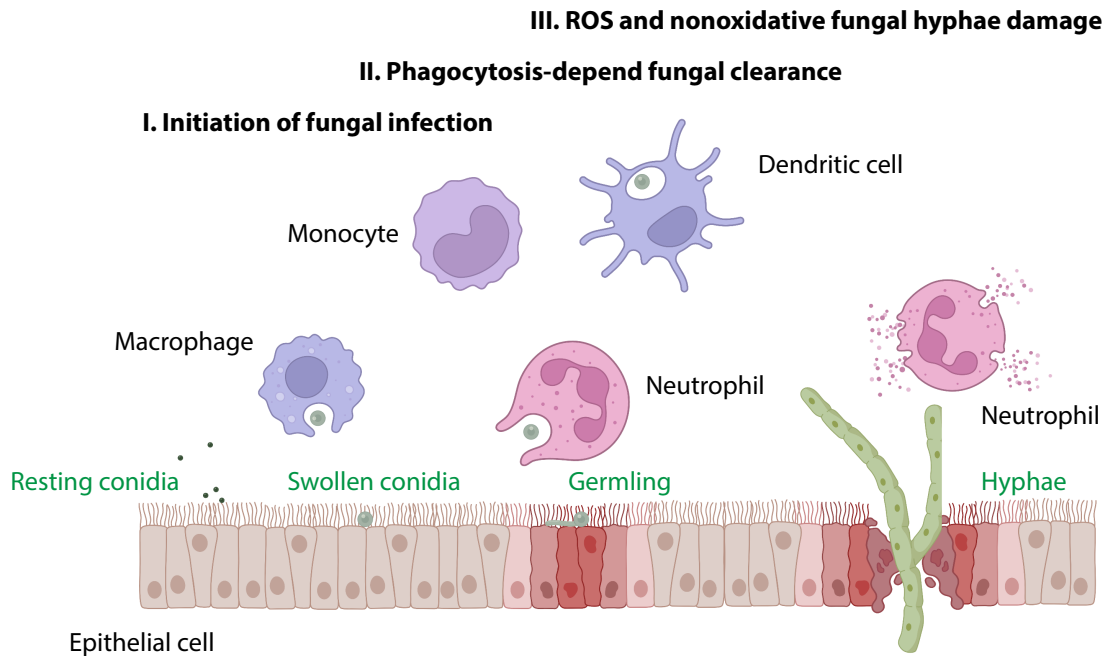


**Fig. 3 Disease progression of *A. fumigatus* and fungal clearance by innate immunity.**

The progression of *A. fumigatus* infection and fungal clearance mediated by innate immunity depends on the stage of fungal growth. I. *A. fumigatus* infection initiates with the entry of resting conidia. II. Upon conidial germination, the alveolar macrophages, neutrophils, dendritic cells, and monocytes recognize fungal conidia/germling and eliminate them through phagocytosis. III. The growth of *Aspergillus* hyphae causes tissue damage and fungal clearance rely on ROS and nonoxidative microbicidal products released from neutrophils.

mechanisms: (1) Blocking transcription factors (NF- $\kappa$ B and AP-1) to prevent cytokine production, (2) production of annexin-I to inhibit cytosolic phospholipase A2a (cPLA2a), and (3) production of MAPK phosphatase I to inhibit AP-1 activation and MAPK cascades (100). GC treatment can affect host innate immunity by affecting cellularity, cytokine production and cellular functions. GC treatment does not lead to neutropenia but can lead to leukocytosis, lymphocytopenia and monocytopenia (101, 102). Alternatively, the inhibition of neutrophil apoptosis by GC can actually lead to an increase of neutrophils at the site of infection (103). The accumulation of neutrophils without negative regulators, such as cytokine (IL-10) and regulatory cell (Treg) at the site of infection can be detrimental because of the increase of tissue damage by robust granule and reactive oxygen intermediate in the local environment (104, 105). Although GC treatment does not affect neutrophil recruitment, the inhibition of E-selectin expression can affect neutrophil movement and attachment at the *A. fumigatus* infection site (106, 107). GC treatment can also affect the antifungal ability of neutrophils, macrophages, monocytes, and DC populations. Previous literature has shown that GC treatment can impair phagocytosis in neutrophils, macrophages and monocytes (108–111). The defective oxidative burst from neutrophils and macrophages in the GC-treated host can contribute to a decrease in fungal conidia and hyphal clearance (109, 112). The cytokine profile is greatly changed in the host with GC treatment. Since GC inhibits NF- $\kappa$ B and AP-1 function, the cytokine production related to pro-inflammatory responses (IL-1, -6, -17 and -18; IFN $\gamma$ ; TNF $\alpha$ ; Granulocyte-macrophage colony-stimulating factor (GM-CSF)) are significantly reduced in the innate immune cells (113–116). The suppression of NF- $\kappa$ B in macrophages by GC can also reduce their *A. fumigatus* conidial and hyphal killing through oxidative and non-oxidative mechanisms (111). Dexamethasone treated neutrophils from healthy donors showed reduced cytokine production (TNF $\alpha$ , IFN $\gamma$  and IL-10) and reduced conidial killing/hyphal damages (117). GC treated monocytes have been shown to have impaired chemotaxis, movement and phagocytosis (110). GC treatment also significantly reduces DC differentiation and will reduce mature DCs for pathogen recognition and antigen presentation during infection (118). In summary, with

GC treatment, the host innate immunity will lose both quantitative and qualitative antifungal responses, and the tissue damage contributed by accumulated neutrophils can be causative to the host mortality during IA.

#### Innate immunity against bacterial infection

Infants or neonates acquire maternal microbiota and establish commensal microbiomes after birth. The commensal bacteria in the lung can be beneficial to the host defense against pathogens. The commensal bacteria can create a microenvironment to restrain the propagation of respiratory pathogens through competition of nutrient and adhesion sites (119, 120). At the same time, the antimicrobial peptides from commensal bacteria and immune training from bacterial stimulation are also critical for elimination of the invading pathogens (121, 122). Infection of bacteria can cause respiratory inflammation, which leads to innate immune cell recruitment and edema. The continuous inflammation and damage contributed by both bacterial colonies and recruited immune cells can lead to pneumonia and sepsis, which can cause high mortality in children, the elderly, or patients with aberrant immune conditions. Common causes of bacterial induced pneumonia can be contributed by *Streptococcus pneumoniae*, *Haemophilus influenzae*, *Pseudomonas aeruginosa*, *Staphylococcus aureus* and *Enterobacteriaceae* (123). While the bacterial infection can be effectively treated with antibiotic treatment, the antibiotic resistant bacteria introduced from the clinic and/or environment have become an emerging issue (124). However, our immune system not only contributes to the pathogen sensing and clearance but also have a dedicated immune resolving phase to prevent a detrimental immune response and maintain the homeostasis of lung environment.

Similar to a fungal infection, AEC and TR-AMs recognize bacterial infection through PRRs. The extracellular TLRs (TLR1, TLR2, TLR4, TLR5, TLR6) and intracellular TLRs (TLR3, TLR7, TLR8, and TLR9) recognize bacterial flagellin, cell wall or cell membrane components and bacterial genetic materials (125). The activation of PRRs



can promote Th1 related cytokine (TNF- $\alpha$ , IL-1 $\beta$ , IL-6, and IL-8) production to initiate antibacterial immune responses and immune cell recruitment (126). Bacterial RNA sensing and activation of NLRs comprising the inflammasome (NLRP3 inflammasome) also promote of IL-1 maturation through caspase I activation (127). Another potent cytokine from AECs, GM-CSF, not only contributes to macrophage differentiation, activation, and bacterial clearance but also to AEC repair during bacterial infections (128, 129). Activated macrophages are involved in bacterial clearance through their iNOS production and phagocytosis (130, 131). However, the balanced polarization of macrophages is critical for the lung environment before and after bacterial clearance. Macrophage polarization can be facilitated by innate lymphoid cells (ILCs). The Th1 cytokines, including IFN from ILC1/NK and IL-17/IL-22 from ILC3, can support M1 macrophage polarization (132). On the other hand, the Th2 cytokines (IL-4 and IL-13) from ILC2 switch the macrophage into M2 state during the immune resolving phase (133). The downstream signaling of Th1 and Th2 cytokines through JAK/STAT pathway determine the polarization of M1/M2 macrophage (134). During the bacterial infection, the polarization of M1 macrophages can further promote inflammatory response and bacterial clearance (135). Furthermore, switching into an M2 macrophage during the immune resolving phase can prevent an overwhelming immune response and tissue damage (136). Macrophage polarization is also critical in sepsis, as controlling the aberrance of macrophage polarization can alleviate the symptoms in both the hyperinflammatory and immune tolerance phase of sepsis (137). The neutrophil is also recruited to the lung following bacterial activation of AECs. The effector functions of neutrophils in antibacterial immunity are similar to antifungal immunity as their migration, pathogen recognition, phagocytosis, ROS production and NETosis are all essential in bacterial clearance (138). In a septic environment, inhibition of neutrophil apoptosis by LPS and complement component 5a (C5a) can extend neutrophil lifespan (139). However, bacterial induced C5a also inhibits neutrophil functions such as migration, phagocytosis, and ROS production (140). Robust immune responses induced by the cytokine storm, hypoxia environment, accumulation of neutrophils without

proper antibacterial functions, and reduction of ILC2 can lead to local cell apoptosis and AEC damage during sepsis (139, 141). In summary, innate immunity and bacteria in the lung have mutual effects on each other (Fig. 4). While the commensal bacteria maintain the basal immunity in the lung, the activated immune cells sense and control the bacterial infection. The balance of inflammatory and anti-inflammation status is critical for maintaining homeostasis of both the host cells and microbiome.

#### Innate immunity against viral infection

Viral infection is another common lung infection that can lead to high mortality in the host. Instead of innate immunity, the clearance of virus and infected cells is mostly mediated by adaptive immunity. However, the innate immunity still plays an important role in initiation of antiviral responses and stimulation to adaptive immunity. Upon viral recognition, innate immunity initiates cytokine production, antigen presentation, complement secretion and induction for T cell activation (142). Similar to other infections, PRRs expressed by AECs and immune cells can recognize a viral infection. These PRRs (RLR, TLR and NLR) specifically bind to genetic material from virus (dsRNA, ssRNA and ssDNA) and promote type I IFN production (143). Upon RNA binding, RLRs, including RIG-1, MDA5 and LGP2, bind to their adaptor, IFN- $\beta$  promoter stimulator-1 (IPS-1) and activate downstream signaling (45). Intracellular TLRs (TLR3, TLR7 and TLR9) that bind to viral DNA and RNA are involved in initiation of antiviral responses (144). Both RLRs and TLRs can promote type I IFN production through IRF-3 and IRF-7 and cytokine production through NF- $\kappa$ B (145, 146). At the same time, NLR downstream inflammasome activation upon viral RNA recognition can induce mature IL-1 production (147). During viral infection, the STING pathway can promote type I IFN production and NF- $\kappa$ B activation (148). These proinflammatory cytokines and type I IFN response can promote activation of both innate immunity and adaptive immunity, especially cytotoxic T lymphocyte (CTL) for viral clearance (149).

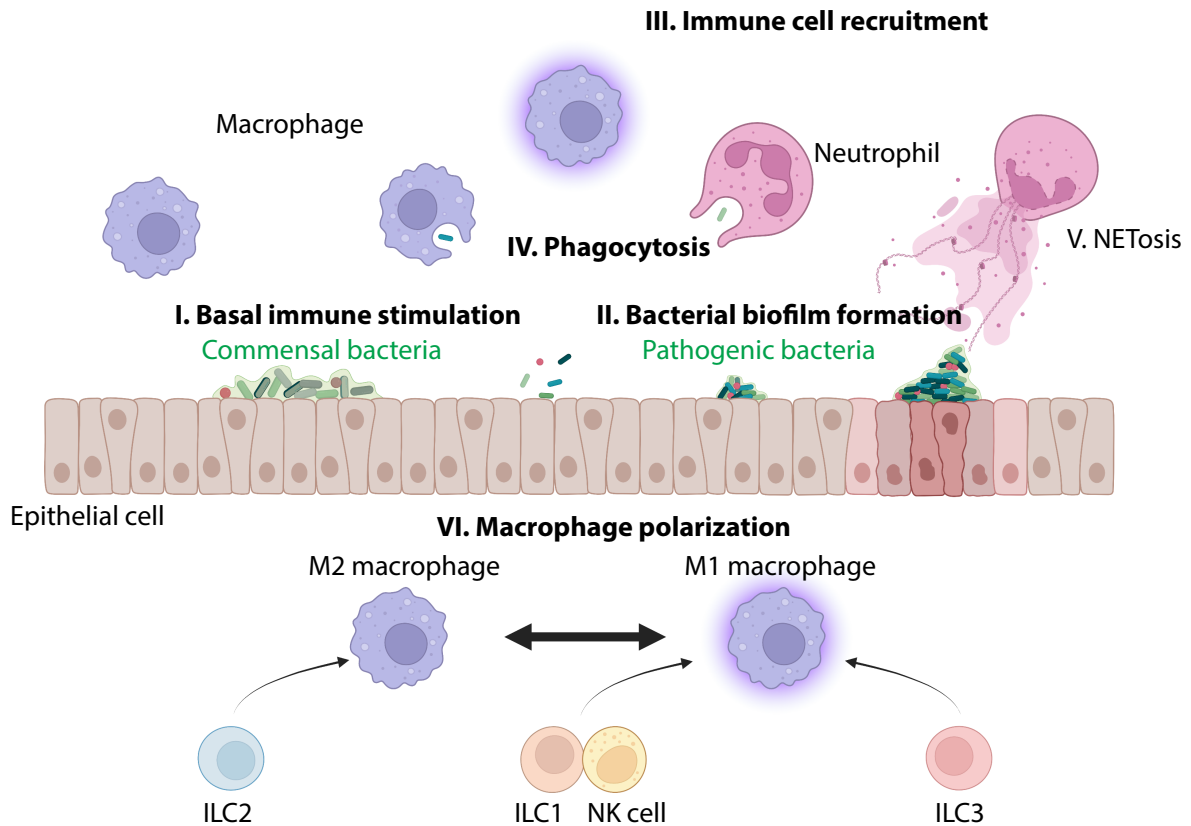


**Fig. 4 Commensal and pathogenic bacteria and innate immunity.**

Innate immune cell regulation and antimicrobial activity during bacterial infection. I. During the homeostasis phase, immune cells receive basal stimulation from commensal bacteria without initiation of inflammatory response. II. The pathogenic bacterial infection starts with planktonic bacteria to mature bacterial biofilm. III. Immune cell recruitment upon the signals from bacterial recognition. IV. Recruited immune cells can eliminate bacterial infection primarily relying on phagocytosis. V. Neutrophils perform NETosis to effectively inhibit bacterial propagation with antimicrobial peptide-decorated chromosome. VI. Macrophage polarization depends on the signal from innate lymphoid cells (ILCs) for inflammatory M1 macrophages or tissue-repairing M2 macrophages.

As the resident cells for immune surveillance, AECs and macrophages recognize viral infection through PRRs (150). Additionally, DC populations play an important role in the interaction between innate and adaptive immunity. pDCs with highly expressed TLR7 and TLR9 are the main source of type I IFN production during viral infection (151, 152). These pDCs can still produce a large amount of type I IFN even without retinoic acid-inducible gene I-like helicase (RLH) signaling (153). Besides viral recognition, DC populations are important for antigen presentation in the lymph node. This DC migration to the lymph node is mediated by complement signaling (154). In addition, complement activation during pulmonary viral infection has also been shown to facilitate T cell response (155, 156). Neutrophils do not significantly contribute to clearance of virus or infected cells, but a significant number of neutrophils are still recruited to the lung during viral infections (157). The recruitment of neutrophils is through both chemokines (IL-8 in human; KC in mouse) and complement (C5a) (158, 159). The activation of neutrophils stimulated by PAMPs, DAMPs, C5a and cytokines can prolong their life span through inhibition of apoptosis (160–162). At the same time, activated neutrophils during viral infection can still enhance their effector function, including degranulation, ROS, phagocytosis, NETosis (163). Although neutrophils are not the major cell type for viral clearance, they can still uptake opsonized virus through phagocytosis and induce ROS production (164). Neutrophils can facilitate antigen presentation by DCs or by themselves to induce adaptive immunity (165, 166). Interestingly, a subset of neutrophils with immune suppressive properties are shown to inhibit T cell proliferation as well as IFN production (167). The detrimental aspect of neutrophil recruitment is their contribution to pathogenesis during viral infection. The excessive neutrophils and NET formation in the lung during the viral infection can damage the AECs and lead to acute lung injury (168, 169). Overall, the innate immune system recognizes viral infection and initiates antiviral responses (Fig. 5). The activation of CTL for viral clearance is mediated by type I IFN production and antigen presentation from innate immunity.

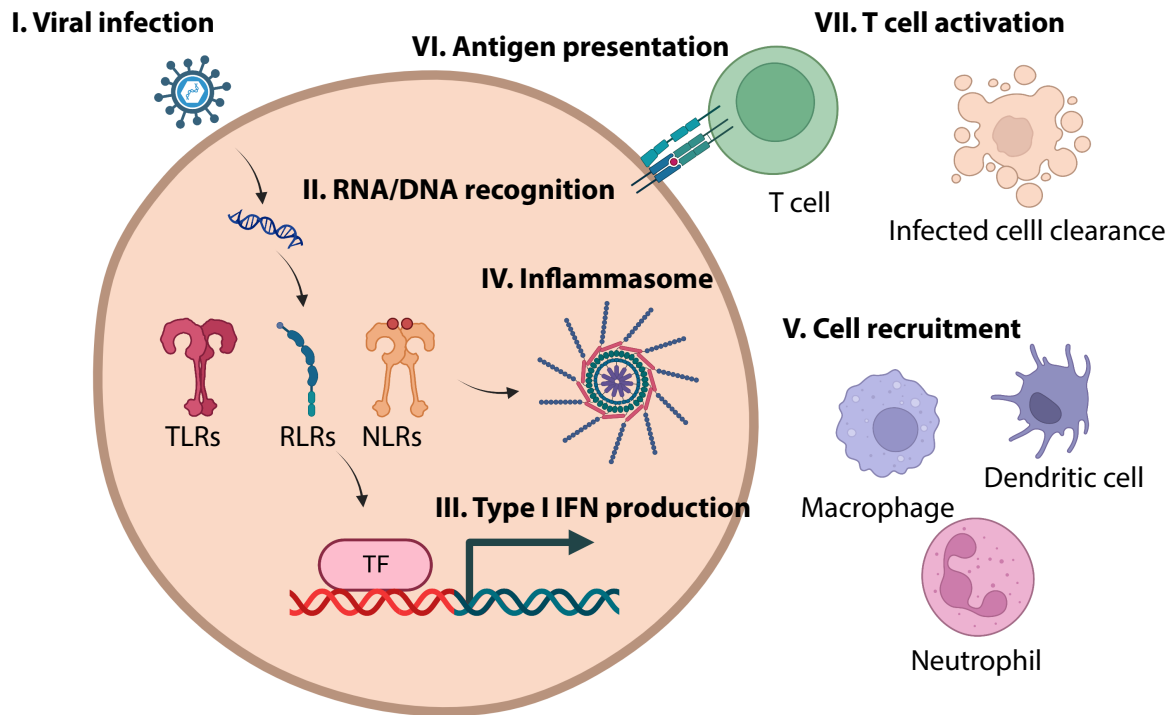


**Fig. 5 Viral infection and innate immune responses.**

The immune response against viral infection is most mediated by adaptive immunity, but host innate immunity still manages the initiation of the immune responses. I. Viral infection initiates with the membrane fusion to the target cell. II. Cytosolic viral RNA or DNA can be recognized by the Pattern recognition receptors (PRRs), including toll-like receptors (TLRs), RIG-I-like receptors (RLRs), and NOD-like receptors (NLRs). III. The stimulated PRRs activate transcriptional factors (TFs) for type I IFN production. IV. The NLRs also contribute to the inflammasome activation and downstream IL-1 maturation for inflammatory response. V. Viral infection leads to the recruitment of innate immune cells, including macrophages, neutrophils, and dendritic cells. VI. The dendritic cells moved to the lymph node can further stimulate the adaptive immunity for viral clearance. VII. Activated cytotoxic T cells can target and kill the virus-infected cells, and the phagocytes (macrophages and neutrophils) are involved in dead cells and viral particle clearance.

## Complexity of host environment during infection

### Airway commensals and their role in pathogen protection

Since oxygen acquisition through respiration is essential for the human body, environmental microbiomes are constantly inhaled and entered into the lung through our life. After acquiring microorganisms *in utero* (170), the microbiome from the upper respiratory tract (URT) gradually shapes our lung microbiota (171). The lung microbiota is contributed by the balance of local microbiome and new immigration, as well as their fitness in the lung environment (pH, temperature, oxygen, nutrient, local microbial competition, binding to AECs, escape from host immunity) (172). The lung microbiome has a much lower abundance of microbes ( $10^3$ - $10^5$  per gram of lung tissue) compared to the gut microbiome ( $10^{11}$ - $10^{12}$  per gram of content) (173, 174), however, the host lung environment still has a high variety of microbes during both homeostasis and infection. The colonization of microbiomes in the lung is dynamic and the growth of different microbiomes in the lung can be mutualism, commensalism or antagonism (175).

The growth and development of a bacterial biofilm can be determined through quorum sensing (QS) to distinguish their own population and other bacteria (176, 177). The competition between the commensal microbiome and new potential pathogens provides the beneficial protection for the host through colonization resistance. Colonization resistance to pathogens in the lung could be similar to what previous studies have shown in the gut (178). After entering the lung, pathogens need to compete for nutrients to be able to initiate growth. Nutrients and metabolites in the lung include sugar, short chain fatty acids (SCFAs) and metals, which can be used by both host cells and microbiomes and are essential for bacterial growth and biofilm formation (179–181). Commensal bacteria can outcompete other bacteria through direct elimination, as *Streptococcus pneumoniae* can target *Staphylococcus aureus* by production of hydrogen peroxide and downstream bacteriophage killing (182, 183). Another important role of commensal bacteria in the host defense is training the

immune response and maintaining innate immunity to prevent pathogen infection. Microbial associated molecular patterns (MAMPs) and PAMPs from the microbiomes provide the stimulation through PPRs to maintain homeostasis of innate immunity (184). Without the proper stimulations from commensals, hosts can be vulnerable to both bacterial and viral infections (185–187). The metabolites, including SCFAs, niacin, indole, retinoic acid, polysaccharide A, bile acid and taurine, from commensal microbes can promote host defense against pathogens and suppress immune response during homeostasis phase (188). Besides commensal bacteria, several viral and fungal species can also be detected in the healthy airway as part of the microbiome (189–192). However, whether these “commensal” viruses and fungi contribute to the immune response in the healthy host require further examinations. Thus, with the complexity of multiple microorganisms in the lung, the interactions between bacteria, fungi, virus and host immune system would determine the lung environment, including the balance of microbiota and host immune status.

#### Multi-microorganisms’ infections and host immune modulation

The microbiome interaction not only shapes the microbiota during the homeostasis condition but also greatly impacts both co-infection and superinfection condition. According to the definition from Centers for Disease Control and Prevention (CDC), the co-infection is the infection of two pathogens occurring at the same time. On the other hand, superinfection means that a secondary infection happens following the initial infection. This could potentially indicate that the previous infection provides some advantages for a secondary infection. For a superinfection, the combinations of pathogens can be bacterial-bacterial, viral-bacterial, viral-viral and viral-fungal. From the 1918 Spanish influenza, 2003 SARS, to 2019 Covid 19 pandemics, clinical reports have shown that the superinfection patients can have much worse clinical outcome and mortality (193–195). In this part, we will discuss about multi-pathogen infection and the interaction between pathogens and the host environment.

The virus-bacteria superinfection population has been extensively studied. The proposed mechanisms of the cause of virus-bacteria superinfection can be related to viral-induced lung damage and immune suppression in the post viral infected environment. During the viral infection, accumulated neutrophils and their NET formation can cause lung tissue damage but does not contribute to bacterial clearance (169, 196). Additionally, the disruption of airway-epithelial barrier provides a niche for bacterial colonization (197–199) and local airway injury can decrease mucociliary repulsion (200), which can also be benefit for bacterial evasion. The host derived nutrients released from the site of injury can further support bacterial growth and their biofilm formation (201, 202). Another important aspect of viral infections is their modulation of host innate and adaptive immunity. As previously mentioned, IL-10 and Th2 cytokines lead to the immune resolving phase after viral clearance to prevent excessive immune response-induced damage. However, during this time period, the immune suppression on the innate immunity could lead to bacterial escape from host immunity. The enhanced IL-10 production in the post viral environment can significantly increase the susceptibility to the bacterial secondary infection (203, 204). Previous literature has shown that viral infection can significantly decrease bacterial clearance by phagocytes (205, 206). Thus, viral induced host damage and defective immune responses can provide a niche for a secondary bacterial infection. However, the initial bacterial infection could be either beneficial or detrimental a subsequent viral infection. Increased expression of adhesion receptor, ICAM-1, on AECs after bacterial infection can facilitate viral infections as well as inflammation through the enhanced binding of human rhinoviruses (HRVs) to AECs (207, 208). Bacterial proteases from *Staphylococcus aureus* and *Aerococcus viridans* in the airway can degrade and activate hemagglutinin (HA), which is involved in fusion of virus and target cells to initiate viral infection (209, 210). On the other hand, the PAMPs from bacteria can prime host immunity to restrain viral infection for both innate and adaptive immunity. LPS-primed macrophages are more resistant to IAV infection with induced anti-viral response genes and antigen presentation ability (211). Decreased signal from commensal bacteria can increase



macrophage activation threshold in response to IFN stimulation for initiation of antiviral responses (212). Commensal bacteria have also been shown to contribute to inflammasome activation, DC migration, and T cell activation for anti-viral immunity (187). Thus, both virus and bacteria can provide increasing fitness for one or the other for initiation of infection, and the signal from commensal bacteria are important for antiviral immunity.

Bacterial and viral infections can also lead to a secondary fungal infection. The bacteria-fungus superinfection correlates with AEC damage as well as immune modulation in the post bacterial infection environment. Co-infection of commensal bacteria *Streptococcus orali* (*S. orali*) and fungal pathogen *C. albicans* caused increased tissue damage, inflammation, *S. orali* colonization and *C. albicans* dissemination (213). Other *in vitro* studies demonstrate biofilm expansion of *Streptococcus* species (*S. orali*, *S. gordonii* and *S. sanguinis*) and enhanced *C. albicans* evasion in the co-infection models (214). Bacteria can also promote fungal growth through production of volatile organic compounds. Dimethyl sulfide (DMS) from *Pseudomonas aeruginosa* can serve as nitrogen source for *Aspergillus fumigatus* growth (215). The co-infection of *C. albicans* and *Pseudomonas aeruginosa* (*P. aeruginosa*) has also been greatly studied due to their physical interaction during infection and contribution to pathogenesis. The antagonistic interaction between these two pathogens can be mediated by their QS system. The *P. aeruginosa* QS signal 3-oxo-C12-HSL and 2-heptyl-4-quinolone can inhibit *C. albicans* yeast-hyphae switch without affecting their growth (216, 217). Co-infection of *C. albicans* and *P. aeruginosa* provides a fitness advantage to *P. aeruginosa* by enhancing bacterial attachment and reducing oxidative stress from the host cells (218, 219). The viral-fungal superinfection has less frequency than viral-bacterial superinfection in the general population, but the patients with this type of superinfection have the worst prognosis compared to all the other superinfections (220–223). The detailed mechanisms about viral-fungal superinfection are not fully understood. The viral induced AEC damage could also provide a niche for initiation of fungal infection as the viral-bacterial superinfection. The IFN signaling during viral

infection and IL-10 during the immune resolving phase could alter innate immunity against fungal infection. Previous studies have proposed that the decreased neutrophils recruitment due to impair STAT3 pathway might contribute to the invasive aspergillosis (224). However, it is unclear whether the immune cells in the post viral infection environment also have defective antifungal effector functions up to date. The immune modulation in the post viral environment could also affect cellular functions, such as ROS and phagocytosis, in the innate immunity as we saw in the viral-bacterial superinfection (Fig. 6).

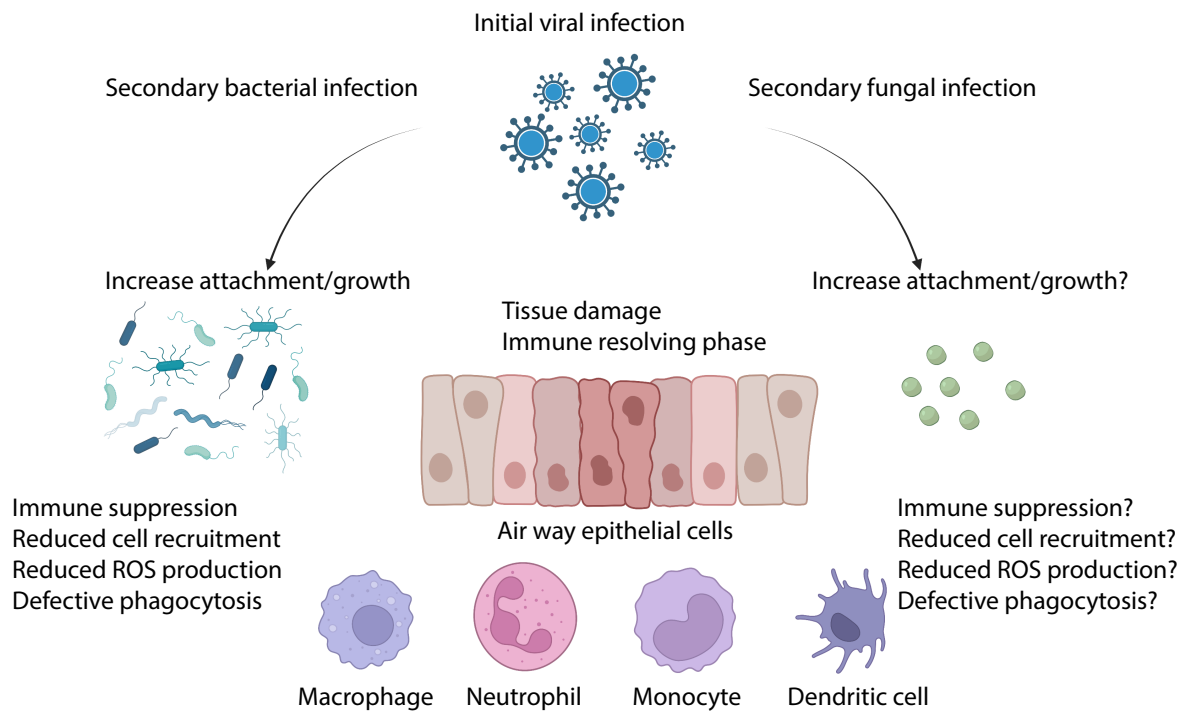


**Fig. 6 Comparison between viral-bacterial and viral-fungal superinfections.**

The initial viral infection can cause tissue damage in lung epithelial cells. And in the post-viral environment, the immune cells are under immune suppression in the immune resolving phase. Bacteria entering the lung in the post-viral environment can initiate secondary bacterial infection due to I. Increase bacterial attachment and nutrient availability at the site of damaged tissue. II. The immune suppression of the innate immune can provide an opportunity for bacterial colonization because of the lack of proper bacterial clearance from the host innate immunity. The cause of viral-fungal superinfection is largely unknown and the immune modulation of the host innate immunity will be the main topic in Chapter 2.

## Thesis overview

In this thesis, we will examine host immune response and immune modulation under different conditions. *Aspergillus fumigatus* (*A. fumigatus*) is a fungal pathogen that can infect the host through the growth of its conidia in the lung. Upon *A. fumigatus* infection, host innate immunity recognizes fungal infection through their pattern recognition receptors (PRRs). The downstream signal of PRRs initiates cytokine and chemokine production to recruit other immune cells to the lung for fungal clearance. The fungal conidia will be uptake by the professional phagocytes (alveolar macrophages (aMac), neutrophils, interstitial macrophages (iMac), monocytes, and conventional dendritic cell 2(cDC2)) through phagocytosis. The activated phagocytes with the signal from PRRs and cytokine induction can increase the acidification and maturation of phagolysosome for conidial killing. After the fungal clearance, the immune resolving phase will come in and switch the lung environment back to its homeostatic phase. With the aberrant immune modulation on the innate immunity, the escape of fungal conidia can lead to the growth of biofilm and invasive aspergillosis (IA) in the lung.

In Chapter 2, we established an Influenza A Virus-*A. fumigatus* (IAV-Af) superinfection mouse model to investigate the immune modulation of innate immunity in the post-viral environment. Previous literature hypothesis that viral-bacterial superinfection is due to tissue damage and immune suppression in the post-viral environment. However, even with many clinical reports about the high mortality and worse clinical outcome of viral-fungal superinfection, the mechanism related to viral-fungal superinfection is largely unknown. With our IAV-Af superinfection model, we showed there was no difference in immune cell recruitment and ROS production in the post-viral environment. Instead, the defective phagolysosome maturation in neutrophils and monocytes leads to a decrease in fungal killing, the development of *A. fumigatus* biofilm in the lung, and the high mortality of hosts in the IAV-Af superinfection group.

In Chapter 3, we characterize a potential fungal recognition receptor LysMD3 in antifungal immunity. LysMD3 has an ancient, structural conserved LysM domain, which is predicted for N-acetylglucosamine (GlcNAc) binding. Previous studies showed that human LYSMD3 can bind to chitin (oligomers of GlcNAc) and  $\beta$ -glucan and induce cytokine and chemokine production in the human epithelial cells. However, the previous studies of LysMD3 KO mice showed no *in vivo* phenotype with a variety of pathogens. In our works, we generated our LysMD3 KO mice and confirm the deletion of LysMD3 production with Western blotting. The LysMD3 KO mice have minor *A. fumigatus* killing defects in neutrophils and iMac but do not significantly affect overall fungal clearance and mice mortality. At the same time, we purified murine LysMD3 ectodomain with human Fc (LysMD3-Fc) to examine LysMD3 binding to *A. fumigatus* conidia and germling. The LysMD3-Fc protein can bind to both surfaces of *A. fumigatus* conidia and germling, but the galactosaminogalactan (GAG)-dependent binding on the fungal surface did not reflect the amount of chitin and  $\beta$ -glucan in the fungal cell wall.

The results presented in this dissertation covered the studies of antifungal innate immunity from immune cell recruitment to their fungal killing ability in different conditions (Chapter 2-3, Appendix IV-V). At the same time, we also investigate the cellularity of mice lungs and adaptive immunity in the allergic bronchopulmonary aspergillosis (ABPA) model (Appendix II-III).

## References

1. Lavelle EC, Murphy C, O'Neill LAJ, Creagh EM. 2010. The role of TLRs, NLRs, and RLRs in mucosal innate immunity and homeostasis. *Mucosal Immunol* 3:17–28.
2. Crystal RG, Randell SH, Engelhardt JF, Voynow J, Sunday ME. 2008. Airway epithelial cells: current concepts and challenges. *Proc Am Thorac Soc* 5:772–777.
3. Gong T, Liu L, Jiang W, Zhou R. 2020. DAMP-sensing receptors in sterile inflammation and inflammatory diseases. *Nat Rev Immunol* 20:95–112.
4. Iwasaki A, Foxman EF, Molony RD. 2017. Early local immune defences in the respiratory tract. *Nat Rev Immunol* 17:7–20.
5. Hussell T, Bell TJ. 2014. Alveolar macrophages: plasticity in a tissue-specific context. *Nature Reviews Immunology* 2014 14:2 14:81–93.
6. Hiemstra PS. 2007. The role of epithelial beta-defensins and cathelicidins in host defense of the lung. *Exp Lung Res* 33:537–542.
7. Bals R. 2000. Epithelial antimicrobial peptides in host defense against infection. *Respir Res* 1.
8. Losa García JE, Rodríguez FM, Martín De Cabo MR, García Salgado MJ, Losada JP, Villarón LG, López AJ, Arellano JLP. 1999. Evaluation of inflammatory cytokine secretion by human alveolar macrophages. *Mediators Inflamm* 8:43–51.
9. Nacu N, Luzina IG, Highsmith K, Lockatell V, Pochetuhenn K, Cooper ZA, Gillmeister MP, Todd NW, Atamas SP. 2008. Macrophages produce TGF-beta-induced (beta-ig-h3) following ingestion of apoptotic cells and regulate MMP14 levels and collagen turnover in fibroblasts. *J Immunol* 180:5036–5044.
10. Gomez Perdiguero E, Klapproth K, Schulz C, Busch K, Azzoni E, Crozet L, Garner H, Trouillet C, de Bruijn MF, Geissmann F, Rodewald HR. 2015. Tissue-resident macrophages originate from yolk-sac-derived erythro-myeloid progenitors. *Nature* 518:547–551.
11. Guillelliams M, de Kleer I, Henri S, Post S, Vanhoutte L, de Prijck S, Deswarte K, Malissen B, Hammad H, Lambrecht BN. 2013. Alveolar macrophages develop from fetal monocytes that differentiate into long-lived cells in the first week of life via GM-CSF. *J Exp Med* 210:1977–1992.

12. Hashimoto D, Chow A, Noizat C, Teo P, Beasley MB, Leboeuf M, Becker CD, See P, Price J, Lucas D, Greter M, Mortha A, Boyer SW, Forsberg EC, Tanaka M, van Rooijen N, García-Sastre A, Stanley ER, Ginhoux F, Frenette PS, Merad M. 2013. Tissue-resident macrophages self-maintain locally throughout adult life with minimal contribution from circulating monocytes. *Immunity* 38:792–804.
13. Davies LC, Jenkins SJ, Allen JE, Taylor PR. 2013. Tissue-resident macrophages. *Nat Immunol* 14:986–995.
14. Beck-Schimmer B, Schwendener R, Pasch T, Reyes L, Booy C, Schimmer RC. 2005. Alveolar macrophages regulate neutrophil recruitment in endotoxin-induced lung injury. *Respir Res* 6.
15. Pribul PK, Harker J, Wang B, Wang H, Tregoning JS, Schwarze J, Openshaw PJM. 2008. Alveolar macrophages are a major determinant of early responses to viral lung infection but do not influence subsequent disease development. *J Virol* 82:4441–4448.
16. Huynh M-LN, Fadok VA, Henson PM. 2002. Phosphatidylserine-dependent ingestion of apoptotic cells promotes TGF-beta1 secretion and the resolution of inflammation. *J Clin Invest* 109:41–50.
17. Cakarova L, Marsh LM, Wilhelm J, Mayer K, Grimminger F, Seeger W, Lohmeyer J, Herold S. 2009. Macrophage tumor necrosis factor-alpha induces epithelial expression of granulocyte-macrophage colony-stimulating factor: impact on alveolar epithelial repair. *Am J Respir Crit Care Med* 180:521–532.
18. Holt PG, Oliver J, Bilyk N, McMenamin C, McMenamin PG, Kraal G, Thepen T. 1993. Downregulation of the antigen presenting cell function(s) of pulmonary dendritic cells in vivo by resident alveolar macrophages. *J Exp Med* 177:397–407.
19. Strickland D, Kees UR, Holt PG. 1996. Regulation of T-cell activation in the lung: isolated lung T cells exhibit surface phenotypic characteristics of recent activation including down-modulated T-cell receptors, but are locked into the G0/G1 phase of the cell cycle. *Immunology* 87:242–249.
20. Thepen T, van Rooijen N, Kraal G. 1989. Alveolar macrophage elimination in vivo is associated with an increase in pulmonary immune response in mice. *J Exp Med* 170:499–509.
21. Shibata T, Makino A, Ogata R, Nakamura S, Ito T, Nagata K, Terauchi Y, Oishi T, Fujieda M, Takahashi Y, Ato M. 2020. Respiratory syncytial virus infection exacerbates pneumococcal pneumonia via Gas6/Axl-mediated macrophage polarization. *J Clin Invest* 130:3021–3037.

22. Roquilly A, Jacqueline C, Davieau M, Mollé A, Sadek A, Fourgeux C, Rooze P, Broquet A, Misme-Aucouturier B, Chaumette T, Vourc'h M, Cinotti R, Marec N, Gauttier V, McWilliam HEG, Altare F, Poschmann J, Villadangos JA, Asehnoune K. 2020. Alveolar macrophages are epigenetically altered after inflammation, leading to long-term lung immunoparalysis. *Nat Immunol* 21:636–648.
23. Ardain A, Marakalala MJ, Leslie A. 2020. Tissue-resident innate immunity in the lung. *Immunology* 159:245–256.
24. Condon TV, Sawyer RT, Fenton MJ, Riches DWH. 2011. Lung dendritic cells at the innate-adaptive immune interface. *J Leukoc Biol* 90:883–895.
25. Rohmann K, Tschernig T, Pabst R, Goldmann T, Drömann D. 2011. Innate immunity in the human lung: pathogen recognition and lung disease. *Cell Tissue Res* 343:167–174.
26. Leiva-Juárez MM, Kolls JK, Evans SE. 2018. Lung epithelial cells: therapeutically inducible effectors of antimicrobial defense. *Mucosal Immunol* 11:21–34.
27. Schneider DS, Hudson KL, Lin TY, Anderson K v. 1991. Dominant and recessive mutations define functional domains of Toll, a transmembrane protein required for dorsal-ventral polarity in the *Drosophila* embryo. *Genes Dev* 5:797–807.
28. Bell JK, Mullen GED, Leifer CA, Mazzoni A, Davies DR, Segal DM. 2003. Leucine-rich repeats and pathogen recognition in Toll-like receptors. *Trends Immunol* 24:528–533.
29. Takeuchi O, Hoshino K, Kawai T, Sanjo H, Takada H, Ogawa T, Takeda K, Akira S. 1999. Differential roles of TLR2 and TLR4 in recognition of gram-negative and gram-positive bacterial cell wall components. *Immunity* 11:443–451.
30. Underhill DM, Ozinsky A, Hajjar AM, Stevens A, Wilson CB, Bassetti M, Aderem A. 1999. The Toll-like receptor 2 is recruited to macrophage phagosomes and discriminates between pathogens. *Nature* 401:811–815.
31. Alexopoulou L, Holt AC, Medzhitov R, Flavell RA. 2001. Recognition of double-stranded RNA and activation of NF-kappaB by Toll-like receptor 3. *Nature* 413:732–738.
32. Poltorak A, He X, Smirnova I, Liu MY, van Huffel C, Du X, Birdwell D, Alejos E, Silva M, Galanos C, Freudenberg M, Ricciardi-Castagnoli P, Layton B, Beutler B. 1998. Defective LPS signaling in C3H/HeJ and C57BL/10ScCr mice: mutations in Tlr4 gene. *Science* 282:2085–2088.



33. Hayashi F, Smith KD, Ozinsky A, Hawn TR, Yi EC, Goodlett DR, Eng JK, Akira S, Underhill DM, Aderem A. 2001. The innate immune response to bacterial flagellin is mediated by Toll-like receptor 5. *Nature* 410:1099–1103.
34. Ozinsky A, Underhill DM, Fontenot JD, Hajjar AM, Smith KD, Wilson CB, Schroeder L, Aderem A. 2000. The repertoire for pattern recognition of pathogens by the innate immune system is defined by cooperation between toll-like receptors. *Proc Natl Acad Sci U S A* 97:13766–13771.
35. Sarvestani ST, Tate MD, Moffat JM, Jacobi AM, Behlke MA, Miller AR, Beckham SA, McCoy CE, Chen W, Minter JD, O’Keeffe M, John M, Williams BRG, Gantier MP. 2014. Inosine-Mediated Modulation of RNA Sensing by Toll-Like Receptor 7 (TLR7) and TLR8. *J Virol* 88:799–810.
36. Hemmi H, Takeuchi O, Kawai T, Kaisho T, Sato S, Sanjo H, Matsumoto M, Hoshino K, Wagner H, Takeda K, Akira S. 2000. A Toll-like receptor recognizes bacterial DNA. *Nature* 408:740–745.
37. Kawasaki T, Kawai T. 2014. Toll-like receptor signaling pathways. *Front Immunol* 5.
38. Takeda K, Akira S. 2005. Toll-like receptors in innate immunity. *Int Immunol* 17:1–14.
39. Akira S, Takeda K, Kaisho T. 2001. Toll-like receptors: critical proteins linking innate and acquired immunity. *Nat Immunol* 2:675–680.
40. Kumar H, Kawai T, Akira S. 2009. Toll-like receptors and innate immunity. *Biochem Biophys Res Commun* 388:621–625.
41. Goubau D, Deddouche S, Reis e Sousa C. 2013. Cytosolic sensing of viruses. *Immunity* 38:855–869.
42. Imaizumi T, Kumagai M, Taima K, Fujita T, Yoshida H, Satoh K. 2005. Involvement of retinoic acid-inducible gene-I in the IFN- $\gamma$ /STAT1 signalling pathway in BEAS-2B cells. *Eur Respir J* 25:1077–1083.
43. Yount JS, Moran TM, López CB. 2007. Cytokine-independent upregulation of MDA5 in viral infection. *J Virol* 81:7316–7319.
44. Loo YM, Gale M. 2011. Immune signaling by RIG-I-like receptors. *Immunity* 34:680–692.

45. Rehwinkel J, Gack MU. 2020. RIG-I-like receptors: their regulation and roles in RNA sensing. *Nat Rev Immunol* 20:537–551.
46. Wilmanski JM, Petnicki-Ocwieja T, Kobayashi KS. 2008. NLR proteins: integral members of innate immunity and mediators of inflammatory diseases. *J Leukoc Biol* 83:13–30.
47. Franchi L, Warner N, Viani K, Nuñez G. 2009. Function of Nod-like receptors in microbial recognition and host defense. *Immunol Rev* 227:106–128.
48. Chaput C, Sander LE, Suttorp N, Opitz B. 2013. NOD-Like Receptors in Lung Diseases. *Front Immunol* 4.
49. Briard B, Place DE, Kanneganti TD. 2020. DNA Sensing in the Innate Immune Response. *Physiology (Bethesda)* 35:112–124.
50. Eaglesham JB, Kranzusch PJ. 2020. Conserved strategies for pathogen evasion of cGAS-STING immunity. *Curr Opin Immunol* 66:27–34.
51. Liu N, Pang X, Zhang H, Ji P. 2022. The cGAS-STING Pathway in Bacterial Infection and Bacterial Immunity. *Front Immunol* 12.
52. Jin T, Perry A, Jiang J, Smith P, Curry JA, Unterholzner L, Jiang Z, Horvath G, Rathinam VA, Johnstone RW, Hornung V, Latz E, Bowie AG, Fitzgerald KA, Xiao TS. 2012. Structures of the HIN domain:DNA complexes reveal ligand binding and activation mechanisms of the AIM2 inflammasome and IFI16 receptor. *Immunity* 36:561–571.
53. Malik A, Kanneganti TD. 2017. Inflammasome activation and assembly at a glance. *J Cell Sci* 130:3955–3963.
54. Almine JF, O’Hare CAJ, Dunphy G, Haga IR, Naik RJ, Atrih A, Connolly DJ, Taylor J, Kelsall IR, Bowie AG, Beard PM, Unterholzner L. 2017. IFI16 and cGAS cooperate in the activation of STING during DNA sensing in human keratinocytes. *Nat Commun* 8.
55. Goyal S, Castrillón-Betancur JC, Klaile E, Slevogt H. 2018. The Interaction of Human Pathogenic Fungi With C-Type Lectin Receptors. *Front Immunol* 9.
56. Mnich ME, van Dalen R, van Sorge NM. 2020. C-Type Lectin Receptors in Host Defense Against Bacterial Pathogens. *Front Cell Infect Microbiol* 10.

57. Bermejo-Jambrina M, Eder J, Helgers LC, Hertoghs N, Nijmeijer BM, Stunnenberg M, Geijtenbeek TBH. 2018. C-Type Lectin Receptors in Antiviral Immunity and Viral Escape. *Front Immunol* 9.
58. Brown GD, Denning DW, Gow NAR, Levitz SM, Netea MG, White TC. 2012. Hidden killers: human fungal infections. *Sci Transl Med* 4.
59. Pathakumari B, Liang G, Liu W. 2020. Immune defence to invasive fungal infections: A comprehensive review. *Biomed Pharmacother* 130.
60. Lionakis MS, Kontoyiannis DP. 2003. Glucocorticoids and invasive fungal infections. *Lancet* 362:1828–1838.
61. Low CY, Rotstein C. 2011. Emerging fungal infections in immunocompromised patients. *F1000 Med Rep* 3.
62. Drummond RA, Gaffen SL, Hise AG, Brown GD. 2015. Innate Defense against Fungal Pathogens. *Cold Spring Harb Perspect Med* 5:1–19.
63. Baltussen TJH, Zoll J, Verweij PE, Melchers WJG. 2019. Molecular Mechanisms of Conidial Germination in *Aspergillus* spp. *Microbiol Mol Biol Rev* 84.
64. Park SJ, Mehrad B. 2009. Innate immunity to *Aspergillus* species. *Clin Microbiol Rev* 22:535–551.
65. Meier A, Kirschning CJ, Nikolaus T, Wagner H, Heesemann J, Ebel F. 2003. Toll-like receptor (TLR) 2 and TLR4 are essential for *Aspergillus*-induced activation of murine macrophages. *Cell Microbiol* 5:561–570.
66. Bellocchio S, Moretti S, Perruccio K, Fallarino F, Bozza S, Montagnoli C, Mosci P, Lipford GB, Pitzurra L, Romani L. 2004. TLRs govern neutrophil activity in aspergillosis. *J Immunol* 173:7406–7415.
67. Werner JL, Metz AE, Horn D, Schoeb TR, Hewitt MM, Schwiebert LM, Faro-Trindade I, Brown GD, Steele C. 2009. Requisite role for the dectin-1 beta-glucan receptor in pulmonary defense against *Aspergillus fumigatus*. *J Immunol* 182:4938–4946.
68. Thammasit P, Sripetchwandee J, Nosanchuk JD, Chattipakorn SC, Chattipakorn N, Youngchim S. 2021. Cytokine and Chemokine Responses in Invasive Aspergillosis Following Hematopoietic Stem Cell Transplantation: Past Evidence for Future Therapy of Aspergillosis. *J Fungi (Basel)* 7.

69. Davies LC, Jenkins SJ, Allen JE, Taylor PR. 2013. Tissue-resident macrophages. *Nat Immunol* 14:986–995.
70. Al-Bader N, Sheppard DC. 2016. Aspergillosis and stem cell transplantation: An overview of experimental pathogenesis studies. *Virulence* 7:950–966.
71. Fu YL, Harrison RE. 2021. Microbial Phagocytic Receptors and Their Potential Involvement in Cytokine Induction in Macrophages. *Front Immunol* 12.
72. Ibrahim-Granet O, Philippe B, Boleti H, Boisvieux-Ulrich E, Grenet D, Stern M, Latgé JP. 2003. Phagocytosis and intracellular fate of *Aspergillus fumigatus* conidia in alveolar macrophages. *Infect Immun* 71:891–903.
73. Philippe B, Ibrahim-Granet O, Prévost MC, Gougerot-Pocidalo MA, Perez MS, van der Meeren A, Latgé JP. 2003. Killing of *Aspergillus fumigatus* by alveolar macrophages is mediated by reactive oxidant intermediates. *Infect Immun* 71:3034–3042.
74. Heung LJ. 2020. Monocytes and the Host Response to Fungal Pathogens. *Front Cell Infect Microbiol* 10.
75. Espinosa V, Jhingran A, Dutta O, Kasahara S, Donnelly R, Du P, Rosenfeld J, Leiner I, Chen CC, Ron Y, Hohl TM, Rivera A. 2014. Inflammatory monocytes orchestrate innate antifungal immunity in the lung. *PLoS Pathog* 10.
76. Chertov O, Ueda H, Xu LL, Tani K, Murphy WJ, Wang JM, Howard OMZ, Sayers TJ, Oppenheim JJ. 1997. Identification of human neutrophil-derived cathepsin G and azurocidin/CAP37 as chemoattractants for mononuclear cells and neutrophils. *J Exp Med* 186:739–747.
77. Bennouna S, Bliss SK, Curiel TJ, Denkers EY. 2003. Cross-talk in the innate immune system: neutrophils instruct recruitment and activation of dendritic cells during microbial infection. *J Immunol* 171:6052–6058.
78. Tsuda Y, Takahashi H, Kobayashi M, Hanafusa T, Herndon DN, Suzuki F. 2004. Three different neutrophil subsets exhibited in mice with different susceptibilities to infection by methicillin-resistant *Staphylococcus aureus*. *Immunity* 21:215–226.
79. Margalit A, Kavanagh K. 2015. The innate immune response to *Aspergillus fumigatus* at the alveolar surface. *FEMS Microbiol Rev* 39:670–687.
80. King J, Henriët SSV, Warris A. 2016. Aspergillosis in Chronic Granulomatous Disease. *J Fungi (Basel)* 2.

81. Gazendam RP, van Hamme JL, Tool ATJ, Hoogenboezem M, van den Berg JM, Prins JM, Vitkov L, van de Veerdonk FL, van den Berg TK, Roos D, Kuijpers TW. 2016. Human Neutrophils Use Different Mechanisms To Kill *Aspergillus fumigatus* Conidia and Hyphae: Evidence from Phagocyte Defects. *J Immunol* 196:1272–1283.
82. Lee WL, Harrison RE, Grinstein S. 2003. Phagocytosis by neutrophils. *Microbes Infect* 5:1299–1306.
83. Diamond RD, Clark RA. 1982. Damage to *Aspergillus fumigatus* and *Rhizopus oryzae* hyphae by oxidative and nonoxidative microbicidal products of human neutrophils in vitro. *Infect Immun* 38:487–495.
84. Bruns S, Kniemeyer O, Hasenberg M, Aimaniananda V, Nietzsche S, Thywien A, Jeron A, Latgé JP, Brakhage AA, Gunzer M. 2010. Production of extracellular traps against *Aspergillus fumigatus* in vitro and in infected lung tissue is dependent on invading neutrophils and influenced by hydrophobin RodA. *PLoS Pathog* 6:1–18.
85. Park SJ, Burdick MD, Brix WK, Stoler MH, Askew DS, Strieter RM, Mehrad B. 2010. Neutropenia enhances lung dendritic cell recruitment in response to *Aspergillus* via a cytokine-to-chemokine amplification loop. *J Immunol* 185:6190–6197.
86. Min J, Yang D, Kim M, Haam K, Yoo A, Choi JH, Schraml BU, Kim YS, Kim D, Kang SJ. 2018. Inflammation induces two types of inflammatory dendritic cells in inflamed lymph nodes. *Exp Mol Med* 50.
87. Figueiredo RT, Carneiro LAM, Bozza MT. 2011. Fungal surface and innate immune recognition of filamentous fungi. *Front Microbiol* 2.
88. Fliesser M, Wallstein M, Kurzai O, Einsele H, Löffler J. 2016. Hypoxia attenuates anti-*Aspergillus fumigatus* immune responses initiated by human dendritic cells. *Mycoses* 59:503–508.
89. Gafa V, Lande R, Gagliardi MC, Severa M, Giacomini E, Remoli ME, Nisini R, Ramoni C, di Francesco P, Aldebert D, Grillot R, Coccia EM. 2006. Human dendritic cells following *Aspergillus fumigatus* infection express the CCR7 receptor and a differential pattern of interleukin-12 (IL-12), IL-23, and IL-27 cytokines, which lead to a Th1 response. *Infect Immun* 74:1480–1489.
90. Ramirez-Ortiz ZG, Lee CK, Wang JP, Boon L, Specht CA, Levitz SM. 2011. A nonredundant role for plasmacytoid dendritic cells in host defense against the human fungal pathogen *Aspergillus fumigatus*. *Cell Host Microbe* 9:415–424.
91. Bozza S, Gaziano R, Spreca A, Bacci A, Montagnoli C, di Francesco P, Romani L.

2002. Dendritic cells transport conidia and hyphae of *Aspergillus fumigatus* from the airways to the draining lymph nodes and initiate disparate Th responses to the fungus. *J Immunol* 168:1362–1371.
92. Cenci E, Mencacci A, del Sero G, Bacci A, Montagnoli C, D'Ostiani CF, Mosci P, Bachmann M, Bistoni F, Kopf M, Romani L. 1999. Interleukin-4 causes susceptibility to invasive pulmonary aspergillosis through suppression of protective type I responses. *J Infect Dis* 180:1957–1968.
93. Dewi IMW, van de Veerdonk FL, Gresnigt MS. 2017. The Multifaceted Role of T-Helper Responses in Host Defense against *Aspergillus fumigatus*. *J Fungi (Basel)* 3.
94. Fei M, Bhatia S, Oriss TB, Yarlagadda M, Khare A, Akira S, Saijod S, Iwakura Y, Fallert Junecko BA, Reinhart TA, Foreman O, Ray P, Kolls J, Ray A. 2011. TNF-alpha from inflammatory dendritic cells (DCs) regulates lung IL-17A/IL-5 levels and neutrophilia versus eosinophilia during persistent fungal infection. *Proc Natl Acad Sci U S A* 108:5360–5365.
95. Chamilos G, Ganguly D, Lande R, Gregorio J, Meller S, Goldman WE, Gilliet M, Kontoyiannis DP. 2010. Generation of IL-23 producing dendritic cells (DCs) by airborne fungi regulates fungal pathogenicity via the induction of T(H)-17 responses. *PLoS One* 5.
96. Pagano L, Caira M, Candoni A, Offidani M, Martino B, Specchia G, Pastore D, Stanzani M, Cattaneo C, Fanci R, Caramatti C, Rossini F, Luppi M, Potenza L, Ferrara F, Mitra ME, Fadda RM, Invernizzi R, Aloisi T, Picardi M, Bonini A, Vacca A, Chierichini A, Melillo L, de Waure C, Fianchi L, Riva M, Leone G, Aversa F, Nosari A. 2010. Invasive aspergillosis in patients with acute myeloid leukemia: a SEIFEM-2008 registry study. *Haematologica* 95:644–650.
97. Singh N, Paterson DL. 2005. *Aspergillus* infections in transplant recipients. *Clin Microbiol Rev* 18:44–69.
98. Dhamija E, Meena P, Ramalingam V, Sahoo R, Rastogi S, Thulkar S. 2020. Chemotherapy-induced pulmonary complications in cancer: Significance of clinicroadiological correlation. *Indian J Radiol Imaging* 30:20–26.
99. Barkati S, Dufresne SF, Belanger S, Vadnais B, Bergeron J, Labbe AC, Laverdiere M. 2014. Incidence of invasive aspergillosis following remission-induction chemotherapy for acute leukemia: a retrospective cohort study in a single Canadian tertiary care centre. *CMAJ Open* 2:E86–E93.
100. Rhen T, Cidlowski JA. 2005. Antiinflammatory action of glucocorticoids--new mechanisms for old drugs. *N Engl J Med* 353:1711–1723.

101. Fauci AS. 1976. Mechanisms of corticosteroid action on lymphocyte subpopulations. II. Differential effects of in vivo hydrocortisone, prednisone and dexamethasone on in vitro expression of lymphocyte function. *Clin Exp Immunol* 24:54.
102. Fauci AS, Dale DC, Balow JE. 1976. Glucocorticosteroid therapy: mechanisms of action and clinical considerations. *Ann Intern Med* 84:304–315.
103. Liles W, Dale D, Klebanoff S. 1995. Glucocorticoids Inhibit Apoptosis of Human Neutrophils. *Blood* 86:3181–3188.
104. Nathan C. 2006. Neutrophils and immunity: challenges and opportunities. *Nat Rev Immunol* 6:173–182.
105. S. Saffar A, Ashdown H, S. Gounni A. 2011. The molecular mechanisms of glucocorticoids-mediated neutrophil survival. *Curr Drug Targets* 12:556–562.
106. Ray KP, Farrow S, Daly M, Talabot F, Searle N. 1997. Induction of the E-selectin promoter by interleukin 1 and tumour necrosis factor alpha, and inhibition by glucocorticoids. *Biochem J* 328 ( Pt 2):707–715.
107. Shimoyama M, Shimmura S, Tsubota K, Oguchi Y. 1997. Suppression of nuclear factor kappa B and CD18-mediated leukocyte adhesion to the corneal endothelium by dexamethasone. *Invest Ophthalmol Vis Sci* 38:2427–2431.
108. Boss B, Neeck G, Engelhardt B, Riedel W. 1999. Influence of corticosteroids on neutrophils, lymphocytes, their subsets, and T-cell activity markers in patients with active rheumatoid arthritis, compared to healthy controls. *Ann N Y Acad Sci* 876:198–200.
109. Goulding NJ, Euzger HS, Butt SK, Perretti M. 1998. Novel pathways for glucocorticoid effects on neutrophils in chronic inflammation. *Inflamm Res* 47 Suppl 3.
110. Rinehart JJ, Balcerzak SP, Sagone AL, LoBuglio AF. 1974. Effects of corticosteroids on human monocyte function. *J Clin Invest* 54:1337–1343.
111. Schaffner A. 1985. Therapeutic concentrations of glucocorticoids suppress the antimicrobial activity of human macrophages without impairing their responsiveness to gamma interferon. *J Clin Invest* 76:1755–1764.
112. Long F, Wang YX, Liu L, Zhou J, Cui RY, Jiang CL. 2005. Rapid nongenomic inhibitory effects of glucocorticoids on phagocytosis and superoxide anion production by macrophages. *Steroids* 70:55–61.

113. Auphan N, DiDonato JA, Rosette C, Helmberg A, Karin M. 1995. Immunosuppression by glucocorticoids: inhibition of NF-kappa B activity through induction of I kappa B synthesis. *Science* 270:286–290.
114. Aghai ZH, Kumar S, Farhath S, Kumar MA, Saslow J, Nakhla T, Eydelman R, Strande L, Stahl G, Hewitt C, Nesin M, Rahman I. 2006. Dexamethasone suppresses expression of Nuclear Factor-kappaB in the cells of tracheobronchial lavage fluid in premature neonates with respiratory distress. *Pediatr Res* 59:811–815.
115. Duncan MD, Wilkes DS. 2005. Transplant-related immunosuppression: a review of immunosuppression and pulmonary infections. *Proc Am Thorac Soc* 2:449–455.
116. Hayashi R, Wada H, Ito K, Adcock IM. 2004. Effects of glucocorticoids on gene transcription. *Eur J Pharmacol* 500:51–62.
117. Ronchetti S, Ricci E, Migliorati G, Gentili M, Riccardi C. 2018. How Glucocorticoids Affect the Neutrophil Life. *International Journal of Molecular Sciences* 2018, Vol 19, Page 4090 19:4090.
118. Rozkova D, Horvath R, Bartunkova J, Spisek R. 2006. Glucocorticoids severely impair differentiation and antigen presenting function of dendritic cells despite upregulation of Toll-like receptors. *Clin Immunol* 120:260–271.
119. Kamada N, Seo SU, Chen GY, Núñez G. 2013. Role of the gut microbiota in immunity and inflammatory disease. *Nat Rev Immunol* 13:321–335.
120. Woo V, Eshleman EM, Rice T, Whitt J, Vallance BA, Alenghat T. 2019. Microbiota Inhibit Epithelial Pathogen Adherence by Epigenetically Regulating C-Type Lectin Expression. *Front Immunol* 10.
121. Abt MC, Pamer EG. 2014. Commensal bacteria mediated defenses against pathogens. *Curr Opin Immunol* 29:16–22.
122. Khan R, Petersen FC, Shekhar S. 2019. Commensal Bacteria: An Emerging Player in Defense Against Respiratory Pathogens. *Front Immunol* 10.
123. Prina E, Ranzani OT, Torres A. 2015. Community-acquired pneumonia. *Lancet* 386:1097–1108.
124. Peterson E, Kaur P. 2018. Antibiotic Resistance Mechanisms in Bacteria: Relationships Between Resistance Determinants of Antibiotic Producers, Environmental Bacteria, and Clinical Pathogens. *Front Microbiol* 9.



125. de Nardo D. 2015. Toll-like receptors: Activation, signalling and transcriptional modulation. *Cytokine* 74:181–189.
126. Kany S, Vollrath JT, Relja B. 2019. Cytokines in Inflammatory Disease. *Int J Mol Sci* 20.
127. Sha W, Mitoma H, Hanabuchi S, Bao M, Weng L, Sugimoto N, Liu Y, Zhang Z, Zhong J, Sun B, Liu YJ. 2014. Human NLRP3 inflammasome senses multiple types of bacterial RNAs. *Proc Natl Acad Sci U S A* 111:16059–16064.
128. Ballinger MN, Paine R, Serezani CHC, Aronoff DM, Choi ES, Standiford TJ, Toews GB, Moore BB. 2006. Role of granulocyte macrophage colony-stimulating factor during gram-negative lung infection with *Pseudomonas aeruginosa*. *Am J Respir Cell Mol Biol* 34:766–774.
129. McCormick TS, Hejal RB, Leal LO, Ghannoum MA. 2022. GM-CSF: Orchestrating the Pulmonary Response to Infection. *Front Pharmacol* 12.
130. MacMicking J, Xie QW, Nathan C. 1997. Nitric oxide and macrophage function. *Annu Rev Immunol* 15:323–350.
131. Nagre N, Cong X, Pearson AC, Zhao X. 2019. Alveolar Macrophage Phagocytosis and Bacteria Clearance in Mice. *J Vis Exp* 2019.
132. Yin G, Zhao C, Pei W. 2022. Crosstalk between macrophages and innate lymphoid cells (ILCs) in diseases. *Int Immunopharmacol* 110.
133. Roszer T. 2015. Understanding the Mysterious M2 Macrophage through Activation Markers and Effector Mechanisms. *Mediators Inflamm* 2015.
134. Labonte AC, Tosello-Tramont AC, Hahn YS. 2014. The role of macrophage polarization in infectious and inflammatory diseases. *Mol Cells* 37:275–285.
135. Benoit M, Desnues B, Mege J-L. 2008. Macrophage polarization in bacterial infections. *J Immunol* 181:3733–3739.
136. Pollard JW. 2009. Trophic macrophages in development and disease. *Nat Rev Immunol* 9:259–270.
137. Chen X, Liu Y, Gao Y, Shou S, Chai Y. 2021. The roles of macrophage polarization in the host immune response to sepsis. *Int Immunopharmacol* 96.
138. Teng TS, Ji AL, Ji XY, Li YZ. 2017. Neutrophils and Immunity: From Bactericidal Action to Being Conquered. *J Immunol Res* 2017.

139. Shen XF, Cao K, Jiang JP, Guan WX, Du JF. 2017. Neutrophil dysregulation during sepsis: an overview and update. *J Cell Mol Med* 21:1687–1697.
140. Bhan C, Dipankar P, Chakraborty P, Sarangi PP. 2016. Role of cellular events in the pathophysiology of sepsis. *Inflamm Res* 65:853–868.
141. Kellner M, Noonepalle S, Lu Q, Srivastava A, Zemskov E, Black SM. 2017. ROS Signaling in the Pathogenesis of Acute Lung Injury (ALI) and Acute Respiratory Distress Syndrome (ARDS). *Adv Exp Med Biol* 967:105–137.
142. Yoo JK, Kim TS, Hufford MM, Braciale TJ. 2013. Viral infection of the lung: host response and sequelae. *J Allergy Clin Immunol* 132:1263–1276.
143. Bowie AG, Unterholzner L. 2008. Viral evasion and subversion of pattern-recognition receptor signalling. *Nat Rev Immunol* 8:911–922.
144. Carty M, Bowie AG. 2010. Recent insights into the role of Toll-like receptors in viral infection. *Clin Exp Immunol* 161:397–406.
145. Levy DE, Marié I, Smith E, Prakash A. 2002. Enhancement and diversification of IFN induction by IRF-7-mediated positive feedback. *J Interferon Cytokine Res* 22:87–93.
146. Santoro MG, Rossi A, Amici C. 2003. NF-kappaB and virus infection: who controls whom. *EMBO J* 22:2552–2560.
147. Zhao C, Zhao W. 2020. NLRP3 Inflammasome-A Key Player in Antiviral Responses. *Front Immunol* 11.
148. Li Z, Cai S, Sun Y, Li L, Ding S, Wang X. 2020. When STING Meets Viruses: Sensing, Trafficking and Response. *Front Immunol* 11.
149. Welsh RM, Bahl K, Marshall HD, Urban SL. 2012. Type 1 Interferons and Antiviral CD8 T-Cell Responses. *PLoS Pathog* 8.
150. Thompson MR, Kaminski JJ, Kurt-Jones EA, Fitzgerald KA. 2011. Pattern recognition receptors and the innate immune response to viral infection. *Viruses* 3:920–940.
151. Asselin-Paturel C, Brizard G, Chemin K, Boonstra A, O’Garra A, Vicari A, Trinchieri G. 2005. Type I interferon dependence of plasmacytoid dendritic cell activation and migration. *J Exp Med* 201:1157–1167.

152. Asselin-Paturel C, Boonstra A, Dalod M, Durand I, Yessaad N, Dezutter-Dambuyant C, Vicari A, O'Garra A, Biron C, Brière F, Trinchieri G. 2001. Mouse type I IFN-producing cells are immature APCs with plasmacytoid morphology. *Nat Immunol* 2:1144–1150.
153. Frenz T, Graalmann L, Detje CN, Döring M, Grabski E, Scheu S, Kalinke U. 2014. Independent of plasmacytoid dendritic cell (pDC) infection, pDC triggered by virus-infected cells mount enhanced type I IFN responses of different composition as opposed to pDC stimulated with free virus. *J Immunol* 193:2496–2503.
154. Kandasamy M, Ying PC, Ho AWS, Sumatoh HR, Schlitzer A, Hughes TR, Kemeny DM, Morgan BP, Ginhoux F, Sivasankar B. 2013. Complement mediated signaling on pulmonary CD103(+) dendritic cells is critical for their migratory function in response to influenza infection. *PLoS Pathog* 9.
155. Stoermer KA, Morrison TE. 2011. Complement and viral pathogenesis. *Virology* 411:362–373.
156. Kopf M, Abel B, Gallimore A, Carroll M, Bachmann MF. 2002. Complement component C3 promotes T-cell priming and lung migration to control acute influenza virus infection. *Nat Med* 8:373–378.
157. McNamara PS, Ritson P, Selby A, Hart CA, Smyth RL. 2003. Bronchoalveolar lavage cellularity in infants with severe respiratory syncytial virus bronchiolitis. *Arch Dis Child* 88:922–926.
158. Nuriev R, Johansson C. 2019. Chemokine regulation of inflammation during respiratory syncytial virus infection. *F1000Res* 8.
159. Garcia CC, Weston-Davies W, Russo RC, Tavares LP, Rachid MA, Alves-Filho JC, Machado A v., Ryffel B, Nunn MA, Teixeira MM. 2013. Complement C5 activation during influenza A infection in mice contributes to neutrophil recruitment and lung injury. *PLoS One* 8.
160. Lindemans CA, Coffey PJ, Schellens IMM, de Graaff PMA, Kimpen JLL, Koenderman L. 2006. Respiratory syncytial virus inhibits granulocyte apoptosis through a phosphatidylinositol 3-kinase and NF-kappaB-dependent mechanism. *J Immunol* 176:5529–5537.
161. Kato T, Kitagawa S. 2006. Regulation of neutrophil functions by proinflammatory cytokines. *Int J Hematol* 84:205–209.

162. Ehrnthaller C, Braumüller S, Kellermann S, Gebhard F, Perl M, Huber-Lang M. 2021. Complement Factor C5a Inhibits Apoptosis of Neutrophils-A Mechanism in Polytrauma? *J Clin Med* 10.
163. Johansson C, Kirsebom FCM. 2021. Neutrophils in respiratory viral infections. *Mucosal Immunol* 14:815–827.
164. LeVine AM, Elliott J, Whitsett JA, Srikiatkachorn A, Crouch E, DeSilva N, Korfhagen T. 2004. Surfactant protein-d enhances phagocytosis and pulmonary clearance of respiratory syncytial virus. *Am J Respir Cell Mol Biol* 31:193–199.
165. Schuster S, Hurrell B, Tacchini-Cottier F. 2013. Crosstalk between neutrophils and dendritic cells: a context-dependent process. *J Leukoc Biol* 94:671–675.
166. Hufford MM, Richardson G, Zhou H, Manicassamy B, García-Sastre A, Enelow RI, Braciale TJ. 2012. Influenza-infected neutrophils within the infected lungs act as antigen presenting cells for anti-viral CD8(+) T cells. *PLoS One* 7.
167. Hong CW. 2017. Current Understanding in Neutrophil Differentiation and Heterogeneity. *Immune Netw* 17:298–306.
168. Camp J v., Jonsson CB. 2017. A Role for Neutrophils in Viral Respiratory Disease. *Front Immunol* 8.
169. Narasaraju T, Yang E, Samy RP, Ng HH, Poh WP, Liew AA, Phoon MC, van Rooijen N, Chow VT. 2011. Excessive neutrophils and neutrophil extracellular traps contribute to acute lung injury of influenza pneumonitis. *Am J Pathol* 179:199–210.
170. al Alam D, Danopoulos S, Grubbs B, Ali NA tikah BM, MacAogain M, Chotirmall SH, Warburton D, Gaggar A, Ambalavanan N, Lal CV. 2020. Human Fetal Lungs Harbor a Microbiome Signature. *Am J Respir Crit Care Med* 201:1002–1006.
171. Gleeson K, Eggli DF, Maxwell SL. 1997. Quantitative aspiration during sleep in normal subjects. *Chest* 111:1266–1272.
172. Yagi K, Huffnagle GB, Lukacs NW, Asai N. 2021. The Lung Microbiome during Health and Disease. *Int J Mol Sci* 22.
173. Remot A, Descamps D, Noordine ML, Boukadiri A, Mathieu E, Robert V, Riffault S, Lambrecht B, Langella P, Hammad H, Thomas M. 2017. Bacteria isolated from lung modulate asthma susceptibility in mice. *ISME J* 11:1061–1074.
174. Lagier JC, Million M, Hugon P, Armougom F, Raoult D. 2012. Human gut microbiota: repertoire and variations. *Front Cell Infect Microbiol* 2:136.

175. Berg G, Rybakova D, Fischer D, Cernava T, Vergès MCC, Charles T, Chen X, Cocolin L, Eversole K, Corral GH, Kazou M, Kinkel L, Lange L, Lima N, Loy A, Macklin JA, Maguin E, Mauchline T, McClure R, Mitter B, Ryan M, Sarand I, Smidt H, Schelkle B, Roume H, Kiran GS, Selvin J, Souza RSC de, van Overbeek L, Singh BK, Wagner M, Walsh A, Sessitsch A, Schlöter M. 2020. Microbiome definition re-visited: old concepts and new challenges. *Microbiome* 8.
176. Singh PK, Schaefer AL, Parsek MR, Moninger TO, Welsh MJ, Greenberg EP. 2000. Quorum-sensing signals indicate that cystic fibrosis lungs are infected with bacterial biofilms. *Nature* 407:762–764.
177. Mashima I, Nakazawa F. 2014. The influence of oral *Veillonella* species on biofilms formed by *Streptococcus* species. *Anaerobe* 28:54–61.
178. Lawley TD, Walker AW. 2013. Intestinal colonization resistance. *Immunology* 138:1–11.
179. She P, Wang Y, Liu Y, Tan F, Chen L, Luo Z, Wu Y. 2019. Effects of exogenous glucose on *Pseudomonas aeruginosa* biofilm formation and antibiotic resistance. *Microbiologyopen* 8.
180. Alemao CA, Budden KF, Gomez HM, Rehman SF, Marshall JE, Shukla SD, Donovan C, Forster SC, Yang IA, Keely S, Mann ER, el Omar EM, Belz GT, Hansbro PM. 2021. Impact of diet and the bacterial microbiome on the mucous barrier and immune disorders. *Allergy* 76:714–734.
181. Healy C, Munoz-Wolf N, Strydom J, Faherty L, Williams NC, Kenny S, Donnelly SC, Cloonan SM. 2021. Nutritional immunity: the impact of metals on lung immune cells and the airway microbiome during chronic respiratory disease. *Respir Res* 22.
182. Regev-Yochay G, Trzciński K, Thompson CM, Malley R, Lipsitch M. 2006. Interference between *Streptococcus pneumoniae* and *Staphylococcus aureus*: In vitro hydrogen peroxide-mediated killing by *Streptococcus pneumoniae*. *J Bacteriol* 188:4996–5001.
183. Selva L, Viana D, Regev-Yochay G, Trzcinski K, Corpa JM, Lasa Í, Novick RP, Penadés JR. 2009. Killing niche competitors by remote-control bacteriophage induction. *Proc Natl Acad Sci U S A* 106:1234–1238.
184. Belkaid Y, Hand TW. 2014. Role of the microbiota in immunity and inflammation. *Cell* 157:121–141.

185. Clarke TB, Davis KM, Lysenko ES, Zhou AY, Yu Y, Weiser JN. 2010. Recognition of peptidoglycan from the microbiota by Nod1 enhances systemic innate immunity. *Nat Med* 16:228–231.
186. Brown RL, Sequeira RP, Clarke TB. 2017. The microbiota protects against respiratory infection via GM-CSF signaling. *Nat Commun* 8.
187. Ichinohe T, Pang IK, Kumamoto Y, Peaper DR, Ho JH, Murray TS, Iwasaki A. 2011. Microbiota regulates immune defense against respiratory tract influenza A virus infection. *Proc Natl Acad Sci U S A* 108:5354–5359.
188. Levy M, Blacher E, Elinav E. 2017. Microbiome, metabolites and host immunity. *Curr Opin Microbiol* 35:8–15.
189. Bogaert D, Keijser B, Huse S, Rossen J, Veenhoven R, van Gils E, Bruin J, Montijn R, Bonten M, Sanders E. 2011. Variability and diversity of nasopharyngeal microbiota in children: a metagenomic analysis. *PLoS One* 6.
190. van den Bergh MR, Biesbroek G, Rossen JWA, de Steenhuijsen P, Pitsers WAA, Bosch AATM, van Gils EJM, Wang X, Boonacker CWB, Veenhoven RH, Bruin JP, Bogaert D, Sanders EAM. 2012. Associations between pathogens in the upper respiratory tract of young children: interplay between viruses and bacteria. *PLoS One* 7.
191. Haleem Khan AA, Mohan Karuppaiyl S. 2012. Fungal pollution of indoor environments and its management. *Saudi J Biol Sci* 19:405–426.
192. Charlson ES, Diamond JM, Bittinger K, Fitzgerald AS, Yadav A, Haas AR, Bushman FD, Collman RG. 2012. Lung-enriched organisms and aberrant bacterial and fungal respiratory microbiota after lung transplant. *Am J Respir Crit Care Med* 186:536–545.
193. Taubenberger JK, Reid AH, Fanning TG. 2000. The 1918 influenza virus: A killer comes into view. *Virology* 274:241–245.
194. Yang Y, Peng F, Wang R, Guan K, Jiang T, Xu G, Sun J, Chang C. 2020. The deadly coronaviruses: The 2003 SARS pandemic and the 2020 novel coronavirus epidemic in China. *J Autoimmun* 109.
195. Musuuza JS, Watson L, Parmasad V, Putman-Buehler N, Christensen L, Safdar N. 2021. Prevalence and outcomes of co-infection and superinfection with SARS-CoV-2 and other pathogens: A systematic review and meta-analysis. *PLoS One* 16.
196. Moorthy AN, Narasaraju T, Rai P, Perumalsamy R, Tan KB, Wang S, Engelward B, Chow VTK. 2013. In vivo and in vitro studies on the roles of neutrophil

- extracellular traps during secondary pneumococcal pneumonia after primary pulmonary influenza infection. *Front Immunol* 4.
197. Sajjan U, Wang Q, Zhao Y, Gruenert DC, Hershenson MB. 2008. Rhinovirus disrupts the barrier function of polarized airway epithelial cells. *Am J Respir Crit Care Med* 178:1271–1281.
198. Ramphal R, Small PM, Shands JW, Fischlschweiger W, Small PA. 1980. Adherence of *Pseudomonas aeruginosa* to tracheal cells injured by influenza infection or by endotracheal intubation. *Infect Immun* 27:614–619.
199. Avadhanula V, Rodriguez CA, DeVincenzo JP, Wang Y, Webby RJ, Ulett GC, Adderson EE. 2006. Respiratory viruses augment the adhesion of bacterial pathogens to respiratory epithelium in a viral species- and cell type-dependent manner. *J Virol* 80:1629–1636.
200. Pittet LA, Hall-Stoodley L, Rutkowski MR, Harmsen AG. 2010. Influenza virus infection decreases tracheal mucociliary velocity and clearance of *Streptococcus pneumoniae*. *Am J Respir Cell Mol Biol* 42:450–460.
201. Berkan Ö, Göl MK, İçağasioğlu S, Çetinkaya Ö, Yıldız E, Doğan K, Günay I. 2004. Sialic acid is a marker of lung injury following lower extremities ischemia/reperfusion. *European Journal of Vascular and Endovascular Surgery* 27:553–558.
202. Siegel SJ, Roche AM, Weiser JN. 2014. Influenza promotes pneumococcal growth during coinfection by providing host sialylated substrates as a nutrient source. *Cell Host Microbe* 16:55–67.
203. van der Sluijs KF, Nijhuis M, Levels JHM, Florquin S, Mellor AL, Jansen HM, van der Poll T, Lutter R. 2006. Influenza-induced expression of indoleamine 2,3-dioxygenase enhances interleukin-10 production and bacterial outgrowth during secondary pneumococcal pneumonia. *J Infect Dis* 193:214–222.
204. van der Sluijs KF, van Elden LJR, Nijhuis M, Schuurman R, Pater JM, Florquin S, Goldman M, Jansen HM, Lutter R, van der Poll T. 2004. IL-10 is an important mediator of the enhanced susceptibility to pneumococcal pneumonia after influenza infection. *J Immunol* 172:7603–7609.
205. Sun K, Metzger DW. 2008. Inhibition of pulmonary antibacterial defense by interferon-gamma during recovery from influenza infection. *Nat Med* 14:558–564.
206. Sun K, Metzger DW. 2014. Influenza infection suppresses NADPH oxidase-dependent phagocytic bacterial clearance and enhances susceptibility to

- secondary methicillin-resistant *Staphylococcus aureus* infection. *J Immunol* 192:3301–3307.
207. Sajjan US, Jia Y, Newcomb DC, Bentley JK, Lukacs NW, LiPuma JJ, Hershenson MB. 2006. *H. influenzae* potentiates airway epithelial cell responses to rhinovirus by increasing ICAM-1 and TLR3 expression. *FASEB J* 20:2121–2123.
  208. Gulraiz F, Bellinghausen C, Bruggeman CA, Stassen FR. 2015. *Haemophilus influenzae* increases the susceptibility and inflammatory response of airway epithelial cells to viral infections. *FASEB J* 29:849–858.
  209. Tashiro M, Ciborowski P, Klenk HD, Pulverer G, Rott R. 1987. Role of *Staphylococcus* protease in the development of influenza pneumonia. *Nature* 325:536–537.
  210. Scheiblaue H, Reinacher M, Tashiro M, Rott R. 1992. Interactions between bacteria and influenza A virus in the development of influenza pneumonia. *J Infect Dis* 166:783–791.
  211. Short KR, Vissers M, de Kleijn S, Zomer AL, Kedzierska K, Grant E, Reading PC, Hermans PWM, Ferwerda G, Diavatopoulos DA. 2014. Bacterial lipopolysaccharide inhibits influenza virus infection of human macrophages and the consequent induction of CD8<sup>+</sup> T cell immunity. *J Innate Immun* 6:129–139.
  212. Abt MC, Osborne LC, Monticelli LA, Doering TA, Alenghat T, Sonnenberg GF, Paley MA, Antenus M, Williams KL, Erikson J, Wherry EJ, Artis D. 2012. Commensal bacteria calibrate the activation threshold of innate antiviral immunity. *Immunity* 37:158–170.
  213. Xu H, Sobue T, Thompson A, Xie Z, Poon K, Ricker A, Cervantes J, Diaz PI, Dongari-Bagtzoglou A. 2014. Streptococcal co-infection augments *Candida* pathogenicity by amplifying the mucosal inflammatory response. *Cell Microbiol* 16:214–231.
  214. Diaz PI, Xie Z, Sobue T, Thompson A, Biyikoglu B, Ricker A, Ikonomou L, Dongari-Bagtzoglou A. 2012. Synergistic interaction between *Candida albicans* and commensal oral streptococci in a novel in vitro mucosal model. *Infect Immun* 80:620–632.
  215. Briard B, Heddergott C, Latgé JP. 2016. Volatile Compounds Emitted by *Pseudomonas aeruginosa* Stimulate Growth of the Fungal Pathogen *Aspergillus fumigatus*. *mBio* 7.
  216. Hogan DA, Vik Å, Kolter R. 2004. A *Pseudomonas aeruginosa* quorum-sensing molecule influences *Candida albicans* morphology. *Mol Microbiol* 54:1212–1223.



217. Reen FJ, Mooij MJ, Holcombe LJ, Mcsweeney CM, Mcglacken GP, Morrissey JP, O’Gara F. 2011. The *Pseudomonas* quinolone signal (PQS), and its precursor HHQ, modulate interspecies and interkingdom behaviour. *FEMS Microbiol Ecol* 77:413–428.
218. Purschke FG, Hiller E, Trick I, Rupp S. 2012. Flexible survival strategies of *Pseudomonas aeruginosa* in biofilms result in increased fitness compared with *Candida albicans*. *Mol Cell Proteomics* 11:1652–1669.
219. Roux D, Gaudry S, Dreyfuss D, El-Benna J, de Prost N, Denamur E, Saumon G, Ricard JD. 2009. *Candida albicans* impairs macrophage function and facilitates *Pseudomonas aeruginosa* pneumonia in rat. *Crit Care Med* 37:1062–1067.
220. Schwartz IS, Friedman DZP, Zapernick L, Dingle TC, Lee N, Sligl W, Zelyas N, Smith SW. 2020. High Rates of Influenza-Associated Invasive Pulmonary Aspergillosis May Not Be Universal: A Retrospective Cohort Study from Alberta, Canada. *Clin Infect Dis* 71:1760–1763.
221. Zou P, Wang C, Zheng S, Guo F, Yang L, Zhang Y, Liu P, Shen Y, Wang Y, Zhang X, Tang L, Gao H, Li L. 2020. Invasive Pulmonary Aspergillosis in Adults With Avian Influenza A (H7N9) Pneumonia in China: A Retrospective Study. *J Infect Dis* 221:S193–S197.
222. Rouzé A, Lemaitre E, Martin-Loeches I, Pova P, Diaz E, Nyga R, Torres A, Metzelard M, du Cheyron D, Lambiotte F, Tamion F, Labruyere M, Boulle Geronimi C, Luyt C-E, Nyunga M, Pouly O, Thille AW, Megarbane B, Saade A, Magira E, Llitjos J-F, Ioannidou I, Pierre A, Reignier J, Garot D, Kreitmann L, Baudel J-L, Voiriot G, Plantefevre G, Morawiec E, Asfar P, Boyer A, Mekontso-Dessap A, Makris D, Vinsonneau C, Floch P-E, Marois C, Ceccato A, Artigas A, Gaudet A, Nora D, Cornu M, Duhamel A, Labreuche J, Nseir S, Bouchereau M, Sendid B, Boyd S, Coelho L, Maizel J, Cuchet P, Zarrougui W, Boyer D, Quenot J-P, Imouloudene M, de Chambrun MP, van der Linden T, Arrive F, Voicu S, Azoulay E, Moglia E, Pene F, Cilloniz C, Thevenin D, Larrat C, Argaud L, Guidet B, Turpin M, Contou D, Beurton A, Demiselle J, Meguerditchian D, Razazi K, Arrestier R, Tsolaki V, Marzouk M, Brunin G, Weiss N, Morales L. 2022. Invasive pulmonary aspergillosis among intubated patients with SARS-CoV-2 or influenza pneumonia: a European multicenter comparative cohort study. *Crit Care* 26:11.
223. Ku YH, Chan KS, Yang CC, Tan CK, Chuang YC, Yu WL. 2017. Higher mortality of severe influenza patients with probable aspergillosis than those with and without other coinfections. *J Formos Med Assoc* 116:660–670.

224. Tobin JM, Nickolich KL, Ramanan K, Pilewski MJ, Lamens KD, Alcorn JF, Robinson KM. 2020. Influenza Suppresses Neutrophil Recruitment to the Lung and Exacerbates Secondary Invasive Pulmonary Aspergillosis. *J Immunol* 205:480–488.

## Chapter 2

### **Postinfluenza Environment Reduces *Aspergillus fumigatus* Conidium Clearance and Facilitates Invasive Aspergillosis *In Vivo***

Ko-Wei Liu, Madeleine S. Grau, Jane T. Jones, Xi Wang, Elisa M. Vesely, Matthew R. James, Cecilia Gutierrez-Perez, Robert A. Cramer, and Joshua J. Obar

Postinfluenza Environment Reduces *Aspergillus fumigatus* Conidium Clearance and Facilitates Invasive Aspergillosis *In Vivo*. mBio. 2022 Nov 15; e0285422  
PMID: 36377895 DOI: 10.1128/mbio.02854-22

KWL designed and performed the experiments, analyzed the results, and wrote the manuscript.

MSG did the survival curves and histology staining in Figure 1 and prepared virus for inoculation.

JTJ assisted with all the animal experiments and helped with the writing.

XW helped with the initial establishment of IAV-Af superinfection model.

EMV did the confocal imaging in Figure 6 and helped with the writing.

MRJ helped with the establishment of FLARE experiments.

CGP helped with the CFU experiments.

RAC and JJO designed the experiments, analyzed the results, and wrote the manuscript.



# Postinfluenza Environment Reduces *Aspergillus fumigatus* Conidium Clearance and Facilitates Invasive Aspergillosis *In Vivo*

 Ko-Wei Liu,<sup>a</sup> Madeleine S. Grau,<sup>a</sup> Jane T. Jones,<sup>a</sup> Xi Wang,<sup>a</sup>  Elisa M. Vesely,<sup>a</sup> Matthew R. James,<sup>a</sup> Cecilia Gutierrez-Perez,<sup>a</sup>  Robert A. Cramer,<sup>a</sup>  Joshua J. Obar<sup>a</sup>

<sup>a</sup>Department of Microbiology and Immunology, Geisel School of Medicine at Dartmouth, Hanover, New Hampshire, USA

**ABSTRACT** *Aspergillus fumigatus* is a human fungal pathogen that is most often avirulent in immunocompetent individuals because the innate immune system is efficient at eliminating fungal conidia. However, recent clinical observations have shown that severe influenza A virus (IAV) infection can lead to secondary *A. fumigatus* infections with high mortality. Little is currently known about how IAV infection alters the innate antifungal immune response. Here, we established a murine model of IAV-induced *A. fumigatus* (IAV-Af) superinfection by inoculating mice with IAV followed 6 days later by *A. fumigatus* conidia challenge. We observed increased mortality in the IAV-Af-superinfected mice compared to mice challenged with either IAV or *A. fumigatus* alone. *A. fumigatus* conidia were able to germinate and establish a biofilm in the lungs of the IAV-Af superinfection group, which was not seen following fungal challenge alone. While we did not observe any differences in inflammatory cell recruitment in the IAV-Af superinfection group compared to single-infection controls, we observed defects in *Aspergillus* conidial uptake and killing by both neutrophils and monocytes after IAV infection. pHrodo Green zymosan bioparticle (pHrodo-zymosan) and CM-H2DCFDA [5-(and-6)-chloromethyl-2',7'-dichlorodihydrofluorescein diacetate] staining, indicators of phagolysosome maturation and reactive oxygen species (ROS) production, respectively, revealed that the fungal killing defect was due in part to reduced phagolysosome maturation. Collectively, our data demonstrate that the ability of neutrophils and monocytes to kill and clear *Aspergillus* conidia is strongly reduced in the pulmonary environment of an IAV-infected lung, which leads to invasive pulmonary aspergillosis and increased overall mortality in our mouse model, recapitulating what is observed clinically in humans.

**IMPORTANCE** Influenza A virus (IAV) is a common respiratory virus that causes seasonal illness in humans, but can cause pandemics and severe infection in certain patients. Since the emergence of the 2009 H1N1 pandemic strains, there has been an increase in clinical reports of IAV-infected patients in the intensive care unit (ICU) developing secondary pulmonary aspergillosis. These cases of flu-*Aspergillus* superinfections are associated with worse clinical outcomes than secondary bacterial infections in the setting of IAV. To date, we have a limited understanding of the cause(s) of secondary fungal infections in immunocompetent hosts. IAV-induced modulation of cytokine production and innate immune cellular function generates a unique immune environment in the lung, which could make the host vulnerable to a secondary fungal infection. Our work shows that defects in phagolysosome maturation in neutrophils and monocytes after IAV infection impair the ability of these cells to kill *A. fumigatus*, thus leading to increased fungal germination and growth and subsequent invasive aspergillosis. Our work lays a foundation for future mechanistic studies examining the exact immune modulatory events occurring in the respiratory tract after viral infection leading to secondary fungal infections.

**Editor** Liise-anne Pirofski, Albert Einstein College of Medicine

**Copyright** © 2022 Liu et al. This is an open-access article distributed under the terms of the [Creative Commons Attribution 4.0 International license](https://creativecommons.org/licenses/by/4.0/).

Address correspondence to Joshua J. Obar, [Joshua.J.Obar@dartmouth.edu](mailto:Joshua.J.Obar@dartmouth.edu), or Robert A. Cramer, [Robert.A.Cramer.Jr@dartmouth.edu](mailto:Robert.A.Cramer.Jr@dartmouth.edu).

The authors declare no conflict of interest.

This article is a direct contribution from Robert A. Cramer, a Fellow of the American Academy of Microbiology, who arranged for and secured reviews by Chad Steele, Tulane University, and Floyd Wormley, Jr., Texas Christian University.

**Received** 13 October 2022

**Accepted** 17 October 2022

**KEYWORDS** *Aspergillus fumigatus*, influenza A virus, superinfection, invasive pulmonary aspergillosis, phagocytosis, phagolysosome maturation, pathogenesis, host-pathogen interactions, antifungal immunity, innate immunity, phagolysosome, monocytes, neutrophils

*Aspergillus fumigatus* is a filamentous fungus that can be commonly found in the environment. In the immunocompetent host, hundreds to thousands of *Aspergillus* conidia can be inhaled every day without disease development. The innate immune system, including macrophages, neutrophils, monocytes, and dendritic cells (DCs), recognizes fungal conidia through pattern recognition receptors (PRRs) leading to their elimination through phagocytosis and killing via reactive oxygen species (ROS) and ROS-independent mechanisms (1). However, when the immune system is impaired, inhaled conidia germinate, become pathogenic, and contribute to multiple diseases collectively termed aspergillosis. Chronic pulmonary colonization with *A. fumigatus* can lead to allergic bronchopulmonary aspergillosis (ABPA), most commonly found in individuals with cystic fibrosis (CF) or chronic obstructive pulmonary disorder (COPD) (2, 3). Conversely, in patients with severe impairments in innate immunity (e.g., chronic granulomatous disease [CGD], prolonged steroid treatment, or neutropenia) acute exposure to *A. fumigatus* can lead to fungal germination and growth into hyphae resulting in biofilm formation, penetration of the lung parenchyma, and systemic dissemination (4–6).

Recent clinical reports indicate that patients admitted to the intensive care unit (ICU) due to severe influenza virus infections may develop secondary fungal infections (7–10). Severe influenza virus infection is now considered a major risk factor for the development of influenza-associated invasive aspergillosis (IAPA) (11). However, the mechanistic causes leading to IAPA, especially in immunocompetent patients, remain poorly understood. The connections between a postinfluenza lung environment and susceptibility to secondary bacterial infection have been well documented (12, 13). In that setting, type I and type II interferons (IFNs) induced by influenza A virus (IAV) infection are known to enhance susceptibility to secondary bacterial infection (14). Furthermore, the postinfluenza environment also affects innate immune cell accumulation and function within the lungs. Specifically, neutrophils and macrophages in the postinfluenza environment have decreased phagocytosis and clearance of bacterial pathogens (15, 16). Taken together, these results demonstrate that innate immune responses observed in the postinfluenza environment lead to defective antibacterial innate immune clearance, which can drive vulnerability to secondary bacterial infections, but the involvement of alterations in the susceptibility to secondary fungal infection remains unresolved. Recent results from a murine model of IAPA suggest that the elevated IFN production post-IAV infection induces STAT1 signaling and inhibits neutrophil recruitment, which leads to IAPA (17). However, a comprehensive study examining innate immune cell function and antifungal immunity following IAV infection is needed to define the cause(s) of IAPA development in these IAV-infected hosts.

In our current study, we established a murine IAV-*A. fumigatus* (IAV-Af) superinfection model that we used to examine the modulation of the antifungal innate immune response within the post-IAV lung environment. As expected, mice from the IAV-Af superinfection group exhibited higher morbidity and mortality, fungal biofilm formation, and increased fungal burden in the lungs. We further observe that normal inflammatory immune cell recruitment occurs in the post-IAV lung environment, yet there is a significant impairment in fungal phagocytosis and killing *in vivo*. The defective killing of *A. fumigatus* observed in pulmonary neutrophils and monocytes after IAV infection is due in part to defective phagolysosome maturation. Therefore, our findings demonstrate that modulation of neutrophil and monocyte function in a post-IAV environment contributes to defective fungal clearance, leading to disease development and eventual mortality of the host.

## RESULTS

**Influenza A virus infection increases susceptibility to invasive pulmonary aspergillosis in mice.** To understand why influenza-infected immunocompetent hosts are more susceptible to invasive pulmonary aspergillosis (IPA), we developed an IAV-Af superinfection model with immunocompetent mice. C57BL/6J mice were first challenged intranasally with either phosphate-buffered saline (PBS) or a sublethal dose of IAV PR/8/34 H1N1 (100 50% egg infective dose [EID<sub>50</sub>]). Six days later, mice were challenged oropharyngeally with either PBS or  $3.4 \times 10^7$  *A. fumigatus* CEA10 conidia for an additional 8 to 36 h (Fig. 1A). C57BL/6J mice first inoculated with IAV and then inoculated with *A. fumigatus* (IAV-Af superinfection) had significantly more mortality than mice challenged with IAV only or *A. fumigatus* only. In the IAV-Af superinfection group, mice succumbed to infection as early as 1 day post-*A. fumigatus* inoculation, with 100% mortality observed by 5 days post-fungal challenge (Fig. 1B). Increased mortality coincided with higher fungal burden in the lungs of the IAV-Af-superinfected group compared to the *A. fumigatus*-only infection group (Fig. 1C). Based on our experimental design, most of the IAV would be cleared by the host at the time we collected the lung samples for viral load (day 7.5 post-IAV infection), but interestingly, the quantification of the influenza viral load by quantitative reverse transcription-PCR (qRT-PCR) showed an even lower virus load in the IAV-Af superinfection group compared to the IAV single-infection group, indicating functional antiviral immunity in the superinfection group (Fig. 1D). To assess the development of IAPA in our mouse model, we examined lung sections with Grocott-Gomori methenamine silver (GMS) and hematoxylin and eosin (H&E) staining for fungal burden and immune cell recruitment, respectively. While most of the inoculated *A. fumigatus* cells remained as conidia at 2 days postinoculation in the *A. fumigatus*-only infection group, in the IAV-Af superinfection group, we observed that *A. fumigatus* conidia had germinated significantly, even forming biofilms at the infection foci (Fig. 1E). These data demonstrate that the respiratory environment found after IAV infection results in defective restriction of *A. fumigatus* germination, which correlated with the development of IAPA in our IAV-Af superinfection model.

**Postinfluenza immunity does not affect immune cell recruitment during infection with the highly virulent *A. fumigatus* CEA10 strain.** Host innate immunity, which is largely mediated by neutrophils, macrophages, and dendritic cells, plays important roles in preventing IPA (18–23). Quantitative deficiency in any of these immune cells can limit fungal recognition and/or inhibition of conidial germination and fungal clearance. H&E staining indicates that substantial inflammatory immune cell accumulation occurs in the infection site of both the *A. fumigatus*-only and IAV-Af superinfection groups, suggesting a robust cellular innate immune response is occurring even in the post-IAV lung environment (Fig. 1F). Since a previous study indicated STAT1-dependent inhibition of neutrophil recruitment in the postinfluenza environment (17), we next asked whether there were any differences in composition and/or absolute number of the infiltrating immune cells in our IAV-Af superinfection model. We leveraged multiple immune staining panels (see Table S1 and Fig. S1 to S3 in the supplemental material) for flow cytometry analysis to examine the lung cellularity in our IAV-Af superinfection model (24). At 36 hours post-*A. fumigatus* challenge, we observed equivalent numbers of total lung cells, neutrophils (Ly6G<sup>+</sup> CD11b<sup>+</sup>), monocytes (CD11b<sup>hi</sup> CD64<sup>+</sup> major histocompatibility complex class II [MHC-II]<sup>+</sup>), and type 2 conventional dendritic cells (cDC2s) (CD103<sup>+</sup> CD11b<sup>+</sup>) in both the *A. fumigatus*-only infection and IAV-Af superinfection groups that were increased compared to the those of the PBS control and IAV single-infection groups (Fig. 2A, B, E, and G). We also observed equivalent increases in interstitial macrophages (CD11b<sup>hi</sup> CD64<sup>+</sup>) and plasmacytoid DCs (pDCs) (CD317<sup>+</sup>) in both the IAV-only infection and IAV-Af superinfection groups compared to the PBS control (Fig. 2D and H). We also examined the cellular composition by calculating the percentage of each cell type (Fig. S4). Similar to cell number observations, both the *A. fumigatus*-only infection and IAV-Af superinfection groups had a significant increase in the percentage of neutrophils in the leukocyte population compared to PBS controls,

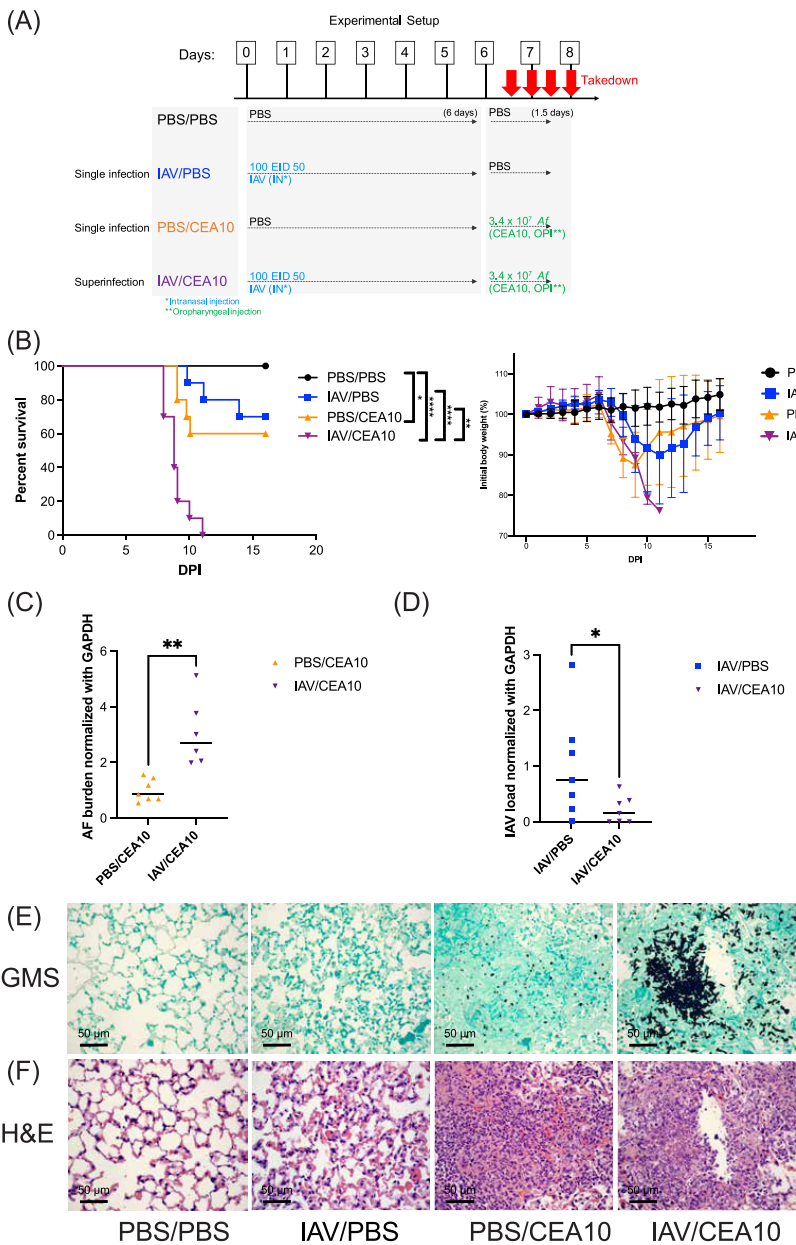


**FIG 1** Influenza A virus infection aggravates invasive aspergillosis disease progression. (A) Schematic design of IAV-Af infection mouse model. C57BL/6J mice were inoculated with 100 EID<sub>50</sub> of A/PR/8/34 (IAV) or PBS at day 0 followed by 3.4 × 10<sup>7</sup> CEA10 conidia or PBS at (Continued on next page)

and there was no difference between those two experimental groups (Fig. S4A). We observe an increased percentage of interstitial macrophages and pDC populations in the IAV-only infection group compared to the *A. fumigatus*-only infection and IAV-*Af* superinfection groups, although there was no difference in total cell numbers (Fig. S4C and G). Collectively, our flow cytometry analysis results suggest that the recruitment of multiple immune cell types to the lung following IAV infection and *A. fumigatus* infection still contributes to corresponsive cell recruitment in the IAV-*Af* superinfection environment.

**Neutrophils and monocytes in the postinfluenza lung environment have defects in antifungal killing mechanisms.** Since we did not observe any differences in either the absolute numbers of innate immune cells or their compositions, we hypothesized that the lung environment after IAV infection results in altered antifungal effector function(s) within the recruited innate immune cells. This seemed likely, since defects in innate immune cell function, rather than recruitment, can lead to IPA development in corticosteroid-treated patients and mice (25, 26). In order to test this hypothesis, we utilized the fluorescent *Aspergillus* reporter (FLARE) assay to quantify both the uptake and viability of *A. fumigatus* conidia within specific immune cell types in the murine lungs (Fig. S5) (27). Thirty-six hours postinoculation of Alexa Fluor 633 (AF633)-labeled monomeric red fluorescent protein (mRFP)-labeled CEA10 (FLARE) conidia, both neutrophils (Fig. 3A) and monocytes (Fig. 3B) showed a slight decrease in conidial uptake, with an almost 2-fold increase in conidial viability within the IAV-*Af* superinfection group compared to *A. fumigatus*-only infection. In contrast, we observed no differences in conidial uptake or viability within alveolar macrophages (Fig. 3C) or interstitial macrophages (Fig. 3D). Within cDC2 cells, we observed a very minor decrease in conidial uptake, but no change in conidial viability (Fig. 3E). Besides the increase in intracellular viability of *A. fumigatus* in neutrophils and monocytes, we also noticed that the remaining extracellular conidia showed higher viability in the single-cell suspension from murine lungs in the FLARE assay (Fig. 3G). In parallel, single-cell lung suspensions showed an almost 2-fold increase in fungal CFU from the IAV-*Af* superinfection group compared to the *A. fumigatus*-only infection group (Fig. 3F), which corroborates our observations with the FLARE assay. Collectively, these data suggest that both neutrophils and monocytes have defects in their antifungal phagocytotic and killing processes in the post-IAV environment, which could explain why *A. fumigatus* can germinate, grow, and form biofilms in the post-IAV lung environment ultimately leading to the development of disease.

**Neutrophils and monocytes induce ROS production normally in the post-IAV lung environment.** ROS production by innate leukocytes plays an important role in controlling pathogen growth, particularly *Staphylococcus aureus* and *A. fumigatus*, as highlighted by infections in patients with X-linked chronic granulomatous disease (28, 29) and mice lacking NADPH oxidase components (30). Previous studies observed that impaired ROS production by innate immune cells is associated with decreased fungal killing and phagocytotic function (21). Therefore, we hypothesized that neutrophils and monocytes in the post-IAV lung environment were impaired in their ability to induce ROS production. To test this hypothesis using the IAV-*Af* superinfection model, we isolated immune cells from infected mice and incubated them with the cellular dye CM-H2DCFDA [5-(and-6)-chloromethyl-2',7'-dichlorodihydrofluorescein diacetate] to detect total ROS production by both neutrophils and monocytes. We then determined both the

#### FIG 1 Legend (Continued)

day 6. Mice were euthanized at either 8, 24, 36, or 48 h post-CEA10 inoculation. (B) Survival curve (left) of mice with PBS inoculation, IAV single infection, CEA10 single infection, and IAV-CEA10 superinfection ( $n = 10$ ) and the weights (right) of mice in each group. Two independent experiments were performed, and data are shown as the representative results. (C) For quantification of pathogen load, RNA was isolated from the lungs of mice exposed to 6 days of either IAV or PBS followed by 36 h of CEA10 or PBS inoculation. Fungal burden was examined by qRT-PCR on *A. fumigatus* 18S rRNA ( $n = 7$ ). (D) Viral load was examined by qRT-PCR on viral matrix protein ( $n = 7$ ). Panels C and D are representative of three independent experiments. (E) For lung histology, mice were euthanized after 6 days of IAV or PBS incubation followed by 48 h postinoculation with CEA10 or PBS. Representative histology images of mice lungs were observed with (E) GMS staining and (F) H&E staining. Two independent experiments were performed with  $n = 5$  per experiment. The log rank test and Gehan-Breslow-Wilcoxon test were performed for statistical analysis of the survival curve, and nonparametric analyses were performed (Mann-Whitney for single comparisons) for the pathogen load. All error bars represent standard deviations. NS, not significant at  $P > 0.05$ ; \*,  $P \leq 0.05$ ; \*\*,  $P \leq 0.01$ ; \*\*\*,  $P \leq 0.001$ ; \*\*\*\*,  $P \leq 0.0001$ .



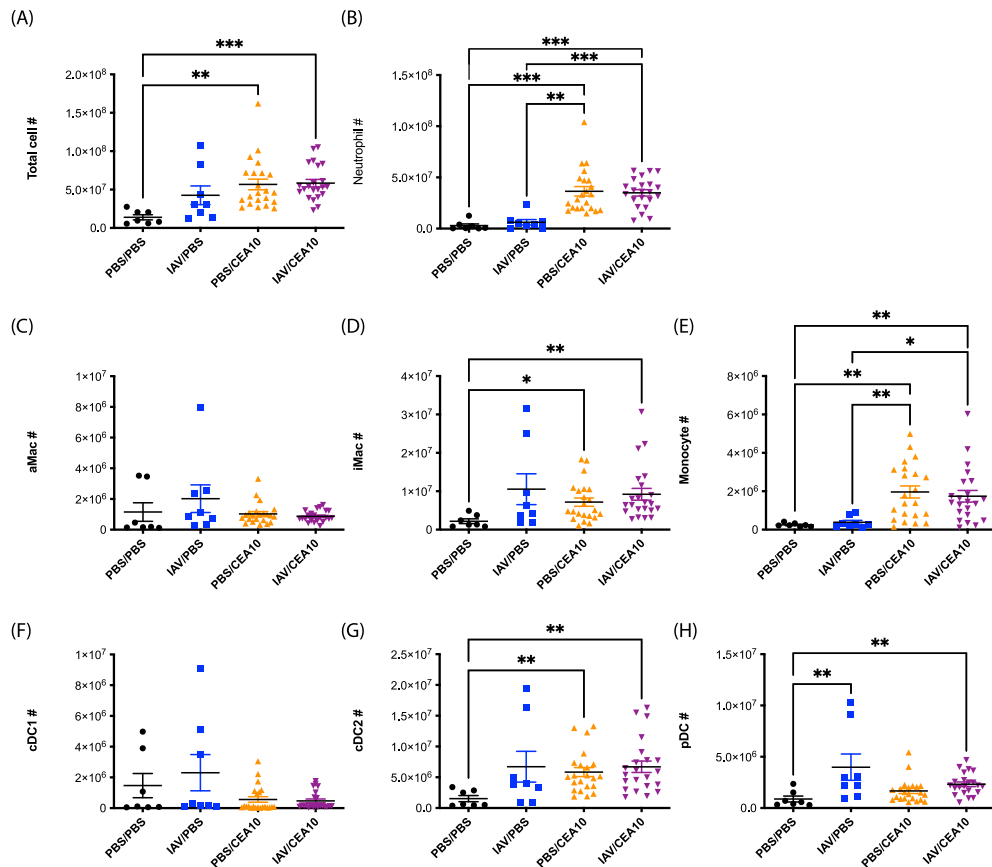


**FIG 2** Influenza A virus infection does not affect lung cellularity during *A. fumigatus* infection. C57BL/6J mice were inoculated with 100 EID<sub>50</sub> of A/PR/8/34 (IAV) or PBS at day 0 followed by  $3.4 \times 10^7$  CEA10 conidia or PBS at day 6. Mice were euthanized at 36 h postinoculation with CEA10 or PBS for lung cellularity experiments. Three independent experiments were performed, and data are shown as the combined results (PBS/PBS group,  $n = 7$ ; IAV/PBS group,  $n = 8$ ; PBS/CEA10 group,  $n = 22$ ; IAV/CEA10 group,  $n = 22$ ). All lung cell numbers were acquired by flow cytometry as indicated: (A) total lung cells, (B) neutrophils (CD45<sup>+</sup> Ly6G<sup>+</sup> CD11b<sup>+</sup>), (C) alveolar macrophages (aMac) (Ly6G<sup>+</sup> CD103<sup>+</sup> SiglecF<sup>+</sup> CD11b<sup>+</sup>), (D) interstitial macrophages (iMac) (Ly6G<sup>+</sup> CD103<sup>+</sup> SiglecF<sup>+</sup> CD11b<sup>+</sup> CD64<sup>+</sup>), (E) monocytes (Ly6G<sup>+</sup> CD103<sup>+</sup> SiglecF<sup>+</sup> CD11b<sup>+</sup> CD64<sup>+</sup> MHC-II<sup>+</sup>), (F) CD103<sup>+</sup> cDC1s (MHC-II<sup>+</sup> CD11c<sup>+</sup> CD11b<sup>+</sup> CD103<sup>+</sup>), (G) CD11b<sup>+</sup> cDC2s (MHC-II<sup>+</sup> CD11c<sup>+</sup> CD103<sup>+</sup> CD11b<sup>+</sup>), (H) pDCs (MHC-II<sup>+</sup> CD11c<sup>+</sup> CD11b<sup>+</sup> CD103<sup>+</sup> CD317<sup>+</sup>). The Kruskal-Wallis test with Dunn's multiple comparisons was performed for statistical analyses. All error bars represent standard deviations. NS, not significant at  $P > 0.05$ ; \*,  $P \leq 0.05$ ; \*\*,  $P \leq 0.01$ ; \*\*\*,  $P \leq 0.001$ ; \*\*\*\*,  $P \leq 0.0001$ .

percentage of cells with a positive signal from CM-H2DCFDA as well as the amount of ROS produced on a per cell basis. We chose to examine the ROS response during early fungal infection since increased fungal germination and growth were observed by 24 h post-*A. fumigatus* infection. To do this, we collected lung cells at 8 h post-*A. fumigatus* infection. We observed increased ROS production in neutrophils and monocytes from both *A. fumigatus*-only infection and IAV-*Af* superinfection groups compared to both the PBS control and IAV-only infection groups. Furthermore, we observed no decrease in ROS production from the neutrophils and monocytes from the IAV-*Af* superinfection group compared to the *A. fumigatus*-only infection, suggesting that the fungus-induced ROS burst was not impaired in the post-IAV lung environment (Fig. 4A and B). For the

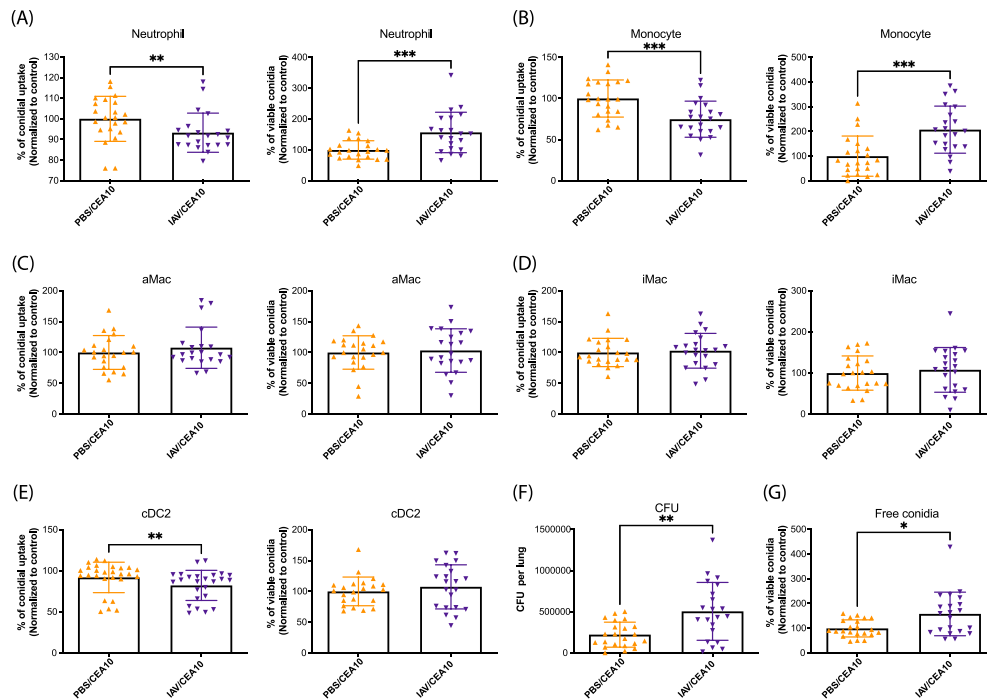


**FIG 3** Defects in leukocyte-mediated fungal killing post-influenza A virus infection. C57BL/6J mice were inoculated with 100 EID<sub>50</sub> of A/PR/8/34 (IAV) or PBS at day 0 followed by  $3.4 \times 10^7$  FLARE (mRFP<sup>+</sup>/AF633<sup>+</sup>) conidia or PBS at day 6. Mice were euthanized at 36 h postinoculation with FLARE conidia or PBS. The percentage of cells positive for conidial tracer (AF633<sup>+</sup>) and conidial viability within the immune cells (mRFP<sup>+</sup>/AF633<sup>+</sup>) were analyzed. Phagocytosis and conidial viability were examined in (A) neutrophils (CD45<sup>+</sup> Ly6G<sup>+</sup> CD11b<sup>+</sup>), (B) monocytes (Ly6G<sup>+</sup> CD103<sup>+</sup> SiglecF<sup>+</sup> CD11b<sup>+</sup> CD64<sup>+</sup> MHC-II<sup>+</sup>), (C) alveolar macrophages (aMac) (Ly6G<sup>+</sup> CD103<sup>+</sup> SiglecF<sup>+</sup> CD11b<sup>+</sup>), (D) interstitial macrophages (iMac) (Ly6G<sup>+</sup> CD103<sup>+</sup> SiglecF<sup>+</sup> CD11b<sup>+</sup> CD64<sup>+</sup>), and (E) CD11b<sup>+</sup> cDC2s (MHC-II<sup>+</sup> CD11c<sup>+</sup> CD103<sup>+</sup> CD11b<sup>+</sup>). (F) The viability of FLARE conidia within immune cells in the lung suspension was assessed by CFU. (G) The viability of free FLARE conidia in the lung suspension is shown as the percentage of mRFP<sup>+</sup> cells in the free conidial population (AF633<sup>+</sup> FSC<sup>low</sup> SSC<sup>low</sup>). Three independent experiments were performed, and data are shown as the combined results (PBS/CEA10 group,  $n = 22$ ; IAV/CEA10 group,  $n = 21$ ). The Mann-Whitney test with single comparisons was performed. All error bars represent standard deviations. NS, not significant at  $P > 0.05$ ; \*,  $P \leq 0.05$ ; \*\*,  $P \leq 0.01$ ; \*\*\*,  $P \leq 0.001$ ; \*\*\*\*,  $P \leq 0.0001$ .

percentage of cells that produced ROS, we observed an increased percentage in IAV-induced neutrophils and *A. fumigatus*-induced monocytes, but there was no significant difference between the IAV- or *A. fumigatus*-only infection and IAV-*Af* superinfection groups (Fig. S7A and B). Our data demonstrate that neutrophils and monocytes are still capable of significant ROS production during early *A. fumigatus* infection in the post-IAV environment, indicating a defect in ROS production from these two critical innate immune cells is not likely responsible for the development of disease in our model.

**Phagolysosome maturation is impaired in neutrophils and monocytes found in the post-IAV lung environment.** Rapid maturation of the phagosome through LC3-associated phagocytosis and subsequent phagosome maturation to the phagolysosome is necessary for antifungal killing and control of *A. fumigatus* germination and growth (31, 32). Since ROS production was not impaired by neutrophils and monocytes isolated from the post-IAV lung environment, we next hypothesized that defects in phagolysosome maturation within leukocytes from the IAV-*Af* superinfection contributes to the impaired antifungal killing. To test this hypothesis, we quantified phagolysosome maturation using pHrodo Green zymosan bioparticle (pHrodo-zymosan) staining in the neutrophils and monocytes 8 h after *A. fumigatus* challenge. We determined the

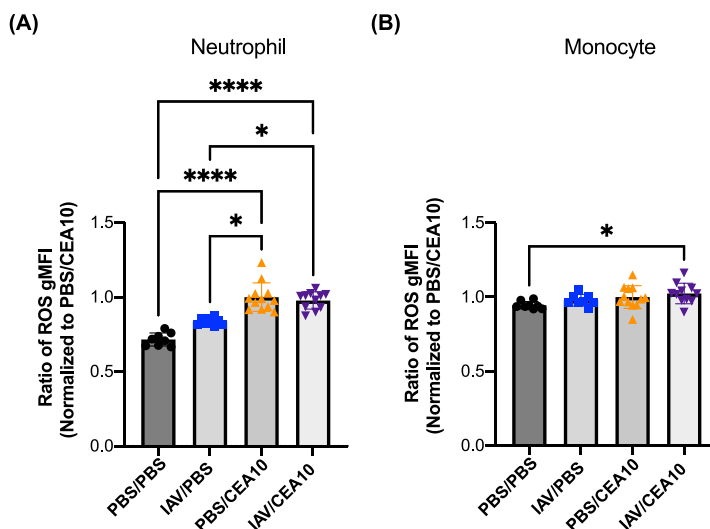


**FIG 4** Postinfluenza immunity does not hinder neutrophil or monocyte ROS production. C57BL/6J mice were inoculated with 100 EID<sub>50</sub> of A/PR/8/34 (IAV) or PBS at day 0 followed by  $3.4 \times 10^7$  CEA10 conidia or PBS at day 6. Mice were euthanized at 8 h postinoculation with CEA10 or PBS for ROS measurement. Lung cell suspensions were stained with CM-H2DCFDA for 30 min and then stained for neutrophils and monocytes. ROS production was measured by the signal from CM-H2DCFDA staining in (A) neutrophils (Ly6G<sup>+</sup>) and (B) monocytes (Ly6G<sup>+</sup> SiglecF<sup>+</sup> CD11b<sup>+</sup> CD64<sup>+</sup> MHC-II<sup>+</sup>). Two independent experiments were performed, and data are shown as the combined results (PBS/PBS group,  $n = 8$ ; IAV/PBS group,  $n = 8$ ; PBS/CEA10 group,  $n = 12$ ; IAV/CEA10 group,  $n = 11$ ). The Kruskal-Wallis test with Dunn's multiple comparisons was performed for statistical analyses. All error bars represent standard deviations. NS, not significant at  $P > 0.05$ ; \*,  $P \leq 0.05$ ; \*\*,  $P \leq 0.01$ ; \*\*\*,  $P \leq 0.001$ ; \*\*\*\*,  $P \leq 0.0001$ .

percentage of active cells by the percentage of cells with a positive signal from a color change of pHrodo-zymosan and the number of mature phagolysosomes in these active cells by the intensity of their pHrodo-zymosan signal. In our murine model, both neutrophils and monocytes from the IAV-only infection group had significant reductions in their pHrodo-zymosan signal from mature phagolysosomes compared to the PBS control (Fig. 5A and B). Similar to our observation in the IAV-only infection group, we also observed reduced signal from mature phagolysosomes in neutrophils and monocytes from the IAV-*Af* superinfection group compared to the PBS control (Fig. 5A and B). These data suggest that the post-IAV lung environment significantly impacts phagolysosome maturation in neutrophils and monocytes, which correlates with the impaired intracellular killing ability against fungal conidia we observed in the IAV-*Af* superinfection group in the FLARE experiment (Fig. 3).

To check for the proportion of cells that are still capable of responding to fungal PAMPs in the post-IAV environment, we examined the percentage of cells with a mature phagolysosome. We observed that the percentages of lung neutrophils with mature phagolysosomes from the *A. fumigatus*-only infection and IAV-*Af* superinfection groups were reduced compared to those in the PBS controls, but there was no difference between the IAV-*Af* superinfection and either of the single-infection groups (Fig. S8A). Intriguingly, lung monocytes from the IAV-only infection and IAV-*Af* superinfection groups showed reduced mature phagolysosome-containing cells in the population compared with both the PBS control and *A. fumigatus*-only infection groups (Fig. S8B). To further test the connection between the phagolysosome maturation defect and conidial killing in the nonexhausted neutrophils from the post-IAV environment, we combined

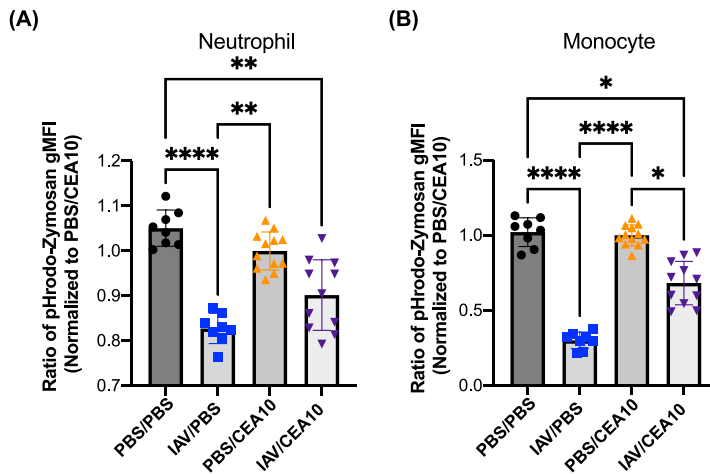


**FIG 5** Reduced phagolysosome maturation can be detected in neutrophils and monocytes during early viral infection. C57BL/6J mice were inoculated with 100 EID<sub>50</sub> of A/PR/8/34 (IAV) or PBS at day 0 followed by  $3.4 \times 10^7$  CEA10 conidia or PBS at day 6. Mice were euthanized at 8 h postinoculation with CEA10 or PBS for phagolysosome maturation analysis. Lung cell suspensions were incubated with pHrodo-zymosan for 2 h and then stained for neutrophils and monocytes. The phagolysosome maturation level was measured by the signal from the color change of pHrodo-zymosan in (A) neutrophils (Ly6G<sup>+</sup>) and (B) monocytes (Ly6G<sup>+</sup> SiglecF<sup>+</sup> CD11b<sup>+</sup> CD64<sup>+</sup> MHC-II<sup>+</sup>). Two independent experiments were performed, and data are shown as the combined results (PBS/PBS group,  $n = 8$ ; IAV/PBS group,  $n = 8$ ; PBS/CEA10 group,  $n = 12$ ; IAV/CEA10 group,  $n = 11$ ). The Kruskal-Wallis test with Dunn's multiple comparisons was performed for statistical analyses. All error bars represent standard deviations. NS, not significant at  $P > 0.05$ ; \*,  $P \leq 0.05$ ; \*\*,  $P \leq 0.01$ ; \*\*\*,  $P \leq 0.001$ ; \*\*\*\*,  $P \leq 0.0001$ .

the FLARE experiment with pHrodo-zymosan staining in our animal model. With confocal imaging, we observed Ly6G<sup>+</sup> neutrophils containing mature phagolysosome signal as well as live or dead conidia (Fig. 6A). The presence of pHrodo-zymosan<sup>+</sup> neutrophils in the lung from IAV-Af superinfection mice suggests these neutrophils were still functional in the post-IAV environment (Fig. 6B). However, these pHrodo-zymosan<sup>+</sup> neutrophils had less mature phagolysosome signal (Fig. 6C) and show decreased conidial killing (Fig. 6E). Collectively, these data suggest that neutrophils and monocytes in the post-IAV environment are impaired in phagolysosome maturation (Fig. 5), which correlates with decreased fungal killing (Fig. 3) and increased fungal burden (Fig. 1).

**Increased inflammation but decreased PRR gene expression in the IAV-Af superinfection environment.** In order to investigate the potential upstream pathway(s) contributing to defective phagolysosome maturation and fungal clearance we saw in the IAV-Af superinfection model, we utilized qRT-PCR of antifungal genes in RT<sup>2</sup> Profiler PCR arrays (PAMM-147ZD) with immune cell RNA from lungs of mice challenged with *A. fumigatus* only and IAV-Af superinfection. At 8 h post-*A. fumigatus* challenge, we found increased mRNA levels for *Nlrp3*, *Pycard*, *Ptgs2*, *Cd36*, *Cxcl10*, *Nfkb1*, *Mapk14*, and *Ccr5* and decreased mRNA levels for *Il10*, *Il2*, and *Jun* in the IAV-Af superinfection group compared to mice challenged only with *A. fumigatus* (Fig. 7). Interestingly, despite an enhanced inflammatory environment under IAV-Af superinfection conditions, which likely reflects the increased fungal growth, we observed a decrease in the mRNA levels of *Tlr9*, *Scarf1*, and *Colec12*, as well as *Irak4*, which is involved in myddosome and Toll-like receptor 9 (TLR9) signaling (Fig. 7). Our data reveal that while IAV-Af superinfected mice have a robust inflammatory response, there is a specific decrease in PRR mRNA levels that could alter the early host-fungus interaction and drive the impaired phagolysosome maturation and antifungal killing observed in neutrophils and monocytes. Future studies will

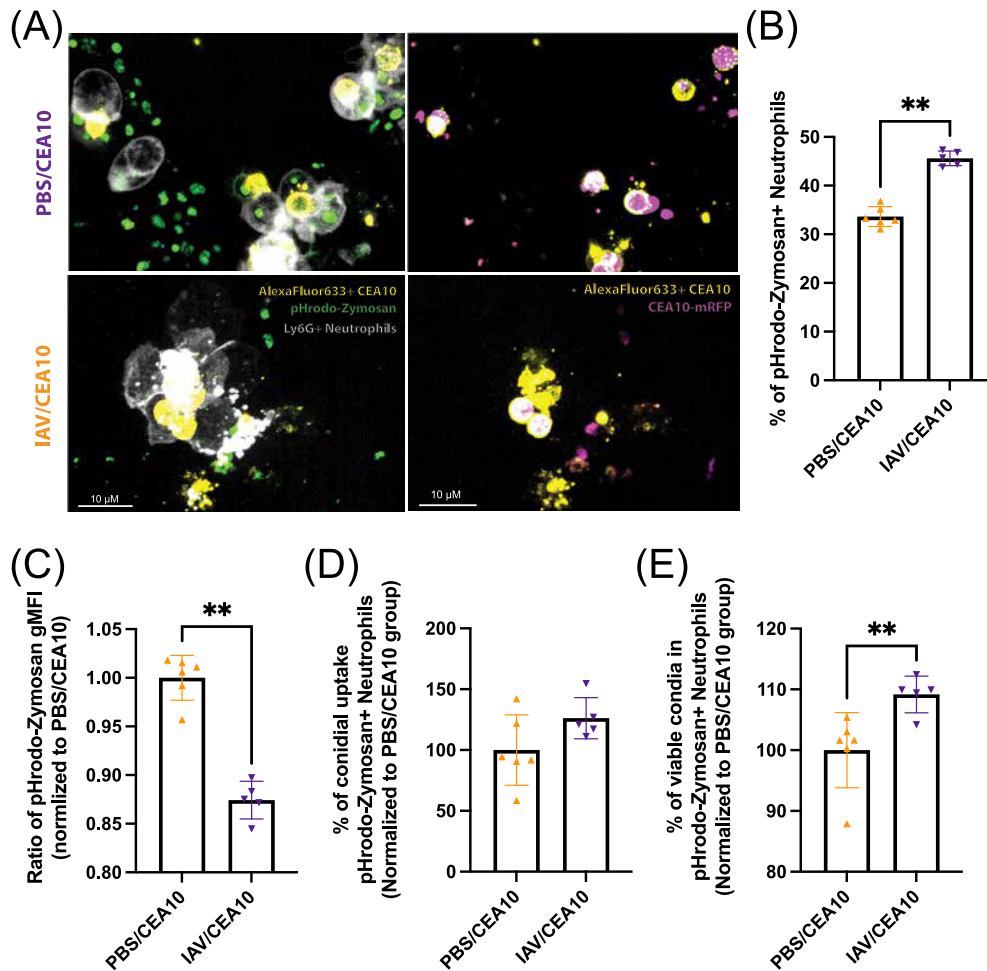


**FIG 6** Functional neutrophils from the post-IAV environment show decreasing phagolysosome maturation and conidial killing. C57BL/6J mice were inoculated with 100 EID<sub>50</sub> of A/PR/8/34 (IAV) or PBS at day 0 followed by  $3.4 \times 10^7$  FLARE (mRFP<sup>+</sup>/AF633<sup>+</sup>) conidia or PBS at day 6. Mice were euthanized at 36 h postinoculation with FLARE conidia or PBS. Lung cell suspensions were incubated with pHrodo-zymosan for 2 h and then stained for neutrophils. (A) Representative confocal images of neutrophil labeling (Ly6G-Pb [white]), mature phagolysosome (pHrodo-zymosan [green]), labeled conidia (AF633 [yellow]), and conidial viable marker (mRFP [pink]). The right images feature labeled conidia, neutrophils, and pHrodo-zymosan signal. The left images feature labeled conidia and RFP to indicate fungal viability. Fungal conidia with no RFP signal are considered "dead." (B) Currently functional neutrophils are indicated as pHrodo-zymosan<sup>+</sup> cells. (C) The number of mature phagolysosomes is shown by the geometric mean fluorescent intensity (gMFI) of pHrodo-zymosan in Ly6G<sup>+</sup> pHrodo-zymosan<sup>+</sup> cells. (D) The percentage of cells positive for conidia (AF633<sup>+</sup>) and conidial viability within the immune cells (mRFP<sup>+</sup>/AF633<sup>+</sup>) were analyzed as (D) the percentage of conidial uptake in Ly6G<sup>+</sup> pHrodo-Zymosan<sup>+</sup> cells and (E) the percentage of viable conidia in Ly6G<sup>+</sup> pHrodo-Zymosan<sup>+</sup> cells. This repeated experiment was done as the combination of FLARE experiment (Fig. 3) and phagolysosome maturation measurement (Fig. 5) (PBS/CEA10 group,  $n = 6$ ; IAV/CEA10 group,  $n = 5$ ). The Mann-Whitney test with single comparisons was performed. All error bars represent standard deviations. NS, not significant at  $P > 0.05$ ; \*,  $P \leq 0.05$ ; \*\*,  $P \leq 0.01$ ; \*\*\*,  $P \leq 0.001$ ; \*\*\*\*,  $P \leq 0.0001$ .

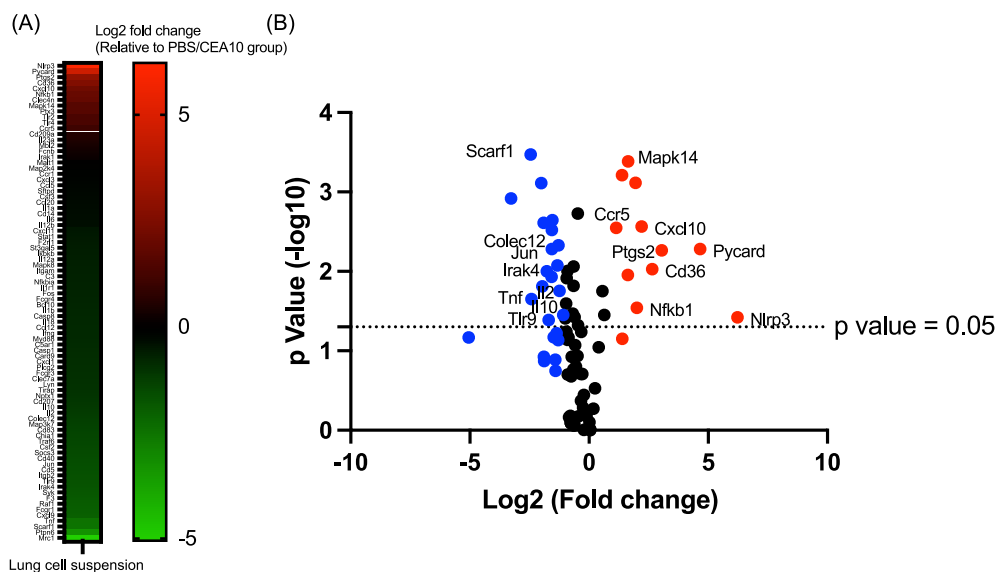


**FIG 7** Influenza A virus infection increases transcripts of genes associated with an inflammatory response but reduces transcript levels of known fungal pattern recognition receptors. C57BL/6J mice were inoculated with 100 EID<sub>50</sub> of A/PR/8/34 (IAV) or PBS at day 0 followed by  $3.4 \times 10^7$  CEA10 conidia or PBS at day 6. Mice were euthanized at 8 h postinoculation with CEA10 or PBS for antifungal gene transcript analysis. Antifungal gene transcript levels were measured by qRT-PCR with RNA from lung cell suspensions. (A) Increased (red) or decreased (green) transcript levels of genes associated with antifungal responses in the IAV/CEA10 group compared to the PBS/CEA10 group are represented by the heat map (PBS/CEA10 group,  $n = 3$ ; IAV/CEA10 group,  $n = 3$ ). (B) A volcano plot shows the distribution of fold changes of antifungal gene transcript levels in the IAV/CEA10 group compared to the PBS/CEA10 group. Genes with an increase in fold changes of >2 are shown in red, and genes with a decrease in fold changes of >2 are shown in blue. The  $P$  value threshold of 0.05 (Student's  $t$  test) is indicated by the line in the plot.

seek to explore the mechanism(s) underlying this virus-induced defect in phagolysosome maturation in the presence of *A. fumigatus* conidia.

## DISCUSSION

Seasonal influenza infection is a common annual respiratory disease among humans, and 1 to 2% of patients with symptomatic illness require hospitalization in the United States (33). Of those hospitalized, ~5 to 10% progress to ICU admission (34). Patients in the ICU due to severe IAV infections are well known to develop secondary bacterial infections, but in recent years the incidence of secondary fungal infections has been reported with a prevalence of IAPA between 5 and 19% and a mortality rate of ~50% (7, 8, 35, 36). Importantly, both immunocompromised and immunocompetent individuals in the ICU were at risk for developing IAPA (35). Moreover, this does not seem to be isolated to severe respiratory infection with IAV, because recent clinical case reports from the current severe acute respiratory syndrome coronavirus 2 (SARS-CoV2) pandemic suggest that secondary fungal infections are observed in patients with severe COVID-19 (37–39). COVID-19-associated pulmonary aspergillosis (CAPA) is reported in 20 to 35% of cases in recent reports from Europe (37). Thus, severe respiratory viral infection is an emerging risk factor for invasive aspergillosis and warrants further mechanistic studies.

Influenza infection can cause epithelial cell damage and leakage, induce antiviral cytokine production, impair further inflammatory cellular recruitment, and impair the phagocytic and antimicrobial activity of macrophages and neutrophils, which can all contribute to the increased risk of developing secondary bacterial infection (12, 13). However, there is a significant knowledge gap in understanding how IAV infection makes the lung environment conducive for fungal growth leading to the development

of IAPA. Recently, in a human retrospective observational study, Feys et al. identified a couple breaches in antifungal immunity in patients with IAPA and CAPA that included decreased integrity of the epithelial barrier, decreased antifungal cytokine expression (e.g., gamma interferon [IFN- $\gamma$ ]), and decreased gene expression for pathways involved in fungal phagocytosis and killing mainly mediated by neutrophils (38). One major hurdle to understanding virus-induced pulmonary aspergillosis has been the lack of experimental models to dissect secondary fungal infection. Our work here, together with the model from Robinson and colleagues (17), has established a robust IAV-*Af* superinfection mouse model that can be used for future mechanistic studies. To this end, we used our new model to determine whether prior IAV infection created a favorable environment for fungal escape from the host antifungal innate immune response, and if so, to experimentally define the host cellular function(s) modulated by the post-IAV lung environment.

Host resistance against *A. fumigatus* can be lost by either quantitative or qualitative defects in the antifungal leukocyte response (39). To begin to investigate how prior IAV infection enhanced susceptibility to *A. fumigatus*, we examined both inflammatory immune cell accumulation in the lungs and their antifungal functions in that environment. Flow cytometry analysis of lung suspensions showed that levels of neutrophil, interstitial macrophage, monocyte, and cDC2 accumulation in the lung parenchyma were similar in IAV-*Af*-superinfected and *A. fumigatus*-only-infected mice (Fig. 2). This is in line with the inferred cellular makeup of the human IAPA bronchoalveolar lavage fluid in human patients with IAPA versus IAV infection alone (38). In contrast, Tobin et al. previously found that the proportion of neutrophils and alveolar macrophages was decreased in IAV-*Af*-superinfected mice compared to *A. fumigatus*-only infection (17). The authors did not quantify absolute numbers of inflammatory cells but did note overall increased inflammation in their histological analysis, which could explain our discrepant results. Additionally, our studies utilized the CEA10 strain of *A. fumigatus*, while Tobin et al. used the ATCC 42202 strain (17), which could also drive the differences in our findings since *A. fumigatus* strain heterogeneity alters virulence and host immune responses (40–45). Future studies will examine the role of *A. fumigatus* strain heterogeneity in driving IAPA.

Since we observed no obvious quantitative differences in the innate immune cell response in the IAV-*Af*-superinfected mice versus mice infected with *A. fumigatus* only, it was likely that the innate immune cells from the IAV-*Af*-superinfected mice had functional defects in their antifungal effector response in the post-IAV lung environment. To examine the overall antifungal effector functions of host leukocytes in our murine IAV-*Af* superinfection model, we used the robust *in vivo* FLARE method to determine both conidial uptake and killing by professional phagocytes in the presence or absence of IAV infection (27). We found that neutrophils and monocytes had defects in both conidial uptake and killing in the post-IAV lung environment (Fig. 3). This is in line with what others have observed with regard to leukocyte function in IAV-induced secondary bacterial infections (16, 46). Moreover, this directly supports the transcriptome correlates identified in human patients with IAPA (38).

Innate immune resistance against *A. fumigatus* requires both ROS-dependent and ROS-independent mechanisms for fungal conidial clearance (39, 47). Oxidative stress from host ROS production is known for preventing fungal conidial germination (48). IAV infection can limit ROS production in neutrophils and monocytes after secondary bacterial challenge (49). In contrast, to what was seen with bacterial challenge, we observed no defect in ROS production by both neutrophils and monocytes from IAV-*Af*-superinfected mice compared to mice infected with only *A. fumigatus* (Fig. 4). We also noticed that there were more ROS-producing neutrophils in IAV single infection, which was consistent with previous IAV infection studies (49, 50). Thus, our data suggest that monocytes and neutrophils from IAV-*Af*-superinfected mice maintain robust ROS production in response to secondary fungal challenge, which may be reflective of

bacterial infections being highly dependent on TLRs for the induction of ROS, whereas fungal infections are highly dependent on CLR for the induction of ROS.

ROS-independent conidial clearance in both macrophages and neutrophils requires phagolysosome maturation to create an acidic environment, which is necessary for conidial killing (51, 52). A recent study also showed that betacoronavirus infection can lead to lysosome destruction, affect its acidification, and reduce bacterial clearance in the macrophage (53). To assess phagolysosome maturation in the neutrophils and monocytes within the IAV-*Af*-superinfected lungs, we used pHrodo-zymosan staining. Both neutrophils and monocytes displayed a significant reduction in pHrodo-zymosan signal following both IAV infection alone or IAV-*Af* superinfection (Fig. 5), which is supportive of impaired or slowed phagolysosome maturation in the post-IAV lung environment. In addition to the phagolysosome maturation level, we also examined the percentage of cells that are still able to take up and send the pHrodo-zymosan into mature phagolysosomes through the percentage of pHrodo-zymosan-positive cells in neutrophil and monocyte populations. Interestingly, we observed a significant reduction of monocytes that can respond to and send pHrodo-zymosan into mature phagolysosomes in the post-IAV environment. This suggests that the defects are in both pathogen-associated molecular pattern (PAMP) responsiveness and phagolysosome maturation in the post-IAV environment for monocytes (Fig. S8B). However, we did not detect a significant reduction in the percentage of pHrodo-zymosan<sup>+</sup> neutrophils from IAV-infected mice, indicating potential differences between neutrophils and monocytes in the post-IAV environment. Instead, the significant reduction of pHrodo-zymosan uptake in both the *A. fumigatus* single-infection and IAV-*Af* superinfection groups might be due to potential neutrophil exhaustion during fungal infection since the pHrodo-zymosan uptake requires the recognition and binding to the Dectin-1 receptor (Fig. S8A). Still, we can detect a decrease in mature phagolysosome and conidial killing in the pHrodo-zymosan<sup>+</sup> neutrophils, suggesting that the phenotype is not contributed by cell exhaustion post-IAV infection (Fig. 6C and E). In summary, our data revealed that the post-IAV environment does not inhibit immune cell recruitment or ROS production in the face of a highly virulent *A. fumigatus* strain, but specifically reduces phagolysosome maturation in neutrophils and monocytes, which can lead to conidial escape from the host innate immunity during fungal infection.

A major question remaining from our study is how the post-IAV lung environment impairs phagolysosome maturation. To investigate the upstream signal that may drive defective fungal clearance in the IAV-*Af* superinfection mice in our model, we examined antifungal gene expression in isolated immune cells. Based on viral-bacterial superinfection literature, we expected to observe an anti-inflammatory gene expression profile after IAV infection and during early fungal infection (53–56). However, we observed that immune cells from IAV-*Af* superinfection mice displayed increased inflammatory gene transcript levels and decreased anti-inflammatory cytokine gene transcript levels (Fig. 7), indicating enhanced immune responses during early fungal infection. This result may be due to the increase in fungal burden in the superinfection group. Interestingly, we found reduced expression of three PRR genes (*Tlr9*, *Scarf1*, and *Clec12*) (Fig. 7). TLR9 is known to be recruited to the *A. fumigatus*-containing phagosome and contribute to fungus-induced immune cell activation (54, 55). On the other hand, TLR9 trafficking to the phagosome is mediated by Dectin-1 signaling and phagolysosome maturation and acidification (56, 57). Although we did not observe a difference in *Clec7a* transcript levels in the IAV-*Af* superinfection mice compared to the *A. fumigatus*-only infection group, the decreased *Tlr9* expression and reduced phagosome acidification in our IAV-*Af* superinfection model suggest impaired TLR9 activation and signaling. In addition to decreased *Tlr9* expression, we also observed decreased *Irak4* expression (Fig. 7), which is a component of the myddosome needed for TLR-dependent signaling (58). Therefore, it is likely that reduction of TLR9 signaling contributes to defects in phagolysosome maturation in neutrophils and monocytes or vice versa.

LC3-associated phagocytosis (LAP) is known to be associated with more rapid phagolysosome maturation (59). LAP is known to be essential for host resistance against *A.*



*fumigatus* (31, 32). In human IAPA and CAPA patients, genes *MAP1LC3B* and *SQSTM1*, related to LAP were decreased, while *CDC20*, the gene encoding for the CDC20 protein which is involved in LC3 degradation, was upregulated in the superinfection group comparing to viral single infection (38). Following CpG oligonucleotide activation of TLR9, LC3 can be recruited to the signaling endosome and mediate IKK $\alpha$  recruitment that leads to TRAF3 and IRF7 activation (60). Additionally, IFN- $\gamma$  enhances LAP following *A. fumigatus* challenge, but in humans with IAPA, the levels of IFN- $\gamma$  are diminished compared to those in infections with IAV only (38). Thus, we hypothesize that reducing TLR9 signaling in our IAV-Af superinfection model contributes to a decrease in LAP, further linking phagolysosome maturation and *A. fumigatus* clearance (32). This link between phagosome maturation and effective fungal clearance is well supported by mechanistic studies in other fungal pathogens, where phagolysosome maturation is key to clearance of infection (61–63). Still, further investigation of the role of LAP components specifically and contributions of TLR9 signaling in our IAV-Af superinfection model is required to address this possibility and to assess whether therapeutically targeting this pathway could restore host resistance against *A. fumigatus* after IAV infection.

In conclusion, we found that the post-IAV lung environment negatively affects phagolysosome maturation, which corresponds to reduced antifungal killing by both neutrophils and monocytes. This reduction in fungal killing leads to increased fungal germination, fungal growth, and eventual establishment of IAPA. Further studies are needed to investigate the upstream signals altering phagolysosome maturation in the presence of IAV. More information could be leveraged therapeutically to restore antifungal activity of impaired neutrophils and monocytes after IAV infection, to enhancing fungal clearance and clinical outcomes in IAPA patients. The findings from this study are also more broadly applicable, as recent clinical case reports have revealed that patients with severe COVID-19 can develop a secondary infection with *A. fumigatus* and these patients had worse clinical outcomes and higher mortality. It remains to be determined what the underlying mechanisms are for SARS-CoV2-induced secondary *A. fumigatus* infection.

## MATERIALS AND METHODS

**Animal inoculation.** C57BL/6J mice between 8 and 10 weeks old were purchased from Jackson Laboratories. Mice were housed in autoclaved cages at  $\leq 4$  mice per cage with a supply of HEPA-filtered air and water. Only mice with a weight under 22 g were selected for all experiments. The stock of influenza A/PR/8/34 H1N1 was purchased from Charles River, and the titer of the virus was quantified by 50% egg infectious dose (EID<sub>50</sub>). *A. fumigatus* strain CEA10 (also called CBS144.89) was grown on a 1% glucose minimal medium (GMM) plate for 3 days at 37°C. The conidia were collected in 0.01% Tween 20 and washed 3 times with sterile PBS. Mice were infected with 100 EID<sub>50</sub> of influenza A/PR/8/34 H1N1 (in 50  $\mu$ L sterile PBS) or control PBS by intranasal instillation under isoflurane anesthesia. After 6 days of viral infection, mice were infected with  $3.4 \times 10^7$  CEA10 conidia (in 100  $\mu$ L sterile PBS) or control PBS by oropharyngeal instillation. Mice were then euthanized between 8 to 48 h post-*Aspergillus* challenge. Animals were monitored daily for disease symptoms, and we carried out our animal studies in strict accordance with the recommendations in the *Guide for the Care and Use of Laboratory Animals* (64). The animal experimental protocol (no. 00002167) was approved by the Institutional Animal Care and Use Committee (IACUC) at Dartmouth College.

**RNA preparation and pathogen quantification.** Mice were inoculated with either PBS, influenza A/PR/8/34 H1N1, or CEA10 as described previously, and the lungs were removed at euthanasia for RNA extraction. Lungs were flash frozen, lyophilized, and homogenized with glass beads using a Mini-Beadbeater (BioSpec Products, Inc., Bartlesville, OK) and resuspended in TRIzol reagent (Thomas Scientific) and chloroform to extract RNA according to the manufacturer's instructions. Five micrograms of RNA was treated with Ambion Turbo DNase (Life Technologies) according to the manufacturer's instructions. One microgram of DNase-treated RNA was further processed with a QuantiTect reverse transcription kit with an additional 0.5 ng of random decamer. The amounts of RNA were normalized to *Gapdh* for fungal and viral burden. For murine GAPDH (glyceraldehyde-3-phosphate dehydrogenase), the following primers were used: forward, 5'-TCATCCCAGAGCTGAACG-3'; reverse, 5'-GGGAGTTGCTGT GAAGTC-3'. The fungal burden was measured by qRT-PCR on *Aspergillus fumigatus* 18S rRNA. For fungal burden, the following primers and probe were used: forward primer, 5'-GGCCCTTAAATAGCCCGGT-3'; reverse primer, 5'-TGAGCCGATAGTCCCCCTAA-3'; TaqMan probe, AGCCAGCGGCCCGCAAATG. The viral load was measured by qRT-PCR on viral matrix protein (17). For viral load, the following primers and probe were used: forward primer, 5'-GGACTGCAGCGTAGACGCTT-3'; reverse primer, 5'-CATCCTGTGT ATATGAGGCCCAT-3'; PrimeTime probe, 5'-56-FAM (carboxyfluorescein)-CTCAGTTAT-ZEN-TCTGCTGGT GCACCTGGCCA-3IABkFQ-3'.

**Histology staining.** Mice were inoculated with either PBS, influenza A/PR/8/34 H1N1, or CEA10 as described previously and euthanized at 48 h post-fungal inoculation. After euthanasia, cannulas were inserted into the trachea and the lungs were removed from the body cavity. The lungs were inflated and immersed in 10% buffered formalin phosphate for 24 h and stored in 70% ethanol until embedding. Paraffin-embedded sections were stained with hematoxylin and eosin (H&E) to observe inflammation and Grocott-Gomori methenamine silver (GMS) to observe fungi. The images of H&E and GMS slides were analyzed microscopically with a Zeiss Axioplan 2 imaging microscope (Carl Zeiss Microimaging, Inc., Thornwood, NY) fitted with a QImaging Retiga-SRV Fast 1394 RGB camera.

**Flow cytometry: lung cellularity and fluorescence *Aspergillus* reporter analysis.** For the fluorescence *Aspergillus* reporter (FLARE) experiments, the CEA10 conidia that expressed mRFP were generated by ectopically insertion of a *gpdA*-driven mRFP construct with the *ptrA* gene as selection marker. To generate FLARE conidia, conidia that expressed mRFP were collected and labeled with Alexa Fluor 633 as described previously (27). Mice were inoculated with either PBS, influenza A/PR/8/34 H1N1, or FLARE conidia as described previously and euthanized at 36 h post-fungal inoculation. To harvest the single-cell suspension from mouse lungs, the whole lungs were minced and digested in buffer containing 2.2 mg/mL collagenase type IV (Worthington), 1 U/mL DNase 1 (New England Biotech), and 5% fetal bovine serum (FBS) at 37°C for 45 min. The digested samples were passed through 18-gauge needle, incubated in red blood cell (RBC) lysis buffer (eBioScience), neutralized in PBS, passed through 100- $\mu$ m-pore filter, and counted. The antibodies used for the flow cytometry analysis of different populations were as follows. For the neutrophil population, lung cells were stained with Survival dye (eFluor780; eBioScience), CD45 (Pacific Orange; Invitrogen), CD64 (BV421; BioLegend), Ly6G conjugated with fluorescein isothiocyanate (FITC) (BioLegend), and CD11b conjugated with peridinin chlorophyll protein (PerCP) and Cy5.5 (BioLegend). For the macrophage/monocyte population, lung cells were stained with Survival dye (eFluor780; eBioScience), IA/IE (MHC-II) (BV605; BioLegend), SiglecF (BV421; BD BioScience), Ly6G-FITC (BioLegend), CD103-FITC (BioLegend), CD11b-PerCP-Cy5.5 (BioLegend), and CD64 conjugated with phycoerythrin (PE)-Cy7 (BioLegend). For DC populations, lung cells were stained with Survival dye (eFluor780; eBioScience), IA/IE (MHC-II) (BV605; BioLegend), CD11b (Pacific Blue; BioLegend), CD103-FITC (BioLegend), CD317-PerCP-Cy5.5 (BioLegend), and CD11c-PE-Cy7 (BioLegend). The gating strategies for each of the cell populations are indicated in Fig. S1 to S3 in the supplemental material. The data were collected by Beckman Coulter Cytoflex S and analyzed with FlowJo version 10.8.1.

To quantify fungal CFU of intracellular conidia, lung cells in the single-cell suspension were further homogenized with glass beads using Mini-Beadbeater (BioSpec Products, Inc., Bartlesville, OK) and resuspended in PBS. The samples were diluted 1:100 and then plated on 1/2 Sabouraud dextrose agar plates, incubated overnight, and counted for CFU.

**Immune cell function: intracellular ROS production and phagolysosome maturation.** Mice were inoculated with either PBS, influenza A/PR/8/34 H1N1, or CEA10 conidia as described previously and euthanized at 8 h post-fungal inoculation. The single-cell suspensions were harvested as described previously. For measurement of intracellular ROS, lung cells from the single-cell suspensions were incubated with 1  $\mu$ M CM-H2DCFDA [5-(and-6)-chloromethyl-2',7'-dichlorodihydrofluorescein diacetate] (Thermo) at 37°C for 30 min according to the manufacturer's instructions. For the measurement of phagolysosome maturation, lung cells were incubated with 0.05 mg/mL of pHrodo Green zymosan bioparticles (Invitrogen) at 37°C for 2 h according to the manufacturer's instructions. CM-H2DCFDA or pHrodo-zymosan-stained lung cells were then stained with Survival dye (eFluor780; eBioScience), IA/IE (MHC-II) (BV605; BioLegend), SiglecF (BV421; BD BioScience), Ly6G-PE (BioLegend), CD11b-PerCP-Cy5.5 (BioLegend), and CD64-PE-Cy7 (BioLegend) for the gating of neutrophils and monocytes. The gating strategies for each of the cell populations are indicated in Fig. S6. To confirm intracellular localization of signals by microscopy and verify flow cytometry results in Fig. 6, mice were inoculated with CEA10-mRFP FLARE conidia, and lung cells were incubated with 0.05 mg/mL of pHrodo-zymosan at 37°C for 2 h and stained with Survival dye (eFluor780; eBioScience) and Ly6G-Pb (BioLegend) or Ly6G-Pb (BioLegend) alone. Images were acquired using an Andor W1 spinning disk confocal microscope mounted with a Nikon Eclipse Ti inverted microscope stand. Lasers with wavelengths of 405 nm (Ly6G-Pb; BioLegend), 488 nm (pHrodo-zymosan; Invitrogen), 561 nm (CEA10-mRFP) and 633 nm (Alexa Fluor 633-labeled conidia) (Invitrogen) were used for excitation. Images were viewed using Fiji software and were used to visualize flow cytometry results. Flow cytometry data were collected by Beckman Coulter Cytoflex S and analyzed with FlowJo version 10.8.1.

**RNA preparation and antifungal gene expression evaluation.** Mice were inoculated with either PBS, influenza A/PR/8/34 H1N1, or CEA10 conidia as described previously and euthanized at 8 h post-fungal inoculation. The single-cell suspensions were harvested as described previously. Following the cell isolation, the cells were lysed and RNA was collected with an RNeasy kit according to the manufacturer's instruction (Qiagen). A 0.5- $\mu$ g sample of RNA was further processed with the RT<sup>2</sup> First Strand kit (Qiagen). cDNA was mixed with RT<sup>2</sup> SYBR green master mix (Qiagen) and loaded onto RT<sup>2</sup> Profiler PCR arrays containing primers for antifungal genes (PAMM-147ZD; Qiagen) (Table S2). The RNA load was normalized with *Actb*, *Gapdh*, and *Hsp90ab1*.

**Statistical analysis.** All statistical analyses were performed with Prism 9.3.0 software (GraphPad Software, Inc., San Diego, CA). The log rank test and Gehan-Breslow-Wilcoxon test were performed for statistical analysis of the survival curve. For animal experiments, nonparametric analyses were performed (Kruskal-Wallis with Dunn's multiple comparisons and Mann-Whitney test with single comparisons). All error bars represent standard deviations, and significance is noted as follows: NS, not significant at  $P > 0.05$ ; \*,  $P \leq 0.05$ ; \*\*,  $P \leq 0.01$ ; \*\*\*,  $P \leq 0.001$ ; \*\*\*\*,  $P \leq 0.0001$ .

## SUPPLEMENTAL MATERIAL

Supplemental material is available online only.

**FIG S1**, TIF file, 1 MB.

**FIG S2**, TIF file, 1 MB.

**FIG S3**, TIF file, 1.1 MB.

**FIG S4**, TIF file, 0.5 MB.

**FIG S5**, TIF file, 1.4 MB.

**FIG S6**, TIF file, 1.4 MB.

**FIG S7**, TIF file, 0.3 MB.

**FIG S8**, TIF file, 0.4 MB.

**TABLE S1**, TIF file, 0.9 MB.

**TABLE S2**, XLSX file, 0.01 MB.

## ACKNOWLEDGMENTS

We give special thanks to Eric Dufour of the Center for Comparative Medicine and Research (CCMR) staff for helping with the animal experiments. Flow cytometry data were collected with technical assistance and resources from the Immune Monitoring and Flow Cytometry Resource (IMFCSR) at the Norris Cotton Cancer Center at Dartmouth.

This project was supported by NIH/NIAID grant R21-AI152019 (J.J.O.), NIH/NIAID R01AI39632 (R.A.C.), and a Cystic Fibrosis Foundation Research Development Grant (STANTO15RO). M.S.G. was supported by the Dartmouth College Immunology Training Program (NIH/NIAID T32 AI007363). We also thank the Imaging Facility at Dartmouth (Ann Lavanway) and the Biomolecular Targeting Core (P20-GM113132) for use of equipment.

## REFERENCES

- Margalit A, Kavanagh K. 2015. The innate immune response to *Aspergillus fumigatus* at the alveolar surface. *FEMS Microbiol Rev* 39:670–687. <https://doi.org/10.1093/femsre/fuv018>.
- Kauffman HF. 2003. Immunopathogenesis of allergic bronchopulmonary aspergillosis and airway remodeling. *Front Biosci* 8:190–196. <https://doi.org/10.2741/990>.
- Pashley CH. 2014. Fungal culture and sensitisation in asthma, cystic fibrosis and chronic obstructive pulmonary disorder: what does it tell us? *Mycopathologia* 178:457–463. <https://doi.org/10.1007/s11046-014-9804-y>.
- Dagenais TRT, Keller NP. 2009. Pathogenesis of *Aspergillus fumigatus* in invasive aspergillosis. *Clin Microbiol Rev* 22:447–465. <https://doi.org/10.1128/CMR.00055-08>.
- El-Baba F, Gao Y, Soubani AO. 2020. Pulmonary aspergillosis: what the generalist needs to know. *Am J Med* 133:668–674. <https://doi.org/10.1016/j.amjmed.2020.02.025>.
- King J, Henriët SSV, Warris A. 2016. Aspergillosis in chronic granulomatous disease. *J Fungi* 2:15. <https://doi.org/10.3390/jof2020015>.
- Schwartz IS, Friedman DZP, Zapernick L, Dingle TC, Lee N, Sligl W, Zelyas N, Smith SW. 2020. High rates of influenza-associated invasive pulmonary aspergillosis may not be universal: a retrospective cohort study from Alberta, Canada. *Clin Infect Dis* 71:1760–1763. <https://doi.org/10.1093/cid/ciaa007>.
- Zou P, Wang C, Zheng S, Guo F, Yang L, Zhang Y, Liu P, Shen Y, Wang Y, Zhang X, Tang L, Gao H, Li L. 2020. Invasive pulmonary aspergillosis in adults with avian influenza A (H7N9) pneumonia in China: a retrospective study. *J Infect Dis* 221(Suppl 2):S193–S197. <https://doi.org/10.1093/infdis/jiz682>.
- Rouzé A, Lemaître E, Martin-Loeches I, Povoja P, Diaz E, Nyga R, Torres A, Metzelard M, Du Cheyron D, Lambiotte F, Tamion F, Labruyere M, Geronimi CB, Luyt C-E, Nyunga M, Pouly O, Thille AW, Megarbane B, Saade A, Magira E, Llitjos J-F, Ioannidou I, Pierre A, Reignier J, Garot D, Kreitmann L, Baudel J-L, Voiriot G, Plantefevre G, Morawiec E, Asfar P, Boyer A, Mekontso-Dessap A, Makris D, Vinsonneau C, Floch P-E, Marois C, Ceccato A, Artigas A, Gaudet A, Nora D, Cornu M, Duhamel A, Labreuche J, Nseir S, coVAPid Study Group. 2022. Invasive pulmonary aspergillosis among intubated patients with SARS-CoV-2 or influenza pneumonia: a European multicenter comparative cohort study. *Crit Care* 26:11. <https://doi.org/10.1186/s13054-021-03874-1>.
- Ku YH, Chan KS, Yang CC, Tan CK, Chuang YC, Yu WL. 2017. Higher mortality of severe influenza patients with probable aspergillosis than those with and without other coinfections. *J Formos Med Assoc* 116:660–670. <https://doi.org/10.1016/j.jfma.2017.06.002>.
- Rijnders BJA, Schauwvlieghe AFAD, Wauters J. 2020. Influenza-associated pulmonary aspergillosis: a local or global lethal combination? *Clin Infect Dis* 71:1764–1767. <https://doi.org/10.1093/cid/ciaa010>.
- McCullers JA. 2014. The co-pathogenesis of influenza viruses with bacteria in the lung. *Nat Rev Microbiol* 12:252–262. <https://doi.org/10.1038/nrmicro3231>.
- Jia L, Xie J, Zhao J, Cao D, Liang Y, Hou X, Wang L, Li Z. 2017. Mechanisms of severe mortality-associated bacterial co-infections following influenza virus infection. *Front Cell Infect Microbiol* 7:338. <https://doi.org/10.3389/fcimb.2017.00338>.
- Barman TK, Racine R, Bonin JL, Califano D, Salmon SL, Metzger DW. 2021. Sequential targeting of interferon pathways for increased host resistance to bacterial superinfection during influenza. *PLoS Pathog* 17:e1009405. <https://doi.org/10.1371/journal.ppat.1009405>.
- Abramson JS, Lewis JC, Lyles DS, Heller KA, Mills EL, Bass DA. 1982. Inhibition of neutrophil lysosome-phagosome fusion associated with influenza virus infection in vitro. Role in depressed bactericidal activity. *J Clin Invest* 69:1393–1397. <https://doi.org/10.1172/jci110580>.
- Sun K, Metzger DW. 2008. Inhibition of pulmonary antibacterial defense by interferon- $\gamma$  during recovery from influenza infection. *Nat Med* 14:558–564. <https://doi.org/10.1038/nm1765>.
- Tobin JM, Nickolich KL, Ramanan K, Pilewski MJ, Lamens KD, Alcorn JF, Robinson KM. 2020. Influenza suppresses neutrophil recruitment to the lung and exacerbates secondary invasive pulmonary aspergillosis. *J Immunol* 205:480–488. <https://doi.org/10.4049/jimmunol.2000067>.
- Bonnett CR, Cornish EJ, Harmsen AG, Burritt JB. 2006. Early neutrophil recruitment and aggregation in the murine lung inhibit germination of *Aspergillus fumigatus* conidia. *Infect Immun* 74:6528–6539. <https://doi.org/10.1128/IAI.00909-06>.
- Mircescu MM, Lipuma L, van Rooijen N, Pamer EG, Hohl TM. 2009. Essential role for neutrophils but not alveolar macrophages at early time points following *Aspergillus fumigatus* infection. *J Infect Dis* 200:647–656. <https://doi.org/10.1086/600380>.

20. Schaffner A, Douglas H, Braude AI, Davis CE. 1983. Killing of *Aspergillus* spores depends on the anatomical source of the macrophage. *Infect Immun* 42:1109–1115. <https://doi.org/10.1128/iai.42.3.1109-1115.1983>.
21. Philippe B, Ibrahim-Granet O, Prévost MC, Gougerot-Pocidallo MA, Sanchez Perez M, van der Meeren A, Latgé JP. 2003. Killing of *Aspergillus fumigatus* by alveolar macrophages is mediated by reactive oxidant intermediates. *Infect Immun* 71:3034–3042. <https://doi.org/10.1128/IAI.71.6.3034-3042.2003>.
22. Gafa V, Lande R, Gagliardi MC, Severa M, Giacomini E, Remoli ME, Nisini R, Ramoni C, di Francesco P, Aldebert D, Grillot R, Coccia EM. 2006. Human dendritic cells following *Aspergillus fumigatus* infection express the CCR7 receptor and a differential pattern of interleukin-12 (IL-12), IL-23, and IL-27 cytokines, which lead to a Th1 response. *Infect Immun* 74:1480–1489. <https://doi.org/10.1128/IAI.74.3.1480-1489.2006>.
23. Bozza S, Gaziano R, Spreca A, Bacci A, Montagnoli C, di Francesco P, Romani L. 2002. Dendritic cells transport conidia and hyphae of *Aspergillus fumigatus* from the airways to the draining lymph nodes and initiate disparate Th responses to the fungus. *J Immunol* 168:1362–1371. <https://doi.org/10.4049/jimmunol.168.3.1362>.
24. Misharin AV, Morales-Nebreda L, Mutlu GM, Scott Budinger GR, Perlman H. 2013. Flow cytometric analysis of macrophages and dendritic cell subsets in the mouse lung. *Am J Respir Cell Mol Biol* 49:503–510. <https://doi.org/10.1165/rcmb.2013-0086MA>.
25. Gustafson TL, Schaffner W, Lavelly GB, Stratton CW, Johnson HK, Hutcheson RH. 1983. Invasive aspergillosis in renal transplant recipients: correlation with corticosteroid therapy. *J Infect Dis* 148:230–238. <https://doi.org/10.1093/infdis/148.2.230>.
26. Balloy V, Huerre M, Latgé JP, Chignard M. 2005. Differences in patterns of infection and inflammation for corticosteroid treatment and chemotherapy in experimental invasive pulmonary aspergillosis. *Infect Immun* 73:494–503. <https://doi.org/10.1128/IAI.73.1.494-503.2005>.
27. Jhingran A, Mar KB, Kumasaka DK, Knoblaugh SE, Ngo LY, Segal BH, Iwakura Y, Lowell CA, Hamerman JA, Lin X, Hohl TM. 2012. Tracing conidia fate and measuring host cell antifungal activity using a reporter of microbial viability in the lung. *Cell Rep* 2:1762–1773. <https://doi.org/10.1016/j.celrep.2012.10.026>.
28. O'Neill S, Brault J, Stasia M-J, Knaus UG. 2015. Genetic disorders coupled to ROS deficiency. *Redox Biol* 6:135–156. <https://doi.org/10.1016/j.redox.2015.07.009>.
29. Anjani G, Vignesh P, Joshi V, Shandilya JK, Bhattarai D, Sharma J, Rawat A. 2020. Recent advances in chronic granulomatous disease. *Genes Dis* 7:84–92. <https://doi.org/10.1016/j.gendis.2019.07.010>.
30. Balloy V, Chignard M. 2009. The innate immune response to *Aspergillus fumigatus*. *Microbes Infect* 11:919–927. <https://doi.org/10.1016/j.micinf.2009.07.002>.
31. Akoumianaki T, Kyrizizi I, Valsecchi I, Gresnigt MS, Samonis G, Drakos E, Boumpas D, Muszkietal L, Prevost MC, Kontoyiannis DP, Chavakis T, Netea MG, van de Veerdonk FL, Brakhage AA, El-Benna J, Beauvais A, Latgé JP, Chamliou G. 2016. *Aspergillus* cell wall melanin blocks LC3-associated phagocytosis to promote pathogenicity. *Cell Host Microbe* 19:79–90. <https://doi.org/10.1016/j.chom.2015.12.002>.
32. Martinez J, Malireddi RKS, Lu Q, Cunha LD, Pelletier S, Gingras S, Orchard R, Guan JL, Tan H, Peng J, Kanneganti TD, Virgin HW, Green DR. 2015. Molecular characterization of LC3-associated phagocytosis (LAP) reveals distinct roles for Rubicon, NOX2, and autophagy proteins. *Nat Cell Biol* 17:893–906. <https://doi.org/10.1038/ncb3192>.
33. Rolfes MA, Foppa IM, Garg S, Flannery B, Brammer L, Singleton JA, Burns E, Jernigan D, Olsen SJ, Bresee J, Reed C. 2018. Annual estimates of the burden of seasonal influenza in the United States: a tool for strengthening influenza surveillance and preparedness. *Influenza Other Respir Viruses* 12:132–137. <https://doi.org/10.1111/irv.12486>.
34. Reed C, Chaves SS, Kirley PD, Emerson R, Aragon D, Hancock EB, Butler L, Baumbach J, Hollick G, Bennett NM, Laidler MR, Thomas A, Meltzer MI, Finelli L. 2015. Estimating influenza disease burden from population-based surveillance data in the United States. *PLoS One* 10:e0118369. <https://doi.org/10.1371/journal.pone.0118369>.
35. Schauwvlieghe AFAD, Rijnders BJA, Philips N, Vanderbeke L, Wauters J, van den Berg CHSB, Juffermans NP, Schauwvlieghe AFAD, Rijnders BJA, Philips N, Verwijs R, Vanderbeke L, van Tienen C, Lagrou K, Verweij PE, van de Veerdonk FL, Gommers D, Spronk P, Bergmans DCJJ, Hoedemaekers A, Andrinopoulou E-R, van den Berg CHSB, Juffermans NP, Hodiadmont CJ, Vonk AG, Depuydt P, Boelens J, Wauters J. 2018. Invasive aspergillosis in patients admitted to the intensive care unit with severe influenza: a retrospective cohort study. *Lancet Respir Med* 6:782–792. [https://doi.org/10.1016/S2213-2600\(18\)30274-1](https://doi.org/10.1016/S2213-2600(18)30274-1).
36. Vanderbeke L, Spriet I, Breynaert C, Rijnders BJA, Verweij PE, Wauters J. 2018. Invasive pulmonary aspergillosis complicating severe influenza: epidemiology, diagnosis and treatment. *Curr Opin Infect Dis* 31:471–480. <https://doi.org/10.1097/QCO.0000000000000504>.
37. Arastehfar A, Carvalho A, van de Veerdonk FL, Jenks JD, Koehler P, Krause R, Cornely OA, Perlin DS, Lass-Floiri C, Hoenigl M. 2020. COVID-19 associated pulmonary aspergillosis (CAPA)—from immunology to treatment. *J Fungi* 6:91–17. <https://doi.org/10.3390/jof6020091>.
38. Feys S, Gonçalves SM, Khan M, Choi S, Boeckx B, Chatelain D, Cunha C, Debaveye Y, Hermans G, Hertoghs M, Humblet-Baron S, Jacobs C, Lagrou K, Marcelis L, Maizel J, Meersseman P, Nyga R, Seldeslachts L, Starick MR, Thevissen K, Vandenbriele C, Vanderbeke L, Vande Velde G, van Regenmortel N, Vanstapel A, Vanmassenhove S, Wilmer A, van de Veerdonk FL, de Hertogh G, Mombaerts P, Lambrechts D, Carvalho A, van Weyenbergh J, Wauters J. 2022. Lung epithelial and myeloid innate immunity in influenza-associated or COVID-19-associated pulmonary aspergillosis: an observational study. *Lancet Respir Med* [https://doi.org/10.1016/S2213-2600\(22\)00259-4](https://doi.org/10.1016/S2213-2600(22)00259-4).
39. Latgé JP, Chamliou G. 2019. *Aspergillus fumigatus* and aspergillosis in 2019. *Clin Microbiol Rev* 33:e00140-18. <https://doi.org/10.1128/CMR.00140-18>.
40. Jones JT, Liu K-W, Wang X, Kowalski CH, Ross BS, Mills KAM, Kerkaert JD, Hohl TM, Lofgren LA, Stajich JE, Obar JJ, Cramer RA. 2021. *Aspergillus fumigatus* strain-specific conidia lung persistence causes an allergic broncho-pulmonary aspergillosis-like disease phenotype. *mSphere* 6:e01250-20. <https://doi.org/10.1128/mSphere.01250-20>.
41. Caffrey-Carr AK, Hilmer KM, Kowalski CH, Shepardson KM, Temple RM, Cramer RA, Obar JJ. 2018. Host-derived leukotriene B<sub>4</sub> is critical for resistance against invasive pulmonary aspergillosis. *Front Immunol* 8:1984. <https://doi.org/10.3389/fimmu.2017.01984>.
42. Caffrey-Carr AK, Kowalski CH, Beattie SR, Blaseg NA, Upshaw CR, Thammahong A, Lust HE, Tang YW, Hohl TM, Cramer RA, Obar JJ. 2017. Interleukin 1 $\alpha$  is critical for resistance against highly virulent *Aspergillus fumigatus* isolates. *Infect Immun* 85:e00661-17. <https://doi.org/10.1128/IAI.00661-17>.
43. Kowalski CH, Beattie SR, Fuller KK, McGurk EA, Tang YW, Hohl TM, Obar JJ, Cramer RA. 2016. Heterogeneity among isolates reveals that fitness in low oxygen correlates with *Aspergillus fumigatus* virulence. *mBio* 7:e01515-16. <https://doi.org/10.1128/mBio.01515-16>.
44. Rizzetto L, Giovannini G, Bromley M, Bowyer P, Romani L, Cavalieri D. 2013. Strain dependent variation of immune responses to *A. fumigatus*: definition of pathogenic species. *PLoS One* 8:e56651. <https://doi.org/10.1371/journal.pone.0056651>.
45. Rosowski EE, Raffa N, Knox BP, Golenberg N, Keller NP, Huttenlocher A. 2018. Macrophages inhibit *Aspergillus fumigatus* germination and neutrophil-mediated fungal killing. *PLoS Pathog* 14:e1007229. <https://doi.org/10.1371/journal.ppat.1007229>.
46. Shahangian A, Chow EK, Tian X, Kang JR, Ghaffari A, Liu SY, Belperio JA, Cheng G, Deng JC. 2009. Type I IFNs mediate development of postinfluenza bacterial pneumonia in mice. *J Clin Invest* 119:1910–1920. <https://doi.org/10.1172/JCI35412>.
47. Urban CF, Backman E. 2020. Eradicating, retaining, balancing, swarming, shuttling and dumping: a myriad of tasks for neutrophils during fungal infection. *Curr Opin Microbiol* 58:106–115. <https://doi.org/10.1016/j.mib.2020.09.011>.
48. Vethanayagam RR, Almyroudis NG, Grimm MJ, Lewandowski DC, Pham CTN, Blackwell TS, Petraitienė R, Petraitis V, Walsh TJ, Urban CF, Segal BH. 2011. Role of NADPH oxidase versus neutrophil proteases in antimicrobial host defense. *PLoS One* 6:e28149. <https://doi.org/10.1371/journal.pone.0028149>.
49. Abramson JS, Mills EL, Giebink GS, Quie PG. 1982. Depression of monocyte and polymorphonuclear leukocyte oxidative metabolism and bactericidal capacity by influenza A virus. *Infect Immun* 35:350–355. <https://doi.org/10.1128/iai.35.1.350-355.1982>.
50. Akaike T, Ando M, Oda T, Doi T, Ijiri S, Araki S, Maeda H. 1990. Dependence on O<sub>2</sub> generation by xanthine oxidase of pathogenesis of influenza virus infection in mice. *J Clin Invest* 85:739–745. <https://doi.org/10.1172/JCI114499>.
51. Ibrahim-Granet O, Philippe B, Boleti H, Boisvieux-Ulrich E, Grenet D, Stern M, Latgé JP. 2003. Phagocytosis and intracellular fate of *Aspergillus fumigatus* conidia in alveolar macrophages. *Infect Immun* 71:891–903. <https://doi.org/10.1128/IAI.71.2.891-903.2003>.
52. Gazendam RP, van Hamme JL, Tool ATJ, Hoogenboezem M, van den Berg JM, Prins JM, Vitkov L, van de Veerdonk FL, van den Berg TK, Roos D, Kuijpers TW. 2016. Human neutrophils use different mechanisms to kill

- Aspergillus fumigatus* conidia and hyphae: evidence from phagocyte defects. *J Immunol* 196:1272–1283. <https://doi.org/10.4049/jimmunol.1501811>.
53. Peng X, Kim J, Gupta G, Agaronyan K, Mankowski MC, Korde A, Takyar SS, Shin HJ, Habet V, Voth S, Audia JP, Chang D, Liu X, Wang L, Cai Y, Tian X, Ishibe S, Kang M-J, Compton S, Wilen CB, Dela Cruz CS, Sharma L. 2022. Coronavirus lung infection impairs host immunity against secondary bacterial infection by promoting lysosomal dysfunction. *J Immunol* 209:1314–1322. <https://doi.org/10.4049/jimmunol.2200198>.
  54. Herbst S, Shah A, Mazon Moya M, Marzola V, Jensen B, Reed A, Birrell MA, Saijo S, Mostowy S, Shaunak S, Armstrong-James D. 2015. Phagocytosis-dependent activation of a TLR9-BTK-calcineurin-NFAT pathway coordinates innate immunity to *Aspergillus fumigatus*. *EMBO Mol Med* 7:240–258. <https://doi.org/10.15252/emmm.201404556>.
  55. Kasperkovitz PV, Cardenas ML, Vyas JM. 2010. TLR9 is actively recruited to *Aspergillus fumigatus* phagosomes and requires the N-terminal proteolytic cleavage domain for proper intracellular trafficking. *J Immunol* 185:7614–7622. <https://doi.org/10.4049/jimmunol.1002760>.
  56. Mansour MK, Tam JM, Khan NS, Seward M, Davids PJ, Puranam S, Sokolovska A, Sykes DB, Dagher Z, Becker C, Tanne A, Reedy JL, Stuart LM, Vyas JM. 2013. Dectin-1 activation controls maturation of  $\beta$ -1,3-glucan-containing phagosomes. *J Biol Chem* 288:16043–16054. <https://doi.org/10.1074/jbc.M113.473223>.
  57. Khan NS, Kasperkovitz P v, Timmons AK, Mansour MK, Tam JM, Seward MW, Reedy JL, Puranam S, Feliu M, Vyas JM. 2016. Dectin-1 controls TLR9 trafficking to phagosomes containing  $\beta$ -1,3 glucan. *J Immunol* 196:2249–2261. <https://doi.org/10.4049/jimmunol.1401545>.
  58. de Nardo D, Balka KR, Gloria YC, Rao VR, Latz E, Masters SL. 2018. Interleukin-1 receptor-associated kinase 4 (IRAK4) plays a dual role in myddosome formation and Toll-like receptor signaling. *J Biol Chem* 293:15195–15207. <https://doi.org/10.1074/jbc.RA118.003314>.
  59. Heckmann BL, Boada-Romero E, Cunha LD, Magne J, Green DR. 2017. LC3-associated phagocytosis and inflammation. *J Mol Biol* 429:3561–3576. <https://doi.org/10.1016/j.jmb.2017.08.012>.
  60. Hayashi K, Taura M, Iwasaki A. 2018. The interaction between IKK $\alpha$  and LC3 promotes type I interferon production through the TLR9-containing LAPosome. *Sci Signal* 11:eaan4144. <https://doi.org/10.1126/scisignal.aan4144>.
  61. Vylkova S, Lorenz MC. 2014. Modulation of phagosomal pH by *Candida albicans* promotes hyphal morphogenesis and requires Stp2p, a regulator of amino acid transport. *PLoS Pathog* 10:e1003995. <https://doi.org/10.1371/journal.ppat.1003995>.
  62. Chen R, Ji G, Ma T, Huang X, Ren H, Xi L. 2015. Role of intracellular free calcium in killing *Penicillium marneffei* within human macrophages. *Microb Pathog* 83–84:29–34. <https://doi.org/10.1016/j.micpath.2015.05.001>.
  63. Isaac DT, Coady A, Prooyen NN, Sil A. 2013. The 3-hydroxy-methylglutaryl coenzyme A lyase HCL1 is required for macrophage colonization by human fungal pathogen *Histoplasma capsulatum*. *Infect Immun* 81:411–420. <https://doi.org/10.1128/IAI.00833-12>.
  64. National Research Council. 2011. Guide for the care and use of laboratory animals, 8th ed. National Academies Press, Washington, DC.

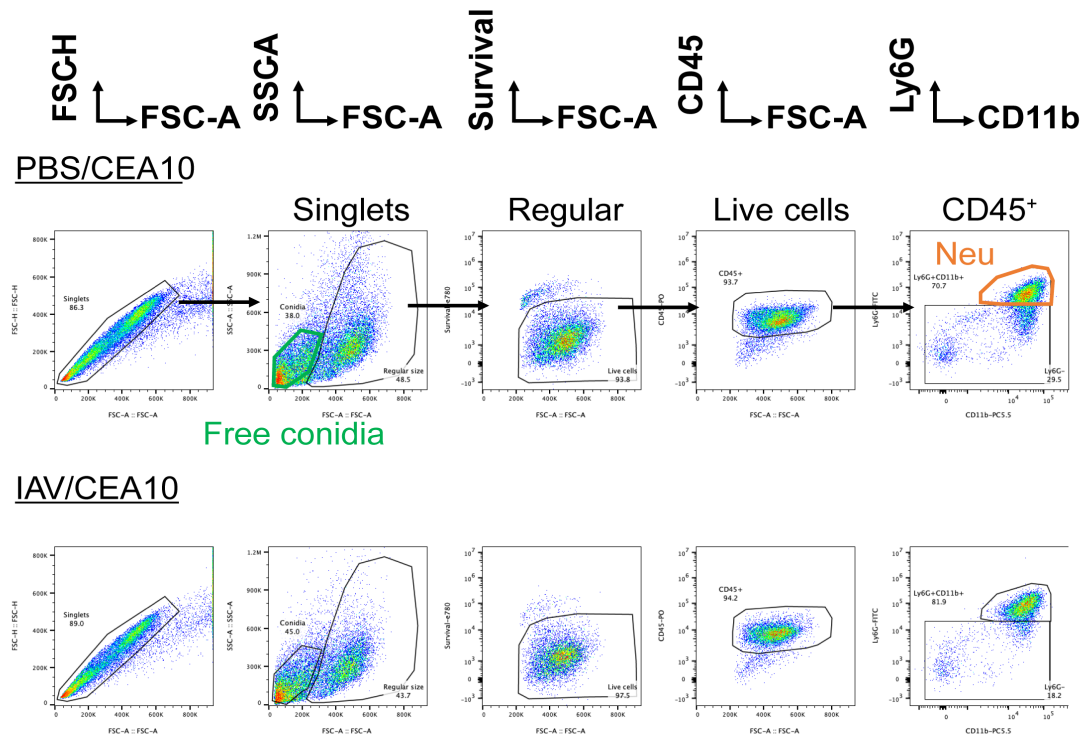


**Fig. S1 Gating strategy for Neutrophils.** The neutrophils were identified as  $\text{CD45}^{(+)}\text{Ly6G}^{(+)}\text{CD11b}^{(+)}$  cells and free conidia as  $\text{FSC}^{(\text{low})}\text{SSC}^{(\text{low})}$  cells.

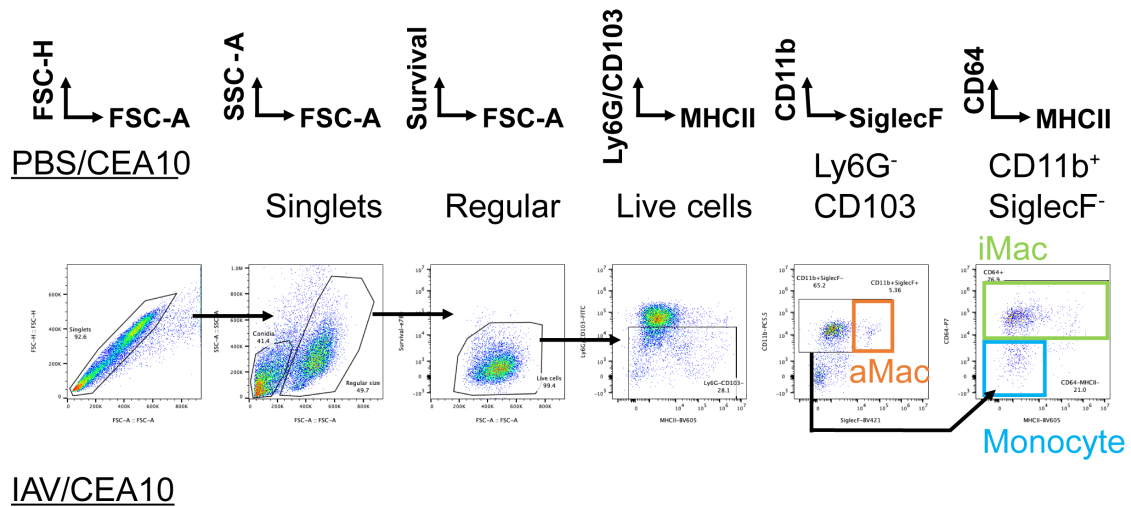


**Fig. S2 Gating strategy for Macrophages/Monocytes.** The alveolar macrophages were identified as Ly6G<sup>(-)</sup>CD103<sup>(-)</sup>SiglecF<sup>(+)</sup>CD11b<sup>(+)</sup> cells, interstitial macrophages as Ly6G<sup>(-)</sup>CD103<sup>(-)</sup>SiglecF<sup>(-)</sup>CD11b<sup>(hi)</sup>CD64<sup>(+)</sup> cells and monocytes as Ly6G<sup>(-)</sup>CD103<sup>(-)</sup>SiglecF<sup>(-)</sup>CD11b<sup>(hi)</sup>CD64<sup>(-)</sup>MHCII<sup>(-)</sup> cells.



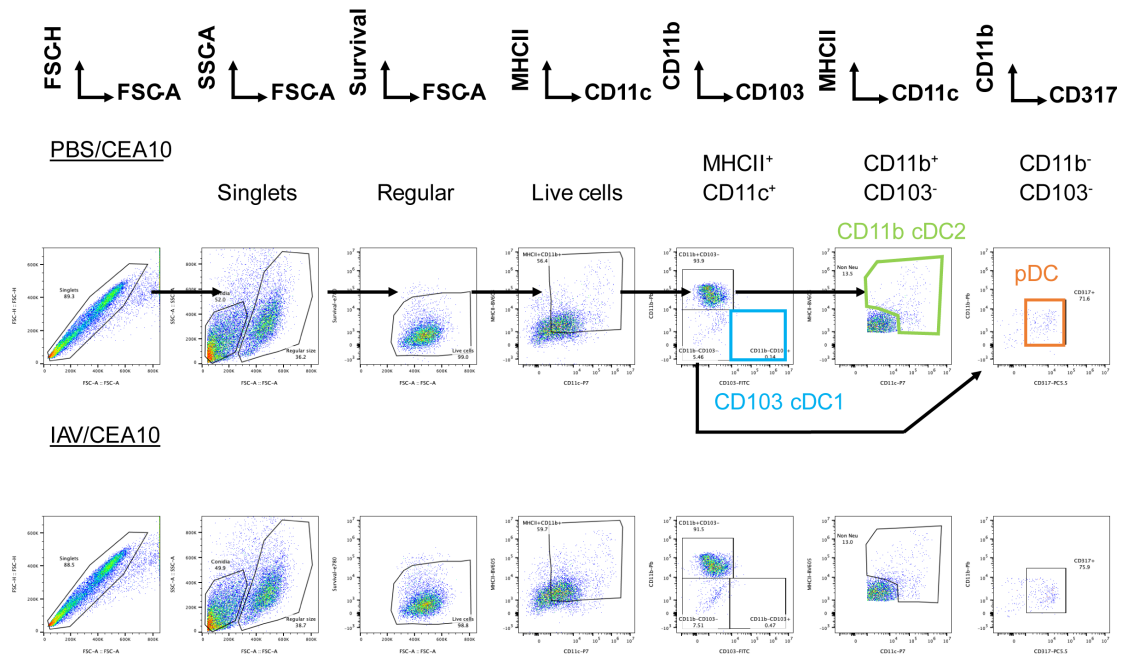


**Fig. S3 Gating strategy for DCs.** The CD103<sup>(+)</sup> cDC1 were identified as MHCII<sup>(+)</sup>CD11c<sup>(+)</sup>CD11b<sup>(-)</sup>CD103<sup>(+)</sup> cells, CD11b<sup>(+)</sup> cDC2 were identified as MHCII<sup>(hi)</sup>CD11c<sup>(hi)</sup>CD103<sup>(-)</sup>CD11b<sup>(+)</sup> cells and pDC were identified as MHCII<sup>(+)</sup>CD11c<sup>(+)</sup>CD11b<sup>(-)</sup>CD103<sup>(-)</sup>CD317<sup>(+)</sup> cells.



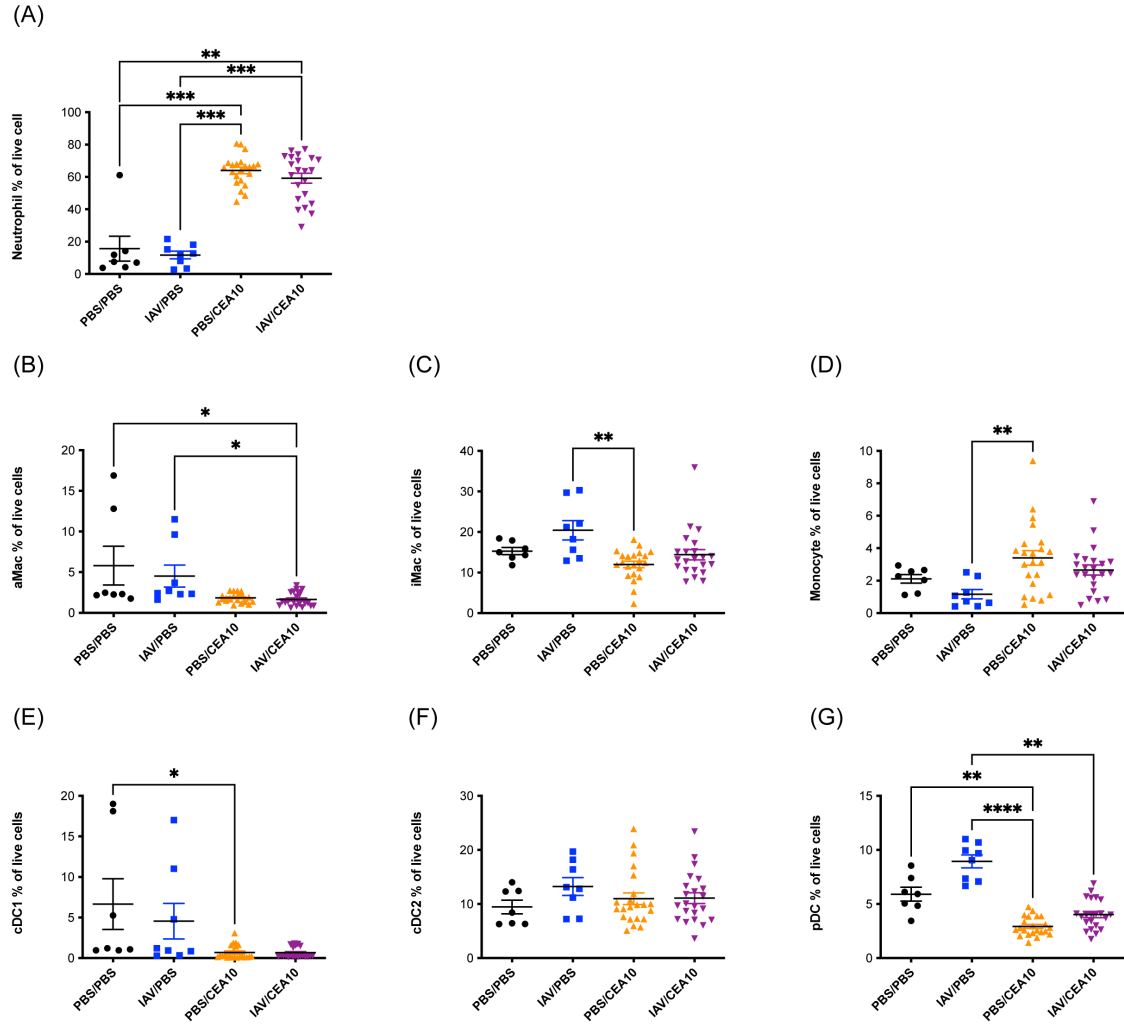


**Fig. S4 Influenza A virus infection does not affect immune cell composition during IA.** C57BL/6 mice were inoculated with 100 EID 50 IAV or PBS at Day 0 followed by  $3.4 \times 10^7$  CEA10 conidia or PBS at Day 6. Mice were euthanized at 36 hours post CEA10 or PBS inoculation for lung cellularity experiments. Three independent experiments were performed and data are shown as the combined results (PBS/PBS group: n=7; IAV/PBS group: n=8; PBS/CEA10 group: n=22; IAV/CEA10 group: n=22). The percentage of lung cells was acquired by flow cytometry as indicated as: (A) neutrophils ( $CD45^{+}Ly6G^{+}CD11b^{+}$ ), (B) alveolar macrophages ( $Ly6G^{-}CD103^{-}SiglecF^{+}CD11b^{+}$ ), (C) interstitial macrophages ( $Ly6G^{-}CD103^{-}SiglecF^{-}CD11b^{(hi)}CD64^{+}$ ), (D) monocytes ( $Ly6G^{-}CD103^{-}SiglecF^{-}CD11b^{(hi)}CD64^{-}MHCII^{-}$ ), (E)  $CD103^{+}cDC1$  ( $MHCII^{+}CD11c^{+}CD11b^{-}CD103^{+}$ ), (F)  $CD11b^{+}cDC2$  ( $MHCII^{(hi)}CD11c^{(hi)}CD103^{-}CD11b^{+}$ ), (G) pDC ( $MHCII^{+}CD11c^{+}CD11b^{-}CD103^{-}CD317^{+}$ ). Kruskal-Wallis with Dunn's multiple comparisons was performed for statistical analyses. All error bars represent standard deviations. NS, not significant at  $P > 0.05$ ; \*  $P \leq 0.05$ ; \*\*  $P \leq 0.01$ ; \*\*\*  $P \leq 0.001$ ; \*\*\*\*  $P \leq 0.0001$ .

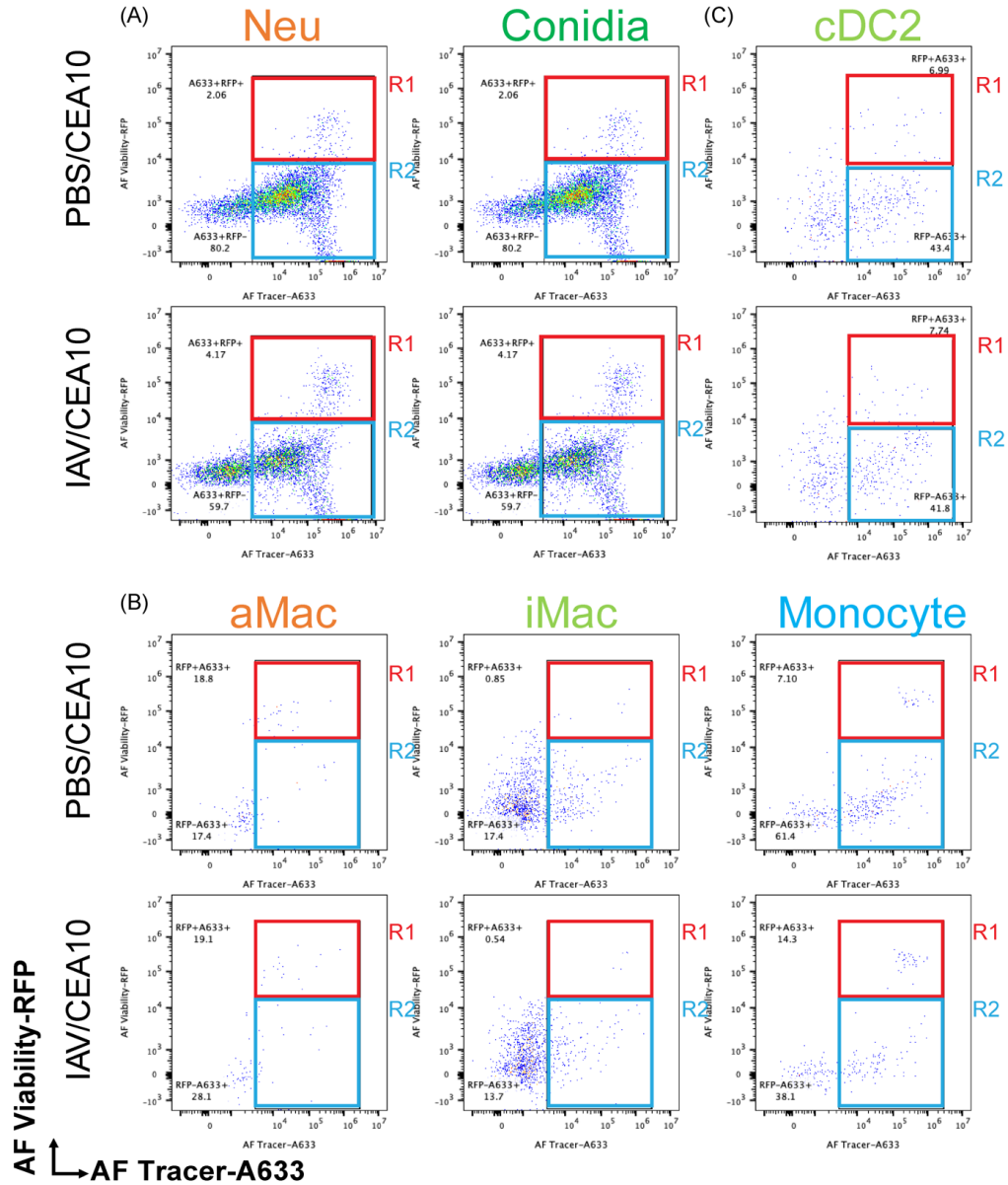


**Fig. S5 FLARE results of lung phagocytes.** The gating for FLARE experiments in the (A) neutrophils and free conidia, (B) alveolar macrophages, interstitial macrophages and monocytes, (C) CD11b<sup>+</sup> cDC2. R1 denotes phagocytes containing live conidia. R2 denotes phagocytes containing killed conidia. (R1+R2) indicates conidial uptake of phagocytes and (R1/(R1+R2)) indicates conidial viability in the phagocytes.

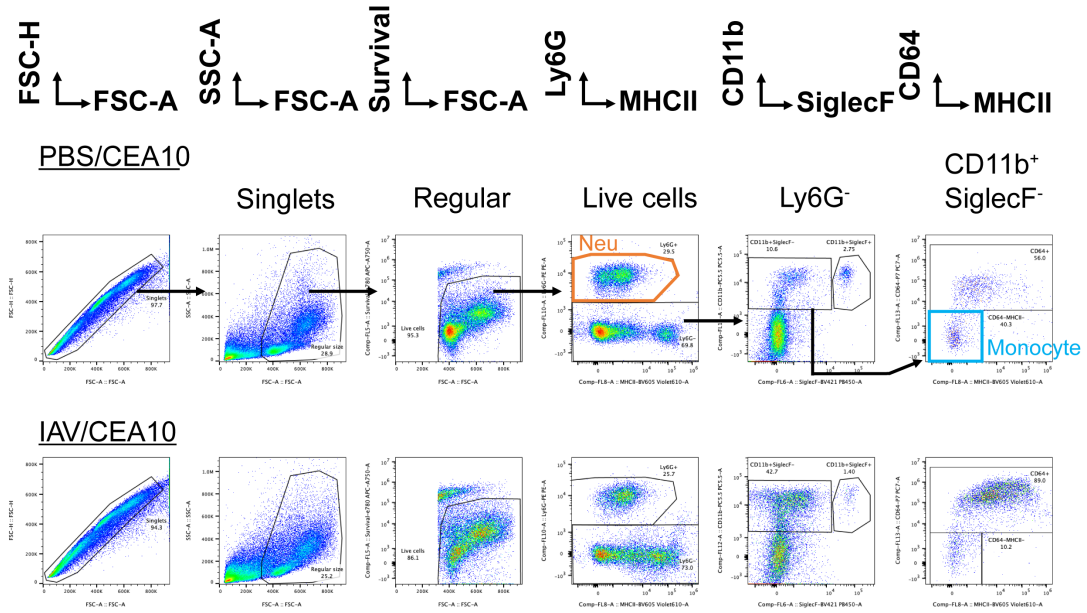


**Fig. S6 Gating strategy for pHrodo/ROS experiments.** The neutrophils were identified as Ly6G<sup>(+)</sup> cells and monocytes as Ly6G<sup>(-)</sup>CD103<sup>(-)</sup>SiglecF<sup>(-)</sup>CD11b<sup>(hi)</sup>CD64<sup>(-)</sup>MHCII<sup>(-)</sup> cells. Representative dot plots were from pHrodo-Zymosan staining experiment.

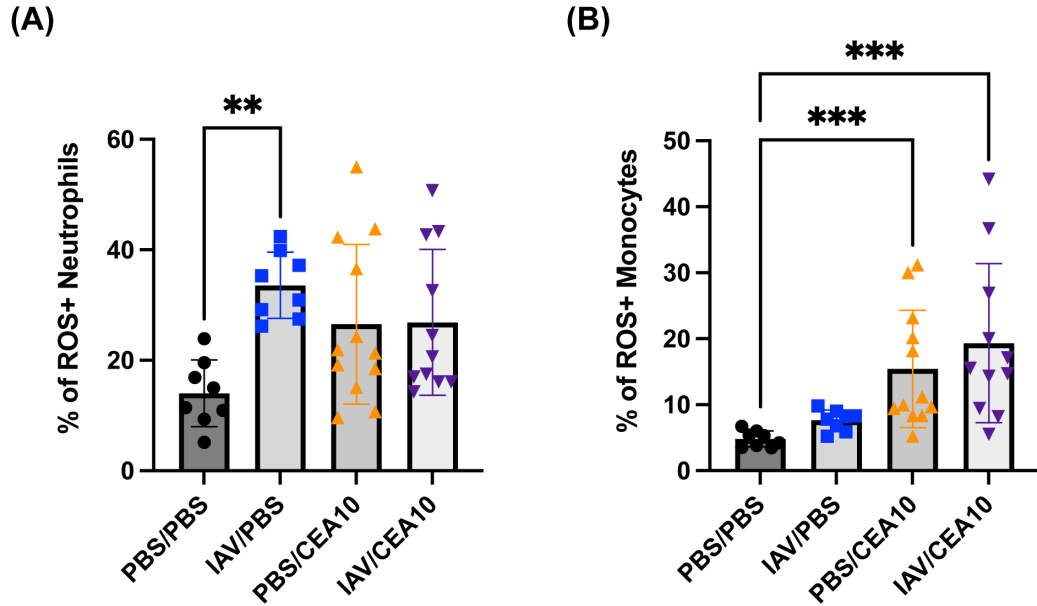


**Fig. S7 Post influenza environment does not reduce ROS productive Neutrophils and Monocytes.** C57BL/6 mice were inoculated with 100 EID 50 IAV or PBS at Day 0 followed by  $3.4 \times 10^7$  CEA10 conidia or PBS at Day 6. Mice were euthanized at 8 hours post CEA10 or PBS inoculation. Lung cell suspensions were stained with CM-H2DCFDA for 30 minutes and then stained for neutrophils and monocytes. The percentage of ROS producing cells was shown as the percentage of cells with positive signal from CM-H2DCFDA staining in (A) neutrophils (Ly6G<sup>(+)</sup>), (B) monocytes (Ly6G<sup>(-)</sup>CD103<sup>(-)</sup>SiglecF<sup>(-)</sup>CD11b<sup>(hi)</sup>CD64<sup>(-)</sup>MHCII<sup>(-)</sup>). Two independent experiments were performed and data are shown as the combined results (PBS/PBS group: n=8; IAV/PBS group: n=8; PBS/CEA10 group: n=12; IAV/CEA10 group: n=11). Kruskal-Wallis with Dunn's multiple comparisons was performed. All error bars represent standard deviations. NS, not significant at  $P > 0.05$ ; \*  $P \leq 0.05$ ; \*\*  $P \leq 0.01$ ; \*\*\*  $P \leq 0.001$ ; \*\*\*\*  $P \leq 0.0001$ .

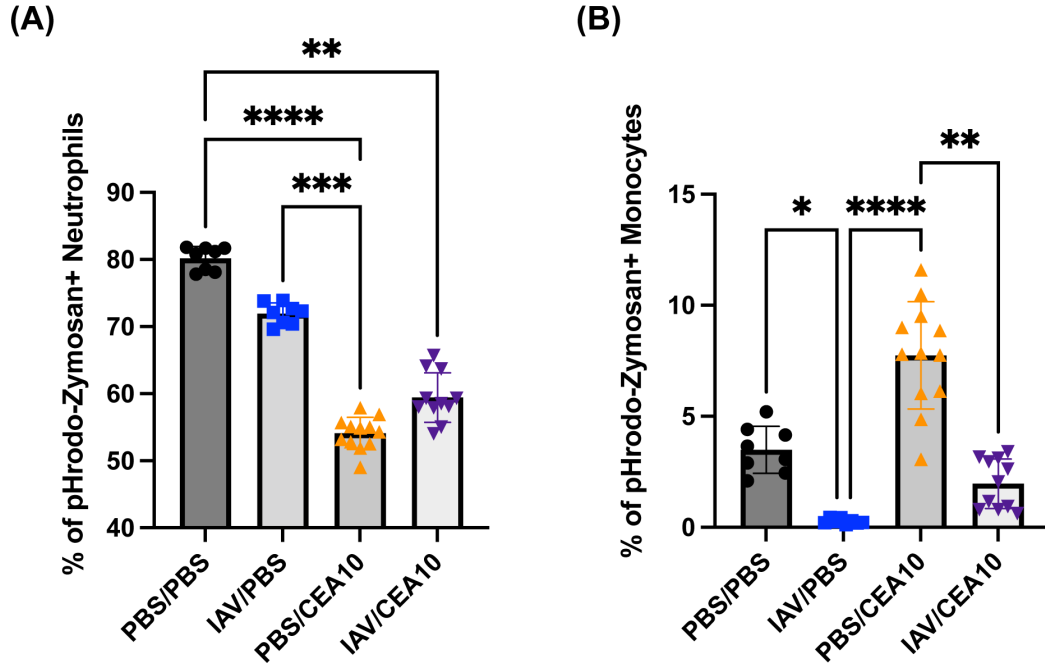


**Fig. S8 Post influenza environment hinders the phagocytosis of Monocytes.** C57BL/6 mice were inoculated with 100 EID 50 IAV or PBS at Day 0 followed by  $3.4 \times 10^7$  CEA10 conidia or PBS at Day 6. Mice were euthanized at 8 hours post CEA10 or PBS inoculation for phagolysosome maturation analysis. Lung cell suspensions were incubated with pHrodo-Zymosan for 2 hours and then stained for neutrophils and monocytes. The percentage of active cells with mature phagolysosome was measure by the percentage of cells with positive signal from the color change of pHrodo-Zymosan in (A) neutrophils ( $\text{Ly6G}^{(+)}$ ), (B) monocytes ( $\text{Ly6G}^{(-)}\text{SiglecF}^{(-)}\text{CD11b}^{(\text{hi})}\text{CD64}^{(-)}\text{MHCII}^{(-)}$ ). Two independent experiments were performed and data are shown as the combined results (PBS/PBS group: n=8; IAV/PBS group: n=8; PBS/CEA10 group: n=12; IAV/CEA10 group: n=11). Kruskal-Wallis with Dunn's multiple comparisons was performed for statistical analyses. All error bars represent standard deviations. NS, not significant at  $P > 0.05$ ; \*  $P \leq 0.05$ ; \*\*  $P \leq 0.01$ ; \*\*\*  $P \leq 0.001$ ; \*\*\*\*  $P \leq 0.0001$ .

(A) Antibody lists

For NØ Population	
Neutrophil	CD45 <sup>(+)</sup> Ly6G <sup>(+)</sup> CD11b <sup>(+)</sup>
For Macrophage/Monocyte populations	
aMac	Ly6G <sup>(-)</sup> CD103 <sup>(-)</sup> SiglecF <sup>(+)</sup> CD11b <sup>(+)</sup>
iMac	Ly6G <sup>(-)</sup> CD103 <sup>(-)</sup> SiglecF <sup>(-)</sup> CD11b <sup>(hi)</sup> CD64 <sup>(+)</sup>
Monocyte	Ly6G <sup>(-)</sup> CD103 <sup>(-)</sup> SiglecF <sup>(-)</sup> CD11b <sup>(hi)</sup> CD64 <sup>(-)</sup> MHCII <sup>(-)</sup>
For DC Populations	
cDC1	MHCII <sup>(+)</sup> CD11c <sup>(+)</sup> CD11b <sup>(-)</sup> CD103 <sup>(+)</sup>
cDC2	MHCII <sup>(hi)</sup> CD11c <sup>(hi)</sup> CD11b <sup>(+)</sup> CD103 <sup>(-)</sup>
pDC	MHCII <sup>(+)</sup> CD11c <sup>(+)</sup> CD11b <sup>(-)</sup> CD103 <sup>(-)</sup> CD317 <sup>(+)</sup>
For pHrodo/ROS staining	
Neutrophil	Ly6G <sup>(+)</sup>
Monocyte	Ly6G <sup>(-)</sup> SiglecF <sup>(-)</sup> CD11b <sup>(hi)</sup> CD64 <sup>(-)</sup> MHCII <sup>(-)</sup>

(B) Cellular markers

For NØ Population								
CD64	CD45	Ly6G	CD11b	Survival	AF Viability	AF Tracer		
BV421	PO	FITC	PC5.5	e780	mRFP	A633		
For Macrophage/Monocyte populations								
Siglec F	MHCII	CD64	CD103	Ly6G	CD11b	Survival	AF Viability	AF Tracer
BV421	BV605	P7	FITC	FITC	PC5.5	e780	mRFP	A633
For DC Populations								
CD11b	MHCII	CD11b	CD103	CD317	Survival	AF Viability	AF Tracer	
Pb	BV605	P7	FITC	PC5.5	e780	mRFP	A633	
For pHrodo/ROS staining								
Siglec F	MHCII	CD64	pHrodo/ROS	CD11b	Survival	Ly6G		
BV421	BV605	P7	FITC	PC5.5	e780	PE		

**Table S1 Staining panels and cellular markers for Flow Cytometry.** (A) Antibody lists for neutrophils and free conidia populations, macrophages and monocytes populations, DC populations and pHrodo/ROS staining experiments. (B) Cellular markers for neutrophils, alveolar macrophages, interstitial macrophages, monocytes, CD103<sup>(+)</sup> cDC1, CD11b<sup>(+)</sup> cDC2, pDC and neutrophils/monocytes in the pHrodo and ROS staining experiments. Cell types within the specific staining panel are highlighted with same color.

Gene name	Fold Change	T-TEST
<i>Nlrp3</i>	74.737	0.038
<i>Pycard</i>	25.333	0.005
<i>Ptgs2</i>	8.280	0.005
<i>Cd36</i>	6.255	0.009
<i>Cxcl10</i>	4.610	0.003
<i>Nfkb1</i>	4.023	0.029
<i>Clec4n</i>	3.860	0.001
<i>Mapk14</i>	3.105	0.000
<i>Ptx3</i>	3.088	0.011
<i>Tlr2</i>	2.620	0.070
<i>Tlr4</i>	2.600	0.001
<i>Ccr5</i>	2.207	0.003
<i>Cd209a</i>	1.552	0.035
<i>Il23a</i>	1.478	0.018
<i>Mbl2</i>	1.323	0.090
<i>Fcnb</i>	1.186	0.297
<i>Irak1</i>	1.139	0.536
<i>Malt1</i>	1.035	0.972
<i>Map2k4</i>	1.032	0.996
<i>Ccr1</i>	1.021	0.987
<i>Cxcl3</i>	1.015	0.794
<i>Ccl5</i>	0.931	0.663
<i>Sftpd</i>	0.860	0.991
<i>Csf3</i>	0.858	0.359
<i>Ccl20</i>	0.840	0.518
<i>Il1a</i>	0.825	0.196
<i>Cd14</i>	0.794	0.058
<i>Il6</i>	0.793	0.424
<i>Il12b</i>	0.789	0.196
<i>Cxcl11</i>	0.733	0.670
<i>Stat1</i>	0.728	0.048
<i>F2rl1</i>	0.721	0.002
<i>St3gal5</i>	0.715	0.116
<i>Ikbbk</i>	0.681	0.158
<i>Il12a</i>	0.668	0.085
<i>Mapk8</i>	0.657	0.038
<i>Itgam</i>	0.652	0.844
<i>C3</i>	0.642	0.872
<i>Nfkbia</i>	0.639	0.015
<i>Il1r1</i>	0.635	0.009
<i>Fos</i>	0.632	0.172
<i>Fcgr4</i>	0.624	0.034

Gene name	Fold Change	T-TEST
<i>Bcl10</i>	0.610	0.804
<i>Il1b</i>	0.603	0.119
<i>Casp8</i>	0.597	0.790
<i>Il18</i>	0.594	0.210
<i>Ccl12</i>	0.588	0.809
<i>Ifng</i>	0.588	0.809
<i>Myd88</i>	0.588	0.809
<i>C5ar1</i>	0.581	0.658
<i>Casp1</i>	0.576	0.716
<i>Card9</i>	0.558	0.684
<i>Cxcl1</i>	0.549	0.068
<i>Plcg2</i>	0.536	0.199
<i>Fcgr3</i>	0.533	0.010
<i>Clec7a</i>	0.532	0.073
<i>Lyn</i>	0.523	0.012
<i>Tirap</i>	0.519	0.057
<i>Nptx1</i>	0.516	0.025
<i>Cd207</i>	0.503	0.039
<i>Il10</i>	0.471	0.035
<i>Il2</i>	0.425	0.018
<i>Colec12</i>	0.410	0.005
<i>Map3k7</i>	0.409	0.073
<i>Cd83</i>	0.398	0.008
<i>Chia1</i>	0.390	0.060
<i>Traf6</i>	0.377	0.179
<i>Csf2</i>	0.374	0.130
<i>Socs3</i>	0.357	0.067
<i>Cd40</i>	0.345	0.002
<i>Jun</i>	0.339	0.005
<i>Cd5</i>	0.339	0.003
<i>Itgb2</i>	0.337	0.012
<i>Tlr9</i>	0.310	0.041
<i>Irak4</i>	0.292	0.010
<i>Syk</i>	0.272	0.135
<i>F3</i>	0.269	0.119
<i>Raf1</i>	0.267	0.002
<i>Fcgr1</i>	0.258	0.015
<i>Cxcl9</i>	0.249	0.001
<i>Tnf</i>	0.187	0.022
<i>Scarf1</i>	0.183	0.000
<i>Ptpn6</i>	0.104	0.001
<i>Mrc1</i>	0.030	0.068

**Table S2 Gene list of antifungal RT2 Profiler PCR Arrays.** cDNA of mice from PBS/CEA10 (n=3) and IAV/CEA10 groups (n=3) was added to the plates containing primer sets in the table. The RNA load was normalized with *Actb*, *Gapdh* and *Hsp90ab1*. The gene expression was compared by IAV/CEA10 group over PBS/CEA10 group. Genes with increase fold changes >2 were shown in red and genes with decrease fold changes >2 were shown in blue.

## Chapter 3

### **LysMD3, a potential mammalian PRR, binds to fungal cell wall and partially contributes to anti-fungal immunity**

Ko-Wei Liu, Jane T. Jones, Elisa M. Vesely, Charles T.S. Puerner, Matthew R. James,  
Cecilia Gutierrez-Perez, Robert A. Cramer

KWL designed and performed the experiments, analyzed the results, and wrote the manuscript.

JTJ assisted with all the animal experiments

EMV helped with the writing.

CTSP helped with confocal imaging

MRJ helped with FLARE experiments.

CGP helped with the CFU experiments.

RAC designed the experiments, analyzed the results, and wrote the manuscript.



## Abstract

Chitin is one of the most abundance molecules on the planet, and also a highly potent pathogenic molecule, composed of oligomerized N-acetylglucosamine (GlcNAc). Chitin is utilized as a metabolite, signaling inducer, and can be recognized by host immune systems to induce complex immunological responses. However, despite numerous reports about chitin binding proteins and capacity for inducing downstream cytokine production, an authentic chitin receptor as the pattern recognition receptor (PRR) responsible for chitin induced signaling is still ill-defined. Here we explored a mammalian protein, LysMD3, with potential fungal cell wall binding activity that features a conserved GlcNAc binding motif, can bind to fungal surface, and has some minor changes to the host immune response. We found that LysMD3 mRNA expression is induced in CD45<sup>(+)</sup> lymphocytes upon *Aspergillus fumigatus* (*A. fumigatus*) infection. Additionally, we observed defects in fungal killing by LysMD3 deficient neutrophils and interstitial macrophages (iMacs), although the LysMD3 knockout (KO) mice we generated revealed largely similar mortality and cell recruitment during *A. fumigatus* infection when compared to wild type (WT) mice. Furthermore, Fc-tagged murine LysMD3 protein reveals binding of the ectodomain of LysMD3 to the surface of both conidia and germlings of *A. fumigatus*. Compared to the cellular patterns of the chitin and  $\beta$ -glucan binding reagents Wheat Germ Agglutinin (WGA) and dectin-1 respectively, the LysMD3 showed a unique binding pattern on both conidia and germlings of *A. fumigatus*, indicating that its binding to fungal surfaces does not simply rely on chitin and  $\beta$ -glucan amount in the cell wall. Leveraging the galactosaminogalactan (GAG) synthase mutant *A. fumigatus* with LysMD3 binding, we demonstrated that GAG is essential for LysMD3 binding on the fungal surface. Overall, our results showed that murine LysMD3, as a potential PRR, can bind to fungal cell wall surfaces in a GAG-dependent manner and this recognition may partially contribute to fungal killing during early *A. fumigatus* infections.

## Introduction

Human bodies inhale hundreds to thousands of fungal conidia each day, yet are highly efficient at fungal clearance after exposure. Upon *A. fumigatus* exposure, fungal recognition through pattern recognition receptors (PRRs) plays an important role in rapid immune cell recruitment, cell activation and antifungal responses (1). Due to the essential role of cell walls in cellular maintenance, the innate immune system recognizes pathogen infection through multiple PRRs that target fungal and bacterial cell wall components to initiate the immune responses (2). One vital cell wall component, chitin, can compose 10-20% of the biomass in the cell wall and induce immune responses *in vitro* and *in vivo* (3–5). Chitin itself is an oligomer of N-acetylglucosamine (GlcNAc) of various sizes and chitin-induced immune responses have been shown to be size-dependent (6). At the initial stages of fungal-host interaction, large polymers of chitin induce AMCase, an enzyme that degrades the larger polymers into intermediate chitin polymers (40-70  $\mu\text{m}$ ). These intermediate-sized chitin polymers can contribute to immune cell activation and downstream cytokine production (4). However, after fungal clearance and resulting accumulation of small chitin particles (<40  $\mu\text{m}$ ) induces anti-inflammatory cytokine production and leads to the immune resolving phase (7). As for chitin receptors in plants, size-dependent binding of chitin oligomers to specific receptors has been correlated with downstream immune responses (8). However, which receptors respond to these different sizes of chitin and how they contribute to different immune responses in the mammalian system are still incompletely described.

Multiple proteins have been proposed as chitin binding proteins in mammals. The Acidic mammalian chitinase (AMCase) and other chitinase-like proteins (C/CLPs) can bind and degrade chitin to inhibit chitin induced inflammatory response (9). Fibrinogen C containing domain 1 (FIBCD1) has strong binding to chitin and fungal surface (10, 11). TLR2 and Dectin-1 were proposed to be involved in chitin induced immune responses (12, 13). However, without a direct link between chitin and a specific

immune response or signaling transduction pathway, these proteins are still not confirmed as chitin receptors, regardless of chitin binding affinity. Here we propose that an ancient protein family containing Lysin Motif domains (LysM) might serve as a mammalian PRR for fungal cell wall recognition. LysM proteins have a structurally conserved, but not sequence-conserved, LysM domain with  $\beta\alpha\alpha\beta$  folding structure that can bind to N-acetylglucosamine (GlcNAc), which is the monomeric constituent of chitin and peptidoglycan (14). The first LysM protein described was found by Garvey et al. in 1986 as a lysozyme of Bacillus phage phi 29 (15). LysM domain-containing proteins are present in most organisms throughout all kingdoms of life including bacteria, plants, fungi and animals, with the notable exception of archaea (14). Combination of LysM domains with other functional protein domains gives LysM proteins specific function after binding to their targets. In the plant field, LysM proteins have been extensively studied due to their role as chitin receptors against fungal infection (16). While fungi can secrete LysM effectors to mask their chitin exposure (17), the LysM receptors in the plant bind to fungal chitin and serve as PRRs for pathogen detection and initiation of immune responses. Plant LysM receptors can further divide into two subtypes: 1) receptor-like kinases (RLKs) and 2) receptor-like proteins (RLPs), both possessing LysM domains in combination with transmembrane domain. RLKs contain canonical arginine/aspartate kinase (RD kinase) domains, which have been shown to result in autophosphorylation activity for downstream signal transduction *in vitro* (18, 19). RLKs with different chitin binding affinities can form homodimers or heterodimers and serve to pass signaling information through the MAPK signaling pathway for immune activation (8, 20, 21). Multiple LysM domains in plant RLKs form a chitin binding pocket with higher affinity for specific size of chitin, greatly affecting the efficacy of chitin-induced signaling (8). Outside of plants, LysM proteins in various shrimp species have been shown to play a role in bacterial detection, antimicrobial peptide expression, and bacterial clearance (22, 23). Thus, we hypothesize that LysM proteins in the mammalian immune system might also serve as bacterial or fungal recognition receptors that recognize surface-exposed pathogen associated molecular patterns (PAMPs).

Similar to the role of LysM effector proteins of fungal pathogens of plants, fungal pathogens of mammals also encode LysM effector proteins to mask their chitin exposure and support their colony expansion in the host or environment (24–26). On the host side, humans and mice both encode 6 LysM domain-containing proteins (LysMD1, LysMD2, LysMD3, LysMD4, Oxr1 and Ncoa7). This cluster of LysM family proteins is encoded in humans, mice, frogs and zebrafish and highlights the conservation of LysM proteins in animals (27). Among these LysM proteins, LysMD3 and LysMD4 both feature a functionally unannotated singular LysM domain, transmembrane domain and a relatively short cytoplasmic-localized region. Previous studies have shown that murine LysMD3 is localized within cells to the Golgi, but LysMD3 deficiency in mice does not reveal increased susceptibility to viral, bacteria, or fungal infections (27). However, a recent report showed that cell surface localized human LYSMD3 has weak binding affinity to chitin beads (50-70  $\mu\text{m}$ ) and chitin oligomers with different degrees of polymerization (DP) of 5 to 7 (DP5-7) (28). Additionally, human lung epithelial cell LYSMD3 responds to exogenous chitin and this response can induce IL-6 and IL-8 production, further highlighting the potential role for LysMD3 in innate immunity signaling processes (28).

In this work, we examined the binding affinity of LysMD3 to different growth stages of *Aspergillus fumigatus* and if murine LysMD3-deficiency affects innate immunity during fungal infection. During early *A. fumigatus* infection, we observed upregulation of LysMD3 mRNA expression and this was specific to immune cells. Although our LysMD3 deficient (knockout, KO) mice did not show drastically altered susceptibility to *A. fumigatus* infection, we did observe that LysMD3 deficient neutrophils and interstitial macrophages (iMacs) show decreased fungal killing during early fungal infection. Furthermore, we confirmed that the ectodomain of murine LysMD3 can bind to both *A. fumigatus* conidia and germling growth stages. LysMD3 binding to fungal conidia and germlings does not reflect the chitin/ $\beta$ -glucan content in

the fungal cell wall but does appear to be GAG-dependent. In summary, our data shows that murine LysMD3 partially contributes to antifungal innate immunity as a fungal binding receptor. The specific fungal binding components and detailed mechanism of LysMD3-regulated antifungal immune response still requires further study.

## Results

### **LysMD3 is a potential pattern recognition receptor with structural conserved LysM domain**

Previous studies about phylogenetic analysis of LysMs protein in human, mice, frog and zebrafish showed high sequence similarity and conservation of LysM domain in LysM family (LysMD1, LysMD2, LysMD3, and LysMD4) (27). In order to examine potential function of murine LysMD3, we generated the predicted protein structure from I-TASSER (<https://zhanggroup.org/I-TASSER/>). As the function of LysM domains is predicted by tertiary protein structure rather than DNA sequence, the predicted LysMD3 protein (C-score=-3.74) has a single LysM domain with conserved  $\beta\alpha\alpha\beta$  structure and transmembrane domain (Fig. 1A, labeled in cyan and yellow). The closest homologous structure found in Protein Data Bank (PDB) is the chitin receptor OsCEBiP from *Oryza sativa var. japonica* (rice) with the TM-score=0.769 (Fig. 1B, labeled in purple). Using COFACTOR and COACH to predict function, the murine LysMD3 protein has a potential binding site for degree of polymerization 3 (DP3) of GlcNAc with T74, L75, N76 and D100 (Fig. 1C), which fit with previous studies and our own preliminary data showing that human LYSMD3 binds to different sizes of chitin ((28), Appendix I, Fig. 1). While human and murine LysMD3 have high similarity in their DNA sequence, the mammalian LysMD3 only shares some conserved key residues in the LysM domain to the plant LysM receptor (OsCEBiP), further highlighting the nature of LysMD3 function is dependent on conserved tertiary structure (Fig 1D). From the I-TASSER protein prediction results, we found that the murine LysMD3 features a structurally conserved LysM domain with structural similarity with plant chitin receptors. As for the predicted

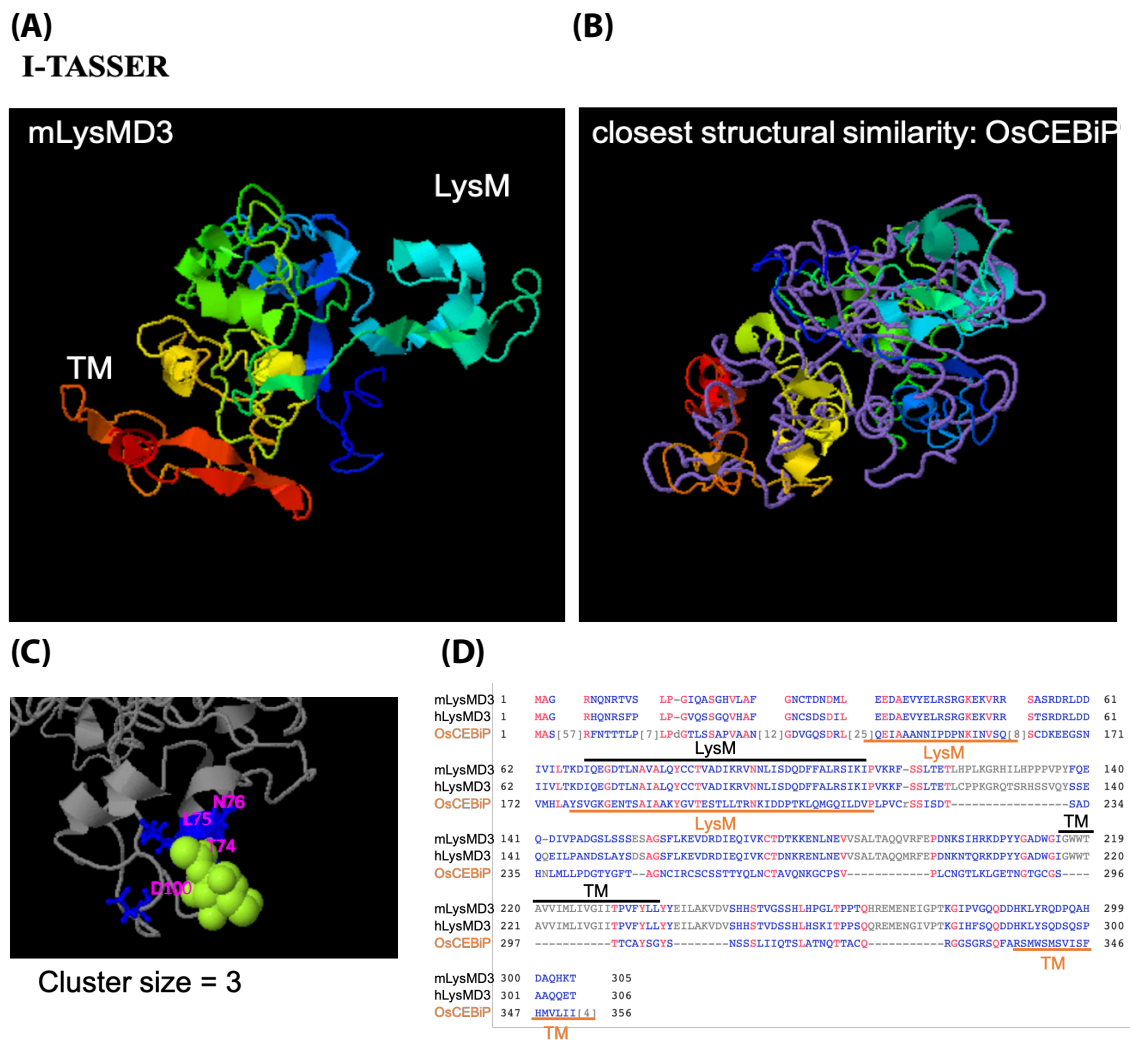


**Fig. 1 LysMD3 is a transmembrane protein with predicted LysM domain and GlcNAcs binding site**

(A) Predicted protein structure of mouse LysMD3 by I-TASSER. (B) Structure comparison between mouse LysMD3 (color labeled as the predicted structure on the left) and rice chitin receptor OsCEBiP (purple). (C) Predicted binding sites (T74, L75, N76 and D100) in LysM domain for GlcNAcs (Cluster size = 3) in the mouse LysMD3. (D) Sequence alignment of mouse LysMD3 (mLysMD3), human LysMD3 (hLysMD3) and rice chitin receptor (OsCEBiP). The functional domains of LysM and transmembrane region (TM) are labeled in black for mouse and human LysMD3 and in orange for rice chitin receptor OsCEBiP.

binding affinity of the LysM domain, structural prediction predicts a potential binding pocket to DP3 chitin.

### **LysMD3 has enhanced expression in the immune cells during early fungal infection**

Previous studies and online database datasets have shown that human LYSMD3 is expressed in epithelial cells and various immune cell types, including neutrophils, monocytes, dendritic cells, nature killer cells and T/B cells ((28);(27); <https://www.proteinatlas.org>; <https://www.immgen.org/>). As enhanced expression of other PRRs can be found during infection or inflammatory responses (29, 30), we hypothesized that LysMD3 expression would be induced upon fungal challenge in a murine model of fungal bronchopneumonia. To examine mRNA expression of LysMD3 during early fungal infection, we sorted CD45<sup>(+)</sup> and CD45<sup>(-)</sup> cells from murine lungs challenged with *A. fumigatus* or PBS at 12 hours post-fungal inoculation. After RNA extraction and cDNA synthesis, we examined LysMD3 expression in CD45<sup>(+)</sup> and CD45<sup>(-)</sup> cells by quantitative reverse transcription-PCR (qRT-PCR). While the CD45<sup>(-)</sup> cells showed similar LysMD3 expression levels between CEA10-challenged and PBS control mice, we found that the CD45<sup>(+)</sup> cells had significant induction of LysMD3 mRNA levels at 12 hours post-*Aspergillus* inoculation (Fig. 2). Thus, LysMD3 is expressed in immune cells and shows increased expression upon *A. fumigatus* challenge of the lungs, specifically in the immune cells (CD45<sup>(+)</sup>).

### **Generation of LysMD3 KO mice by CRISPR/Cas9 system**

To further investigate the function of LysMD3 and its role in anti-fungal immunity, we generated a LysMD3 knockout (LysMD3 KO) mouse using a CRISPR/Cas9 system to target the N-terminus of LysMD3. The mutant LysMD3 mouse generated features a 16 base pair deletion in the 5' region of LysMD3, upstream of the LysM domain (Fig 3A and 3B). This 16 base pairs deletion results in the introduction of a premature stop codon, culminating in a LysMD3 protein with 55 amino acids and no known functional domains (for comparison, the native protein length is 305 amino

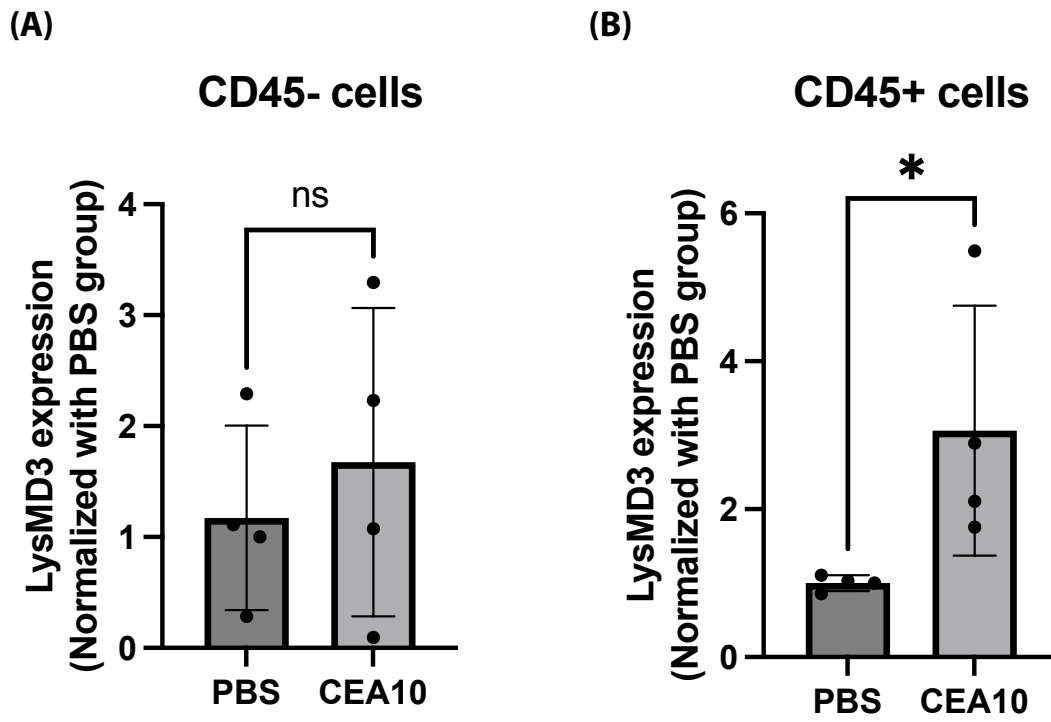


**Fig. 2 LysMD3 expression is induced in the immune cells during early fungal infection**

C57BL/6 mice were inoculated with  $5 \times 10^7$  CEA10 conidia or PBS and euthanized at 12 hours post CEA10 inoculation. The RNA was isolated from sorted CD45<sup>(-)</sup> or CD45<sup>(+)</sup> lung cells. LysMD3 expression was examined by quantitative RT-PCR on LysMD3. Samples from (A) CD45<sup>(-)</sup> cells and (B) CD45<sup>(+)</sup> cells were shown with their normalized LysMD3 expression. Two independent experiments were performed and data are shown as the combined results (PBS group: n=4; CEA10 group: n=4). Mann-Whitney, with single comparisons were performed. All error bars represent standard deviations. NS, not significant at  $P > 0.05$ ; \*  $P \leq 0.05$ ; \*\*  $P \leq 0.01$ ; \*\*\*  $P \leq 0.001$ ; \*\*\*\*  $P \leq 0.0001$ .

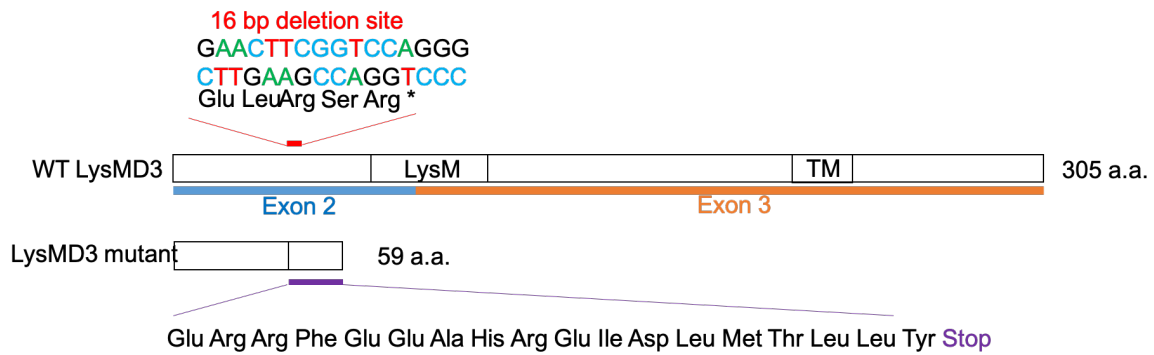


acids) (Fig 3A). The genotypes of LysMD3 WT, LysMD3<sup>+/-</sup> and LysMD3 KO mice were confirmed with PCR primer set for LysMD3 WT and KO sequences (Fig. 3C). With results from the 3' rapid amplification of cDNA ends (RACE) experiments, we found both WT and LysMD3 KO mice can still produce stable *LysMD3* transcripts (Fig. 3D). To confirm if the truncated LysMD3 can still be made, we extracted protein from isolated lung cells and examined LysMD3 protein expression with Western blot. The binding of LysMD3 antibody was confirmed with dot blot experiment. The LysMD3 antibody can specifically bind to LysMD3 protein from isolated WT neutrophils, lung from WT mouse, purified human and murine LysMD3, but not the negative control proteins from LysMD3 KO lung or *A. fumigatus* (Fig. 3E). The Western blot analysis of the protein from isolated WT immune cells revealed a lower band with predicted size of LysMD3 (34 kDa) and a higher, smear band, which might be the modified LysMD3 (Fig 3F). Furthermore, we saw no detectable band in the LysMD3 KO group indicating that cells from LysMD3 KO mice no longer have detectable LysMD3 protein production (Fig 3F). In summary, we generated a LysMD3 KO mouse line with CRISPR/Cas9 genetic manipulation and confirmed the loss of LysMD3 protein expression.

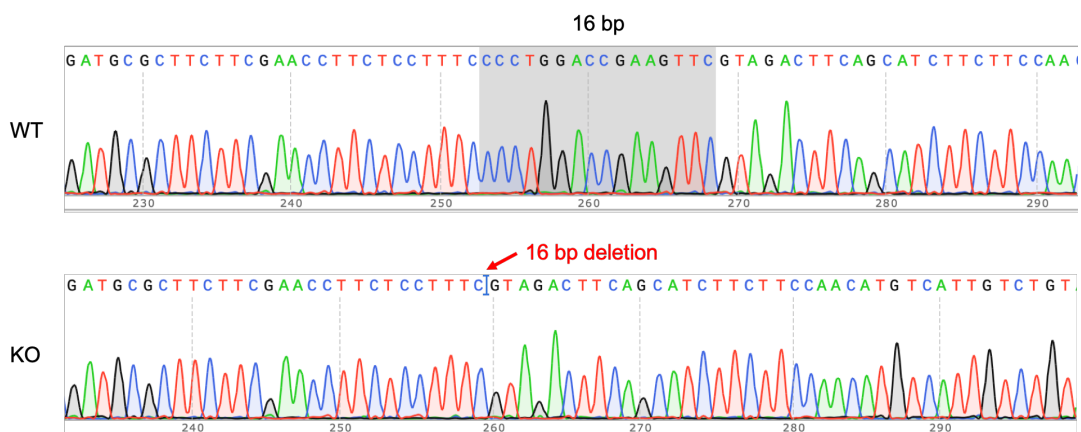
### **LysMD3 deficient mice feature largely similar lung cellularity profiles during early fungal infection as WT**

One previous study showed that infection with fungal strains featuring high chitin levels, *A. fumigatus* (Af5517), can lead to increased eosinophil recruitment (31). At the same time, chitin treatment can induce chemokine production in keratinocytes and epithelial cells (28, 32). Thus, we next investigated if LysMD3 deficient mice maintained similar cell recruitment profiles during early *A. fumigatus* challenge. We leveraged different flow cytometry staining panels to examine lung cellularity during early fungal infection (Fig. S1-S3). At 12 hours post-*A. fumigatus* (CEA10) inoculation, we observed equivalent numbers of total lung cells, neutrophils (CD45<sup>(+)</sup>Ly6G<sup>(+)</sup>CD11b<sup>(+)</sup>), eosinophils (Ly6G<sup>(-)</sup>SiglecF<sup>(+)</sup>CD11b<sup>(dim or -)</sup>), alveoli macrophages (aMac; Ly6G<sup>(-)</sup>CD103<sup>(-)</sup>SiglecF<sup>(+)</sup>CD11b<sup>(+)</sup>), interstitial macrophages (iMac; Ly6G<sup>(-)</sup>CD103<sup>(-)</sup>SiglecF<sup>(-)</sup>CD11b<sup>(hi)</sup>CD64<sup>(+)</sup>), Type I conventional CD103<sup>(+)</sup> cDC1 cells

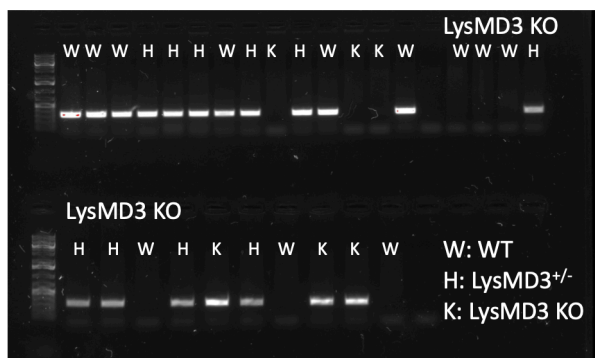
(A)



(B)



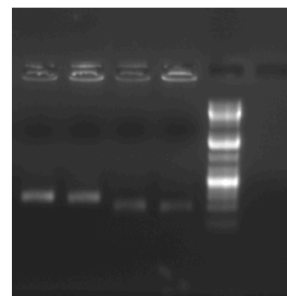
(C)



LysMD3 WT (317 bp): RAC3611+RAC2813  
LysMD3 KO (311 bp): RAC7241+RAC2813

(D)

3'RACE -1 3'RACE-2  
WT KO WT KO



LysMD3 3' RACE primer set 1 (308 bp):  
RAC4755+RACE4344  
LysMD3 3' RACE primer set 2 (214 bp):  
RAC4755+RACE3484  
Exon 1 Exon 2

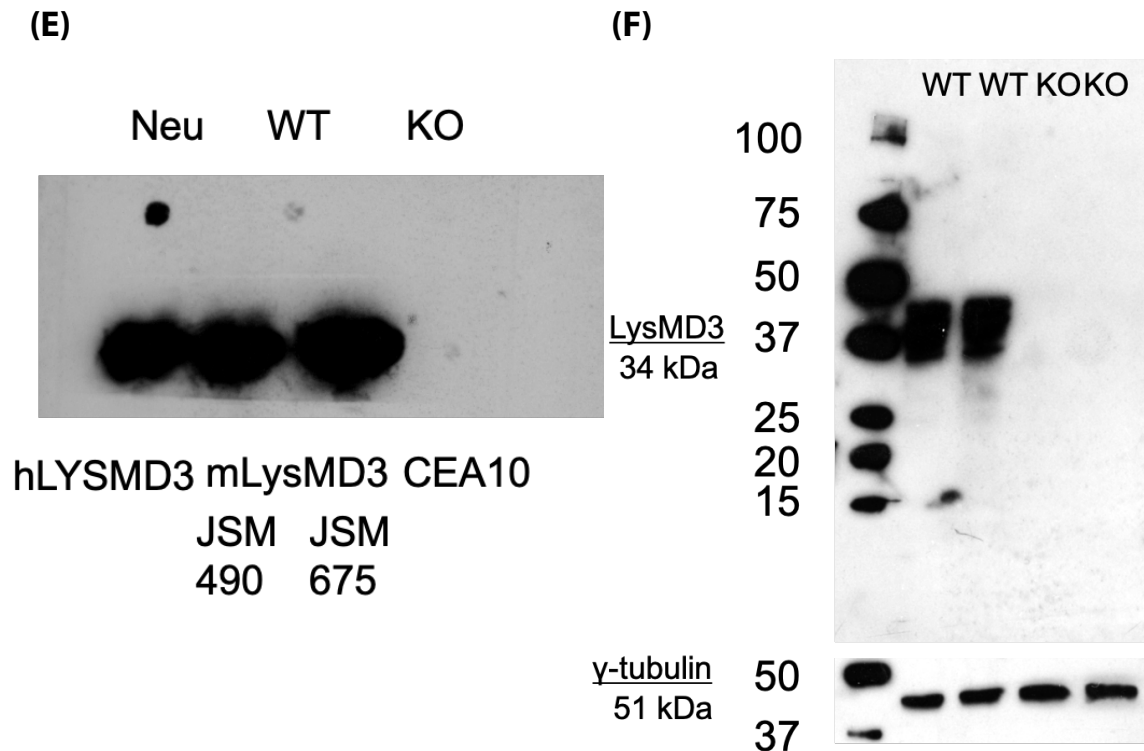


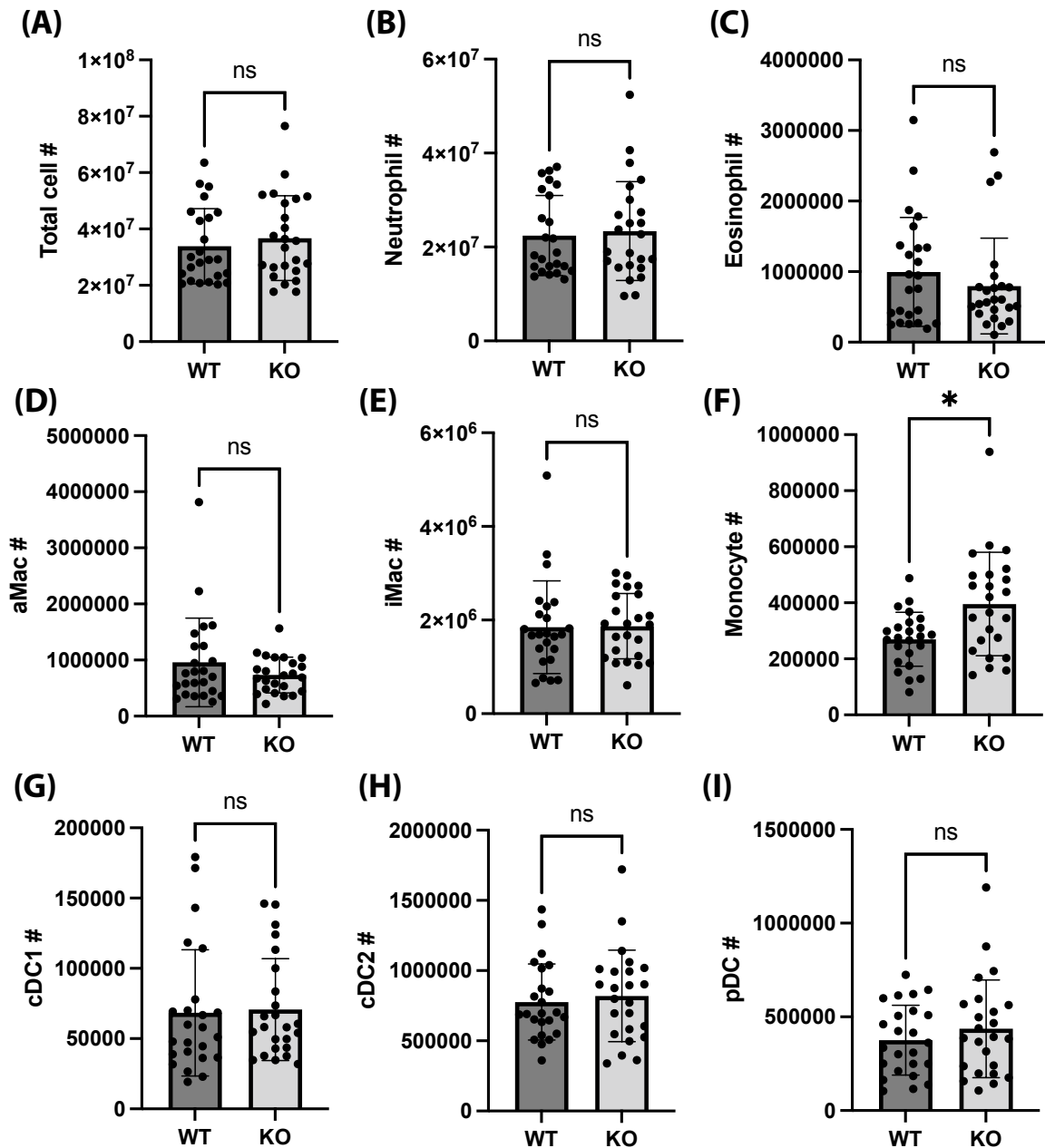
**Fig. 3 Generation of LysMD3 deficiency mice through CRISPR targeting method**

(A) Schematic figures of wild type LysMD3 protein (top) and potential truncated LysMD3 protein (bottom) from CRISPR mutant mice. The site of CRISPR deletion sequence was indicated as 16 base pair (16 bp) deletion (red) with corresponded nucleotide and peptide sequences. The peptide sequence before the premature stop codon (purple) was indicated with LysMD3 mutant peptide. (B) Sequencing results of genomic DNA from WT (top) and LysMD3 mutant (bottom) mice. The 16 bp deletion is noted as indicated. (C) Genotyping results of WT, LysMD3<sup>+/-</sup> and LysMD3 KO mice with primer sets for WT and KO sequence. (D) 3' RACE results with two primer sets crossing exon1 and exon 2 of LysMD3. (E) Dot blot of protein isolated from WT neutrophils (Neu), WT mouse lung (WT), LysMD3 KO mouse lung (KO), purified human LYSMD3 protein (hLYSMD3), purified murine LysMD3 (mLysMD3-JSM490 and -JSM675) and fungal hyphae (CEA10). (F) Western blot of protein isolated from immune cells of uninfected wild type (n=2) and LysMD3 KO (n=2) mice. The LysMD3 protein (predicted size: 34 kDa) was shown on the top and endogenous control (γ-tubulin; predicted size: 51 kDa) at the bottom. Three independent experiments were performed and data are shown as the representative results.

(MHCII<sup>(+)</sup>CD11c<sup>(+)</sup>CD11b<sup>(-)</sup>CD103<sup>(+)</sup>), Type II conventional CD11b<sup>(+)</sup> cDC2 cells (MHCII<sup>(hi)</sup>CD11c<sup>(hi)</sup>CD103<sup>(-)</sup>CD11b<sup>(+)</sup>), and pDCs (MHCII<sup>(+)</sup>CD11c<sup>(+)</sup>CD11b<sup>(-)</sup>CD103<sup>(-)</sup>CD317<sup>(+)</sup>) (Fig. 4A-4E, 4G-4I). Among the cell types we investigated, we only observed increased monocyte recruitment (Ly6G<sup>(-)</sup>CD103<sup>(-)</sup>SiglecF<sup>(-)</sup>CD11b<sup>(hi)</sup>CD64<sup>(-)</sup>MHCII<sup>(-)</sup>) in the LysMD3 KO group at 12 hours post-*A. fumigatus* challenge (Fig. 4F) when compared with WT cellularity profiles. These cellularity data from LysMD3 KO and WT mice showed that the deficiency of LysMD3 did not affect cell recruitment against fungal infection except for the monocyte population.

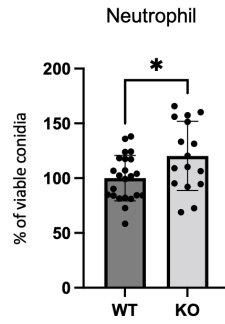
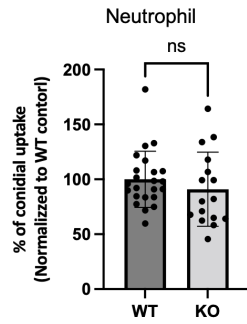
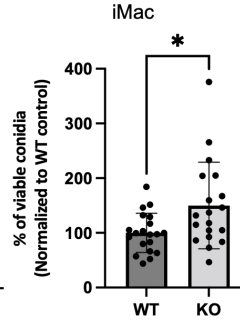
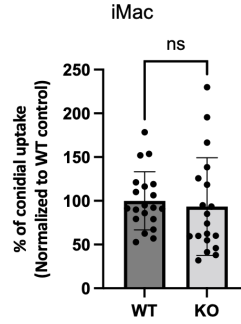
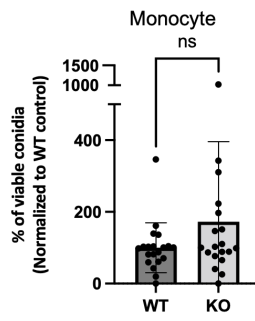
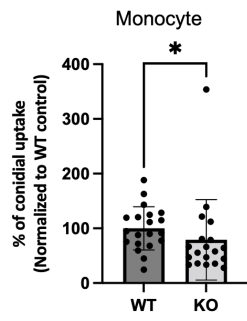
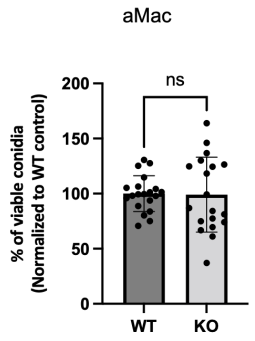
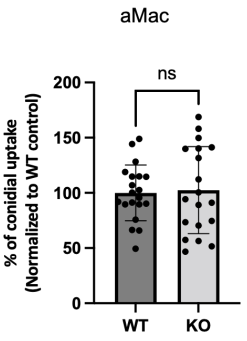
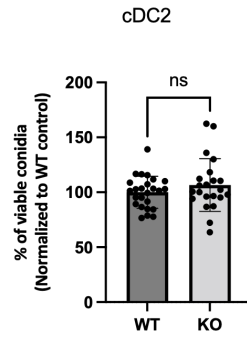
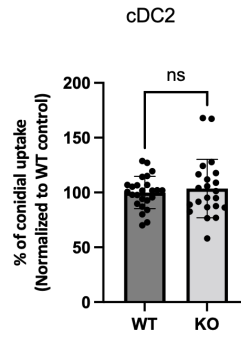
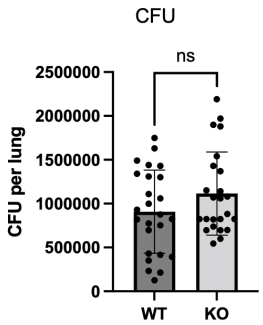
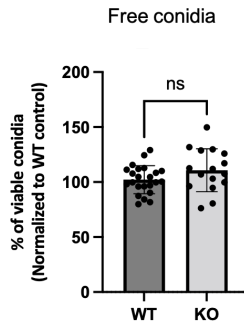
### **LysMD3 deficient immune cells are defective at fungal killing, but this deficiency does not contribute to a significant increase in overall fungal viability**

Because the predicted LysMD3 structure has potential fungal cell binding ability and enhanced expression in immune cells during fungal infection, LysMD3 might be involved in fungal recognition during early fungal infection. As with other PRRs, like Dectin-1 and TLRs, we hypothesize that LysMD3 might modulate *A. fumigatus* uptake and killing through ligand recognition on the fungal surface (33, 34). Using a fluorescent *Aspergillus* reporter (FLARE) assay, we quantified both the uptake and viability of *A. fumigatus* conidia within specific immune cell types in the murine lungs to test this hypothesis (35). At 12 hours post-inoculation of AF633 labeled mRFP-CEA10 (FLARE) conidia, we examined the conidial uptake and killing in immune cells as previous described (Fig. S4) (35, 36). Among all the professional phagocytes we examined, LysMD3 deficient neutrophils and iMacs showed higher conidial viability but no significant difference in conidial uptake (Fig. 5A and 5B). At the same time, LysMD3 KO monocytes showed lower conidial uptake but no significant difference in conidial viability (Fig. 5C). Other phagocytes, including aMacs and cDC2s, showed no significant difference in either conidial uptake or viability between WT and LysMD3 KO groups (Fig. 5D and 5E). Of note, we did not observe significant differences in overall conidial viability for both immune cell-engulfed conidia or free conidia in the lungs between WT and LysMD3 KO groups (Fig. 5F and 5G). Overall, LysMD3 KO mice feature slight conidial



**Fig. 4 LysMD3 KO mice showed similar cellularity during early fungal infection**

WT or LysMD3 KO C57BL/6 mice were inoculated with  $5 \times 10^7$  CEA10 conidia and euthanized at 12 hours post CEA10 inoculation for lung cellularity experiments. All lung cell numbers were acquired by flow cytometry as indicated: (A) total lung cells, (B) neutrophils (CD45<sup>(+)</sup>Ly6G<sup>(+)</sup>CD11b<sup>(+)</sup>), (C) eosinophils (CD45<sup>(+)</sup>Ly6G<sup>(-)</sup>SiglecF<sup>(+)</sup>CD11c<sup>(-)</sup>), (D) alveolar macrophages (Ly6G<sup>(-)</sup>CD103<sup>(-)</sup>SiglecF<sup>(+)</sup>CD11b<sup>(+)</sup>), (E) interstitial macrophages (Ly6G<sup>(-)</sup>CD103<sup>(-)</sup>SiglecF<sup>(-)</sup>CD11b<sup>(hi)</sup>CD64<sup>(+)</sup>), (F) monocytes (Ly6G<sup>(-)</sup>CD103<sup>(-)</sup>SiglecF<sup>(-)</sup>CD11b<sup>(hi)</sup>CD64<sup>(-)</sup>MHCII<sup>(-)</sup>), (G) CD103<sup>(+)</sup> cDC1 (MHCII<sup>(+)</sup>CD11c<sup>(+)</sup>CD11b<sup>(-)</sup>CD103<sup>(+)</sup>), (H) CD11b<sup>(+)</sup> cDC2 (MHCII<sup>(hi)</sup>CD11c<sup>(hi)</sup>CD103<sup>(-)</sup>CD11b<sup>(+)</sup>), (I) pDC (MHCII<sup>(+)</sup>CD11c<sup>(+)</sup>CD11b<sup>(-)</sup>CD103<sup>(-)</sup>CD317<sup>(+)</sup>). Three independent experiments were performed and data are shown as the combined results (WT group: n=24; LysMD3 KO group: n=24). Mann-Whitney, with single comparisons were performed. All error bars represent standard deviations. NS, not significant at  $P > 0.05$ ; \*  $P \leq 0.05$ ; \*\*  $P \leq 0.01$ ; \*\*\*  $P \leq 0.001$ ; \*\*\*\*  $P \leq 0.0001$ .

**(A)****(B)****(C)****(D)****(E)****(F)****(G)**

**Fig. 5 LysMD3 KO mice showed minor defect in fungal killing during early fungal infection**

WT or LysMD3 KO C57BL/6 mice were inoculated with  $5 \times 10^7$  FLARE (mRFP<sup>(+)</sup>/AF633<sup>(+)</sup>) CEA10 conidia. Mice were euthanized at 12 hours post FLARE conidia inoculation. The percentage of cells positive for conidial tracer (AF633<sup>(+)</sup>) and conidial viability within the immune cells (mRFP<sup>(+)</sup>/AF633<sup>(+)</sup>) were analyzed. Phagocytosis and conidial viability were examined in (A) neutrophils (CD45<sup>(+)</sup>Ly6G<sup>(+)</sup>CD11b<sup>(+)</sup>), (B) interstitial macrophages (Ly6G<sup>(-)</sup>CD103<sup>(-)</sup>SiglecF<sup>(-)</sup>CD11b<sup>(hi)</sup>CD64<sup>(+)</sup>), (C) monocytes (Ly6G<sup>(-)</sup>CD103<sup>(-)</sup>SiglecF<sup>(-)</sup>CD11b<sup>(hi)</sup>CD64<sup>(-)</sup>MHCII<sup>(-)</sup>), (D) alveolar macrophages (Ly6G<sup>(-)</sup>CD103<sup>(-)</sup>SiglecF<sup>(+)</sup>CD11b<sup>(+)</sup>), and (E) CD11b<sup>(+)</sup> cDC2 (MHCII<sup>(hi)</sup>CD11c<sup>(hi)</sup>CD103<sup>(-)</sup>CD11b<sup>(+)</sup>). (F) The viability of FLARE conidia within immune cells in the lung suspension was assessed by colony forming units (CFUs). (G) The viability of free FLARE conidia in the lung suspension was shown as the percentage of mRFP<sup>(+)</sup> cells in free conidia population (Alexa633<sup>(+)</sup>FSC<sup>(low)</sup>SSC<sup>(low)</sup>). Three independent experiments were performed and data are shown as the combined results (For neutrophil: WT group: n=23; LysMD3 KO group: n=16; For iMac, monocyte and aMac: WT group: n=20; LysMD3 KO group: n=19; For cDC2: WT group: n=25; LysMD3 KO group: n=22). Mann-Whitney, with single comparisons were performed. All error bars represent standard deviations. NS, not significant at  $P > 0.05$ ; \*  $P \leq 0.05$ ; \*\*  $P \leq 0.01$ ; \*\*\*  $P \leq 0.001$ ; \*\*\*\*  $P \leq 0.0001$ .

killing defects in neutrophils and iMacs, but we anticipate that such a minor defect in fungal killing is likely not strong enough to significantly impact total conidial viability during early infection.

**Murine LysMD3-deficiency does not significantly alter mortality outcomes during fungal infection**

We next investigated if the loss of LysMD3 contributes to fungal virulence, specifically using mortality in an invasive aspergillosis model as an experimental outcome. Interestingly, a recently published study observed that there was no difference in LysMD3-dependent mortality when using a sublethal dose of *A. fumigatus* infection (CEA10;  $10^7$  conidia with intranasal injection) (27). To further contextualize these findings upon *A. fumigatus* infection, we leveraged multiple high virulent *A. fumigatus* strains (CEA10, EVOL20 and ATCC46645) in both immune competent and immune suppression mouse models of fungal infection. However, we did not find any significant differences in murine mortality between LysMD3 KO and WT mice in this immune competent model (Fig. 6A, 6B and 6C) or in an immune suppressed model with

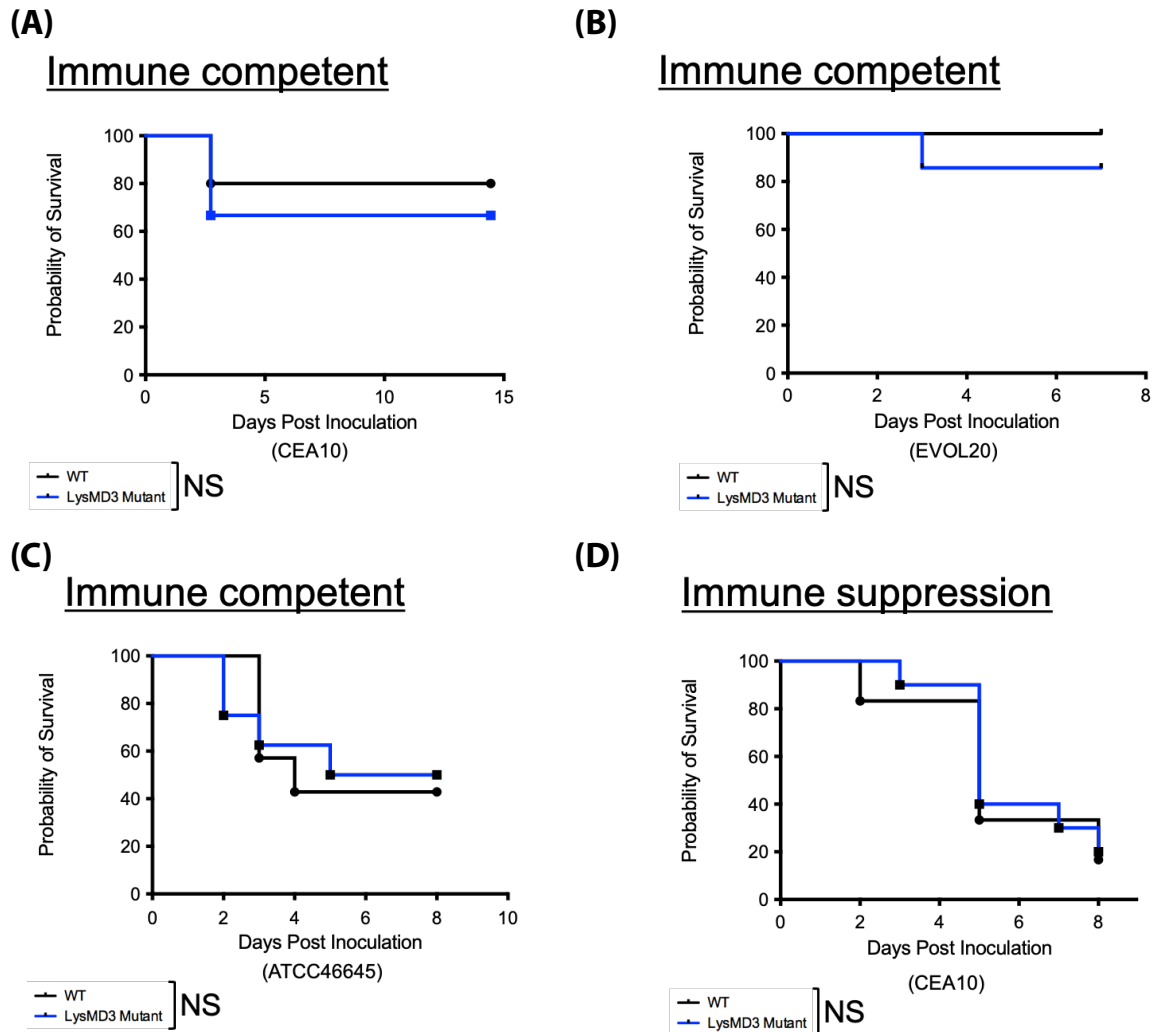


**Fig. 6 LysMD3 deficiency is not sufficient to contribute to mice mortality during fungal infection**

(A) Survival curve of WT (n=6) or LysMD3 KO (n=5) C57BL/6 mice with  $5 \times 10^7$  CEA10 conidia with immune competent mice model. Three independent experiments were performed and data are shown as the representative results. (B) Survival curve of WT (n=6) or LysMD3 KO (n=7) C57BL/6 mice with  $5 \times 10^7$  EVOL20 conidia with immune competent mice model. The experiment was performed once. (C) Survival curve of WT (n=7) or LysMD3 KO (n=8) C57BL/6 mice with  $8 \times 10^7$  ATCC46645 conidia with immune competent mice model. The experiment was performed once. (D) Survival curve of WT (n=6) or LysMD3 KO (n=10) C57BL/6 mice pre-treated with KENALOG-10 for 24 hours and inoculated  $1 \times 10^6$  CEA10 conidia as immune suppression mice model. Two independent experiments were performed and data are shown as the representative results. The Log-rank test and Gehan-Breslow-Wilcoxon test were performed for statistical analysis of the survival curve. NS, not significant at  $P > 0.05$ ; \*  $P \leq 0.05$ ; \*\*  $P \leq 0.01$ ; \*\*\*  $P \leq 0.001$ ; \*\*\*\*  $P \leq 0.0001$ .



corticosteroid treatment (Fig. 6D). As we saw no significant difference of fungal killing in LysMD3 KO mice, here we have also confirmed that LysMD3 deficiency in mice does not lead to significant differences in mortality when tested in various invasive aspergillosis models.

### **LysMD3 can recognize *A. fumigatus* at both conidia and germling growth stages**

Even though LysMD3 deficiency did not significantly impact overall fungal uptake or clearance, we still found a slight reduction in conidial killing by neutrophils and iMacs and a reduction in fungal uptake in monocytes. As previous studies showed that human LYSMD3 can bind to chitin and  $\beta$ -glucan (28), we hypothesize that murine LysMD3 can bind to the fungal cell wall and initiate immune modulation related to fungal clearance, as we saw in neutrophils, iMac and monocytes. To test LysMD3 binding capability and affinity to *A. fumigatus*, we generated a fusion protein containing the ectodomain of LysMD3 and human IgG Fc as the binding target to examine the localization of LysMD3 binding, differing from the detection method (staining) used in the previous studies to determine subcellular localization of protein binding (37, 38). With the purified LysMD3-Fc, we aimed to use LysMD3-Fc as a LysMD3-specific reagent to examine if LysMD3 can bind to *A. fumigatus* surface at different growth stages. The purified biological control, dectin-1-Fc - which binds to  $\beta$ -glucan in the fungal cell wall, specifically recognized and bound to swollen conidia (when comparing swollen conidia to resting conidia or secondary antibody controls, Fig. 7A). Similarly, LysMD3-Fc staining showed a pattern of recognition where swollen conidia showed ubiquitous LysMD3-Fc<sup>(+)</sup> signal (Fig. 7B). Using confocal microscopy, we also see LysMD3-Fc binding to the surface of swollen conidia/germlings and enhanced signal at the tip of the germ tubes of *A. fumigatus* (Fig. 7C). To confirm the signal is specific for LysMD3-Fc staining, we used a serial dilution of LysMD3-Fc concentrations for staining and the intensity of LysMD3 signal was dose-dependent (Fig. 7D). Thus, experiments with LysMD3-Fc staining demonstrates that murine LysMD3 can bind to the surface of *A. fumigatus* at both conidia and germling growth stages. As it is possible that there is a potential for

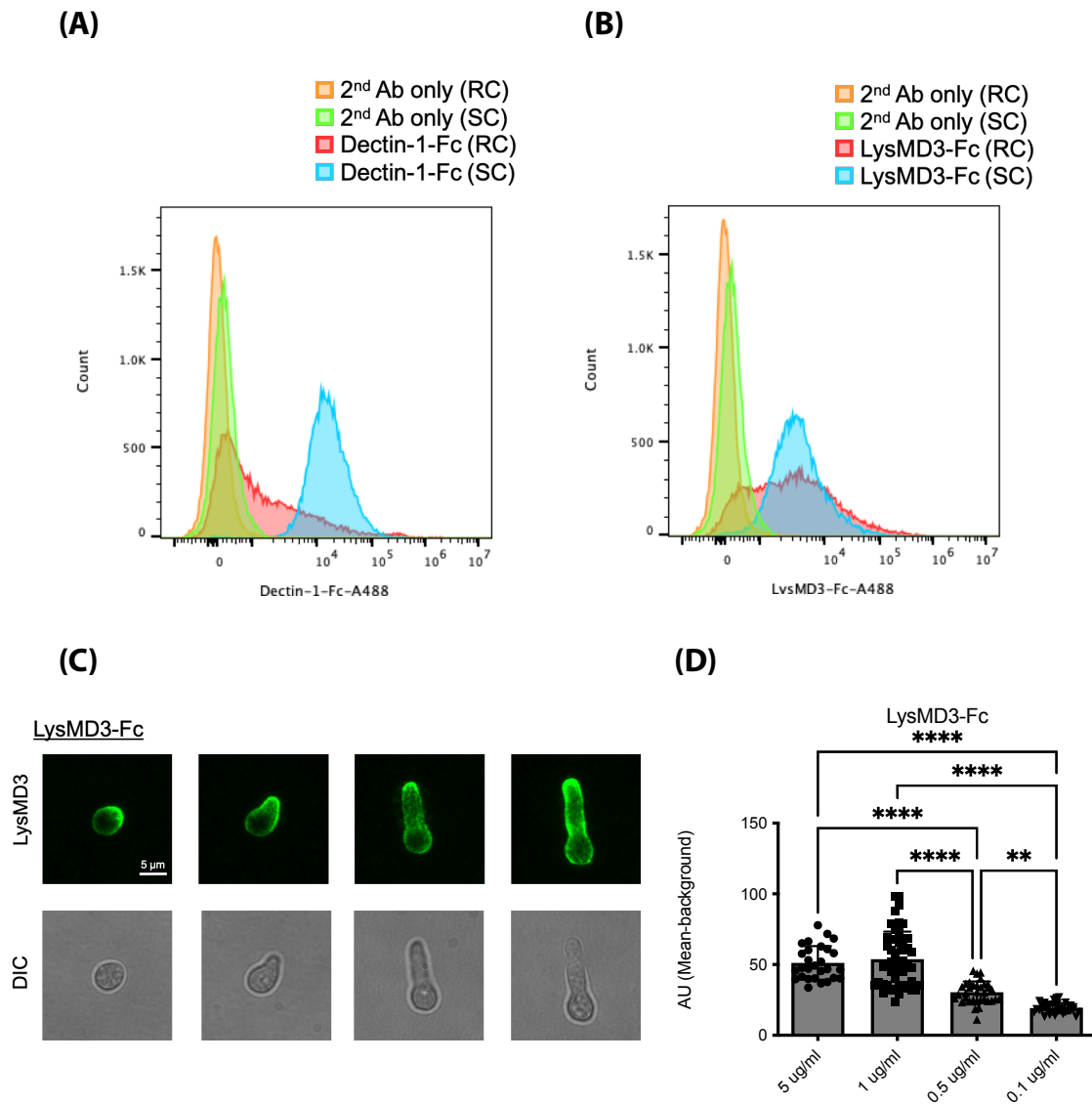


**Fig. 7 LysMD3 binds to both fungal conidia and hyphae**

CEA10 conidia was grown in LGMM at 37 °C 5 hours for swollen conidia (SC) and 14 hours for germlings. CEA10 conidia and germling were stained with LysMD3-Fc to examine the LysMD3 binding to fungal surface. For resting conidia (RC) and swollen conidia (SC), the samples were staining with (A) Dectin-1-Fc or (B) LysMD3-Fc. The anti-Fc secondary antibody staining (2<sup>nd</sup> Ab only) was used as the negative control. Three independent experiments were performed and data are shown as the representative results. (C) Confocal images of different stages of conidia/germling with LysMD3-Fc staining. The images of LysMD3-Fc binding were shown on top and corresponded DIC images were shown at bottom. Three independent experiments were performed and data are shown as the representative results for LysMD3 binding. (D) Titration of LysMD3-Fc staining on germling. The corrected total cell fluorescence was calculated for individual germling. The experiment was performed once. Kruskal-Wallis with Dunn's multiple comparisons were performed for statistical analyses. All error bars represent standard deviations. NS, not significant at  $P > 0.05$ ; \*  $P \leq 0.05$ ; \*\*  $P \leq 0.01$ ; \*\*\*  $P \leq 0.001$ ; \*\*\*\*  $P \leq 0.0001$ .

overlapping/masking of binding patterns from other cell wall components also present on the fungal cell wall, we next aimed to investigate the specific binding target of murine LysMD3.

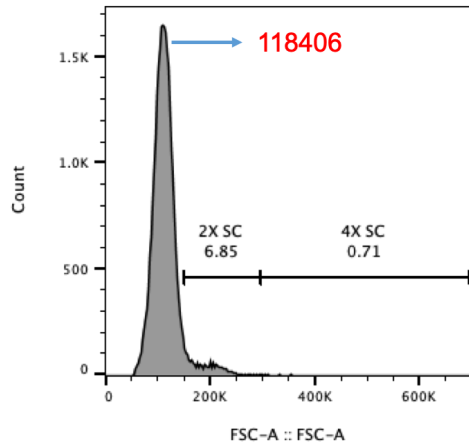
### **LysMD3-Fc staining reveals a unique binding pattern on the fungal surface**

*A. fumigatus* has complex cell wall composition and there are many changes in the exposure of each particular cell wall components during growth from resting conidia stages to hyphae (39). To examine what LysMD3 recognizes on the *A. fumigatus* surface, we tested LysMD3-Fc binding to a triple  $\alpha$ -(1,3)-Glucan Synthases (AGS) mutant of *A. fumigatus*, which features increased chitin and  $\beta$ -glucan exposure compared to its parental  $\Delta ku80$  background strain (40). We started our analysis of LysMD3 binding at the swollen conidial growth stage and then separated the analysis of by cell sizes, an indicator of general growth state. These conidial subpopulations were then examined for recognition by staining with LysMD3-Fc, Dectin-1-Fc and Wheat Germ Agglutinin (WGA) to compare fungal recognition in the  $\Delta ags$  strain versus the parental  $\Delta ku80$  strain. To ensure that our comparison of binding was analyzing swollen conidia at the same growing stage, we grouped swollen conidia with two-fold and four-fold increase in forward scatter (FSC) compared to resting conidia group, as this indicates the relative size of swollen conidia (2X SC and 4X SC) (Fig. 8A). The  $\Delta ags$  swollen conidia (2X SC and 4X SC) revealed higher dectin-1-Fc and WGA binding, which nicely confirms the reported increase in exposure of  $\beta$ -glucan and chitin on the fungal surface (Fig. 8C, 8D, 8F and 8G). However, we did not detect significant differences in binding of LysMD3-Fc between  $\Delta ags$  and  $\Delta ku80$  parental background at 2X SC and 4X SC stages (Fig. 8B and 8E). Furthermore,  $\Delta ags$  germlings reveal enhanced dectin-1-Fc and WGA binding compared to  $\Delta ku80$  as swollen conidia (Fig. 8I and 8J), but the binding of LysMD3-Fc was actually significantly decreased on the  $\Delta ags$  fungal surface in germlings compared to the control group (Fig. 8H). Besides chitin and  $\beta$ -glucan, we next examined another cell wall component that might be correlated with the binding of LysMD3 on the fungal surface. The hyphae of *A. fumigatus* produce galactosaminoglycan (GAG), which is present on the fungal cell wall surface and

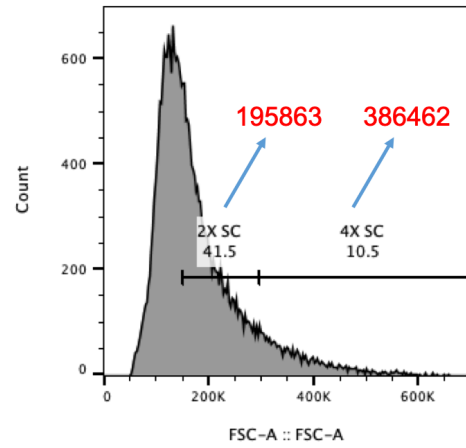
(A)

Ku80 Rest conidia

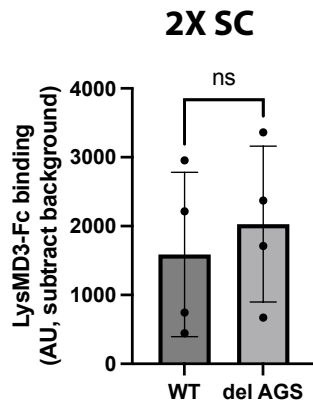
MFI of FSC



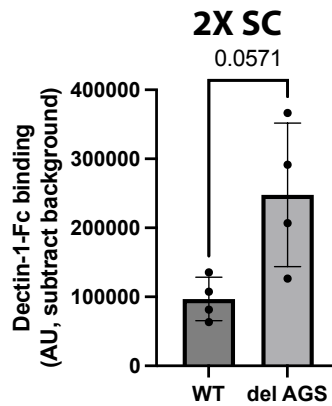
Ku80 Swollen conidia



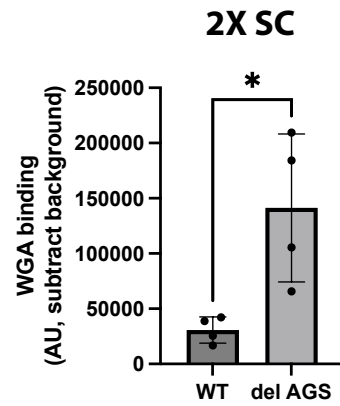
(B)



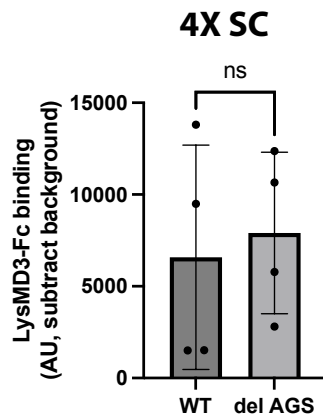
(C)



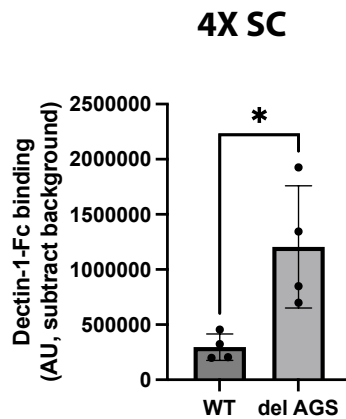
(D)



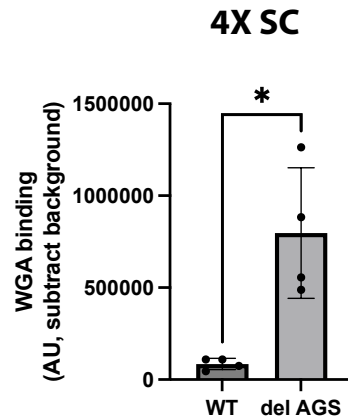
(E)



(F)



(G)



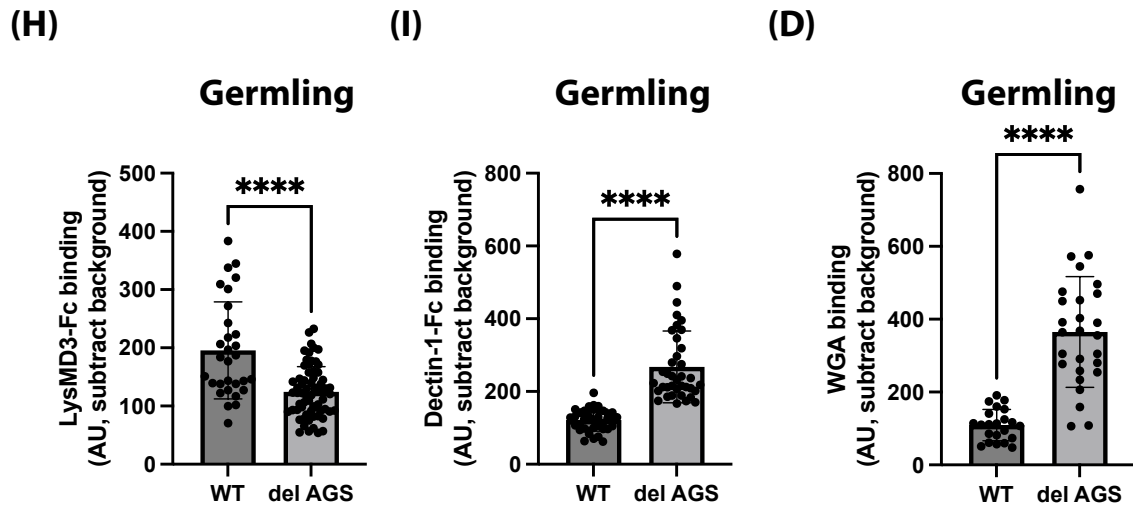


**Fig. 8 LysMD3 does not have similar binding pattern correlated to  $\beta$ -glucan and chitin exposure on the fungal surface**

For  $\alpha$ -glucan synthase deletion mutant (del AGS) and its parental Ku80 strain, conidia was grown in LGMM at 37 °C 5 hours for swollen conidia (SC) and 14 hours for germlings. The gating strategy for 2X and 4X swollen conidia (SC) were shown in the (A) and the MFI of FSC was shown for each population. The swollen conidia and germling were stained with LysMD3-Fc (B, E and H) , Dectin-1-Fc (C, F and I) and WGA (D, G and J). The intensity of stained swollen conidia was acquired by flow cytometry and gated as 2X (B-D) and 4X (E-G) swollen conidia as indicated in (A). Four independent experiments were performed and data are shown as the combined results. The intensity of stained germling was acquired by confocal microscope and the corrected total cell fluorescence was shown in (H-J). Two independent experiments were performed and data are shown as the representative results. Mann-Whitney with single comparisons was performed for statistical analyses. All error bars represent standard deviations. NS, not significant at  $P > 0.05$ ; \*  $P \leq 0.05$ ; \*\*  $P \leq 0.01$ ; \*\*\*  $P \leq 0.001$ ; \*\*\*\*  $P \leq 0.0001$ .

within the extracellular matrix (ECM) (39). GAG production is involved in fungal adhesion, immune cell recognition and immune modulation, which can be largely disrupted by deleting a critical epimerase, Uge3 (41). Thus, we stained the germlings of  $\Delta uge3$  with LysMD3-Fc and compared its binding to the parental AF293 strain. Surprisingly, and unlike the complete loss of Soybean Agglutinin (SBA) binding on  $\Delta uge3$  germlings, the LysMD3-Fc binding profile revealed punctate signals in the extracellular medium instead of germling surface (Fig. 9). In summary, we found LysMD3 shows different binding patterns

in comparison to known cell wall binding reagents (dectin-1, WGA and SBA), and the loss of GAG production on the germling surface disrupts LysMD3-Fc binding. Further studies will be needed to determine the actual LysMD3 binding component(s) in the fungal cell wall.

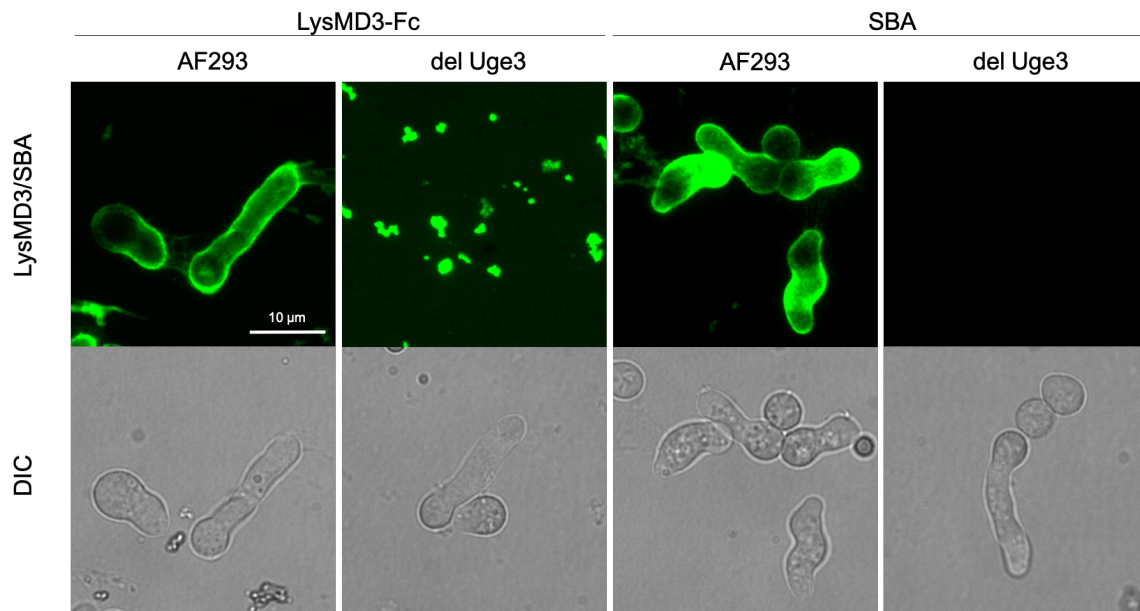


**Fig. 9 GAG on the fungal surface regulates LysMD3 binding pattern**

Uge3 deletion mutant (del Uge3) and parental AF293 strains were grown in LGMM at 37 °C 18 hours for germlings. The germlings were stained with LysMD3-Fc or SBA for confocal imaging. The images of LysMD3-Fc/SBA binding were shown on top and corresponded DIC images were shown at bottom. Two independent experiments were performed and data are shown as the representative results.

## Discussion

The human and murine LysMD3 both feature a conserved LysM domain, which is conserved in other animals, as mentioned previously (27). Through protein structure prediction, we can see the characteristic  $\beta\alpha\beta$  structure of LysM domains and a predicted binding pocket for DP3 of chitin oligomers (Fig. 1A and 1B). We also found the predicted DP3 GlcNAc binding site with T74, L75, N76 and D100 is conserved in both human and murine LysMD3, which might suggest the conserved function of LysMD3 in mammalian for pathogen recognition (Fig. 1D). However, the localization of LysMD3 (which is correlated to its binding to pathogens) remains controversial. Previous studies demonstrated that murine and human LysMD3 is a type II integral membrane protein that co-localizes with Golgi marker GM130 in mouse embryonic fibroblast cells (MEFs) and HeLa cells (27). Another group also showed the localization of human LYSMD3 within Golgi and proposed a function related to Golgi stress in HeLa cells (42). However, the authors also found that the enhanced LYSMD3 expression in HeLa cells changes its localization to the cell membrane (42). In our invasive aspergillosis model, we can see the enhanced LysMD3 expression in CD45<sup>(+)</sup> cells, but not CD45<sup>(-)</sup> cells (Fig. 2), which might suggest different LysMD3 localization dynamics during fungal infection. Such difference of LysMD3 expression and potentially a change of localization could affect the function and kinetics of its role as a potential pathogen recognition receptor in the immune cells, but the actual localization of LysMD3 during fungal recognition by immune cells remains an open question for further research.

Previous studies, supported by the use of two different LysMD3 KO mouse lines, found no significant *in vivo* virulence phenotypes in LysMD3 deficient mice when assessing extracellular and intracellular bacterial infections, influenza A virus infection, and *A. fumigatus* infection (27). We generated our LysMD3 deficient mouse line through a CRISPR/Cas9 system that resulted in a truncated and non-functional protein, then crossed heterozygous LysMD3<sup>+/-</sup> individuals to generate homozygous LysMD3<sup>-/-</sup> individuals and LysMD3<sup>+/+</sup> littermate controls. We further confirmed the CRISPR/Cas9-

directed 16 base pairs deletion and the introduction of a premature stop codon before the LysM domain (Fig. 3A and 3B). Even with stable *Lysmd3* transcript (Fig. 3D), *LysMD3*<sup>-/-</sup> deficient mice showed no *LysMD3* protein production from immune cells in the lung (Fig. 3F) and we used this mouse line to further study the role of *LysMD3* in antifungal immunity. Due to the heterogeneity of *A. fumigatus* in models of invasive aspergillosis (43–47), we further confirmed that *LysMD3*<sup>-/-</sup> mice have a similar mortality with increase dose of *A. fumigatus* infection in an immune competent model of infection with various *A. fumigatus* strains (CEA10, EVOL20 and ATCC46645), comparing *LysMD3* deficient mice to littermate controls (Fig. 6A-6C). We observed that *LysMD3* deficient mice have similar mortality in a model of immune suppression invasive aspergillus (Fig. 6D), which notably features a different immune profile and host cell functionalities than an immune competent model (48). Thus, similar to previous findings, our newly generated *LysMD3* KO mice are still able to recover from *A. fumigatus* infection.

Although we did not observe differences in mortality in an invasive aspergillosis model, previous work has shown that *LysMD3* expression in human epithelial cells contributes to cytokine production (IL-6, IL-8 and IL-33) upon stimulation (28). We next aim to see if *LysMD3* plays a role in immune modulation during early fungal infection. Despite the *LYSMD3*-dependent regulation of chemokines (IL-8) in human epithelial cells, our *LysMD3* KO mice revealed similar cell recruitment during early fungal infection (Fig. 5). When investigating infection through a FLARE assay, we see both neutrophils and iMacs from *LysMD3* KO mice did have defects in intracellular fungal killing when compared to controls (Fig. 6A and 6B). The relative *LysMD3* expression level in these cell populations, or whether there is an induction of *LysMD3* expression, can be correlated to functional defects in fungal killing, as high expression of *LysMD3* is reported in neutrophils (proteinatlas and IMMGEN). Still, even with a 13.7% and 33.22% increased intracellular fungal viability in neutrophils and iMacs, we found no significant difference in overall intracellular and extracellular fungal viability between *LysMD3* KO mice and controls (Fig. 6F and 6G). Thus, we found that *LysMD3* KO mice do



show minor defects in intracellular fungal killing in specific cell types, but these mice are still able to control the fungal burden within the lung, potentially explaining why we did not see differences in mortality between LysMD3 KO and controls invasive *A. fumigatus* infection.

From literatures on plant LysM receptors, it has been reported that chitin recognition can be through LysM homodimers and heterodimers (8, 20, 21). The predicted LysMD3 protein predicted in this work only features a short cytoplasmic tail without annotated functional domains, so it might form a heterodimer with other PRRs to initiate downstream signaling. It is also possible that even without chitin recognition through LysMD3, other PRRs are still able to induce host antifungal responses, as dectin-1, TLRs and mannose receptor have all been implied to mediate chitin induced immune responses (49). Even if LysMD3 is essential for chitin recognition, host innate immunity might still be able to initiate immune responses through the recognition of other PAMPs on fungal surface by TLRs or C-type lectin receptors (CLRs) (50). At the same time, the high similarity of protein sequence between LysMD3 and LysMD4 suggests potential functional redundancy of murine LysM proteins. Due to this redundancy, the loss of LysMD3 might only partially disrupt host immune modulation, explaining why we only see minor defects in fungal killing in LysMD3 KO mice. Another potential explanation for the minor change of antifungal response in LysMD3 KO mice is related to the role of chitin in antifungal immunity. Since the concentration of chitin (250–1000 µg/ml) required to induce immune response toward inflammation might be higher than the physiological chitin concentration (5), chitin sensing might not be the main input for immune activation. Instead, as the anti-inflammatory response can be induced by smaller sizes of chitin (4), chitin sensing and signaling might be more important in the immune resolving phase after fungal clearance. As the predicted ligand for LysMD3 is DP3 GlcNAc, this suggests that LysMD3 signaling is involved in anti-inflammatory responses after fungal clearance, rather than contributing to early antifungal immunity. To fully understand the role of LysMD3 in innate immunity, we will need a complete

examination of 1) the inflammatory and anti-inflammatory responses in LysMD3 KO mice, and 2) insight into if LysMD3 deficiency in conjunction with other PRRs addresses the potential for functional redundancy of PRRs in fungal recognition.

Besides the role in immune modulation, the potential binding target of LysMD3 is another focus of this work. As the predicted function of LysM domain in the LysMD3, human LYSD3 has been shown bind to chitin oligomers (DP5-7), chitin beads, and fungal species (*Candida albicans* and *Alternaria alternata*) (28). We first aimed to test if murine LysMD3 binds to *A. fumigatus* in our invasive aspergillosis model. We harvested tagged LysMD3 protein (LysMD3-Fc) comprised of the LysMD3 ectodomain and human Fc as the binding target for secondary antibody recognition. The goal is to use LysMD3-Fc staining to examine the binding of LysMD3 to *A. fumigatus*, similar to experiments where dectin-1-Fc binding is used to detect  $\beta$ -glucan (37). As fungal cell wall components are masked by hydrophobin rodlets (39), dectin-1-Fc staining showed no recognition for resting conidia and strong binding to swollen conidia (Fig. 7A). However, binding of LysMD3-Fc revealed heterogeneous recognition of resting conidia and stronger and more uniform binding to swollen conidia (Fig. 7B). The signal resulting from LysMD3-Fc binding is about 10-fold lower than the dectin-1-Fc signal, but we do see binding of LysMD3 on the fungal surface by confocal microscopy (Fig. 7C). The binding pattern of LysMD3-Fc suggests that it might bind to cell wall components as the loose structure at the tip of the germ tube features higher exposure of cell wall components (51). To examine the binding target of LysMD3-Fc, we stained swollen conidia and hyphae of  $\Delta$ ags *A. fumigatus* because this strain features increased exposure of chitin and  $\beta$ -glucan compared to parental controls (Fig. 8C, 8D, 8F, 8G, 8I and 8J). However, the LysMD3-Fc staining on the  $\Delta$ ags strain did not show the same trend as dectin-1-Fc and WGA staining. There were no significant differences in the pattern of LysMD3-Fc staining between  $\Delta$ ags and control group at the conidia stage, and the germling stage appears to show opposite results when comparing dectin-1-Fc and WGA staining (Fig. 8B, 8E and 8H). These results indicate that the binding of LysMD3-Fc

to *A. fumigatus* does not reflect chitin and  $\beta$ -glucan exposure and it is possible that LysMD3-Fc binding to the fungal surface depends on  $\alpha$ -glucan binding or other receptors that involve in  $\alpha$ -glucan recognition (52, 53). To further investigate other cell wall components that may be important for LysMD3 binding, we next examined if GAG on the surface of germlings is essential for LysMD3-Fc binding. Surprisingly, the germlings of  $\Delta uge3$  cells, which lack GAG on the fungal surface, completely abolished the binding of LysMD3-Fc to the fungal surface (Fig. 9). However, the binding pattern of LysMD3-Fc does not match WT patterns of GAG distribution. In  $\Delta uge3$  cells, LysMD3-Fc shows aggregated clumps of signal in the media which differs from the complete absence of GAG recognition by SBA. We also noticed some net structures between germlings stained with LysMD3-Fc, which could indicate binding of LysMD3-Fc to the extracellular matrix (ECM) of *A. fumigatus*. With the LysMD3-Fc binding data, we have shown that murine LysMD3 does bind to the surface of *A. fumigatus* at both conidia and germling growth stages. In summary, the changes in fungal cell wall or ECM components does affect LysMD3 binding to the fungal surface, but the exact binding target and potential regulation of LysMD3 both require further studies.

## Materials and Methods

### Strains and media

*A. fumigatus* strain CEA10, AF293, Ku80, EVOL20, ATCC46645 and mutants derived from these WT strains were grown on a 1% glucose minimal media (GMM) plates for 3 days at 37 °C. For animal experiments, conidia were collected in 0.01% Tween-20 and washed 3 times with sterile PBS.

### LysMD3 protein prediction

Murine LysMD3 protein structure was predicted by I-TASSER (<https://zhanggroup.org/I-TASSER/>). The predicted model with higher C-score, which indicates higher confidence, was selected. For protein structure comparison, the protein with highest TM-score, which indicates the closest structure similarity, was identified by TM-align from Protein Data Bank (PDB). For potential binding site prediction, the predicted site was annotated by COFACTOR and COACH. The potential binding pocket and ligand was selected based on highest C-score (Confidence Score).

### Animal inoculation

To generate LysMD3 knockout (KO) mice, the eggs from WT C57BL/6J mice were injected with 5-7.5 ng/ul of our CRISPR/Cas9 construct to target LysMD3 by the Transgenic Service of Dartmouth Cancer Center. Through the sequencing results, we picked the LysMD3 mutant mouse with 16 bp deletion, which introduces a premature stop codon before LysM domain, for the LysMD3 KO mice line. LysMD3<sup>+/+</sup> (WT) and LysMD3<sup>-/-</sup> C57BL/6J mice were generated from the intercross of LysMD3<sup>+/-</sup> heterozygous mice. For mouse genotyping, genomic DNA was isolated from mice tail by Quick DNA Mini-Prep plus kit manufacturer's instruction (ZYMO). Primers used were: Forward primer for WT LysMD3: 5'- GCTGAAGTCTACGAACTTCGGTCCA-3'. Forward primer for mutant LysMD3: 5'- CTGAAGTCTACGAAAGGAGAAG-3'. Common reverse primer for LysMD3: 5'- GGTCATGTCCACAGGACTAGGAGATTTC-3'. Age-matched, inbred mice between 8-12 weeks old were used for animal experiments. Mice were housed in

autoclaved cages at  $\leq 4$  mice per cage with a supply of HEPA-filtered air and sterile water. For invasive aspergillosis model, mice were inoculated with  $5 \times 10^7$  CEA10 (in 100  $\mu$ l sterile PBS) or control PBS by oropharyngeal instillation under isoflurane anesthesia. For cellularity and FLARE experiments, mice were humanely euthanized 12 hours post-*Aspergillus* challenge. In immune suppressed invasive aspergillosis model, mice between 20-24 grams were immune-suppressed with 40 mg/kg triamcinolone acetonide (Kenalog-10, Bristol-Myers Squibb) subcutaneously 24 hours prior fungal challenge. Mice were then infected with  $1 \times 10^6$  CEA10 (in 50  $\mu$ l sterile PBS) by intranasal instillation under isoflurane anesthesia. Survival metrics were plotted on Kaplan-Meier curves and statistical significance between curves was determined using Log-rank test and Gehan-Breslow-Wilcoxon test. Animals were monitored daily for morbidity symptoms and all animal studies were performed in strict accordance with the recommendations and guidelines in the Guide for the Care and Use of Laboratory Animals. Experimental protocol #00002167 was approved by the Dartmouth College Institutional Animal Care and Use Committee (IACUC).

#### LysMD3 expression (qPCR, 3'RACE and Western blot)

To harvest single cell suspensions from murine lungs, the whole lungs were minced and digested in buffer containing 2.2 mg/ml Collagenase type IV (Worthington), 1 U/ml DNase1 (New England Biotech) and 5% FBS at 37 °C for 45 min. The digested samples were passed through an 18-gauge needle, incubated in RBC Lysis buffer, neutralized in PBS, passed through 100  $\mu$ m filter, and enumerated. The isolated lung cells were stained with Propidium iodide (eBioScience) and CD45 (Pacific Orange, Invitrogen). Live CD45<sup>(+)</sup> and CD45<sup>(-)</sup> cells were sorted by FACS Aria III Cell Sorter. These sorted cells were first stored in RNeasy Lysis Solution (Qiagen), lysed, and harvested for RNA with Trisure according manufacturer's instruction (Molecular Research Laboratories). 5  $\mu$ g of RNA was treated with Ambion Turbo DNase (Life Technologies) according to the manufacturer's instruction. 1  $\mu$ g of DNase treated RNA was further processed with QuantiTect Reverse Transcription kit. cDNA amplification was normalized to *Gapdh*,

*Rpl13a* and *Hprt* for LysMD3 expression. Primers used were: Forward primer for murine GAPDH: 5'-TCATCCCAGAGCTGAACG-3', reverse primer for murine GAPDH: 5'-GGGAGTTGCTGTTGAAGTC-3'. Forward primer for murine RPL13A: 5'-CTCTGGAGGAGAAACGGAAGGAAA-3', reverse primer for murine RPL13A: 5'-GGTCTTGAGGACCTCTGTGAACTT-3'. Forward primer for murine HPRT: 5'-GGAGTCCTGTTGATGTTGCCAGTA-3', reverse primer for murine HPRT: 5'-GGGACGCAGCAACTGACATTTCTA-3'. Forward primer for murine LysMD3: 5'-CATATGCCAAGGTGTGTGGCG-3', reverse primer for murine LysMD3: 5'-CGCAAATCAGACCCCACTCC-3'. For 3'RACE experiment, cDNA from WT and LysMD3 KO mice were used for first round of PCR with LysMD3 3'RACE Forward primer-1: 5'-GATGACGCACCGCAGGTTTG-3'. Q0: 5'-CCAGTGAGCAGAGTGACG-3'. Primers for the second round of PCR: LysMD3 3'RACE Forward primer-1: 5'-GTGGAGGACATAACCGTGTGCG-3'. LysMD3 3'RACE reverse primer-after 16 bp del: 5'-CGTACAGCAGTACTGAAGGGCTACTG-3'. LysMD3 reverse primer for HRM: 5'-GCGCTTCTTCGAACCTTCTCC-3'. LysMD3 protein was examined by Western blot from isolated lung cells as previous described. Protein was extracted from freshly collected cells with protein extraction Buffer A (10 mM Tris-HCl; 1.5 mM MgCl<sub>2</sub>; 10 mM KCl; 2mM DTT; 0.4 mM PMSF; 1X HALT). The primary antibody for LysMD3 (Proteintech; 1:1500) and  $\gamma$ -tubulin (Sigma; 1:2000) was used for overnight incubation at 4 °C and the anti-rabbit secondary antibody for LysMD3 (Proteintech; 1:5000) and  $\gamma$ -tubulin (Sigma; 1:100000) was incubated for one hour at room temperature. For chemifluorescence imaging, the Clarity Western ECL Substrate kit (Bio-rad) was used according to the manufacturer's instruction.

#### Flow cytometry: Cellularity experiments and **FLuorescence Aspergillus REporter (FLARE)**

##### Assay Analysis

For FLARE experiments, CEA10-mRFP conidia were generated by ectopic insertion of pGpdA-mRFP construct, using the *ptrA* gene as selection marker. To generate FLARE conidia, CEA10-mRFP conidia were collected and labeled with Alexafluor

633 as described previously (35, 36). Mice were inoculated with FLARE conidia as described previously and euthanized at 12 hours post fungal inoculation. Single cell suspensions from the lungs were harvested and prepared as previously described. Antibodies used for Flow cytometry analysis on different populations were as follows: For neutrophil and eosinophil population, lung cells were stained with Survival dye (eFluor780, eBioScience), CD45 (Pacific Orange, Invitrogen), SiglecF (BV421, BD BioScience), Ly6G (FITC, BioLegend), and CD11b (PerCPy5.5, BioLegend). For macrophage/monocyte population, lung cells were stained with Survival dye (eFluor780, eBioScience), IA/IE (MHCII) (BV605, BioLegend), SiglecF (BV421, BD BioScience), Ly6G (FITC, BioLegend), CD103 (FITC, BioLegend), CD11b (PerCPy5.5, BioLegend), and CD64 (PECy7, BioLegend). For DC populations, lung cells were stained with Survival dye (eFluor780, eBioScience), IA/IE (MHCII) (BV605, BioLegend), CD11b (Pacific Blue, BioLegend), CD103 (FITC, BioLegend), CD317 (PerCPy5.5, BioLegend), and CD11c (PECy7, BioLegend). The gating strategy of each cell population is described in prior published work (PMID: 36377895). Data were collected by Beckman Coulter Cytoflex S and analyzed with FlowJo version 10.8.1. To quantify fungal viability, colony forming units (CFUs) were plated from single cell suspensions that were further homogenized with glass beads using a Mini Bead Beater (BioSpec Products Inc, Bartlesville, OK) and resuspended in PBS. Samples were diluted 1:100 and then plated on 1/2 Sabouraud dextrose agar plates, incubated overnight, and counted for CFUs.

#### Cell wall staining: Conidia and germling LysMD3-Fc binding profiles

FreeStyle™ 293-F Cells were incubated at 37°C until confluence according to the manufacturer's instruction (Gibco). The cells were transfected with LysMD3-fc protein constructs (LysMD3-Fc-pSecTag2) with a concentration of 0.5 mg plasmid/L Cell culture. At Day 6 post transfection, cell supernatant was harvested and transferred to the Protein A Column. After the flow-through of the cell supernatant, the Protein A column was washed with Equilibrium buffer (1X PBS, 5% glycerol, 0.05% Tween 20). The proteins were eluted with Elution buffer (0.1 M Glycine (pH 3.0), 5% glycerol, 0.05%

Tween 20) and loaded into size exclusive column (S200) with Equilibrium buffer (1X PBS, 5% glycerol, 0.05% Tween 20) for further separation by protein sizes. *A. fumigatus* conidia were cultured in liquid GMM without yeast extract at 37 °C for different times to enrich for swollen conidia or germlings. Conidia were cultured for 5-9 hours for swollen conidia in 96 well plates and 14-18 hours for germlings on glass coverslips, depending on the strains tested. Swollen conidia and germlings were blocked for non-specific binding in blocking reagent (RPMI/10% FBS/0.025% Tween20) for 1 hour at room temperature and then incubated with 5 µg/ml of LysMD3-Fc (or concentration as indicated) or dectin-1-Fc in PBS/0.05% Tween-20 for 1 hour at room temperature. Following primary antibody incubation, the samples were stained with Alexaflour 488 anti-human IgG (Thermo; 1:300) antibody in PBS/0.05% Tween-20 for 1 hour at room temperature. Samples were then washed with PBS/0.05% Tween-20 twice between each step. For WGA and SBA staining, samples were incubated with 5 µg/ml of fluorescein-labeled WGA or SBA after blocking. In swollen conidia samples, conidia were passed through 100 µm filter, and data was collected by Beckman Coulter Cytoflex S before analysis with FlowJo version 10.8.1. Swollen conidia were gated as shown in Fig 8A. The intensity of conidial cell wall labeling was calculated as “((geometric mean fluorescence intensity (gMFI) of stained group) – (gMFI of secondary antibody or unstained controls)) / ((gMFI of parental strains) – (gMFI of secondary antibody or unstained parental strains)) \* 100%. For germling samples, samples were mounted with Prolong Diamond Antifade Mountant (Thermofisher) and sealed with clear nail polish. Images were acquired using an Andor W1 spinning disk confocal microscope mounted with a Nikon Eclipse Ti inverted microscope stand. Images were viewed and analyzed using Fiji Software. The corrected total cell fluorescence for confocal images was calculated as “Integrated Density - (Area of selected cell \* Mean fluorescence of background readings)”.



## References

1. Figueiredo RT, Carneiro LAM, Bozza MT. 2011. Fungal surface and innate immune recognition of filamentous fungi. *Front Microbiol* 2.
2. Erwig LP, Gow NAR. 2016. Interactions of fungal pathogens with phagocytes. *Nat Rev Microbiol* 14:163–176.
3. Garcia-Rubio R, de Oliveira HC, Rivera J, Trevijano-Contador N. 2020. The Fungal Cell Wall: *Candida*, *Cryptococcus*, and *Aspergillus* Species. *Front Microbiol* 10.
4. da Silva CA, Chalouni C, Williams A, Hartl D, Lee CG, Elias JA. 2009. Chitin is a size-dependent regulator of macrophage TNF and IL-10 production. *J Immunol* 182:3573–3582.
5. Wagener J, Malireddi RKS, Lenardon MD, Köberle M, Vautier S, MacCallum DM, Biedermann T, Schaller M, Netea MG, Kanneganti TD, Brown GD, Brown AJP, Gow NAR. 2014. Fungal chitin dampens inflammation through IL-10 induction mediated by NOD2 and TLR9 activation. *PLoS Pathog* 10.
6. Lee CG, da Silva CA, Lee JY, Hartl D, Elias JA. 2008. Chitin regulation of immune responses: an old molecule with new roles. *Curr Opin Immunol* 20:684–689.
7. da Silva CA, Chalouni C, Williams A, Hartl D, Lee CG, Elias JA. 2009. Chitin is a size-dependent regulator of macrophage TNF and IL-10 production. *J Immunol* 182:3573–3582.
8. Liu T, Liu Z, Song C, Hu Y, Han Z, She J, Fan G, Wang J, Jin C, Chang J, Zhou JM, Chai J. 2012. Chitin-induced dimerization activates a plant immune receptor. *Science* 336:1160–1164.
9. Lee CG, da Silva CA, dela Cruz CS, Ahangari F, Ma B, Kang MJ, He CH, Takyar S, Elias JA. 2011. Role of chitin and chitinase/chitinase-like proteins in inflammation, tissue remodeling, and injury. *Annu Rev Physiol* 73:479–501.
10. Moeller JB, Leonardi I, Schlosser A, Flamar AL, Bessman NJ, Putzel GG, Thomsen T, Hammond M, Jepsen CS, Skjødte K, Füchtbauer EM, Farber DL, Sorensen GL, Iliev ID, Holmskov U, Artis D. 2019. Modulation of the fungal mycobiome is regulated by the chitin-binding receptor FIBCD1. *J Exp Med* 216:2689–2700.
11. Jepsen CS, Dubey LK, Colmorton KB, Moeller JB, Hammond MA, Nielsen O, Schlosser A, Templeton SP, Sorensen GL, Holmskov U. 2018. FIBCD1 Binds *Aspergillus fumigatus* and Regulates Lung Epithelial Response to Cell Wall Components. *Front Immunol* 9.

12. Fuchs K, Cardona Gloria Y, Wolz O, Herster F, Sharma L, Dillen CA, Täumer C, Dickhöfer S, Bittner Z, Dang T, Singh A, Haischer D, Schlöffel MA, Koymans KJ, Sanmuganantham T, Krach M, Roger T, le Roy D, Schilling NA, Frauhammer F, Miller LS, Nürnberger T, LeibundGut-Landmann S, Gust AA, Macek B, Frank M, Gouttefangeas C, dela Cruz CS, Hartl D, Weber AN. 2018. The fungal ligand chitin directly binds TLR2 and triggers inflammation dependent on oligomer size. *EMBO Rep* 19.
13. Mora-Montes HM, Netea MG, Ferwerda G, Lenardon MD, Brown GD, Mistry AR, Kullberg BJ, O'Callaghan CA, Sheth CC, Odds FC, Brown AJP, Munro CA, Gow NAR. 2011. Recognition and blocking of innate immunity cells by *Candida albicans* chitin. *Infect Immun* 79:1961–1970.
14. Buist G, Steen A, Kok J, Kuipers OP. 2008. LysM, a widely distributed protein motif for binding to (peptido)glycans. *Mol Microbiol* 68:838–847.
15. Garvey KJ, Saedi MS, Ito J. 1986. Nucleotide sequence of *Bacillus* phage phi 29 genes 14 and 15: homology of gene 15 with other phage lysozymes. *Nucleic Acids Res* 14:10001–10008.
16. Gust AA, Willmann R, Desaki Y, Grabherr HM, Nürnberger T. 2012. Plant LysM proteins: modules mediating symbiosis and immunity. *Trends Plant Sci* 17:495–502.
17. de Jonge R, van Esse HP, Kombrink A, Shinya T, Desaki Y, Bours R, van der Krol S, Shibuya N, Joosten MHAJ, Thomma BPHJ. 2010. Conserved fungal LysM effector Ecp6 prevents chitin-triggered immunity in plants. *Science* 329:953–955.
18. Limpens E, Franken C, Smit P, Willemse J, Bisseling T, Geurts R. 2003. LysM domain receptor kinases regulating rhizobial Nod factor-induced infection. *Science* 302:630–633.
19. Zeng L, Velásquez AC, Munkvold KR, Zhang J, Martin GB. 2012. A tomato LysM receptor-like kinase promotes immunity and its kinase activity is inhibited by AvrPtoB. *Plant J* 69:92–103.
20. Cao Y, Liang Y, Tanaka K, Nguyen CT, Jedrzejczak RP, Joachimiak A, Stacey G. 2014. The kinase LYK5 is a major chitin receptor in *Arabidopsis* and forms a chitin-induced complex with related kinase CERK1. *Elife* 3.
21. Yamada K, Yamaguchi K, Yoshimura S, Terauchi A, Kawasaki T. 2017. Conservation of Chitin-Induced MAPK Signaling Pathways in Rice and *Arabidopsis*. *Plant Cell Physiol* 58:993–1002.

22. Shi X-Z, Zhou J, Lan J-F, Jia Y-P, Zhao X-F, Wang J-X. 2013. A Lysin motif (LysM)-containing protein functions in antibacterial responses of red swamp crayfish, *Procambarus clarkii*. *Dev Comp Immunol* 40:311–319.
23. Shi XZ, Feng XW, Sun JJ, Yang MC, Lan JF, Zhao XF, Wang JX. 2016. Involvement of a LysM and putative peptidoglycan-binding domain-containing protein in the antibacterial immune response of kuruma shrimp *Marsupenaeus japonicus*. *Fish Shellfish Immunol* 54:489–498.
24. Martinez DA, Oliver BG, Gräser Y, Goldberg JM, Li W, Martinez-Rossi NM, Monod M, Shelest E, Barton RC, Birch E, Brakhage AA, Chen Z, Gurr SJ, Heiman D, Heitman J, Kostl I, Rossi A, Saif S, Samalova M, Saunders CW, Shea T, Summerbell RC, Xu J, Young S, Zeng Q, Birren BW, Cuomo CA, White TC. 2012. Comparative genome analysis of *Trichophyton rubrum* and related dermatophytes reveals candidate genes involved in infection. *mBio* 3.
25. de Jonge R, Thomma BPHJ. 2009. Fungal LysM effectors: extinguishers of host immunity? *Trends Microbiol* 17:151–157.
26. Kombrink A, Thomma BPHJ. 2013. LysM effectors: secreted proteins supporting fungal life. *PLoS Pathog* 9:1–4.
27. Yokoyama CC, Baldridge MT, Leung DW, Zhao G, Desai C, Liu TC, Diaz-Ochoa VE, Huynh JP, Kimmey JM, Sennott EL, Hole CR, Idol RA, Park S, Storek KM, Wang C, Hwang S, Milam AV, Chen E, Kerrinnes T, Starnbach MN, Handley SA, Mysorekar IU, Allen PM, Monack DM, Dinanuer MC, Doering TL, Tsolis RM, Dworkin JE, Stallings CL, Amarasinghe GK, Micchelli CA, Virginia HW. 2018. LysMD3 is a type II membrane protein without an in vivo role in the response to a range of pathogens. *J Biol Chem* 293:6022–6038.
28. He X, Howard BA, Liu Y, Neumann AK, Li L, Menon N, Roach T, Kale SD, Samuels DC, Li H, Kite T, Kita H, Hu TY, Luo M, Jones CN, Okaa UJ, Squillace DL, Klein BS, Lawrence CB. 2021. LYSMD3: A mammalian pattern recognition receptor for chitin. *Cell Rep* 36.
29. Marakalala MJ, Kerrigan AM, Brown GD. 2011. Dectin-1: a role in antifungal defense and consequences of genetic polymorphisms in humans. *Mamm Genome* 22:55–65.
30. Muzio M, Bosisio D, Polentarutti N, D'amico G, Stoppacciaro A, Mancinelli R, van't Veer C, Penton-Rol G, Ruco LP, Allavena P, Mantovani A. 2000. Differential expression and regulation of toll-like receptors (TLR) in human leukocytes: selective expression of TLR3 in dendritic cells. *J Immunol* 164:5998–6004.

31. O'Dea EM, Amarsaikhan N, Li H, Downey J, Steele E, van Dyken SJ, Locksley RM, Templeton SP. 2014. Eosinophils are recruited in response to chitin exposure and enhance Th2-mediated immune pathology in *Aspergillus fumigatus* infection. *Infect Immun* 82:3199–3205.
32. Koller B, Müller-Wiefel AS, Rupec R, Korting HC, Ruzicka T. 2011. Chitin modulates innate immune responses of keratinocytes. *PLoS One* 6.
33. Goodridge HS, Reyes CN, Becker CA, Katsumoto TR, Ma J, Wolf AJ, Bose N, Chan ASH, Magee AS, Danielson ME, Weiss A, Vasilakos JP, Underhill DM. 2011. Activation of the innate immune receptor Dectin-1 upon formation of a “phagocytic synapse.” *Nature* 472:471–475.
34. Doyle SE, O'Connell RM, Miranda GA, Vaidya SA, Chow EK, Liu PT, Suzuki S, Suzuki N, Modlin RL, Yeh WC, Lane TF, Cheng G. 2004. Toll-like receptors induce a phagocytic gene program through p38. *J Exp Med* 199:81–90.
35. Jhingran A, Mar KB, Kumasaka DK, Knoblaugh SE, Ngo LY, Segal BH, Iwakura Y, Lowell CA, Hamerman JA, Lin X, Hohl TM. 2012. Tracing conidial fate and measuring host cell antifungal activity using a reporter of microbial viability in the lung. *Cell Rep* 2:1762–1773.
36. Liu K-W, Grau MS, Jones JT, Wang X, Vesely EM, James MR, Gutierrez-Perez C, Cramer RA, Obar JJ. 2022. Postinfluenza Environment Reduces *Aspergillus fumigatus* Conidium Clearance and Facilitates Invasive Aspergillosis In Vivo. *mBio* 13.
37. Graham LM, Tsoni SV, Willment JA, Williams DL, Taylor PR, Gordon S, Dennehy K, Brown GD. 2006. Soluble Dectin-1 as a tool to detect beta-glucans. *J Immunol Methods* 314:164–169.
38. Stappers MHT, Clark AE, Aimaniananda V, Bidula S, Reid DM, Asamaphan P, Hardison SE, Dambuza IM, Valsecchi I, Kerscher B, Plato A, Wallace CA, Yuecel R, Hebecker B, da Glória Teixeira Sousa M, Cunha C, Liu Y, Feizi T, Brakhage AA, Kwon-Chung KJ, Gow NAR, Zanda M, Piras M, Zanato C, Jaeger M, Netea MG, van de Veerdonk FL, Lacerda JF, Campos A, Carvalho A, Willment JA, Latgé JP, Brown GD. 2018. Recognition of DHN-melanin by a C-type lectin receptor is required for immunity to *Aspergillus*. *Nature* 555:382–386.
39. Gow NAR, Latge J-P, Munro CA. 2017. The Fungal Cell Wall: Structure, Biosynthesis, and Function. *Microbiol Spectr* 5.

40. Beauvais A, Bozza S, Kniemeyer O, Formosa C, Balloy V, Henry C, Roberson RW, Dague E, Chignard M, Brakhage AA, Romani L, Latgé JP. 2013. Deletion of the  $\alpha$ -(1,3)-glucan synthase genes induces a restructuring of the conidial cell wall responsible for the avirulence of *Aspergillus fumigatus*. *PLoS Pathog* 9.
41. Speth C, Rambach G, Lass-Flörl C, Howell PL, Sheppard DC. 2019. Galactosaminogalactan (GAG) and its multiple roles in *Aspergillus* pathogenesis. *Virulence* 10:976–983.
42. Serebrenik Y v., Hellerschmied D, Toure M, López-Giráldez F, Brookner D, Crews CM. 2018. Targeted protein unfolding uncovers a Golgi-specific transcriptional stress response. *Mol Biol Cell* 29:1284–1298.
43. Caffrey-Carr AK, Hilmer KM, Kowalski CH, Shepardson KM, Temple RM, Cramer RA, Obar JJ. 2018. Host-Derived Leukotriene B4 Is Critical for Resistance against Invasive Pulmonary Aspergillosis. *Front Immunol* 8.
44. Caffrey-Carr AK, Kowalski CH, Beattie SR, Blaseg NA, Upshaw CR, Thammahong A, Lust HE, Tang YW, Hohl TM, Cramer RA, Obar JJ. 2017. Interleukin 1 $\alpha$  Is Critical for Resistance against Highly Virulent *Aspergillus fumigatus* Isolates. *Infect Immun* 85.
45. Kowalski CH, Beattie SR, Fuller KK, McGurk EA, Tang YW, Hohl TM, Obar JJ, Cramer RA. 2016. Heterogeneity among Isolates Reveals that Fitness in Low Oxygen Correlates with *Aspergillus fumigatus* Virulence. *mBio* 7.
46. Rizzetto L, Giovannini G, Bromley M, Bowyer P, Romani L, Cavalieri D. 2013. Strain dependent variation of immune responses to *A. fumigatus*: definition of pathogenic species. *PLoS One* 8.
47. Rosowski EE, Raffa N, Knox BP, Golenberg N, Keller NP, Huttenlocher A. 2018. Macrophages inhibit *Aspergillus fumigatus* germination and neutrophil-mediated fungal killing. *PLoS Pathog* 14.
48. Kale SD, Ayubi T, Chung D, Tubau-Juni N, Leber A, Dang HX, Karyala S, Hontecillas R, Lawrence CB, Cramer RA, Bassaganya-Riera J. 2017. Modulation of Immune Signaling and Metabolism Highlights Host and Fungal Transcriptional Responses in Mouse Models of Invasive Pulmonary Aspergillosis. *Sci Rep* 7.
49. Bueter CL, Specht CA, Levitz SM. 2013. Innate sensing of chitin and chitosan. *PLoS Pathog* 9.

50. Taghavi M, Khosravi A, Mortaz E, Nikaein D, Athari SS. 2017. Role of pathogen-associated molecular patterns (PAMPS) in immune responses to fungal infections. *Eur J Pharmacol* 808:8–13.
51. Latgé JP, Beauvais A, Chamilos G. 2017. The Cell Wall of the Human Fungal Pathogen *Aspergillus fumigatus*: Biosynthesis, Organization, Immune Response, and Virulence. *Annu Rev Microbiol* 71:99–116.
52. Geurtsen J, Chedammi S, Mesters J, Cot M, Driessen NN, Sambou T, Kakutani R, Ummels R, Maaskant J, Takata H, Baba O, Terashima T, Bovin N, Vandenbroucke-Grauls CMJE, Nigou J, Puzo G, Lemassu A, Daffé M, Appelmelk BJ. 2009. Identification of mycobacterial alpha-glucan as a novel ligand for DC-SIGN: involvement of mycobacterial capsular polysaccharides in host immune modulation. *J Immunol* 183:5221–5231.
53. Bittencourt VCB, Figueiredo RT, da Silva RB, Mourão-Sá DS, Fernandez PL, Sasaki GL, Mulloy B, Bozza MT, Barreto-Bergter E. 2006. An alpha-glucan of *Pseudallescheria boydii* is involved in fungal phagocytosis and Toll-like receptor activation. *J Biol Chem* 281:22614–22623.

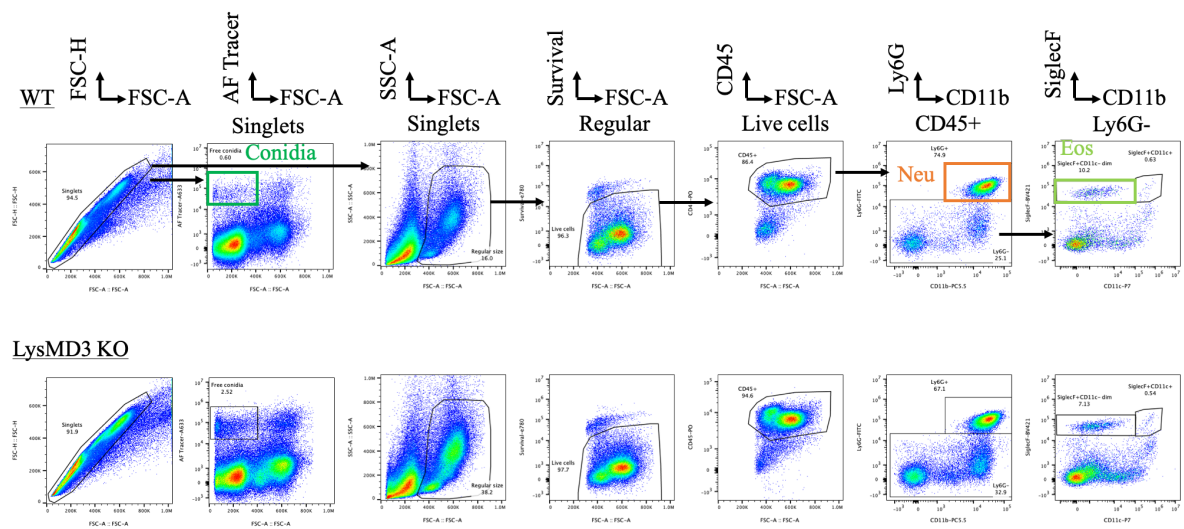


**Fig. S1 Gating strategy for Neutrophils.** The neutrophils were identified as CD45<sup>(+)</sup>Ly6G<sup>(+)</sup>CD11b<sup>(+)</sup> cells, eosinophils as Ly6G<sup>(-)</sup>SiglecF<sup>(+)</sup>CD11b<sup>(dim or -)</sup> and free conidia as FSC<sup>(low)</sup>AF Tracer<sup>(+)</sup> cells.





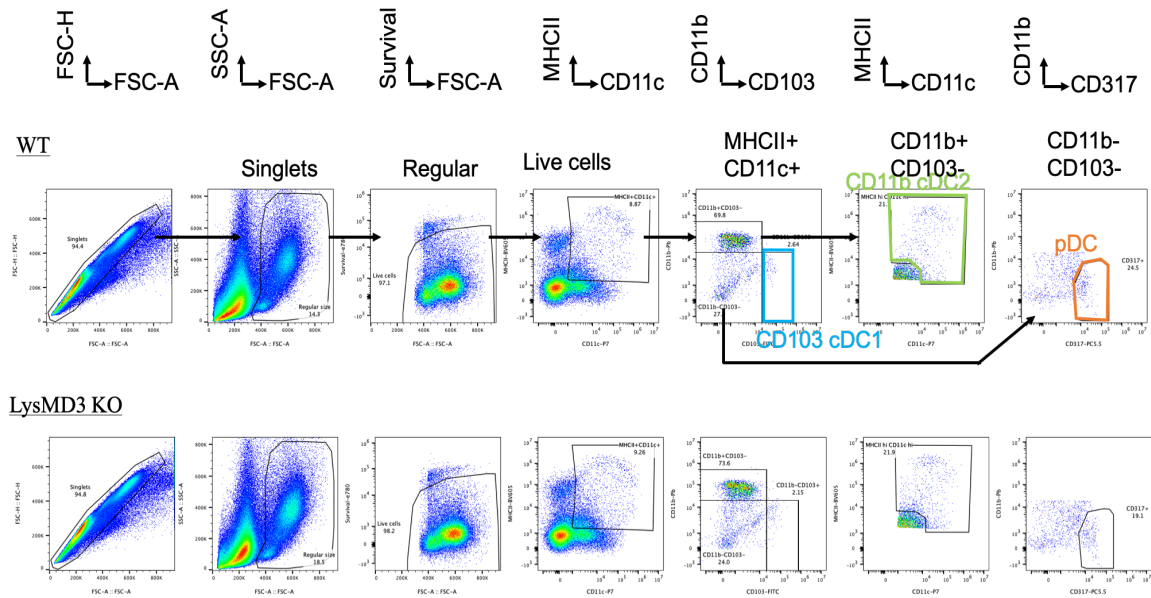


**Fig. S3 Gating strategy for DCs.** The CD103<sup>(+)</sup> cDC1 were identified as MHCII<sup>(+)</sup> CD11c<sup>(+)</sup>CD11b<sup>(-)</sup>CD103<sup>(+)</sup> cells, CD11b<sup>(+)</sup> cDC2 were identified as MHCII<sup>(hi)</sup>CD11c<sup>(hi)</sup> CD103<sup>(-)</sup>CD11b<sup>(+)</sup> cells and pDC were identified as MHCII<sup>(+)</sup>CD11c<sup>(+)</sup>CD11b<sup>(-)</sup>CD103<sup>(-)</sup> CD317<sup>(+)</sup> cells.

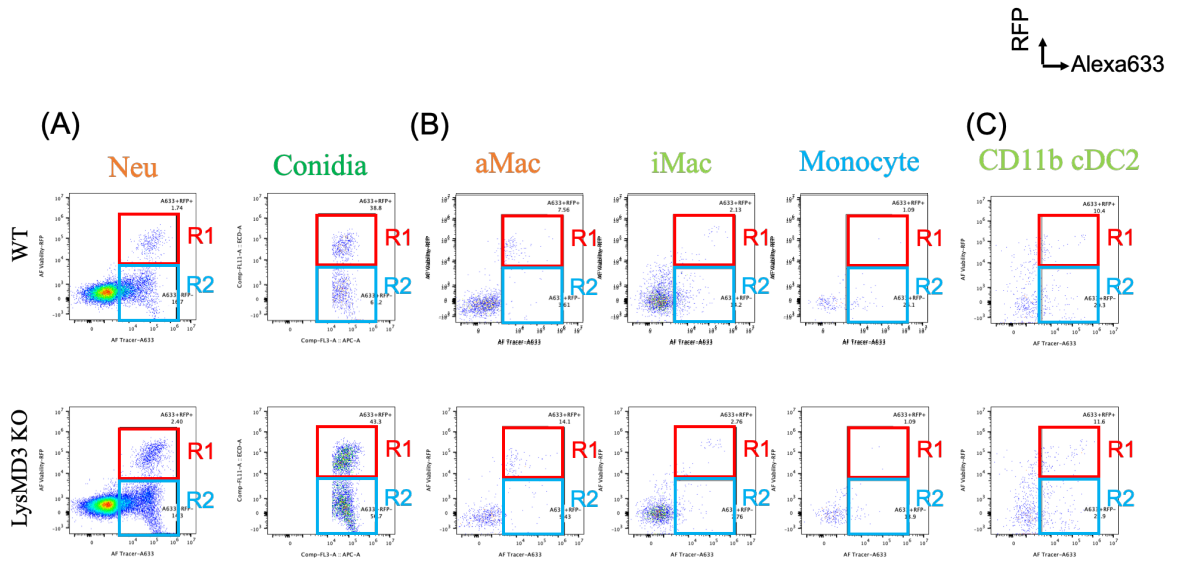


**Fig. S4 FLARE results of lung phagocytes.** The gating for FLARE experiments in the (A) neutrophils and free conidia, (B) alveolar macrophages, interstitial macrophages and monocytes, (C) CD11b<sup>+</sup> cDC2. R1 denotes phagocytes containing live conidia. R2 denotes phagocytes containing killed conidia. (R1+R2) indicates conidial uptake of phagocytes and (R1/(R1+R2)) indicates conidial viability in the phagocytes.

## **Chapter 4**

Discussion and Perspectives

Ko-Wei Liu

## Host innate immunity, from antifungal immunity to multiplex superinfection

In this dissertation, we covered many aspects of how innate immunity is involved in antifungal responses. In Chapter 1, we discussed the complexity of the lung environment. Multiple organisms, including commensal and pathogens, constantly interact with the host cells. Our immune system needs to maintain a basal level of immune response for them to be able to quickly respond to pathogenic infection. At the same time, setting the threshold to initiate inflammatory responses is also critical to prevent excessive immune response, since unbiased damage from innate immunity can also cause local tissue damage. The signal for reaching the threshold to initiate immune responses could come from tissue injury or exposure to a high number of pathogens, which the latter is more similar to our common laboratory inoculation condition. The other potential situation that causes severe inflammation is the propagation of pathogens escaping from host immunity to provide a significant amount of input for immune activation. Moreover, the lung environment is way more complex than the host response to a single pathogen infection, our lung immune system constantly receives signals from both the commensals and evaded pathogens, which can be bacteria, fungi, or viruses. In this case, the host's innate immunity needs to integrate the PRR signals from microbiome recognition and decide whether it is time to break the homeostasis and initiate immune responses.

The initiation of bacterial and fungal infections shares many common characteristics. Bacteria in the host lung are very small microorganisms that have an average size is about 0.5-5  $\mu\text{m}$  in diameter. The fungal conidia are slightly bigger but still within 2-10  $\mu\text{m}$  in diameter for them to be able to get into the lung (1). Due to their small size, these bacterial and fungal pathogens can enter the host airway and initiate their colonization. To initiate growth in the lung, both bacteria and fungi need to adapt to a new environment in the host. In the lung, the change of temperature, pH, oxygen tension, and ion/nutrient availability will stimulate the change of transcriptional profile

and turn them into an “active” stage to initiate colonization. The bacterial colonization starts with attaching to a niche in the host (2). While they lose their mobility, the quick propagation and secreted extracellular matrix (ECM) gradually form the bacterial biofilm, which greatly enhances their fitness in the host environment as well as competing with other organisms (3). The yeast form of fungi has a similar initial adhesion process as bacterial infections. However, as the yeast grows, the transition to pseudohyphal cells and hyphal cells increases their ECM secretion as the maturation of fungal biofilm (4). For the filament fungi, the resting conidia break their dormancy by sensing environmental clues such as oxygen in the lung (5). After the degradation of surface hydrophobin, environmental nutrients and liquid enter the conidia, change the osmotic tension, swell the conidia and initiate their growth as the process of germination (6). Forming the germling tube and the continuing growth as hyphae, the filament fungi can form their biofilm with secreted ECM, the establishment of hypoxia gradient, and protection from the host immune responses. Although the resting conidia are immunologically inert, once the conidia break their dormancy and initiate germination, the swollen conidia and germlings can be recognized by the host immune system and induce immune responses, just like bacteria. Pathogen associated molecular patterns (PAMPs) from bacteria and fungi can be recognized by pattern recognition receptors (PRRs) as we mentioned in Chapter 1. These PRRs activate common transcriptional factors to induce cytokine production for proinflammation responses. Although the signal from bacteria and fungi might be more prominent with specific PRRs, the downstream signaling is highly overlapped. The immune responses from innate immunity for bacterial and fungal clearance are also very similar. The cytokine/chemokine production, immune cell recruitment, phagocytosis, and ROS production mediated by innate immunity are equally important for bacterial and fungal clearance. After the clearance of bacterial or fungal infection, the immune system needs to “turn off” its inflammatory responses and back to the homeostasis condition. The immune resolving phase in the post-bacterial and post-fungal environment requires IL-10 signaling to prevent further immune activation and cell recruitment. The remaining

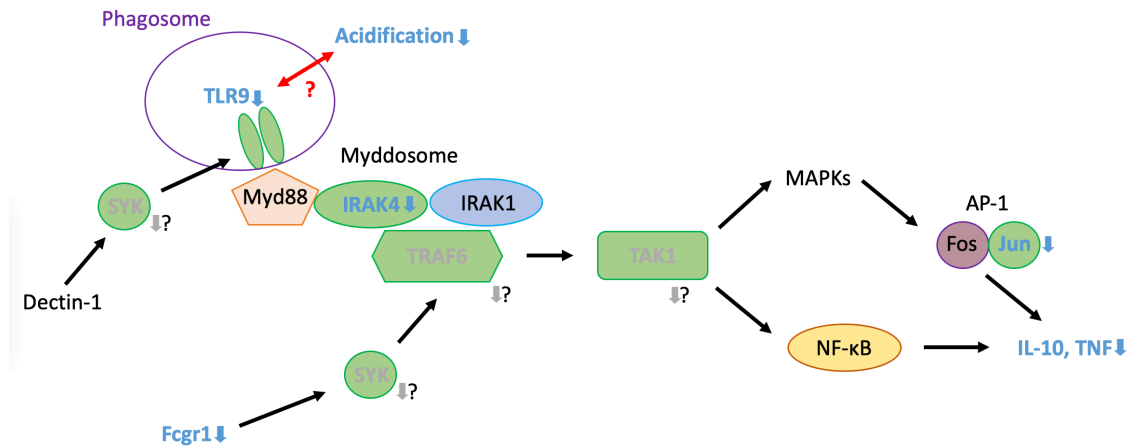
activated innate immune cells receiving anti-inflammatory cytokines or loss stimulation from the pathogens will turn them into quiescence stage or lead to cell death (7). During and after bacterial/fungal infections, the host lung environment requires tissue-resident macrophages and epithelial cells for tissue repair (8, 9). Because of the high overlapped between anti-bacterial and anti-fungal innate immunity, it is less likely to have prolonged bacterial-fungal co-infection in the immune competent hosts (10).

The lifestyle of viruses and their propagation in the host is quite different from bacteria and fungi. The viral infection initiates from membrane fusion with target cells and the delivery of their genetic materials into the host cells. These genetic materials are the main source of PAMPs to promote type I IFN production and antiviral responses. The host PRRs recognized viral DNA/RNA will activate the transcription factors to initiate immune responses as we discussed before. Unlike bacterial and fungal clearance by innate immunity, antiviral immunity is mediated by cytotoxic T cells, as part of adaptive immunity, to eliminate virus-infected cells (11). The phagocytes, like macrophages and neutrophils, are still accounted for the clearance of dead cells and viral particles, but the recruited DC and their antigen presentation to the T cells are a more potent part of innate immunity for antiviral responses (12). During bacterial, fungal, and viral infection, tissue damage can be contributed by the excesses of ROS from recruited immune cells. In addition to that, the killing of infected host cells during the viral infection also causes a significant amount of tissue injury. The tissue damage will release damage associated molecular patterns (DAMPs), which will further stimulate the immune response. At the same time, nutrient releasement, as well as binding capacity in the damage site, can provide a niche for secondary infection, in terms of superinfection as we explored in Chapter 2. During the viral infection, the robust immune responses in the innate immunity should halt the secondary bacterial/fungal infection and the aberrant growth of the commensal bacteria. However, in the post-viral environment with tissue damage as well as immune suppression in the immune resolving phase, the viral-bacterial or

viral-fungal superinfection could happen and initiate the second round of immune responses.

Immune status in the post-viral environment and their similarity/difference against secondary fungal/bacterial infections

Because of the similarity of bacterial/fungal infection and the host responses against them, there might be some overlaps of the cause of viral-bacterial or viral-fungal superinfection. The damaged lung tissue can provide binding and initiation of bacterial/fungal colonies. The immune suppression condition in the post-viral environment could reduce the pro-inflammatory responses and restrain host phagocytes for bacterial/fungal clearance. However, we found the post-viral environment (Day 6 post-viral infection) is still toward the inflammatory responses upon secondary fungal infection, in the term of anti-fungal gene transcripts (Chapter 2, Fig. 7). We found the transcripts related to inflammasome (*Nlrp3* and *Pycard*), chemokine (*Cxcl10*), chemokine receptor (*Ccr5*), genes activated by proinflammatory cytokines (*Nfkb1* and *Mapk14*) and stress response (*Ptgs2*) are significantly enhanced in the IAV-*Af* superinfection group comparing to *A. fumigatus* single infection group. On the other hand, we also found that the gene transcripts of anti-inflammation (*Il10* and *Jun*) and Th2 response (*Il2*) were downregulated in the IAV-*Af* superinfection group compared to *A. fumigatus* single infection group. These data suggested that the robust Th1 immune responses can still be found in the post-viral environment upon *A. fumigatus* infection, instead of immune suppression described in the viral-bacterial superinfection. Thus, the concept of immune suppression from the immune resolving phase in the post-viral environment might not be the case in viral-fungal superinfection. However, in our viral-fungal superinfection mice model, we still saw the fungal escape from host innate immunity in the post-viral lung environment, and all the mice in the superinfection group died at Day 5 post *A. fumigatus* inoculation (Chapter 2, Fig. 1). The proposed mechanism contributed to the increase fungal burden and host mortality in the post-viral environment is due the defective phagolysosome maturation and related fungal



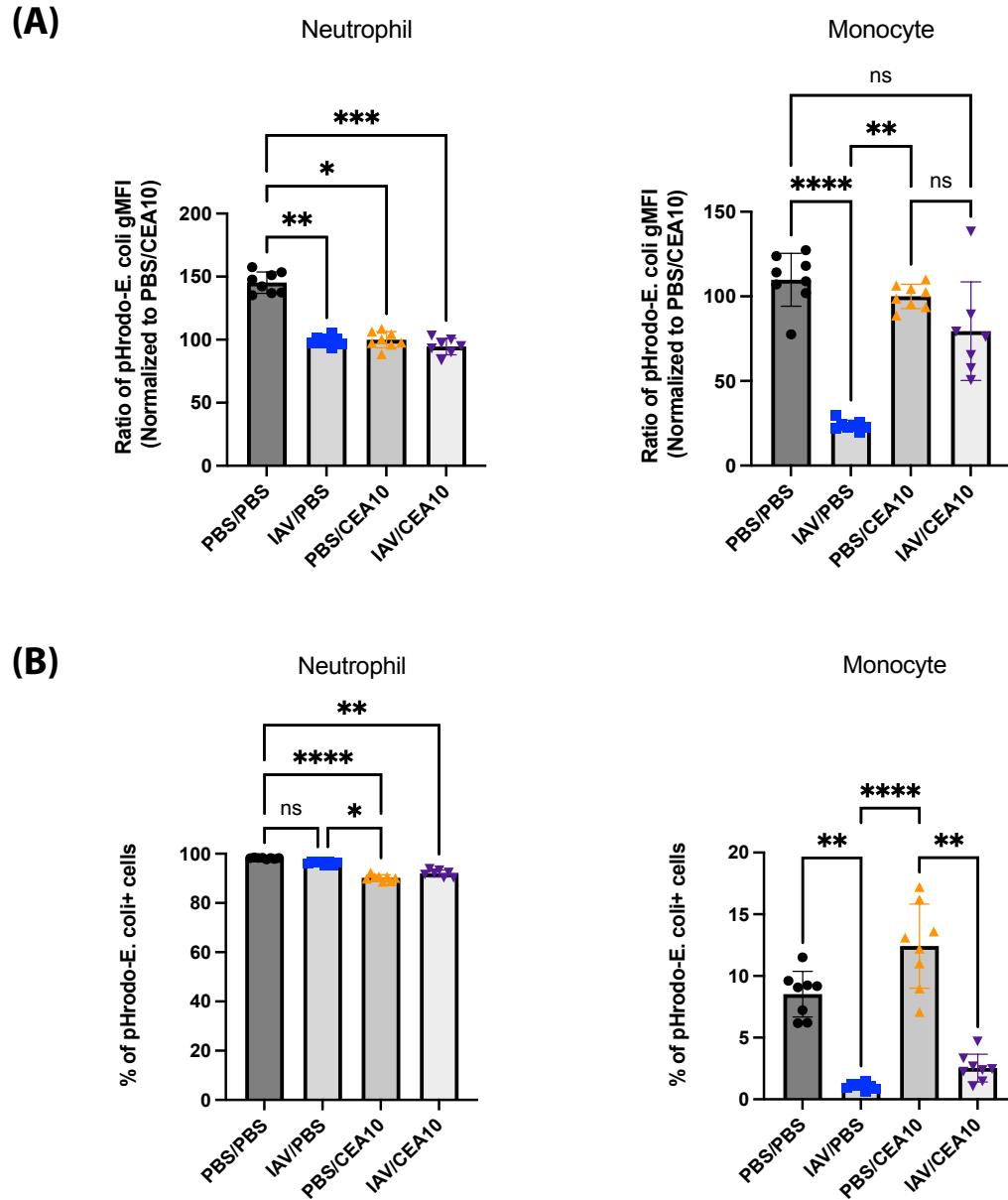
**Fig. 1 Potential signaling pathway related to immune modulation of antifungal responses in post-viral environment.**

Illustration of potential genes involved in immune regulation in the post viral environment. Genes and cell function were significant downregulated were labeled in blue. Genes shown trend to downregulation were labeled in grey. Other genes might be correlated with the signaling pathway were labeled in black.

conidial killing (Chapter 2, Fig. 6). The potential upstream signal contributes to this phenotype might come from intracellular fungal recognition, as we saw the significant transcriptional reduction of PRR (*Tlr9*), signaling component (*Irak4*), transcription factor (*Jun*) and downstream genes (*Il10* and *Tnf*) in the lung from viral-fungal superinfection group. Thus, we hypothesize that the downregulation of TLR9 signaling for fungal recognition in the phagosome in the post-viral could lead to local inflammation due to the downregulation of IL-10 and impaired immune cell function because of reduced TNF production (Chapter 4, Fig. 1). However, whether the downregulation of TLR9 signaling is leading to defective phagolysosome maturation or the decrease of phagosome acidification is contributing to reduced TLR9 signaling still require proof from future experiments. The decreased signal from other receptors might also contribute to this signaling transduction as the dectin-1 signaling can regulate TLR9 recruitment to the phagosome (13) and Fcgr shared downstream signal components with TLR9 (Chapter 4, Fig. 1).



Although the immune response upon secondary infection in a post-viral environment is different between viral-bacterial and viral-fungal superinfection, the phagocytosis process, including uptake and killing in the mature phagolysosome, is equally important for both bacterial and fungal clearance. We hypothesize that the defective phagolysosome maturation may not be specific to the uptake of zymosan from *S. cerevisiae*. To test if the defective phagolysosome maturation can also be found upon the uptake of bacteria, the neutrophils, and monocytes from PBS-treated, IAV, CEA10 single infection, and IAV/CEA10 superinfection groups were incubated with the pHrodo-*E. coli* to examine the phagolysosome maturation (Chapter 4, Fig. 2). With the neutrophils and monocytes from IAV single infection group, we saw similar defective phagolysosome maturation with pHrodo-*E. coli* staining in the post-viral environment. The equal cellular responsiveness of neutrophils and significant reduction in monocytes can also be found with the pHrodo-*E. coli* staining as the previous results with pHrodo-zymosan. These data suggest that immune modulation on phagolysosome maturation in the post-viral environment could be a conserved phenotype against secondary bacterial and fungal infection. However, the pHrodo-*E. coli* treated neutrophils from both fungus single infection and viral-fungal superinfection groups have a similar reduction of phagolysosome maturation. This is different from the neutrophils from CEA10 single infection group with pHrodo-zymosan, which have relatively normal phagolysosome maturation compared to the PBS group. This suggests neutrophils undergoing antifungal responses might lose their capacity for phagocytosis of another pathogen. Whether this is due to the temporary availability of neutrophils or the cells were actually becoming exhausted in the acute fungal infection will need more experiments to examine. Surprisingly, monocytes from a fungal single infection environment still have the capability for phagolysosome maturation with pHrodo-*E. coli*. This suggests there might be different modulations on neutrophils and monocytes as we mentioned before. With the results from pHrodo-*E. coli* staining, we found that defective phagolysosome maturation can also be found with the uptake of *E. coli* in the post-viral environment. Although the immune modulation on neutrophils and monocytes is not exactly the



**Fig. 2 Neutrophils and monocytes in the post-viral environment revealed decreased bacterial uptake.**

C57BL/6 mice were inoculated with 100 EID<sub>50</sub> of IAV or PBS at day 0 followed by  $3.4 \times 10^7$  CEA10 conidia or PBS at day 6. Mice were euthanized at 8 hours post inoculation with CEA10 or PBS for phagolysosome maturation analysis. Lung cell suspensions were incubated with pHrodo-*E. coli* for 2 hours and then stained for neutrophils and monocytes. (A) The phagolysosome maturation level was measured by the signal from the color change of pHrodo-*E. coli* in neutrophils (Ly6G<sup>+</sup>; left) and monocytes (Ly6G<sup>-</sup> SiglecF<sup>-</sup>CD11b<sup>(hi)</sup>CD64<sup>-</sup>MHC-II<sup>-</sup>; right). (B) The percentage of active cells with mature phagolysosome was measure by the percentage of cells with positive signal from the color change of pHrodo-*E. coli* in neutrophils (left) and monocytes (right). The experiment were performed once (PBS/ PBS group, n=8; IAV/PBS group, n=8; PBS/CEA10 group, n=8; IAV/CEA10 group, n =7). The Kruskal-Wallis test with Dunn's multiple comparisons was performed for statistical analyses. All error bars represent standard deviations. NS, not significant at  $P > 0.05$ ; \*,  $P \leq 0.05$ ; \*\*,  $P \leq 0.01$ ; \*\*\*,  $P \leq 0.001$ ; \*\*\*\*,  $P \leq 0.0001$ .

same, the defective bacterial clearance due to phagolysosome maturation might also be found in the viral-bacterial superinfection.

Pinocytosis is the other part of endocytosis that is without stimulation for cell activation. Thus, we hypothesize that the post-viral environment might also affect the pinocytosis and the maturation of the endosome. To test this hypothesis, neutrophils and monocytes from PBS control, IAV or CEA10 single infection, and IAV-Af superinfection groups were incubated with the pHrodo-dextran to examine the endosome maturation in the viral-fungal superinfection (Chapter 4, Fig. 3). The post-viral environment has similar regulation on the pinocytosis for monocyte population as we could see the decrease endosome maturation and cellular responsiveness with pHrodo-dextran in both viral single infection and viral-fungal superinfection groups. Interestingly, neutrophils from the post-viral environment did not have defective endosome maturation. These neutrophils were shown with higher responsiveness, which might be correlated with their role in dead cells and debris clearance during viral infection (14). On the other hand, neutrophils from fungal single infection and viral-fungal superinfection environments have an equal decrease in endosome maturation and similar responsiveness compared to the PBS control group. This might be due to neutrophil exhaustion after encountering fungal infection as we saw the decreased neutrophil responsiveness to pHrodo-zymosan in CEA10 single infection and IAV/CEA10 superinfection group (Chapter 2, Fig. S8). A similar potential exhaustion phenotype was found with additional bacteria uptake as we saw the reduction of phagolysosome maturation in neutrophils from fungal-infected mice with pHrodo-*E. coli*.

With the pHrodo-zymosan, -*E. coli* and -dextran, we showed that the post-viral environment has different modulation on neutrophils and monocytes. For the monocyte population, the post-viral environment significantly inhibits their phagocytosis and pinocytosis as we saw the decreased uptake and killing of fungal conidia in the IAV-Af model. The acute immune response to the *A. fumigatus* single infection (8 hours) did

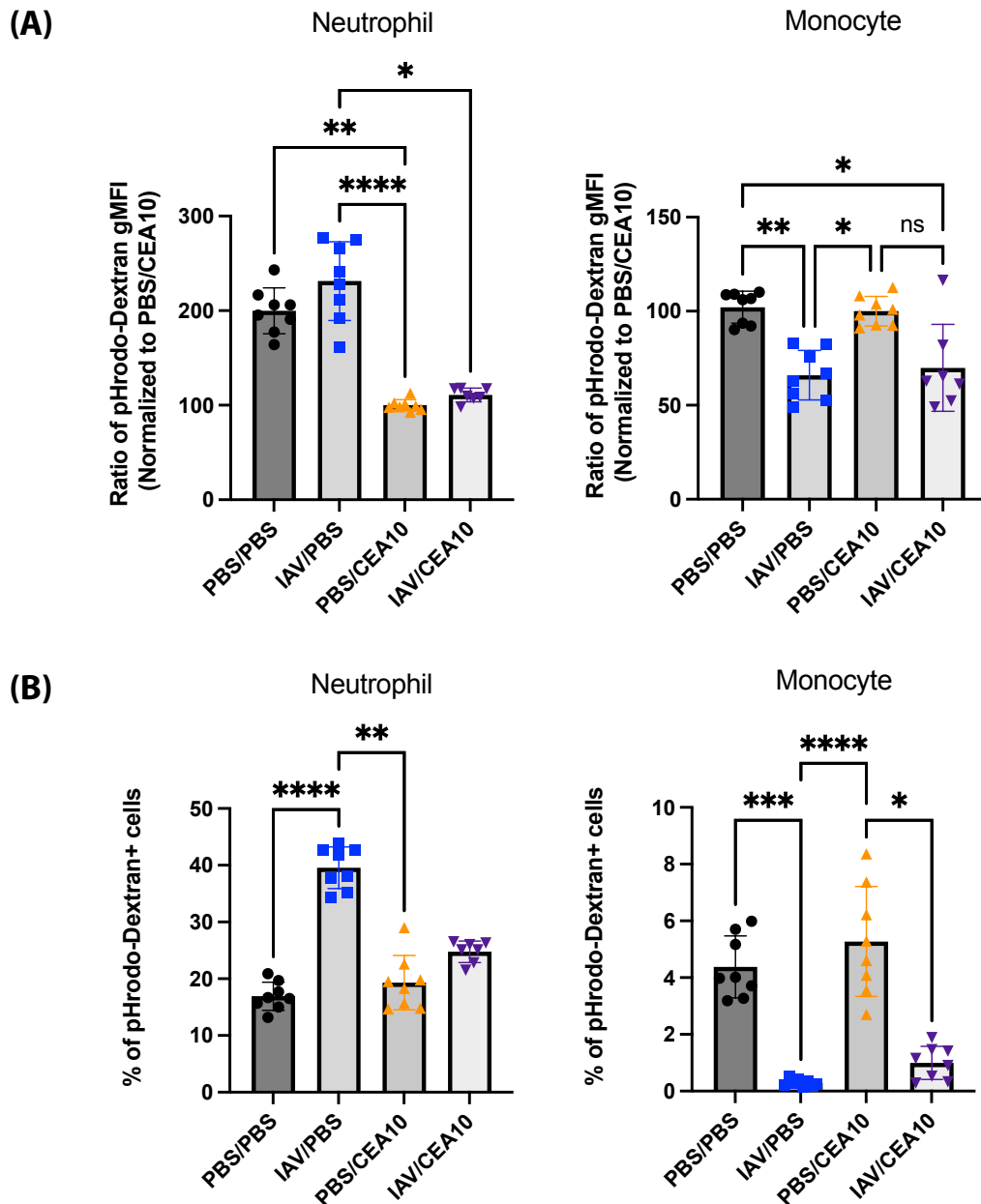


**Fig. 3 Neutrophils and monocytes in the post-viral environment revealed decreased endocytosis.**

C57BL/6 mice were inoculated with 100 EID<sub>50</sub> of IAV or PBS at day 0 followed by  $3.4 \times 10^7$  CEA10 conidia or PBS at day 6. Mice were euthanized at 8 hours post inoculation with CEA10 or PBS for phagolysosome maturation analysis. Lung cell suspensions were incubated with pHrodo-dextran for 2 hours and then stained for neutrophils and monocytes. (A) The phagolysosome maturation level was measured by the signal from the color change of pHrodo-dextran in neutrophils (Ly6G<sup>(+)</sup>; left) and monocytes (Ly6G<sup>(-)</sup> SiglecF<sup>(-)</sup>CD11b<sup>(hi)</sup>CD64<sup>(-)</sup>MHC-II<sup>(-)</sup>; right). (B) The percentage of active cells with mature phagolysosome was measure by the percentage of cells with positive signal from the color change of pHrodo-dextran in neutrophils (left) and monocytes (right). . The experiment were performed once (PBS/ PBS group, n=8; IAV/PBS group, n=8; PBS/CEA10 group, n=8; IAV/CEA10 group, n=7). The Kruskal-Wallis test with Dunn's multiple comparisons was performed for statistical analyses. All error bars represent standard deviations. NS, not significant at  $P > 0.05$ ; \*,  $P \leq 0.05$ ; \*\*,  $P \leq 0.01$ ; \*\*\*,  $P \leq 0.001$ ; \*\*\*\*,  $P \leq 0.0001$ .

not have much impact on the monocytes suggesting that the immune modulation on monocytes might be contributed by the immune suppression from the immune resolving phase in the post-viral environment. For the neutrophil population, the viral infection and fungal infection have the similar effect on their bacterial phagocytosis with the pHrodo-*E. coli* staining, which might be due to cell exhaustion. Intriguingly, neutrophils lost their responsiveness to zymosan and dextran during fungal infection but most of the neutrophils were still able to uptake *E. coli*. Thus, with different pHrodo staining, we further demonstrated that endocytosis against pathogens might be modulated in the post-viral environment. The similar and different immune modulations in the post-viral environment on endocytosis of pathogens and other materials might allow us to explore the upstream mechanism that controls the endosome maturation process.

#### Future directions for the IAV-Af superinfection model

With our IAV-Af superinfection mouse model, we showed that host immunity has similar cell recruitment and ROS production in the post-viral environment. The enhanced inflammation in the superinfection environment does not help with fungal clearance due to defective phagolysosome maturation. Besides immune modulation on antifungal cellular function in the post-viral environment, there are still many remaining questions that can be further addressed with our viral-fungal superinfection model.

**Can the phagolysosome maturation defect also be found in the viral-bacterial superinfection?** As we discussed previously, both bacterial and fungal clearance require the integration of PAMP signals from bacteria or fungi. The regulation of phagocytosis can affect bacterial clearance in the post-viral environment. Previous studies have shown that influenza infection can suppress phagocytic bacterial clearance through the inhibition of ROS production in macrophages and neutrophils (15). Overexpression of GM-CSF can alleviate viral-bacterial superinfection by enhancing macrophages and

neutrophils recruitment and ROS production specifically in macrophages (16). But these results were quite different from what we saw in our viral-fungal superinfection mice model since we saw no difference in cell recruitment as well as ROS production (Chapter 2, Fig.2 and Fig. 4) and the phagocytes with defective fungal clearance are neutrophils and monocytes instead of macrophages (Chapter 2, Fig. 3). Thus, our proposed model of ROS-independent phagocytic defect might provide a novel immune modulation in the viral-bacterial superinfection. The reduction of phagolysosome maturation with pHrodo-*E. coli* in the post-viral environment did fit with this hypothesis, but we will need bacterial viability data to further support this hypothesis.

**Why do we see different immune modulation in the viral-fungal superinfection**

**compared to viral bacterial superinfection?** In our IAV-*Af* superinfection mouse model, we saw no difference in cell recruitment and ROS production. Instead, the phagolysosome maturation defect leads to defective fungal killing and IA progression in the lung. Previous studies showed the desensitization of macrophage TLR for bacterial ligands in the post-viral environment (17). And these TLR signals are essential for ROS production and bacterial killing (18).

However, the activation of CLRs by the variety of cell wall components from fungal infection is triggering phagocytosis and ROS production in innate immunity (19). Was the phenotype due to the distinct integration of PAMP signals from fungi and bacteria? This comes to the next big question we need to address: What is/are the upstream signal(s) contributing to the phagolysosome maturation defect? The qPCR data from CEA10 single infection and IAV-*Af* superinfection mice showed a transcriptional reduction of TLR9 and other downstream signaling components. But at the same time, we saw no difference in dectin-1 expression and enhanced TLR4 and Dectin-2 expression. This could suggest the modulation might specifically rely on intracellular pathogen detection and the stimulation for the killing through phagolysosome maturation. We still need to examine the gene expression profile in the viral single infection group to further confirm if the phenotype is specific to the viral-fungal infection or if it is a conserved phenotype in the post-viral environment. Another part of

the transcriptional profile that needs further addressed is the cell type. The samples we used for the qPCR were the RNA from total lung immune cells. As we know that the majority of cell types contributing to the bulk RNA will be the neutrophils (~60%). Thus, the dataset we have shown is more likely representative of neutrophil phenotypes. Since we saw the difference between neutrophils and monocytes in the pHrodo experiments, whether we can see a similar gene expression profile in the minor monocyte population (~4%) requires further examination. A single-cell RNA sequencing data of mice with PBS treatment, IAV or CEA10 single infection and IAV/CEA10 superinfection can help to distinguish the gene expression profile in the specific cell type. The “monocyte” population we gated in our works is the  $\text{Ly6G}^{(-)}\text{CD103}^{(-)}\text{SiglecF}^{(-)}\text{CD11b}^{(\text{hi})}\text{CD64}^{(-)}\text{MHCII}^{(-)}$  cells. We did not see a similar phenotype in the  $\text{CD11b}^{(+)}\text{cDC2}$ , so there was less likelihood of contamination from DC population. However, we will need more markers (Ly6C, Cx3cr1, Ccr2, CD62L, CD43, and Trem14) to further confirm whether these monocytes are non-classical monocytes or other monocyte populations (20).

**Was the phenotype contributed by immune suppression or cell exhaustion?** The ImmGen data indicate that blood monocytes have much higher TLR9 expression than bone marrow neutrophils. The actual TLR9 expression in the lung monocytes and neutrophils requires further confirmation, but this might explain why we saw much stronger inhibition in the monocytes compared to the neutrophils. The other explanation could be the capability for dealing with multiple pathogens. The phagocytosis of innate immune cells is not infinite. After encountering certain amounts of pathogens, the cells will reach their capacity and become exhausted as shown in macrophage hypophagia (21). Unlike the cell recovery of monocyte and macrophage lineages, the short-lived neutrophils become “paralysis” once they reach their limitation (22). The neutrophils under paralysis or exhausted condition are less likely to recover and perform the functional activity for secondary pathogen encounters. In our pHrodo-zymosan experiments, more than half of the neutrophils (70% for IAV single infection,

55% for CEA10 single infection, and 60% for IAV/CEA10 superinfection) were still capable of uptaking the pHrodo-zymosan. In the pHrodo-*E. coli* experiments, over 90% of neutrophils were still capable of uptaking the pHrodo-*E. coli*. These data suggest that the neutrophils in our IAV/CEA10 model were not paralyzed or exhausted. But these phagosomes in the neutrophils were not able to have full acidification and maturation, so there should be some immune modulation upstream of phagolysosome maturation. We hypothesize that the phagocytes might miss a secondary signal (like TLR9 signal) from the phagosome to stimulate the following maturation process. To further examine the phagolysosome maturation process, we could co-stain the cells with endosome markers (Rba5, Rab7, and Lamp1) to further examine the progression of phagocytosis in the post-viral environment (23). However, the monocytes from IAV infected were almost no response to the pHrodo-zymosan, pHrodo-*E. coli* or pHrodo-dextran incubation, suggesting that these monocytes might actually be exhausted or under immune suppression in the post-viral environment. Staining the monocytes from the post-viral environment with exhaustion related marker (CD38) or exploring the genetic profile for the immune suppression target genes in the monocytes could the experiments we can try to further distinguish these two conditions (24, 25). It is interesting that acute immune response to fungal infection did not lead to defective phagolysosome maturation in monocytes, which could once again suggest that the immune modulation of the monocyte population is contributed by immune suppression in the post-viral environment.

Overall, our studies in IAV-*Af* superinfection mouse model provide some candidate pathways with key cell types in the innate immunity to examine the causes of viral-fungal superinfection. What the upstream genes/signals controlling the defect of phagolysosome maturation remain an open question for future works. To answer these questions, we really need to have a broader view of the immune modulation in the superinfection condition and the upstream signaling that contributes to the phenotypes. The similarity and difference between antifungal and antibacterial innate immunity



together with the phenotypes we found in our model versus the previous results in the viral-bacterial superinfection literature could set up the ground to move forward.

#### LysMD3 protein – does it actually bind to chitin?

The second part of the dissertation is about fungal recognition through a potential fungal recognition receptor – LysMD3. In Chapter 1, we emphasized the importance of pathogen recognition and different PRRs that are involved in bacterial, fungal, and viral detection and their downstream signalings. In Chapter 3, we showed enhanced transcripts of LysMD3 in leukocytes upon fungal infection and the LysMD3 binding to the fungal conidia and germling. However, even with enhanced expression and fungal binding ability, LysMD3 only has a very minimal effect on host antifungal innate immunity. The FLARE experiments showed that the LysMD3 deficient neutrophils and interstitial macrophages have increased intracellular conidial viability (Chapter 3, Fig. 5A and 5B). However, 13.7% and 33.22% increased intracellular fungal viability in neutrophils and iMacs in the LysMD3 KO mice compared to WT mice were not able to contribute to overall fungal viability (CFU) in the lung. In our IAV-*Af* superinfection models, there were 56.7% and 107.3% increased intracellular fungal viability in neutrophils and monocytes in the FLARE experiments and 2.27 folds increase in overall fungal viability in the lung. With such a minor difference in fungal killing, we saw no difference in mice mortality and cellularity in the lung. However, the tagged LysMD3 ectodomain (LysMD3-Fc) did show its binding to both fungal conidia and germling (Chapter 3, Fig. 7A and 7C). Based on the predicted protein structure, LysMD3 has one annotated LysM domain, which has a potential binding pocket for N-acetylglucosamine (GlcNAc) binding. However, unlike the specific binding of dectin-1 to the exposed  $\beta$ -glucan on the swollen conidia, the LysMD3-Fc did have some binding to resting conidia, which have surface hydrophobin for GlcNAc masking (Chapter 3, Fig. 7B). Also, the LysMD3-Fc binding pattern on the  $\alpha$ -glucan synthase deletion *A. fumigatus* strain was different from their  $\beta$ -glucan and chitin exposure (Chapter 3, Fig. 8). The loss of LysMD3

binding on the fungal surface of Uge3 deletion *A. fumigatus* strain is intriguing (Chapter 3, Fig. 9), but so far we don't have much clue about the LysMD3 binding target. We have some preliminary data from biochemistry approaches to study the binding of LysMD3 to chitin polymers. The previous studies suggested that human LYSMD3 can bind to chitin and  $\beta$ -glucan (26). Thus, we examined the purchased human LYSMD3 binding to a different degree of polymerization (DP) of chitin polymers through isothermal titration calorimetry (ITC) (Appendix I, Fig. 1). Based on the dissociation constant ( $K_d$ ), human LYSMD3 does have the binding ability to different sizes of chitin from DP3 to DP6, but not DP7. However, this is contradictory to the previous works as they showed the LYSMD3 binding with DP7 chitin and cytokine production with DP7 chitin stimulation (26). Another concern about the experiment is that the differential power of each titration did not have much add-up over time, indicating the weak binding between LYSMD3 and chitin. The weak binding between LYSMD3 and chitin was shown in the previous literature as most loaded LYSMD3 did not bind to the chitin beads in the column (26). Thus, human LYSMD3 might have some binding capacity to certain sizes of chitin but the binding might be relatively weak. We also aimed to produce and purify murine LysMD3 for the ITC experiments. We constructed a murine LysMD3 ectodomain with His-tag for purification and Strep-tag for Western blotting. To harvest the murine LysMD3 from the transfected cell culture (Freestyle 293 cells) supernatant, the LysMD3 constructs were made in the plasmids without (JSM490) or with (JSM675) artificial secretory peptide. We were able to harvest LysMD3 protein from both LysMD3 constructs but there was a size difference between these two constructs (Appendix I, Fig. 2A). The LysMD3 peptides without secretory peptides (JSM490) was a single band with a slight increase in size (predicted size: 27 kDa). However, the LysMD3 peptides with secretory peptides (JSM675) had two sizes of proteins, the smaller size band was close to the predicted size (32 kDa) but the larger size of the smear band was at the size around 40 kDa. The protein of LysMD3ect\_JSM490 and two sizes of LysMD3ect\_JSM675 were confirmed as our constructed proteins since they can be recognized by the anti-Strep antibody in the Western blotting (Appendix I, Fig. 2B). Interestingly, the upper

smear band of LysMD3ect\_JSM675 was the glycosylated LysMD3 and the glycosylation can be removed by the PNGase F treatment (Appendix I, Fig. 2C). Thus, we were able to harvest the purified murine LysMD3 ectodomain from the transfected cell supernatant, and we found the addition of glycosylation on the murine LysMD3 through the secretory pathway. With the purified murine LysMD3 proteins (LysMD3ect\_JSM490 and \_JSM675), we next examined their binding with chitin (DP5) through ITC experiments. Similar to human LYSMD3, both constructs of murine LysMD3 were able to show some bindings to the DP5 of chitin but the bindings were not very strong compared to differential power in the WGA-chitin binding (Appendix I, Fig. 3). Overall, both the human and murine LysMD3 did show with some chitin binding capacity comparing to WGA, fungal LysM protein ECP6 and plant chitin receptor CERK1 based on their K<sub>d</sub> value from ITC experiment (Appendix I, Table 1). But whether the LysMD3 binding we saw in Chapter 3 relied upon their chitin binding will require more experimental support. As we mentioned in the discussion of Chapter 3, LysMD3 might require other proteins to form a heterodimer for its binding to chitin since the knockdown of human LYSMD3 in epithelial cell line did reduce their response to chitin treatment with IL-8 production (26).

Besides ITC experiments, we also did the competition assays as an alternative way to test whether the LysMD3 binding to the fungal surface is through chitin recognition. We first tested if LysMD3-Fc can compete with WGA binding to the exposed chitin on the fungal surface (Appendix I, Fig. 4). The co-staining of LysMD3-Fc and WGA on the fungal germlings revealed an overlap signal at the tip of germling tube. The reduction of LysMD3-Fc and WGA signal in the co-staining group compared to single staining further supported that LysMD3-Fc and WGA were binding to the same target. We also pre-incubated LysMD3-Fc with different sizes of chitin to see if that will block their binding to the fungal surface (Appendix I, Fig. 5). Surprisingly, the pre-incubation of chitin greatly enhanced the LysMD3-Fc binding to the fungal surface. We even need to reduce the exposure time to show the different binding of LysMD3-Fc with or without

chitin pre-incubation to fungal germlings. The results from the competition assays provided us with some thoughts about LysMD3 binding. First, LysMD3 does bind to the fungal surface, specifically the area with more cell wall component exposure. The loose cell wall structures, including the tip and new forming area of the germling tube, are also the binding target for other cell wall binding materials. This may explain why we were able to see the competition between LysMD3 and WGA, but the previous LysMD3 single staining on the  $\alpha$ -glucan synthase deletion strain did not reflect their increased chitin exposure (Chapter 3, Fig. 8). Secondly, the enhanced binding to the fungal surface by the pre-incubated LysMD3 with chitin suggested that LysMD3 might have multiple binding sites for fungal surface components. If that is the case, the pre-incubation of chitin with LysMD3 might actually facilitate the LysMD3 binding to the other binding targets instead of blocking its binding to fungal surface chitin. This could explain why LysMD3 has different binding patterns on the *A. fumigatus* mutant but did not reflect a trend of the known cell wall components. However, we will need to repeat these competition experiments before we make any conclusion about LysMD3 binding target. Other competition experiments we can try will be the pre-incubation with other cell wall or ECM components, such as  $\alpha$ -glucan,  $\beta$ -glucan, GAG, or mannan, to see if any of them can block the LysMD3 binding to the fungal surface.

#### The potential role of LysMD3 in host adaptive immunity

Previous studies and our works about the in vivo role of LysMD3 in antifungal immunity were mainly focused on the early stages of *A. fumigatus* infection due to its potential function as a PRR. However, our early transcriptional study with the RNA from LysMD3 KO mice and non-littermate WT mice control at 10 hours post *A. fumigatus* inoculation showed not much difference in the gene expression in the Nanostring experiment (Appendix II, Fig. 1). The only three genes showed significant difference were IL-23a, Ccr3, and Hamp. None of them is really correlated with early innate immune responses, especially functionally related to fungal clearance by macrophages

and neutrophils. The cell type profiling based on gene expression data suggested that LysMD3 deficiency might affect T cells instead of innate immunity. Thus, instead of focusing on early immune modulation, we might want to further examine the kinetics of LysMD3 expression and find the potential timing that it might play a role in immune regulation. Because of the potential role of LysMD3 in adaptive immunity, we examined the LysMD3 KO mice with allergic bronchopulmonary aspergillosis (ABPA) model. We published a paper using serial inoculations of W72310 to induce ABPA in the mice (Appendix III). With the sensitization and sensitization with a fungal challenge, we collected blood from the LysMD3 KO mice and their littermate control to see if there was a difference in IgE production, indicating regulation of adaptive immunity in the ABPA model (Appendix II, Fig. 2). However, there was no significant difference in IgE production between LysMD3 KO and WT mice in both models. The transcriptional profiles of LysMD3 KO and WT controls with the sensitization model have also been examined by Nanostring (Appendix II, Fig. 3). There was also not much difference in transcriptional profiles between LysMD3 KO and WT controls, but we did find significantly reduced expression of allergy-related gene IL-33 in the LysMD3 KO mice. The cell type profiling also suggested that LysMD3 deficiency might affect T cells in the sensitization model. Even though we did not see much difference in IgE production from LysMD3 KO mice, we did see a significant difference in lung and spleen cellularity in the sensitization and challenge model (Appendix II, Fig. 4). There was no significant difference in the neutrophil and eosinophil numbers between LysMD3 KO and WT mice, but we found significant increase of B and T cells (CD4 T cells and CD8a T cells) in both lung and spleen from LysMD3 KO mice comparing to WT controls. Thus, the data from Nanostrings and cellularity of LysMD3 KO mice with ABPA models suggested that LysMD3 might actually play a role in adaptive immunity instead of innate immunity. Intriguingly, the role of LysMD3 in adaptive immunity might be both locally or systematically regulated since we can see an increase in T and B cells in both the lung and spleen. How does LysMD3 contribute to the increase of T and B cells and do these

regulations come from their fungal recognition ability will be an interesting future direction for the LysMD3 project.

#### The redundancy of other PPRs for antifungal immunity

As we mentioned in Chapter 3, there are seven LysM-containing proteins in the mammalian. Among all the LysM proteins, LysMD3 and LysMD4 share similar sequences with their LysM domain and transmembrane domain. Thus, it is possible that LysMD4 can have a similar function as LysMD3. We crossed the LysMD4 heterozygous mice purchased from Jackson lab to generate LysMD4 homozygous KO mice and their littermate controls. The LysMD4 KO mice and their WT controls were inoculated with CEA10 conidia as the immune-competent IA model (Appendix II, Fig. 5). The LysMD4 KO mice were able to recover from the *A. fumigatus* infection but with delayed recovery. Thus, it is possible that LysMD4 can compensate for the role of LysMD3 in the LysMD3 KO mice, and that might explain why we can see the binding capacity of LysMD3 but not much contribution to the innate immunity. We can also test if LysMD4 has a similar role as LysMD3 with the previous experimental design for LysMD3. We can examine their binding to fungi or different cell wall components with LysMD4-Fc protein. The expression of LysMD4 RNA and protein in the immune cells upon *A. fumigatus* infection can be addressed as their role in antifungal immunity. The cellularity and FLARE experiments with the LysMD4 KO mice can further address if the LysMD4 proteins can serve as a redundant receptor in the LysMD3 KO mice. We can also try the ABPA model with LysMD4 KO mice to see if we can also detect an increase of T/B cells in the lung and spleen. However, **the key experiment for the LysMD3 project will be the survival curve of LysMD3/LysMD4 double KO mice with immune competent IA model.** We are currently breeding for the LysMD3/LysMD4 double KO mice for future experiments. LysMD3 or LysMD4 single KO mice do not have any breeding issue. We were also able to cross LysMD3/LysMD4 double heterozygous mice to generate LysMD3/LysMD4 double KO mice. However, we do have a breeding issue to expand the mice colony by crossing

the male and female LysMD3/LysMD4 double KO mice. The breeding cages of male LysMD3/LysMD4 double KO mouse with either LysMD3/LysMD4 double KO or LysMD3 heterozygous/LysMD4 KO female mouse never have the new pups. At the same time, we already lost two female LysMD3/LysMD4 double KO mice when we crossed them with LysMD3 heterozygous/LysMD4 KO or LysMD3 KO/LysMD4 heterozygous male mouse. The N number of these breeding tests was low, but it could suggest that there might be fertility issues for LysMD3/LysMD4 double KO mice. The alternative breeding strategy will be breeding the LysMD3 heterozygous/LysMD4 KO mouse with LysMD3 KO/LysMD4 heterozygous mouse to avoid the potential fertility issues for LysMD3/LysMD4 double KO mice.

As we mentioned in the discussion of Chapter 3, other PRRs (TLRs or CLRs) might compensate for the deficiency of LysMD3. This compensation could be directly binding to LysMD3 target(s) to induce immune responses or their activation are already sufficient for antifungal responses, even without a LysMD3 signal. A double KO mouse with a deficiency of LysMD3 and other PRRs can be an alternative way to explore the role of LysMD3 in antifungal immunity. Among all the PRRs, TLR2 might be a good candidate. Previous reports showed that TLR2 can recognize chitin and induce antifungal immunity, including phagocytosis and cytokine production (27, 28). As the original hypothesis about the size of chitin and their induced immune responses, these chitin-induced TLR2-dependent immune responses were contributed by the large size of chitin microparticles (1-10  $\mu\text{m}$ ) or the larger chitin oligomers (DP6, DP7, and DP10-15). Instead, our ITC experiments suggested LysMD3 might bind to smaller sizes of chitin oligomers (DP3-6). Thus, the LysMD3 and TLR2 double KO mice could potentially lose their responses to the whole spectrum of different sizes of chitin.

Another future direction of the LysMD3 project could be moving out from acute innate immunity. As LysMD3 binds to smaller sizes of chitin, it is less likely that LysMD3 signaling can be stimulated during the early fungal infection. Instead, it might

contribute to the immune resolving phase or Th2 responses. We can add the chitin oligomers into the immune cell from WT or LysMD3 KO mice and examine their cytokine production. The induction of proinflammatory cytokines or immune suppression cytokines with a specific size of chitin can further support whether LysMD3 is involved in antifungal immunity or the immune resolving phase in a post-fungal environment. Another direction for the LysMD3 project could be looking for its role in stress response as it was proposed to be related to Golgi stress (29). LysMD3 could have its role in stress response during fungal infection, but detailed mechanisms or regulation require more experimental data supporting.

#### Host immunity of antifungal responses

Through the dissertation, we explored the function and regulation of host immunity with various models. The viral-fungal superinfection model demonstrated the complexity of the host innate immune response to multi microbiome environment. The experiments we perform in the studies provide qualitative and quantitative functional analysis of innate immunity against fungal infection. We performed the traditional mouse survival experiments and qualitative analysis of fungal burden and immune response with lung histology samples. To have a more quantitative analysis of the host-fungal interaction, we did various experiments with flow cytometry. The different staining panels for flow cytometry provide us with a broader view of different cell populations of innate immunity in antifungal response. The inoculation of the FLARE strain combined with cellularity in the flow cytometry experiments gives us the capability to examine antifungal immunity at the cell level. The ROS and pHrodo staining combined with cellularity in the flow cytometry experiments provide us with specific functional analysis during the fungal killing. These tools are not just specifically for the viral-fungal superinfection model but also can be applied to any other project related to antifungal or antibacterial responses. The findings of our IAV-*Af* superinfection model



could also be crucial in other superinfection models, including the recent pandemic of SARS-CoV-2.

To characterize the role of LysMD3 in host immunity, we leveraged tools for molecular studies and different animal models. The western blot with LysMD3 antibody confirmed the protein deletion in the newly generated LysMD3 KO mice line. The qPCR and Nanostring data provided thoughts about genetic regulation in both WT and LysMD3 KO mice. For the early innate immune response against fungal infection, we performed the IA models with immune-competent mice or immune-compromised mice. At the same time, we examined the chronic adaptive immune responses through APBA models with sensitization or sensitization with a fungal challenge. These models let us explore the role of LysMD3 in both innate and adaptive immunity during early fungal infection and long-term Th2 response. The purification of LysMD3 protein provides some thoughts about the modification of LysMD3 proteins. The staining of purified Fc proteins (LysMD3-Fc and Dectin-1-Fc) with *A. fumigatus* or other microbes can be used to study the cell wall composition at the conidial and germling stage. The characteristic of the role of LysMD3 in immune modulation could be important for exploring alternative fungal recognition in host immunity if we can figure out its binding target(s) and potential redundancy of other receptor proteins.

## References

1. Patel TY, Buttner M, Rivas D, Cross C, Bazylnski DA, Seggev J. 2018. Variation in airborne fungal spore concentrations among five monitoring locations in a desert urban environment. *Environ Monit Assess* 190.
2. Muhammad MH, Idris AL, Fan X, Guo Y, Yu Y, Jin X, Qiu J, Guan X, Huang T. 2020. Beyond Risk: Bacterial Biofilms and Their Regulating Approaches. *Front Microbiol* 11.
3. Kostakioti M, Hadjifrangiskou M, Hultgren SJ. 2013. Bacterial biofilms: development, dispersal, and therapeutic strategies in the dawn of the postantibiotic era. *Cold Spring Harb Perspect Med* 3.
4. Talapko J, Juzbašić M, Matijević T, Pustijanac E, Bekić S, Kotris I, Škrlec I. 2021. *Candida albicans*- The Virulence Factors and Clinical Manifestations of Infection. *J Fungi (Basel)* 7:1–19.
5. Taubitz A, Bauer B, Heesemann J, Ebel F. 2007. Role of respiration in the germination process of the pathogenic mold *Aspergillus fumigatus*. *Curr Microbiol* 54:354–360.
6. Baltussen TJH, Zoll J, Verweij PE, Melchers WJG. 2019. Molecular Mechanisms of Conidial Germination in *Aspergillus* spp. *Microbiol Mol Biol Rev* 84.
7. Ayala A, Chung CS, Grutkoski PS, Song GY. 2003. Mechanisms of immune resolution. *Crit Care Med* 31.
8. Wynn TA, Vannella KM. 2016. Macrophages in Tissue Repair, Regeneration, and Fibrosis. *Immunity* 44:450–462.
9. Blanpain C, Fuchs E. 2014. Stem cell plasticity. Plasticity of epithelial stem cells in tissue regeneration. *Science* 344.
10. Zhao Z, Song J, Yang C, Yang L, Chen J, Li X, Wang Y, Feng J. 2021. Prevalence of Fungal and Bacterial Co-Infection in Pulmonary Fungal Infections: A Metagenomic Next Generation Sequencing-Based Study. *Front Cell Infect Microbiol* 11.
11. Hope JL, Bradley LM. 2021. Lessons in antiviral immunity. *Science* 371:464–465.
12. Summerfield A, McCullough KC. 2009. Dendritic Cells in Innate and Adaptive Immune Responses against Influenza Virus. *Viruses* 1:1022–1034.

13. Khan NS, Kasperkovitz P v., Timmons AK, Mansour MK, Tam JM, Seward MW, Reedy JL, Puranam S, Feliu M, Vyas JM. 2016. Dectin-1 Controls TLR9 Trafficking to Phagosomes Containing  $\beta$ -1,3 Glucan. *J Immunol* 196:2249–2261.
14. Kolaczowska E, Kubes P. 2013. Neutrophil recruitment and function in health and inflammation. *Nat Rev Immunol* 13:159–175.
15. Sun K, Metzger DW. 2014. Influenza infection suppresses NADPH oxidase-dependent phagocytic bacterial clearance and enhances susceptibility to secondary methicillin-resistant *Staphylococcus aureus* infection. *J Immunol* 192:3301–3307.
16. Subramaniam R, Barnes PF, Fletcher K, Boggaram V, Hillberry Z, Neuenschwander P, Shams H. 2014. Protecting against post-influenza bacterial pneumonia by increasing phagocyte recruitment and ROS production. *J Infect Dis* 209:1827–1836.
17. Didierlaurent A, Goulding J, Patel S, Snelgrove R, Low L, Bebien M, Lawrence T, van Rijt LS, Lambrecht BN, Sirard JC, Hussell T. 2008. Sustained desensitization to bacterial Toll-like receptor ligands after resolution of respiratory influenza infection. *J Exp Med* 205:323–329.
18. West AP, Brodsky IE, Rahner C, Woo DK, Erdjument-Bromage H, Tempst P, Walsh MC, Choi Y, Shadel GS, Ghosh S. 2011. TLR signalling augments macrophage bactericidal activity through mitochondrial ROS. *Nature* 472:476–480.
19. Tang J, Lin G, Langdon WY, Tao L, Zhang J. 2018. Regulation of C-Type Lectin Receptor-Mediated Antifungal Immunity. *Front Immunol* 9.
20. Han S, Zhuang H, Arja RD, Reeves WH. 2022. A novel monocyte differentiation pattern in pristane-induced lupus with diffuse alveolar hemorrhage. *Elife* 11.
21. Pinney JJ, Rivera-Escalera F, Chu CC, Whitehead HE, Vandermeid KR, Nelson AM, Barbeau MC, Zent CS, Elliott MR. 2020. Macrophage hypophagia as a mechanism of innate immune exhaustion in mAb-induced cell clearance. *Blood* 136:2065–2079.
22. Hong CW. 2017. Current Understanding in Neutrophil Differentiation and Heterogeneity. *Immune Netw* 17:298–306.
23. Kinchen JM, Ravichandran KS. 2008. Phagosome maturation: going through the acid test. *Nat Rev Mol Cell Biol* 9:781–795.
24. Pradhan K, Yi Z, Geng S, Li L. 2021. Development of Exhausted Memory Monocytes and Underlying Mechanisms. *Front Immunol* 12.

25. Kiefer J, Zeller J, Bogner B, Hörbrand IA, Lang F, Deiss E, Winninger O, Fricke M, Kreuzaler S, Smudde E, Huber-Lang M, Peter K, Woollard KJ, Eisenhardt SU. 2021. An Unbiased Flow Cytometry-Based Approach to Assess Subset-Specific Circulating Monocyte Activation and Cytokine Profile in Whole Blood. *Front Immunol* 12.
26. He X, Howard BA, Liu Y, Neumann AK, Li L, Menon N, Roach T, Kale SD, Samuels DC, Li H, Kite T, Kita H, Hu TY, Luo M, Jones CN, Okaa UJ, Squillace DL, Klein BS, Lawrence CB. 2021. LYSMD3: A mammalian pattern recognition receptor for chitin. *Cell Rep* 36.
27. Davis S, Cirone AM, Menzie J, Russell F, Dorey CK, Shibata Y, Wei J, Nan C. 2018. Phagocytosis-mediated M1 activation by chitin but not by chitosan. *Am J Physiol Cell Physiol* 315:C62–C72.
28. Fuchs K, Cardona Gloria Y, Wolz O, Herster F, Sharma L, Dillen CA, Täumer C, Dickhöfer S, Bittner Z, Dang T, Singh A, Haischer D, Schlöffel MA, Koymans KJ, Sanmuganantham T, Krach M, Roger T, le Roy D, Schilling NA, Frauhammer F, Miller LS, Nürnberger T, LeibundGut-Landmann S, Gust AA, Macek B, Frank M, Gouttefangeas C, dela Cruz CS, Hartl D, Weber AN. 2018. The fungal ligand chitin directly binds TLR2 and triggers inflammation dependent on oligomer size. *EMBO Rep* 19.
29. Serebrenik Y v., Hellerschmied D, Toure M, López-Giráldez F, Brookner D, Crews CM. 2018. Targeted protein unfolding uncovers a Golgi-specific transcriptional stress response. *Mol Biol Cell* 29:1284–1298.

# Appendix I

Biochemistry property of LysMD3 proteins

Ko-Wei Liu, Andreia Isabel Ferreira Verissimo, Fangfang Zhong, Ekaterina V Pletneva,  
and Robert A. Cramer

This Appendix contains data as the additional results from Chapter 3 and figures for  
discussion in Chapter 4.

KWL designed and performed the experiments, analyzed the results, and wrote the  
manuscript.

AIV helped with the protein purification.

FFZ and EVP designed and performed the ITC experiments, and analyzed the results.

RAC designed the experiments, analyzed the results, and wrote the manuscript.

**Abstract**

The conserved annotated LysM domain suggested that human and murine LysMD3 can bind to N-acetylglucosamine (GlcNAc), which is the building block for chitin and peptidoglycan. The previous works showed that human LYSMD3 can bind to chitin oligomers with the degree of polymerization (DP) 5 and 7, as well as chitin beads. However, even with the sequence similarity between human and murine LysMD3, the binding of murine LysMD3 to different sizes of chitin oligomers has not been addressed. Here we harvested and purified murine LysMD3 proteins (LysMD3ect-JSM490, LysMD3ect-JSM675, and LysMD3-Fc) from the transfected cell line. The purchased human LYSMD3 and our purified LysMD3 (LysMD3ect-JSM490 and LysMD3ect-JSM675) were shown with binding capacity with different sizes of chitin, which have similar dissociation constant ( $K_d$ ) as WGA and LysM proteins in the literature. The co-staining of murine LysMD3-Fc and WGA suggested that they might have a similar binding site on the fungal surface. Interestingly, the pre-incubation of LysMD3-Fc with different sizes of chitin can strongly enhance their binding to the fungal surface. These results support our hypothesis that LysMD3 can bind to chitin and potentially contribute to their fungal binding capacity.

## Results

### Human LYSMD3 can bind to specific sizes of chitin

Previous experiments done by Xin He *et al.* showed that human LYSMD3 can bind to different sizes of chitin by ELISA-based assays. Here we collaborated with Fangfang Zhong and Ekaterina V Pletneva with purchased human LYSMD3 and different degree of polymerizations (DPs) of chitin with isothermal titration calorimetry (ITC). The PBS with DP5 chitin was done as a negative control as no heat was released from the titration (Fig. 1A). The human LYSMD3 showed their binding capacity with DP3 chitin ( $K_d:38\pm14.6\mu M$ ), DP4 chitin ( $K_d:409\pm203\mu M$ ), DP5 chitin ( $K_d:30.7\pm32.2\mu M$ ), and DP6 chitin ( $K_d:116\pm90.2\mu M$ ) (Fig. 1B-1E). Based on the dissociation constant ( $K_d$ ) value, human LYSMD3 has a stronger binding with DP3 and DP5 chitin and weaker binding with DP4 and DP6 chitin. In contrast to the ELISA-based binding shown in the previous literature, human LYSMD3 showed no binding to DP7 chitin based on the ITC result (Fig. 1F). Note that we were able to calculate the  $K_d$  from the differential power with LYSMD3 and chitin binding, but the value was kind of low, indicating the weak binding between LYSMD3 and different sizes of chitin.

### Murine LysMD3 is glycosylated through the secretory pathway

We harvested and purified murine ectodomain of LysMD3 (LysMD3ect) from a transfected cell line (FreeStyle™ 293-F Cells) with protein construct without (JSM490) or with (JSM675) artificial secretory peptide. The proteins were purified from supernatant of transfected cells through the Ni column and size-exclusive column S200. The purified LysMD3ect-JSM490 showed a single band with slightly bigger size than its prediction (27 kDa) (Fig. 2A). Interestingly, the purified LysMD3ect-JSM675 from the secretory pathway has a lower band with predicted size (32 kDa), and a smear upper band (Fig. 2A). Both constructs, including the smear band in the LysMD3ect-JSM675 group, were confirmed as our LysMD3 proteins by the recognition of anti-Strep antibody to our tagged proteins (Fig. 2B). The smear band of LysMD3ect-JSM675 was confirmed to be the glycosylated proteins as we can reverse the protein size back to the predicted

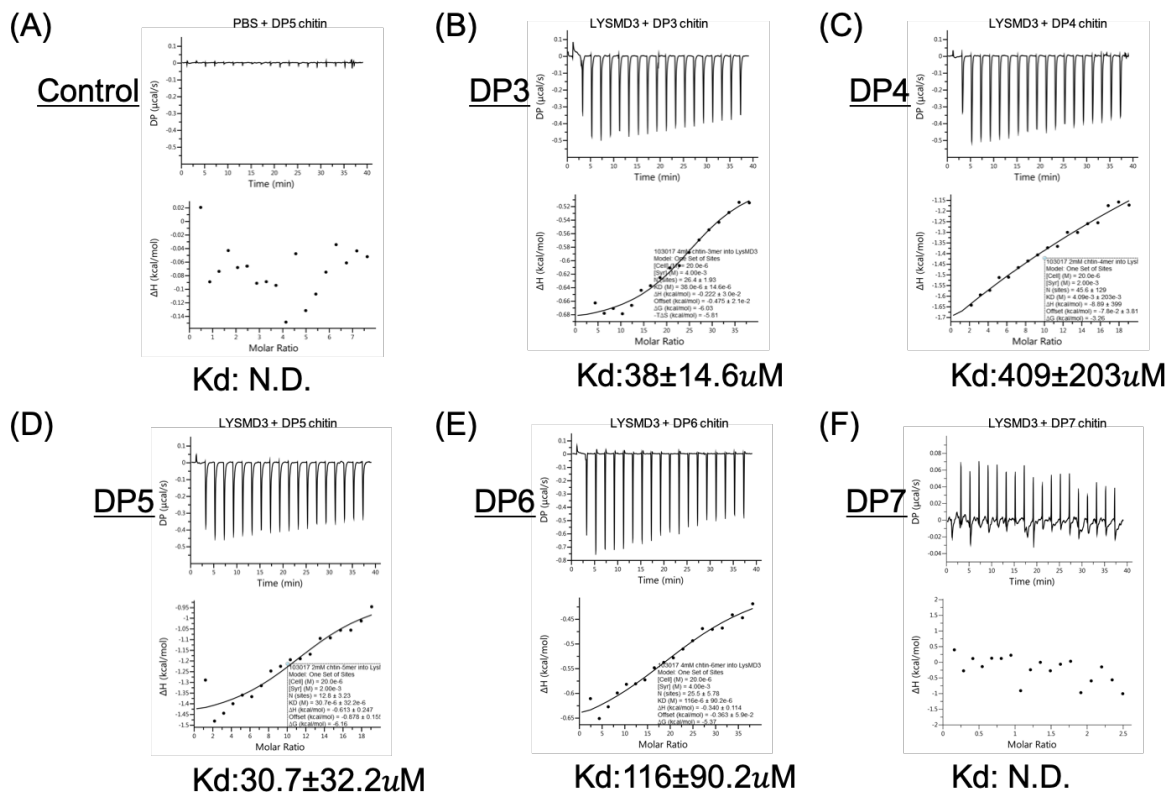
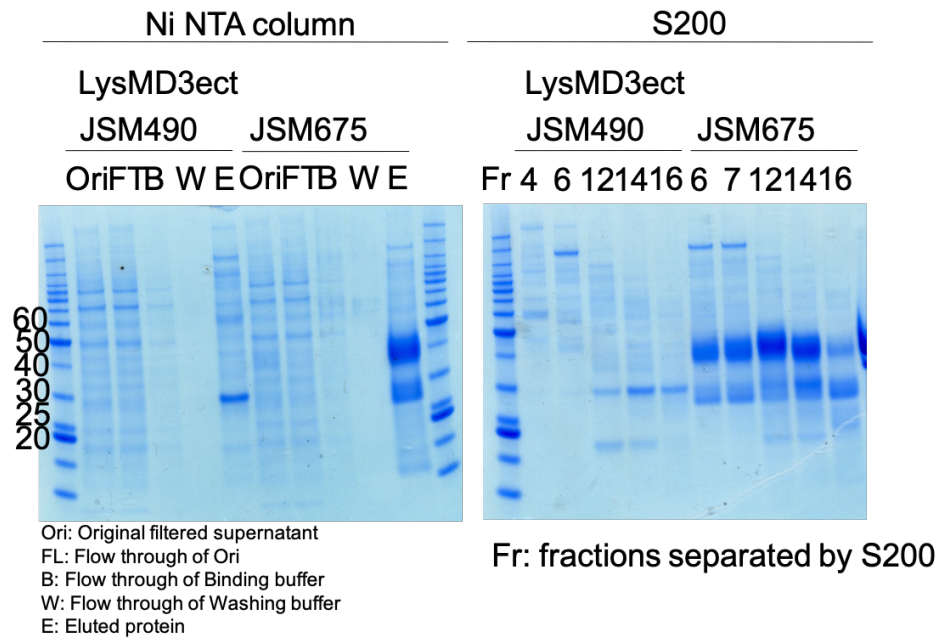


**Fig. 1 Human LYSD3 showed their binding to specific size of chitin**

The binding of human LYSD3 with different degree of polymerization (DP) of chitin was examined by isothermal titration calorimetry (ITC). The differential power (DP ( $\mu\text{cal/s}$ ); Top) of each group was measured by their energy release to the medium (PBS). The binding curve (Bottom) of each group was calculated based on the differential power with unit of energy release per second ( $\mu\text{cal/s}$ ) measured at each time point. The binding of LYSD3 to chitin was shown with their dissociation constant (Kd) in the unit of concentration ( $\mu\text{M}$ ). The differential power and binding curve were shown for (A) PBS with DP5 chitin as negative control. (B) LYSD3 with DP3 chitin. (C) LYSD3 with DP4 chitin. (D) LYSD3 with DP5 chitin. (E) LYSD3 with DP6 chitin. (F) LYSD3 with DP7 chitin. The experiments were performed once. N.D.: not determined

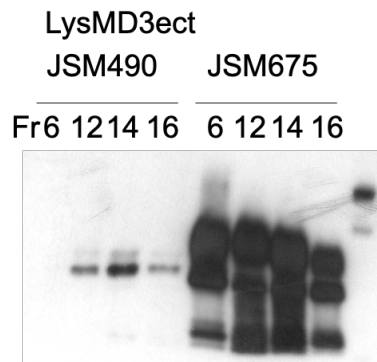


(A)



(B)

Anti-strep Ab



(C)

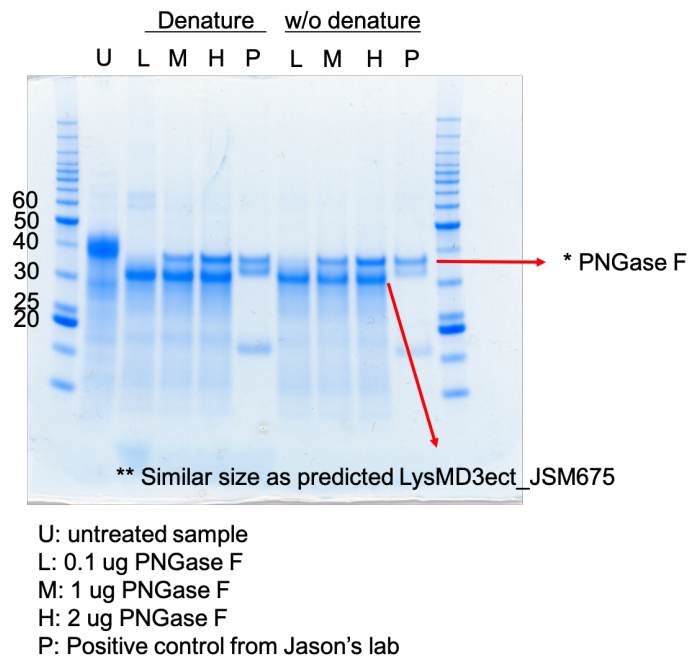


**Fig. 2 Murine LysMD3 protein received glycosylated modification through secretory pathway.**

Freestyle 293 cells were transfected with plasmids containing murine LysMD3 ectodomain fused with 6 His tags and Strep tag without secretory peptide (JSM490; predicted size: 27 kDa) or with secretory peptide (JSM675; predicted size: 32 kDa). (A) Fractions of samples with different purification steps were ran with SDS PAGE and stained with coomassie blue to show the sizes of proteins. Samples before and after passing through column with Ni-NTA His-Bind Resin was shown on the left. Ori: Original filtered supernatant. FL: Flow through of Ori. B: Flow through of Binding buffer. W: Flow through of Washing buffer. E: Eluted protein. Eluted proteins from Ni-NTA column were further separated by their sizes through size exclusive column (S200) and shown on the right. (B) Purified LysMD3 without or with secretory peptide were stained with anti-strep antibody for Western Blotting. (C) Purified LysMD3-JSM675 was treated with different concentrations of PNGase F under denature (10% SDS and 1M DTT) or without denature condition. The treated proteins were ran with SDS PAGE and stained with coomassie blue to show the sizes of proteins. U: untreated sample. L: 0.1  $\mu$ g PNGase F. M: 1  $\mu$ g PNGase F. H: 2  $\mu$ g PNGase F. P: Positive control from PNGase F digestion. \* the upper band was the loaded PNGase F protein. \*\* the lower band was with similar size as the predicted LysMD3ect\_JSM675 (32 kDa). The experiment was performed once.

lower band with PNGaseF treatment (Fig. 2C). Thus, we confirmed that we can harvest purified ectodomain of murine LysMD3 from our two constructs, and the LysMD3 through secretory pathway was shown to have the glycosylation modification.

Both glycosylated and non-glycosylated murine LysMD3 can bind to chitin

To test if our newly purified murine LysMD3 proteins can bind to the chitin, we performed the ITC experiments with the DP5 chitin, which has the strongest binding potential based on the  $K_d$  value. As we saw previously, PBS with DP5 chitin as a negative control showed no energy release from binding (Fig. 3A). When we used Wheat germ agglutinin (WGA), a known chitin-binding lectin, we can detect the binding to DP5 chitin through ITC ( $K_d$ :  $201 \pm 847 \mu M$ ) (Fig. 3B). Both the non-glycosylated (LysMD3ect-JSM490) and glycosylated (LysMD3ect-JSM675) form of the LysMD3 also showed their binding to DP5 chitin (LysMD3ect-JSM490:  $K_d$ :  $159 \pm 402 \mu M$ ; LysMD3ect-JSM675:  $K_d$ :  $51.3 \pm 52.6 \mu M$ ) (Fig. 3C and 3D). Based on the  $K_d$  value, both LysMD3 proteins have similar binding

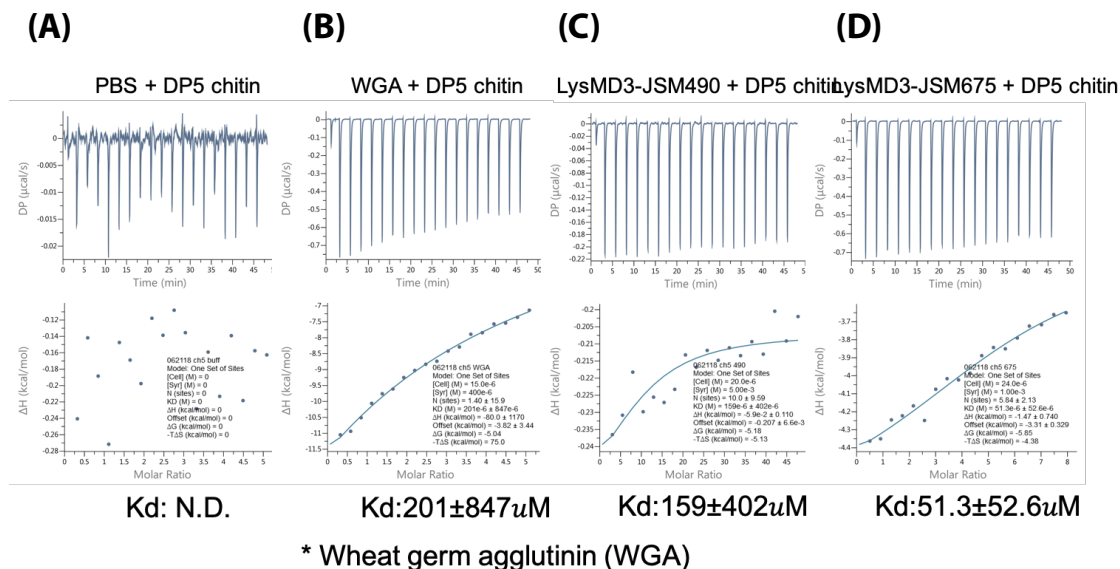


### Fig. 3 Murine LysMD3 also showed their binding to specific size of chitin

The binding of murine LysMD3 with different degree of polymerization (DP) of chitin was examined by isothermal titration calorimetry (ITC). The differential power (DP (μcal/s); Top) of each group was measured by their energy release to the medium (PBS). The binding curve (Bottom) of each group was calculated based on the differential power with unit of energy release per second (μcal/s) measured at each time point. The binding of LysMD3 to chitin was shown with their dissociation constant (Kd) in the unit of concentration (μM). The differential power and binding curve were shown for (A) PBS with DP5 chitin as negative control. (B) Wheat germ agglutinin (WGA) with DP5 chitin as positive control. (C) LysMD3-JSM490 with DP5 chitin. (D) LysMD3-JSM675 with DP5 chitin. The experiments were performed once. N.D.: not determined.

affinity to DP5 chitin as WGA, and glycosylated LysMD3 has stronger binding affinity than the non-glycosylated form. Note that the binding between both murine LysMD3 proteins with DP5 chitin is also weak compared to WGA, based on the differential power at each titration. Based on the ITC experiments, we showed both human and murine LysMD3 can bind to different sizes of chitin with reasonable  $K_d$  value compared to known chitin-binding lectin and LysM proteins (Table 1), but the small change of the differential power at each titration suggests that the binding between LysMD3 and chitin is not very strong.

#### Murine LysMD3 can compete with the WGA binding on the fungal surface

For the ITC experiments, we showed that murine LysMD3 has the binding capacity to chitin, which is one of the major components in the fungal cell wall. Our LysMD3-Fc construct also showed its binding to the fungal surface (Chapter 3, Fig. 7). We next aim to examine if LysMD3 can compete for the fungal surface binding with WGA. As we saw in previous LysMD3-Fc staining, LysMD3-Fc can bind to the loosed structure at the tip of *A. fumigatus* germling (Fig. 4A). We can see the co-localized signals from LysMD3-Fc and WGA binding on the fungal surface, suggesting that they might have similar binding sites (Fig. 4A). Next we examined if co-staining of LysMD3-Fc and WGA can reduce their binding signal comparing to single staining due to the competition for fungal surface binding. Through the quantification of confocal imaging, we can detect the significant reduction of both LysMD3-Fc and WGA signal in the co-staining compared to single staining (Fig. 4B and 4C). These results further support our hypothesis that LysMD3 can bind to the fungal surface through their chitin recognition.

#### Murine LysMD3 with Chitin incubation revealed enhanced binding to the fungal surface

Due to the chitin capacity of LysMD3 and their competition with WGA on the fungal surface, we next aim to examine if the pre-occupied murine LysMD3 chitin binding pocket can diminish their binding to the fungal surface. We pre-incubated the LysMD3-Fc with different sizes of chitin overnight and applied them for fungal staining

(A)

Samples	Kd ( $\mu$ M)
hLysMD3+DP3	38
hLysMD3+DP4	409
hLysMD3+DP5	30.7
hLysMD3+DP6	116
hLysMD3+DP7	n.d.

(B)

Samples	Kd ( $\mu$ M)
mLysMD3-JSM490+DP5	159
mLysMD3-JSM675+DP5	51.3
WGA+DP5	201

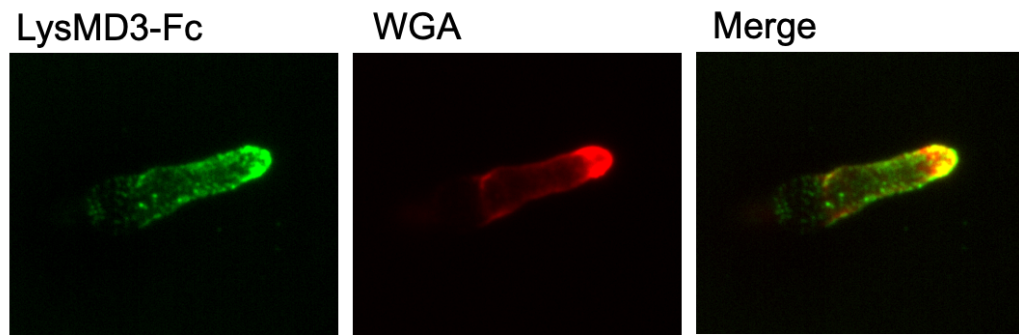
(C)

Samples	Kd ( $\mu$ M)
ECP6+DP4	11.5
ECP6+DP5	8.6
ECP6+DP6	6.4
ECP6+DP8	3.7
CERK1+DP8	455

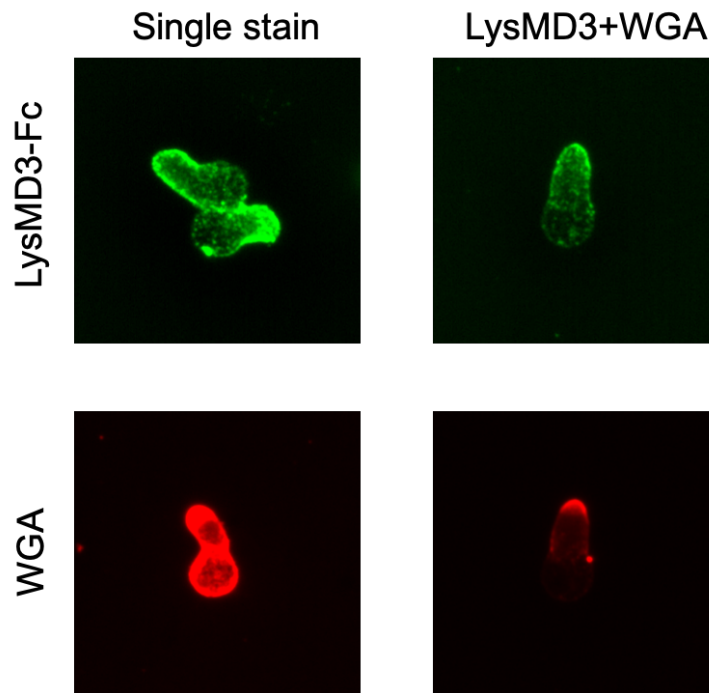
**Table 1. Human and murine LysMD3 proteins shows different binding affinities to different sizes of chitin oligomers.**

Dissociation constant (Kd) from isothermal titration calorimetry (ITC) experiments for the binding between chitin and (A) human LysMD3, (B) murine LysMD3, wheat germ agglutinin (WGA) and (C) fungal/plant LysM proteins from the literatures were shown in each table.

(A)



(B)



(C)

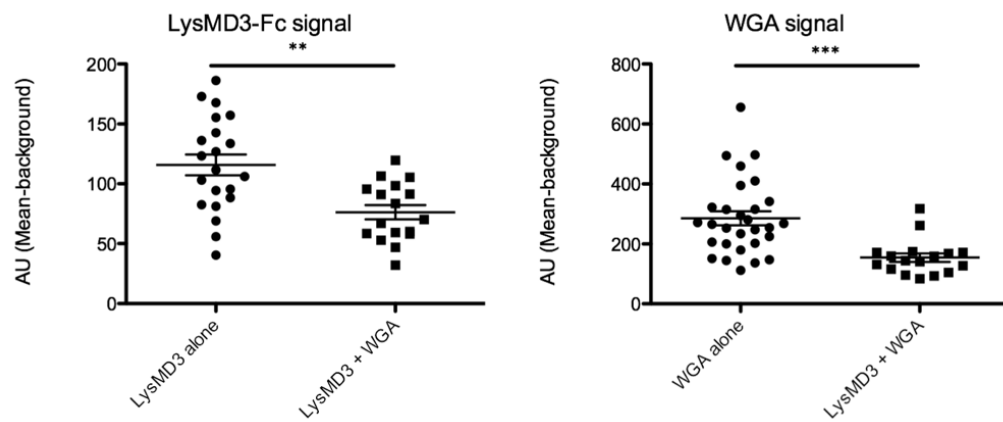


**Fig. 4 Competitive binding between LysMD3-Fc and WGA on the fungal surface**

CEA10 conidia was grown in LGMM at 37 °C 14 hours for germlings. CEA10 germlings were stained with LysMD3-Fc and wheat germ agglutinin (WGA) to examine their competitive binding to fungal surface. The samples were staining with (A) co-localization of LysMD3-Fc and WGA signal in the co-staining samples. (B) Confocal images of single staining with either LysMD3-Fc (Left, top) or WGA (Left, bottom) or co-staining group with their signals from either LysMD3-Fc (Right, top) or WGA (Right, bottom). (C) Quantification of LysMD3-Fc (Left) and WGA (Right) signals were shown in the single staining and co-staining groups. The corrected total cell fluorescence was calculated for individual germling. The experiment was performed once. Mann-Whitney, with single comparisons were performed. All error bars represent standard deviations. NS, not significant at  $P > 0.05$ ; \*  $P \leq 0.05$ ; \*\*  $P \leq 0.01$ ; \*\*\*  $P \leq 0.001$ ; \*\*\*\*  $P \leq 0.0001$ .

as previously. However, we surprisingly found that we need to reduce the exposure time on the confocal microscope from 100 ms to 20 ms to avoid signal saturation in the chitin pre-incubated groups. The LysMD3-Fc pre-incubated with DP2-DP6 chitin showed an enhanced LysMD3-Fc signal on the fungal surface (Fig. 5A). If we compare the enhancement of LysMD3 binding with different sizes of chitin, the DP3, DP5, and DP6 chitin had significant enhanced LysMD3 binding signal on the fungal surface comparing to DP2 and DP4 chitin (Fig. 5B). In summary, our LysMD3-Fc staining results showed that occupied chitin binding pocket in the LysMD3-Fc with chitin oligomers can enhance the LysMD3 binding to the fungal surface and the enhancement might be related to sizes of chitin.

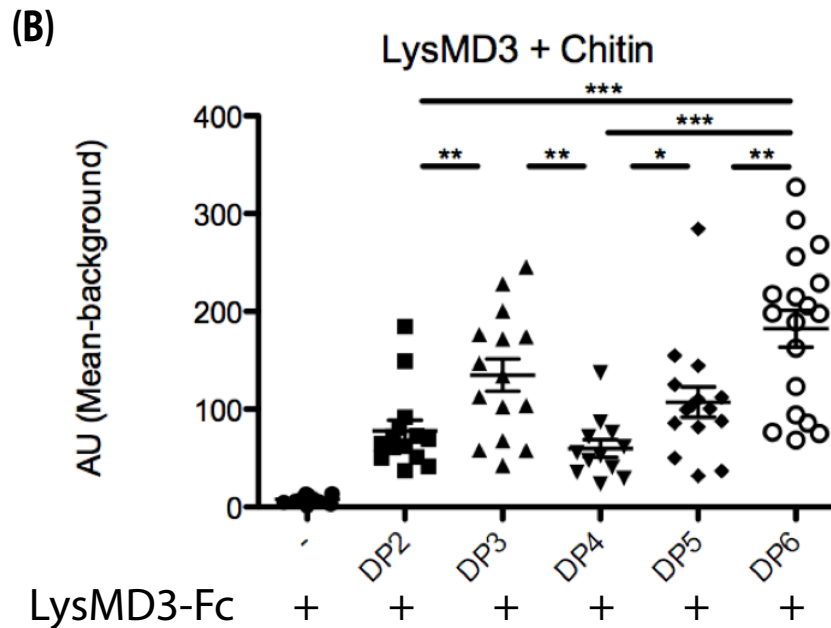
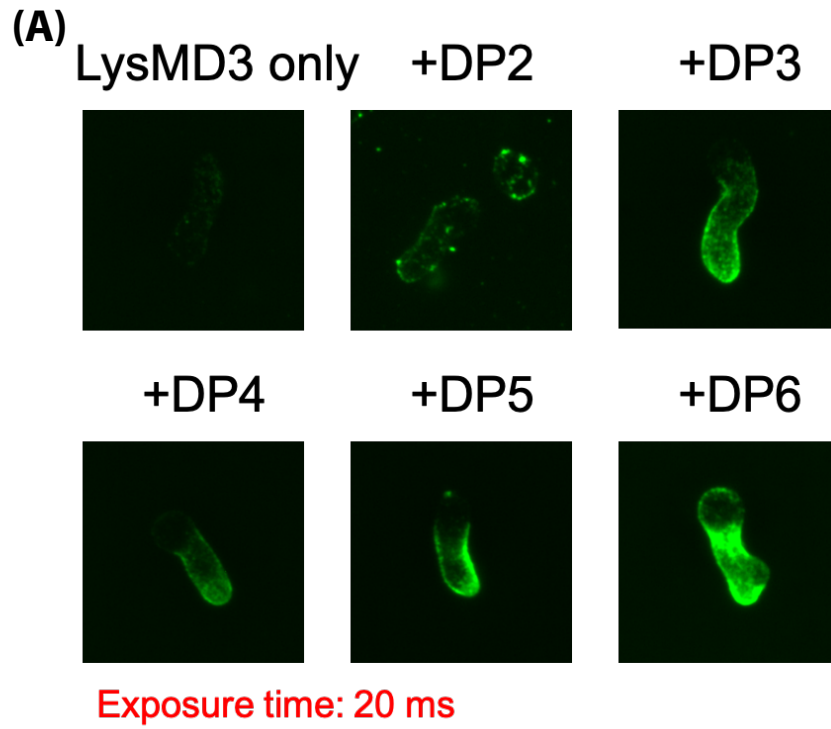


**Fig. 5 Chitin enhanced LysMD3 binding to the fungal surface.**

LysMD3-Fc was pre-incubated with different sizes of chitin at 4°C overnight. CEA10 conidia was grown in LGMM at 37 °C 14 hours for germlings. The CEA10 germlings were stained with the mixtures of LysMD3-Fc and chitin. Note that the exposure time was reduced from 100 ms to 20 ms in this experiment due to high intensity of the enhanced LysMD3 signaling in the chitin pretreated group. (A) confocal images of CEA10 germlings with the staining of LysMD3 alone or pre-incubated with different degree of polymerization (DP) of chitin. (B) Quantification of LysMD3-Fc binding on the fungal surface. The corrected total cell fluorescence was calculated for individual germling. The experiment was performed once. Mann-Whitney, with single comparisons were performed. All error bars represent standard deviations. NS, not significant at  $P > 0.05$ ; \*  $P \leq 0.05$ ; \*\*  $P \leq 0.01$ ; \*\*\*  $P \leq 0.001$ ; \*\*\*\*  $P \leq 0.0001$ .



## **Materials and Methods**

### Human LYSMD3 and Chitin oligomers

Human LYSMD3 was purchased from GenScript and reconstituted in PBS. Different sizes of chitin oligomers (DP2, DP3, DP4, DP5, DP6, DP7) were purchased from OligoTech and reconstituted in PBS.

### Harvest of murine LysMD3 proteins

FreeStyle™ 293-F Cells were incubated at 37°C until confluence according to the manufacturer's instruction (Gibco). The cells were transfected with two LysMD3 protein constructs (LysMD3ect-JSM490 and -JSM675) with a concentration of 0.5 mg plasmid/L Cell culture. At Day 5 post transfection, cell supernatant was harvested and transferred to the Ni-NTA Column containing HisPur Ni-NTA Superflow Agarose. After the flow-through of the cell supernatant, the Ni-NTA column was washed with Binding buffer (20 mM Tris, pH 8.0; 20 mM imidazole, pH 8.0; 300 mM NaCl) and Wash buffer (20 mM Tris, pH 8.0; 50 mM imidazole, pH 8.0; 300 mM NaCl). The proteins were eluted with Elution buffer (20 mM Tris, pH 8.0; 250 mM imidazole, pH 8.0; 300 mM NaCl) and loaded into size exclusive column (S200) for further separation by protein sizes. Protein samples from different purification steps were run with SDS-PAGE and stained with GelCode Blue Safe Protein Stain. LysMD3ect-JSM675 (2.5  $\mu$ g) was treated with 0.1, 1, and 2  $\mu$ g PNGaseF with or without denature condition (10% SDS and 1M DTT) at 37°C for 12 hours.

### Isothermal Titration Calorimetry (ITC)

All experiments were performed at 25°C using MicroCal ITC instrument. All the samples ran with PBS. As the negative control, DP5 chitin (800  $\mu$ M) was added to PBS. For human LYSMD3 with different sizes of chitin, the concentrations were used as follows: DP3 chitin (4000  $\mu$ M) with human LYSMD3 (20  $\mu$ M); DP4 chitin (2000  $\mu$ M) with human LYSMD3 (20  $\mu$ M); DP5 chitin (2000  $\mu$ M) with human LYSMD3 (20  $\mu$ M); DP6 chitin (4000  $\mu$ M) with human LYSMD3 (20  $\mu$ M); DP7 chitin (400  $\mu$ M) with human LYSMD3 (30

μM). For different murine LysMD3 constructs and WGA with chitin, the concentrations were used as follows: DP5 chitin (400 μM) with WGA (15 μM); DP5 chitin (5000 μM) with LysMD3ect-JSM490 (20 μM); DP5 chitin (1000 μM) with LysMD3ect-JSM675 (24 μM).

#### Competition for fungal cell wall staining

CEA10 conidia were grown in LGMM at 37 °C 14 hours for germlings. For LysMD3 and WGA co-staining, the germlings were stained with 0.5 μg/ml of LysMD3-Fc or WGA as previously described (Chapter 3; Materials and methods). For chitin pre-incubation, 0.5 μg/ml LysMD3-Fc was pre-incubated with 9 μM of different sizes of chitin (DP2, DP3, DP4, DP5, and DP6) at 4°C overnight. The mixture of LysMD3-Fc and chitin was then used for germling staining. The samples were mounted with Prolong Diamond Antifade Mountant (Thermofisher) and sealed with clear nail polish. Images were acquired using an Andor W1 spinning disk confocal microscope mounted with a Nikon Eclipse Ti inverted microscope stand. Images were viewed and analyzed using Fiji Software. The corrected total cell fluorescence for confocal images was calculated as “Integrated Density - (Area of selected cell \* Mean fluorescence of background readings)”.

## Appendix II

Additional animal models of LysMD3/LysMD4 KO mice

Ko-Wei Liu, and Robert A. Cramer

This Appendix contains data as the additional results from Chapter 3 and figures for discussion in Chapter 4.

KWL designed and performed the experiments, analyzed the results, and wrote the manuscript.

RAC designed the experiments, analyzed the results, and wrote the manuscript.

## Abstract

Our LysMD3-Fc binding experiments revealed that LysMD3 can recognize fungal surfaces. However, previous studies and our animal experiments showed that LysMD3 KO mice have no *in vivo* phenotype in the invasive aspergillosis (IA) model. The nature of small sizes chitin oligomers (DP3, DP4, DP5, DP6) binding by LysMD3 suggested that LysMD3 might be involved in immune modulation post initial fungal clearance. Here we examined the transcriptomic profile of LysMD3 KO mice at early fungal infection in the IA model and chronic Allergic bronchopulmonary aspergillosis (ABPA) model. Both data suggested that LysMD3 KO mice might have different genetic profiles that affect T cell populations. With our previously established ABPA model, we showed that LysMD3 KO mice did not affect IgE production but have increasing T and B cell populations. In addition to regulation in adaptive immunity, we also found a delayed recovery from *A. fumigatus* infection in the LysMD4 KO mice, which suggests that LysMD4 might play a role in antifungal immunity. These additional animal experiments provide additional hints for the future direction of the LysMD3 project.

## Results

### LysMD3 KO mice have similar gene expression profiles during IA

In our previous results, LysMD3 KO mice have similar cell recruitment and mortality in the IA model (Chapter 3, Fig. 4 and 6). At the same time, the LysMD3 deficient neutrophils and interstitial macrophages (iMacs) had slightly defective fungal killing but were not sufficient to contribute to overall fungal viability. Here we examined the immune-related gene expression profile by the Nanostring at 10 hours post *A. fumigatus* inoculation to see if LysMD3 has immune modulation for antifungal immunity. In this data set, we saw only three genes (*Il23*, *Ccr3*, and *Hamp*) that were significantly different in the LysMD3 KO mice compared to the WT group (Fig. 1A). The expression of IL-23 can support the survival of myeloid cells for antifungal immunity (1). *Ccr3* is expressed in eosinophils, basophils, mast cells, epithelial cells, and T cells (2–6). And the expression of *Ccr3* is correlated with allergy responses (7, 8). The *Hamp* gene encodes for hepcidin, which is induced by the systemic iron level and inflammation responses. The function of hepcidin is known for its role in iron homeostasis but the infection-induced hepcidin also acts as an antimicrobial peptide (9). Based on the gene expression profile, the potential difference of immune modulation in the LysMD3 KO mice was shown with the highest correlation with the T cell population (Fig. 1B). These Nanostring data showed that there was not much difference in gene transcripts related to immune responses in LysMD3 KO mice. The potential gene regulation in the T cells suggests that LysMD3 might play a role in adaptive immunity.

### LysMD3 KO mice have similar IgE production in the ABPA model

Because of the potential immune modulation in T cells in LysMD3 KO mice and the recognition of small sizes of chitin oligomers by LysMD3 protein, we next applied our LysMD3 KO mice to our recently established ABPA mouse model (Appendix III). In short, we inoculated  $10^7$  W72310 conidia at day 0, 7, 8, 9, 10, and 11 as the ABPA sensitization model and one additional challenge at day 14 as the ABPA sensitization plus challenge model (Fig. 2). We euthanized the mice at day 12 and day 15 for the two

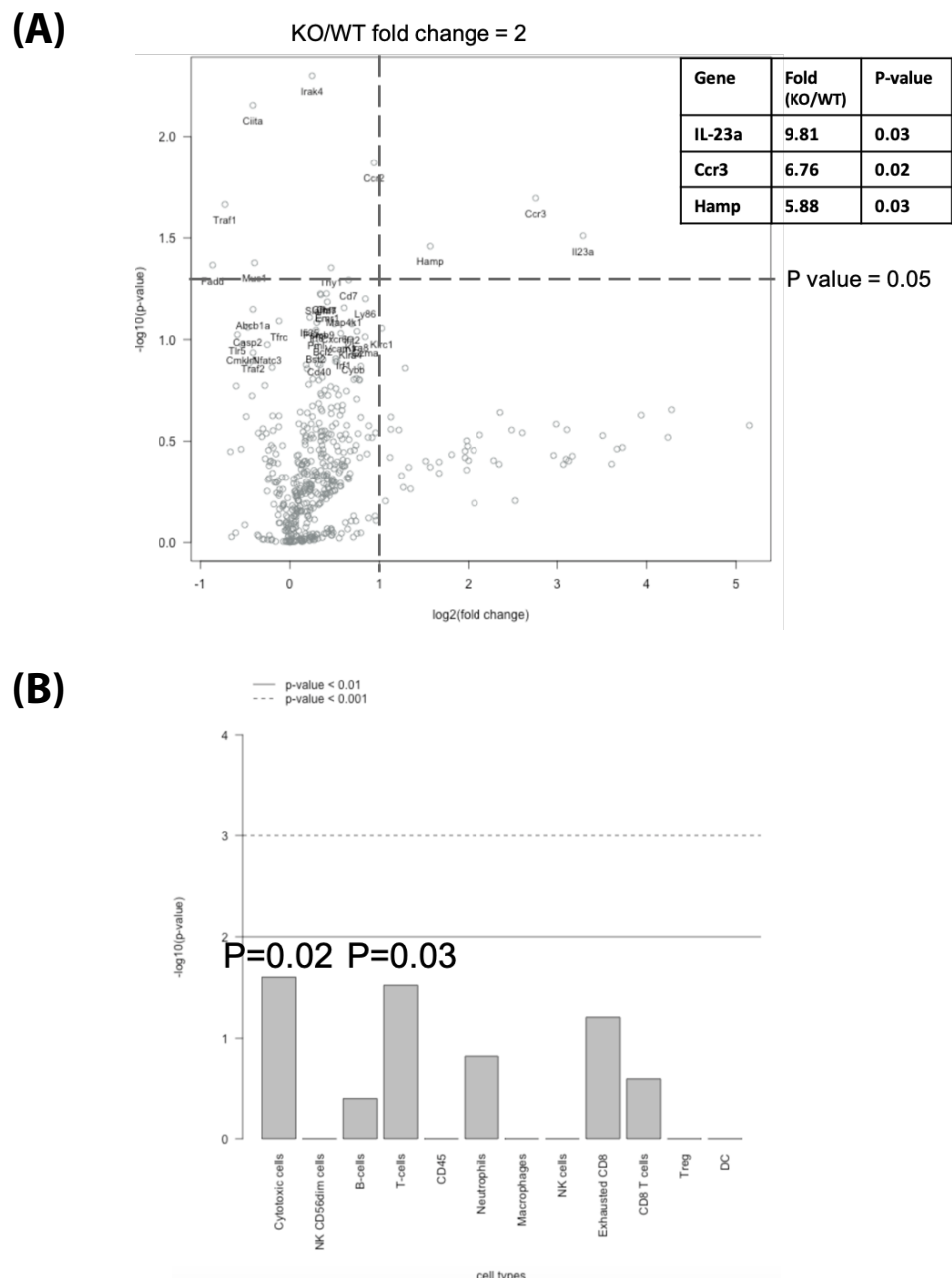


**Fig. 1 LysMD3 KO mice revealed similar gene expression profile comparing to WT mice in the IA model**

WT (n=3) or LysMD3 KO (n=3) C57BL/6 mice with  $7 \times 10^7$  CEA10 conidia with immune competent mice model. Note that the WT mice were purchased from Jackson lab instead of littermate control from LysMD3 KO mice breeding. Mice were euthanized at 10 hours post-inoculation with CEA10 for immune gene transcript analysis. Immune related gene transcript levels were measured by Nanostring with RNA from total lung. (A) A volcano plot shows the distribution of fold changes of immune related gene transcript levels in the LysMD3 KO mice compared to the WT mice group. The P value threshold of 0.05 (Welch's t-test) and fold change threshold of 2 were indicated by the lines in the plot. Table listed the three genes with significant difference and fold change >2. (B) Cell type profiling based on gene expression data in the Fig. 1A. The experiment was performed once. Heteroscedastic t-test (Welch's), with single comparisons were performed.

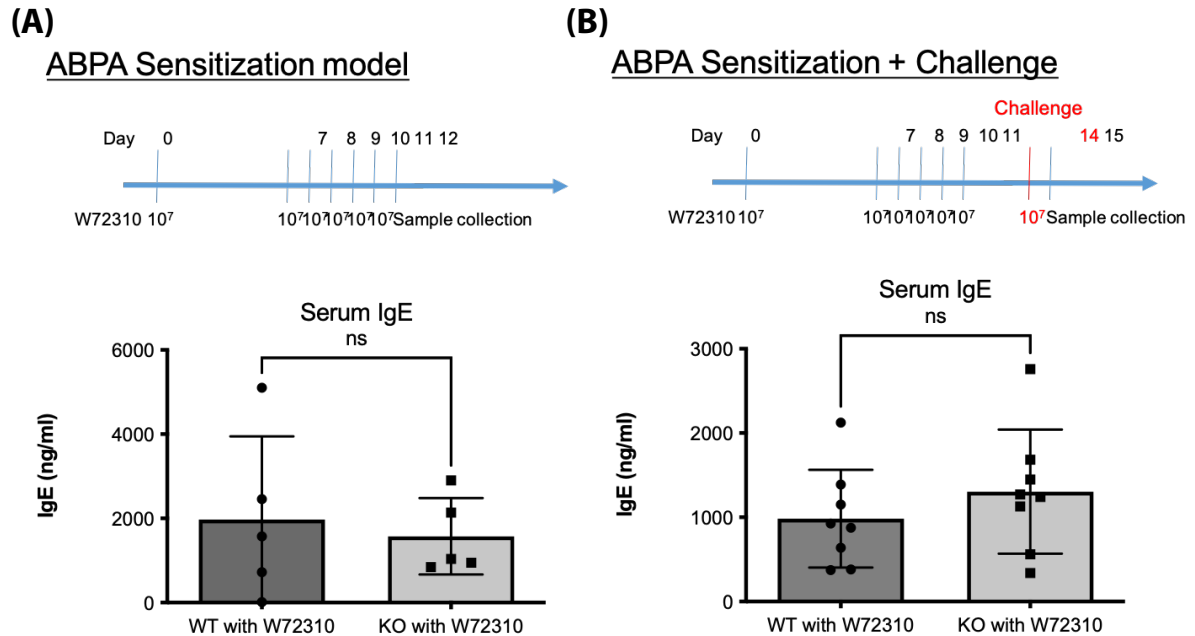


**Fig. 2 No significant difference of IgE production in the ABPA model between WT and KO mice.**

WT or LysMD3 KO C57BL/6 mice were inoculated with W72310 conidia for allergic bronchopulmonary aspergillosis (ABPA) mouse model. Blood samples were collected at day 12 or day 15 for IgE quantification by ELISA. (A) For ABPA Sensitization mice model, WT (n=5) or LysMD3 KO (n=5) C57BL/6 mice were inoculated with  $10^7$  W72310 conidia at day 0, 7, 8, 9, 10 and 11. Mice were euthanized at day 12 post initial W72310 inoculation. (B) For ABPA Sensitization mice model with fungal challenge, WT (n=8) or LysMD3 KO (n=8) C57BL/6 mice were inoculated with  $10^7$  W72310 conidia at day 0, 7, 8, 9, 10, 11 and extra challenge at day 14. Mice were euthanized at day 15 post initial W72310 inoculation. The experiment was performed once. Mann-Whitney, with single comparisons were performed. All error bars represent standard deviations. NS, not significant at  $P > 0.05$ ; \*  $P \leq 0.05$ ; \*\*  $P \leq 0.01$ ; \*\*\*  $P \leq 0.001$ ; \*\*\*\*  $P \leq 0.0001$ .

models and harvested the blood to examine the IgE production. The ELISA results showed that in both sensitization and sensitization plus challenge models, LysMD3 KO mice still produce a similar amount of IgE (Fig. 2).

#### LysMD3 KO mice have similar gene expression profiles during ABPA

Even though we saw similar IgE production in our ABPA models, we next aimed to see if there was a difference in genetic profiles between LysMD3 KO and WT mice. The RNA was extracted from the ABPA sensitization mouse model and applied to Nanostring for immune gene profiles in LysMD3 KO mice. As shown in the volcano plot, most of the genes were shown with similar expression levels between LysMD3 KO and WT mice (Fig. 3A). The top three genes with a significant difference between LysMD3 KO and WT mice were *Cul9*, *Il33*, and *Cxcr3*. The *Cul9* gene is encoded for a putative E3 ligase related to genome integrity and tumor suppression (10, 11). IL-33 signaling can suppress IL-17/IL-22 during fungal infection and promote Th2 cytokines for allergy responses (12–14). *Cxcr3* signaling in pDCs can promote fungal killing by neutrophils (15). At the same time, *Cxcr3* is highly expressed in T cells and correlated to their trafficking and activation (16, 17). Similar to the cell modulation in the IA model, LysMD3 KO mice in the ABPA model also showed a potential immune modulation in the T cell population (Fig. 3B). Thus, LysMD3 KO mice with the ABPA model also did not show much difference in gene transcripts of immune responses. However, the decrease in *Il-33* and potential regulation in T cell populations suggest that LysMD3 might affect the T cell population in the ABPA model.

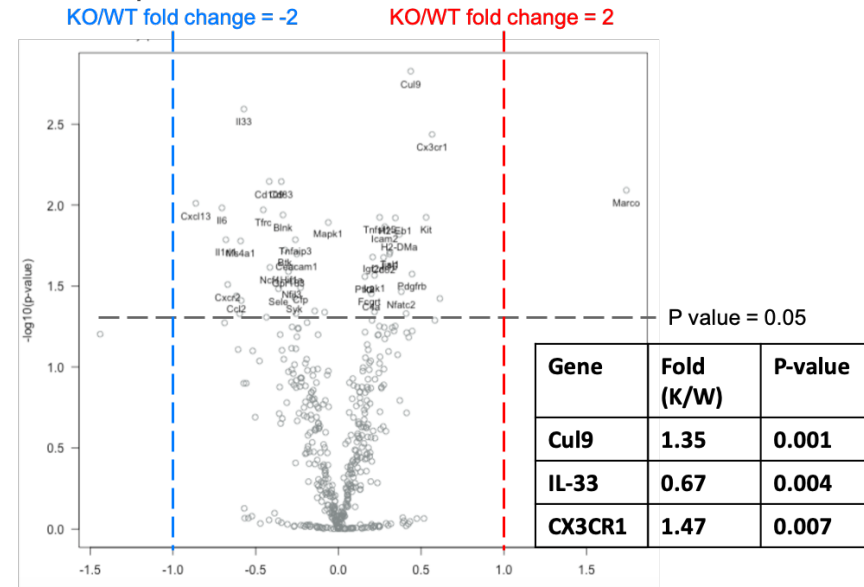
#### LysMD3 KO mice showed both local and systematic increases of T and B cells in the ABPA model

Although we did not see a difference in IgE production between LysMD3 KO and WT mice in our ABPA model, the Nanostring data in both IA and ABPA models suggested that there might be immune modulation in T cells. Thus, we examined the cellularity in the lung and spleen with our sensitization plus challenge ABPA model (Fig.



(A)

### Volcano plot



(B)

### Cell type profiling

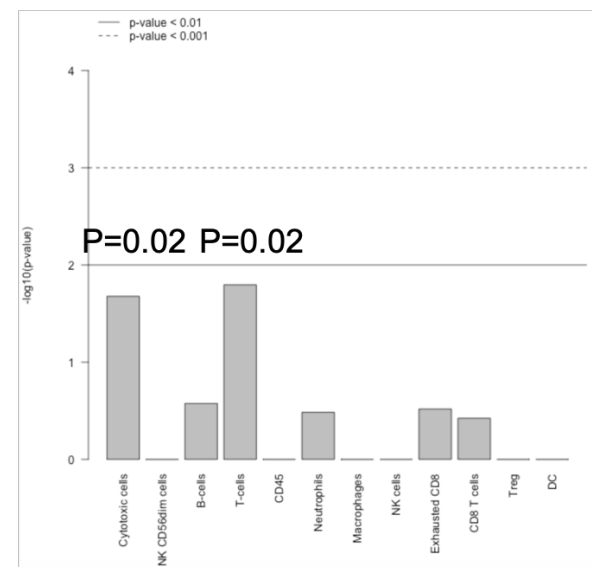


**Fig. 3 LysMD3 KO mice revealed similar gene expression profile comparing to WT mice in the ABPA model.**

For ABPA Sensitization mice model, WT (n=3) or LysMD3 KO (n=3) C57BL/6 mice were inoculated with  $10^7$  W72310 conidia at day 0, 7, 8, 9, 10 and 11. Mice were euthanized at day 12 post initial W72310 inoculation for immune gene transcript analysis. Immune related gene transcript levels were measured by Nanostring with RNA from total lung. (A) A volcano plot shows the distribution of fold changes of immune related gene transcript levels in the LysMD3 KO mice compared to the WT mice group. The P value threshold of 0.05 (Welch's t-test) and fold change threshold of 2 (labeled with red) or -2 (labeled with blue) were indicated by the lines in the plot. Table listed the top three genes with most significant difference. (B) Cell type profiling based on gene expression data in the Fig. 4A. The experiment was performed once. Heteroscedastic t-test (Welch's), with single comparisons were performed.

4). We saw no difference in cell recruitment for neutrophils and eosinophils in bronchoalveolar Lavage (BAL) and lung (Fig. 4C and 4D). Although there were no difference in total CD45<sup>(+)</sup> cells, we saw a significant increase of B cells and T cells (CD4<sup>(+)</sup> and CD8a<sup>(+)</sup> T cells) in the lung (Fig. 4A, 4E-4H). For the splenocytes, we can detect a significant increase of CD45<sup>(+)</sup> cells, which was mainly contributed by the increase of B cells and T cells (CD4<sup>(+)</sup> and CD8a<sup>(+)</sup> T cells) (Fig. 4A, 4E-4H). Thus, although we did not see a functional difference in IgE production in our ABPA model with LysMD3 KO mice, the cellularity data showed that LysMD3 might affect the B/T cell recruitment to the lung and spleen.

#### LysMD4 KO mice can recover from *A. fumigatus* infection but with delayed recovery

Human and murine LysMD3 and LysMD4 share high similarity in their LysM domain, which suggests that there might be functional redundancy between these two LysM receptor proteins (18). To examine if LysMD4 deficient mice are susceptible to fungal infection, we purchased the LysMD4<sup>+/-</sup> mice for Jackson Lab. We cross-breed the LysMD4<sup>+/-</sup> mice to obtain the LysMD4 KO mice and their littermate WT controls and tested their mortality with our immune competent IA model. Both the LysMD4 KO and WT mice were able to survive the acute *A. fumigatus* infection, but we saw a delayed weight recovery in the LysMD4 KO mice (Fig. 5). This might suggest that the LysMD4 KO mice also have some minor defects in fungal clearance, similar to what we saw in the LysMD3 KO mice.

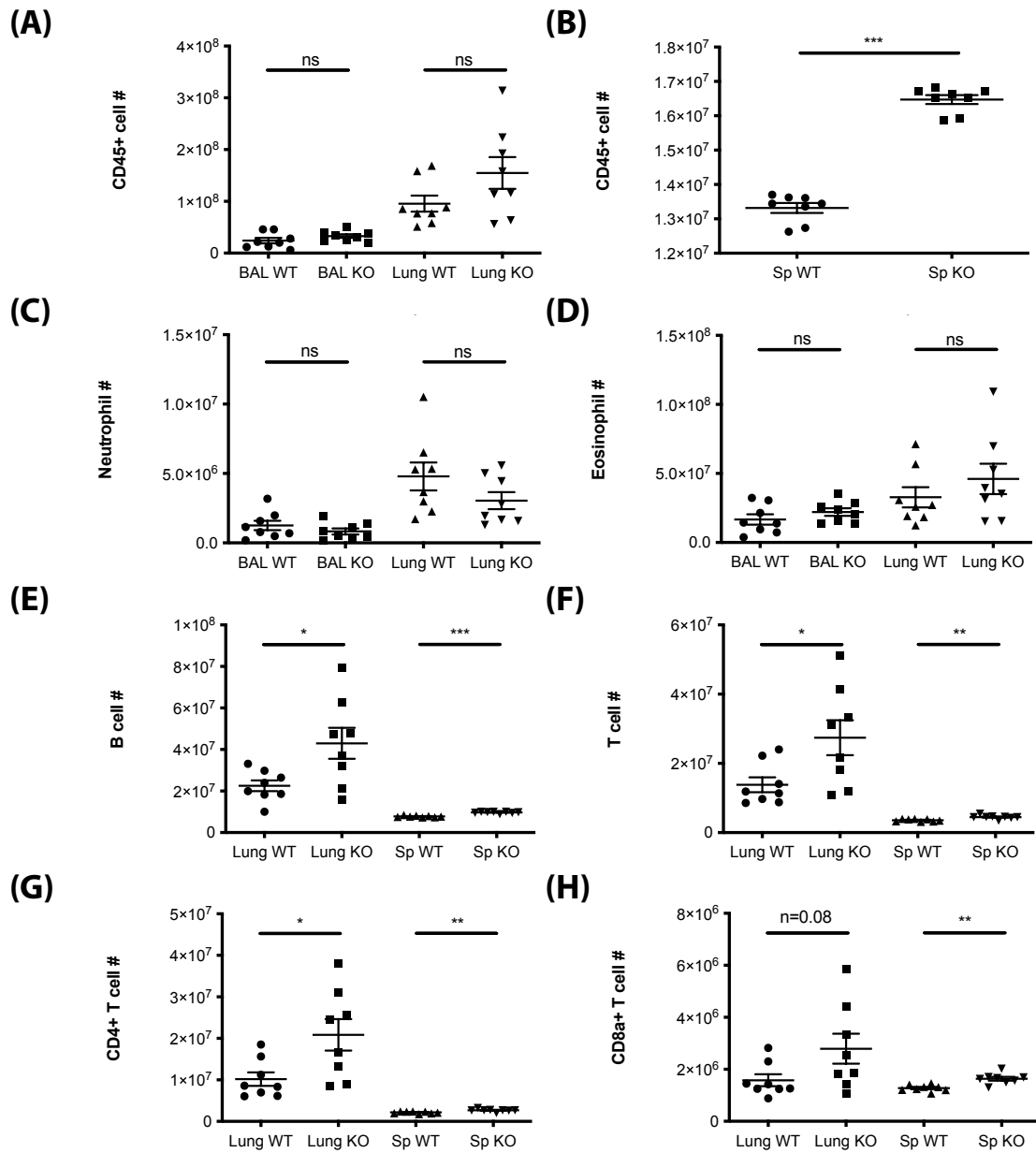


**Fig. 4 Challenged LysMD3 KO mice have more T/B cells in both lung and spleen comparing to WT mice in the ABPA model.**

For ABPA Sensitization mice model with fungal challenge, WT (n=8) or LysMD3 KO (n=8) C57BL/6 mice were inoculated with  $10^7$  W72310 conidia at day 0, 7, 8, 9, 10, 11 and extra challenge at day 14. Mice were euthanized at day 15 post initial W72310 inoculation for lung and spleen cellularity experiments. All lung cell numbers were acquired by flow cytometry as indicated: (A) CD45<sup>(+)</sup> cells in BAL and lung. (B) CD45<sup>(+)</sup> cells in spleen. (C) Neutrophils (CD45<sup>(+)</sup> SiglecF<sup>(-)</sup> Ly6G<sup>(+)</sup>) in BAL and lung. (D) Eosinophils (CD45<sup>(+)</sup> SiglecF<sup>(-)</sup> Ly6G<sup>(-)</sup> CD11c<sup>(-)</sup>) in BAL and lung. (E) B cells (CD45<sup>(+)</sup> CD19<sup>(+)</sup> CD3<sup>(-)</sup>) in lung and spleen. (F) Total T cells (CD45<sup>(+)</sup> CD19<sup>(-)</sup> CD3<sup>(+)</sup>) in lung and spleen. (G) CD4<sup>(+)</sup> T cells (CD45<sup>(+)</sup> CD19<sup>(-)</sup> CD3<sup>(+)</sup> CD4<sup>(+)</sup> CD8a<sup>(-)</sup>) in lung and spleen. (H) CD8a<sup>(+)</sup> T cells (CD45<sup>(+)</sup> CD19<sup>(-)</sup> CD3<sup>(+)</sup> CD4<sup>(-)</sup> CD8a<sup>(+)</sup>) in lung and spleen. The experiment was performed once. Mann-Whitney, with single comparisons were performed. All error bars represent standard deviations. NS, not significant at  $P > 0.05$ ; \*  $P \leq 0.05$ ; \*\*  $P \leq 0.01$ ; \*\*\*  $P \leq 0.001$ ; \*\*\*\*  $P \leq 0.0001$ .

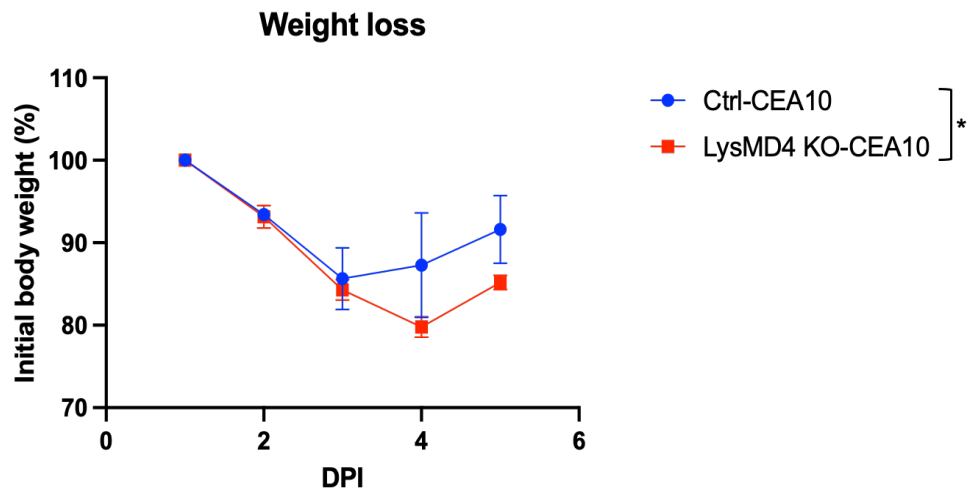


**Fig. 5 LysMD4 KO mice can survive from *A. fumigatus* infection but with potential delayed of recovery.**

WT (n=5) or LysMD4 KO (n=5) C57BL/6 mice were inoculated with  $5 \times 10^7$  CEA10 conidia with immune competent mice model. Three independent experiments were performed and the data was shown as the representative. The weight loss curves were shown as mean and error and the log rank (Mantel-cox) test were performed for statistical analysis of the curves.

## Materials and Methods

### Mice inoculation

LysMD3 KO and WT mice between 8 and 12 weeks old were bred and genotyped as previously described (Chapter 3). LysMD4<sup>+/-</sup> mice were purchased from Jackson lab and bred for LysMD4 KO mice and WT littermate controls. For mouse genotyping, genomic DNA was isolated from the mouse tail by Quick DNA Mini-Prep plus kit according to the manufacturer's instruction (ZYMO). Primers used for LysMD4 KO mice were: Forward primer for LysMD4 WT: 5'-AAAGCTGAGAAAGGGACAGC-3'. Forward primer for LysMD4 KO: 5'-GGAAGAAGGGTGGGGAATCT-3'. And Common reverse primer for LysMD3: 5'-TCCCTGGCCACATAAGGA-3'. Mice were housed in autoclaved cages at ≤ 4 mice per cage with a supply of HEPA-filtered air and water. *A. fumigatus* strain CEA10 and W72310 were grown on 1% glucose minimal media (GMM) plates for 3 days at 37 °C. For animal experiments, conidia were collected in 0.01% Tween-20 and washed 3 times with sterile PBS. For the IA model, mice were inoculated with 5x10<sup>7</sup> CEA10 (in 100 µl sterile PBS) and euthanized at 10 hours post-inoculation. For ABPA sensitization mice models, mice were inoculated with 1x10<sup>7</sup> W72310 (in 100 µl sterile PBS) at day 0, 7, 8, 9, 10, and 11 and euthanized at day 12 post initial inoculation. For ABPA sensitization plus challenge mice models, mice were inoculated with 1x10<sup>7</sup> W72310 (in 100 µl sterile PBS) at day 0, 7, 8, 9, 10, 11, and 14 and euthanized at day 15 post initial inoculation. The murine lungs were harvested for RNA extraction and blood was extracted for IgE ELISA. For the survival experiments of LysMD4 KO mice and WT controls, the weights of the mice were monitored daily. Animals were monitored daily for disease symptoms, and we carried out our animal studies in strict accordance with the recommendations in the Guide for the Care and Use of Laboratory Animals. The animal experimental protocol (no. 00002167) was approved by the Institutional Animal Care and Use Committee (IACUC) at Dartmouth College.

### RNA extraction and Nanostring

Mice were inoculated with CEA10 or W72310 as described previously, and the lungs were removed at euthanasia for RNA extraction. Lungs were flash frozen, lyophilized, and homogenized with glass beads using a Mini Beadbeater (BioSpec Products, Inc., Bartlesville, OK) and resuspended in TRIzol reagent (Thomas Scientific) and chloroform. The upper aqueous phase was transferred to a column from the RNeasy kit to extract RNA according to the manufacturer's instructions (Qiagen). The purified RNA was mixed with Reporter CodeSet and Capture ProbeSet reagent according to the manufacturer's instructions (Nanostring; Mouse immunology panel). The samples were then added to NanoString prep station and digital analyzer to acquire gene expression profiles.

### Flow cytometry: Cellularity experiments

For ABPA sensitization plus challenge mice models, mice were inoculated with  $1 \times 10^7$  W72310 (in 100  $\mu$ l sterile PBS) at day 0, 7, 8, 9, 10, 11, and 14 and euthanized at day 15 post initial inoculation. Single-cell suspensions from the lungs were harvested and prepared as previously described. Antibodies used for Flow cytometry analysis on different populations were as follows: For neutrophil and eosinophil populations, lung cells were stained with Survival dye (PI, eBioScience), CD45 (Pacific Orange, Invitrogen), SiglecF (BV421, BD BioScience), CD11b (PerCPy5.5, BioLegend), Ly6G (FITC, BioLegend), and CD11c (PECy7, BioLegend). For the T/B cells population, lung cells and splenocytes were stained with Survival dye (PI, eBioScience), CD45 (Pacific Orange, Invitrogen), CD19 (PECy7, BioLegend), CD3 (PE, BioLegend), CD4 (APC, BioLegend), CD8a (Pb, BioLegend). The gating strategy of each cell population is shown in Fig S1 and S2. Data were collected by Beckman Coulter Cytoflex S and analyzed with FlowJo version 10.8.1.

## References

1. Nur S, Sparber F, Lemberg C, Guiducci E, Schweizer TA, Zwicky P, Becher B, LeibundGut-Landmann S. 2019. IL-23 supports host defense against systemic *Candida albicans* infection by ensuring myeloid cell survival. *PLoS Pathog* 15.
2. Heath H, Qin S, Rao P, Wu L, LaRosa G, Kassam N, Ponath PD, Mackay CR. 1997. Chemokine receptor usage by human eosinophils. The importance of CCR3 demonstrated using an antagonistic monoclonal antibody. *J Clin Invest* 99:178–184.
3. Hausmann O v., Gentinetta T, Fux M, Ducrest S, Pichler WJ, Dahinden CA. 2011. Robust expression of CCR3 as a single basophil selection marker in flow cytometry. *Allergy* 66:85–91.
4. de Paulis A, Annunziato F, di Gioia L, Romagnani S, Carfora M, Beltrame C, Marone G, Romagnani P. 2001. Expression of the chemokine receptor CCR3 on human mast cells. *Int Arch Allergy Immunol* 124:146–150.
5. Stellato C, Brummet ME, Plitt JR, Shahabuddin S, Baroody FM, Liu MC, Ponath PD, Beck LA. 2001. Expression of the C-C chemokine receptor CCR3 in human airway epithelial cells. *J Immunol* 166:1457–1461.
6. Sallusto F, Mackay CR, Lanzavecchia A. 1997. Selective expression of the eotaxin receptor CCR3 by human T helper 2 cells. *Science* 277:2005–2007.
7. Ma W, Bryce PJ, Humbles AA, Laouini D, Yalcindag A, Alenius H, Friend DS, Oettgen HC, Gerard C, Geha RS. 2002. CCR3 is essential for skin eosinophilia and airway hyperresponsiveness in a murine model of allergic skin inflammation. *J Clin Invest* 109:621–628.
8. Yuan J, Liu Y, Yu J, Dai M, Zhu Y, Bao Y, Peng H, Liu K, Zhu X. 2022. Gene knockdown of CCR3 reduces eosinophilic inflammation and the Th2 immune response by inhibiting the PI3K/AKT pathway in allergic rhinitis mice. *Sci Rep* 12.
9. Michels K, Nemeth E, Ganz T, Mehrad B. 2015. Hepcidin and Host Defense against Infectious Diseases. *PLoS Pathog* 11.
10. Li Z, Pei XH, Yan J, Yan F, Cappell KM, Whitehurst AW, Xiong Y. 2014. CUL9 mediates the functions of the 3M complex and ubiquitylates survivin to maintain genome integrity. *Mol Cell* 54:805–819.

11. Li Z, Xiong Y. 2017. Cytoplasmic E3 ubiquitin ligase CUL9 controls cell proliferation, senescence, apoptosis and genome integrity through p53. *Oncogene* 36:5212–5218.
12. Garth JM, Reeder KM, Godwin MS, Mackel JJ, Dunaway CW, Blackburn JP, Steele C. 2017. IL-33 Signaling Regulates Innate IL-17A and IL-22 Production via Suppression of Prostaglandin E2 during Lung Fungal Infection. *J Immunol* 199:2140–2148.
13. Miller AM. 2011. Role of IL-33 in inflammation and disease. *J Inflamm (Lond)* 8.
14. Ding W, Zou GL, Zhang W, Lai XN, Chen HW, Xiong LX. 2018. Interleukin-33: Its Emerging Role in Allergic Diseases. *Molecules* 23.
15. Guo Y, Kasahara S, Jhingran A, Tosini NL, Zhai B, Aufiero MA, Mills KAM, Gjonbalaj M, Espinosa V, Rivera A, Luster AD, Hohl TM. 2020. During Aspergillus Infection, Monocyte-Derived DCs, Neutrophils, and Plasmacytoid DCs Enhance Innate Immune Defense through CXCR3-Dependent Crosstalk. *Cell Host Microbe* 28:104-116.e4.
16. Hu JK, Kagari T, Clingan JM, Matloubian M. 2011. Expression of chemokine receptor CXCR3 on T cells affects the balance between effector and memory CD8 T-cell generation. *Proc Natl Acad Sci U S A* 108.
17. Groom JR, Luster AD. 2011. CXCR3 in T cell function. *Exp Cell Res* 317:620–631.
18. Yokoyama CC, Baldrige MT, Leung DW, Zhao G, Desai C, Liu TC, Diaz-Ochoa VE, Huynh JP, Kimmey JM, Sennott EL, Hole CR, Idol RA, Park S, Storek KM, Wang C, Hwang S, Milam AV, Chen E, Kerrinnes T, Starnbach MN, Handley SA, Mysorekar IU, Allen PM, Monack DM, Dinauer MC, Doering TL, Tsolis RM, Dworkin JE, Stallings CL, Amarasinghe GK, Micchelli CA, Virginia HW. 2018. LysMD3 is a type II membrane protein without an in vivo role in the response to a range of pathogens. *J Biol Chem* 293:6022–6038.



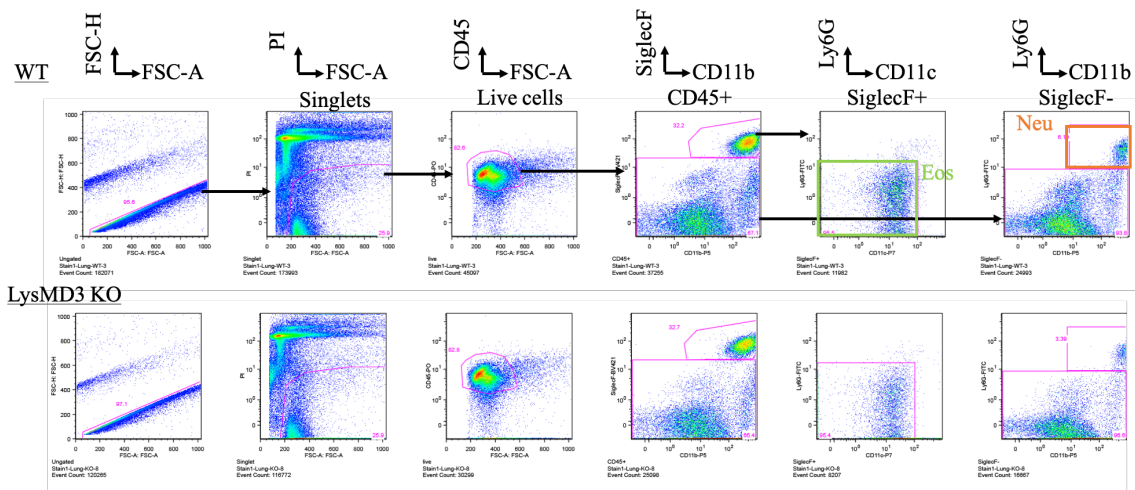


**Fig. S1 Gating strategy for neutrophils and eosinophils.** The neutrophils were identified as  $CD45^{+}$   $SiglecF^{-}$   $Ly6G^{+}$   $CD11b^{+}$  cells, and eosinophils as  $CD45^{+}$   $SiglecF^{+}$   $Ly6G^{-}$   $CD11c^{(dim\ or\ -)}$ .

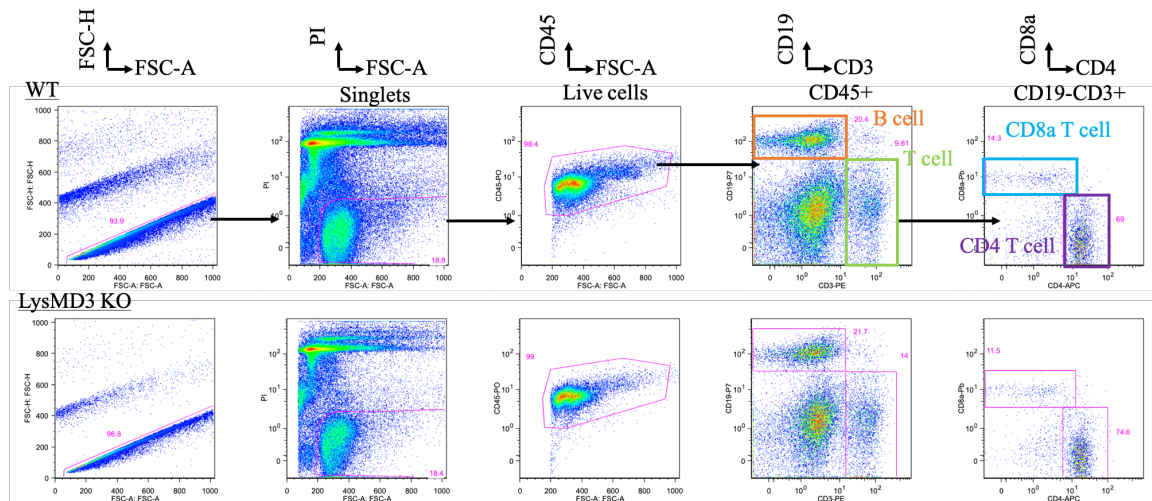


**Fig. S2 Gating strategy for T cells and B cells.** The B cells were identified as  $CD45^{(+)}$  $CD19^{(+)}$  $CD3^{(-)}$  cells, and T cells as  $CD45^{(+)}$  $CD19^{(+)}$  $CD3^{(-)}$  cells (subpopulations as  $CD4^{(+)}$  $CD8a^{(-)}$  and  $CD4^{(-)}$  $CD8a^{(+)}$  T cells)

## Appendix III

### *Aspergillus fumigatus* Strain-Specific Conidia Lung Persistence Causes an Allergic Broncho-Pulmonary Aspergillosis-Like Disease Phenotype

Jane T. Jones, Ko-Wei Liu, Xi Wang, Caitlin H. Kowalski, Brandon S. Ross, Kathleen A. M. Mills, Joshua D. Kerkaert, Tobias M. Hohl, Lotus A. Lofgren, Jason E. Stajich, Joshua J. Obar, Robert A. Cramer

KWL designed and performed the experiments, analyzed the results in Figure 1B-1H, and 6B



# *Aspergillus fumigatus* Strain-Specific Conidia Lung Persistence Causes an Allergic Broncho-Pulmonary Aspergillosis-Like Disease Phenotype

Jane T. Jones,<sup>a</sup> Ko-Wei Liu,<sup>a</sup> Xi Wang,<sup>a</sup> Caitlin H. Kowalski,<sup>a</sup> Brandon S. Ross,<sup>a</sup> Kathleen A. M. Mills,<sup>b,c</sup> Joshua D. Kerkaert,<sup>a</sup> Tobias M. Hohl,<sup>b,c</sup> Lotus A. Lofgren,<sup>d</sup> Jason E. Stajich,<sup>d</sup> Joshua J. Obar,<sup>a</sup> Robert A. Cramer<sup>a</sup>

<sup>a</sup>Geisel School of Medicine, Department of Microbiology and Immunology, Dartmouth, Hanover, New Hampshire, USA

<sup>b</sup>Infectious Disease Service, Department of Medicine, Memorial Sloan Kettering Cancer Center, New York, New York, USA

<sup>c</sup>Immunology and Microbial Pathogenesis Graduate Program, Weill Cornell Graduate School, New York, New York, USA

<sup>d</sup>Department of Microbiology and Plant Pathology, University of California Riverside, Riverside, California, USA

**ABSTRACT** *Aspergillus fumigatus* is a filamentous fungus which can cause multiple diseases in humans. Allergic broncho-pulmonary aspergillosis (ABPA) is a disease diagnosed primarily in cystic fibrosis patients caused by a severe allergic response often to long-term *A. fumigatus* colonization in the lungs. Mice develop an allergic response to repeated inhalation of *A. fumigatus* spores; however, no strains have been identified that can survive long-term in the mouse lung and cause ABPA-like disease. We characterized *A. fumigatus* strain W72310, which was isolated from the expectorated sputum of an ABPA patient, by whole-genome sequencing and *in vitro* and *in vivo* viability assays in comparison to a common reference strain, CEA10. W72310 was resistant to leukocyte-mediated killing and persisted in the mouse lung longer than CEA10, a phenotype that correlated with greater resistance to oxidative stressors, hydrogen peroxide, and menadione, *in vitro*. In animals both sensitized and challenged with W72310, conidia, but not hyphae, were viable in the lungs for up to 21 days in association with eosinophilic airway inflammation, airway leakage, serum IgE, and mucus production. W72310-sensitized mice that were recall challenged with conidia had increased inflammation, Th1 and Th2 cytokines, and airway leakage compared to controls. Collectively, our studies demonstrate that a unique strain of *A. fumigatus* resistant to leukocyte killing can persist in the mouse lung in conidial form and elicit features of ABPA-like disease.

**IMPORTANCE** Allergic broncho-pulmonary aspergillosis (ABPA) patients often present with long-term colonization of *Aspergillus fumigatus*. Current understanding of ABPA pathogenesis has been complicated by a lack of long-term *in vivo* fungal persistence models. We have identified a clinical isolate of *A. fumigatus*, W72310, which persists in the murine lung and causes an ABPA-like disease phenotype. Surprisingly, while viable, W72310 showed little to no growth beyond the conidial stage in the lung. This indicates that it is possible that *A. fumigatus* can cause allergic disease in the lung without any significant hyphal growth. The identification of this strain of *A. fumigatus* can be used not only to better understand disease pathogenesis of ABPA and potential antifungal treatments but also to identify features of fungal strains that drive long-term fungal persistence in the lung. Consequently, these observations are a step toward helping resolve the long-standing question of when to utilize antifungal therapies in patients with ABPA and fungal allergic-type diseases.


**KEYWORDS** *Aspergillus fumigatus*, chronic infection, allergic broncho-pulmonary aspergillosis, oxidative stress, genomics, ABPA, strain heterogeneity

**Citation** Jones JT, Liu K-W, Wang X, Kowalski CH, Ross BS, Mills KAM, Kerkaert JD, Hohl TM, Lofgren LA, Stajich JE, Obar JJ, Cramer RA. 2021. *Aspergillus fumigatus* strain-specific conidia lung persistence causes an allergic broncho-pulmonary aspergillosis-like disease phenotype. mSphere 6:e01250-20. <https://doi.org/10.1128/mSphere.01250-20>.

**Editor** Aaron P. Mitchell, University of Georgia

**Copyright** © 2021 Jones et al. This is an open-access article distributed under the terms of the Creative Commons Attribution 4.0 International license.

Address correspondence to Robert A. Cramer, robert.a.cramer.jr@dartmouth.edu.

 *Aspergillus fumigatus* strain persistence in the murine lung induces ABPA-like disease

**Received** 4 December 2020

**Accepted** 27 January 2021

**Published** 17 February 2021

Individuals with atopic asthma, chronic obstructive pulmonary disease (COPD), and particularly cystic fibrosis (CF) are susceptible to chronic fungal colonization and infections in the lung (1). For example, 30 to 80% of CF patients persistently test positive for growth of the filamentous fungus *Aspergillus fumigatus* in expectorated sputum (2–4), and this finding is associated with overall decreased lung function (5). These findings demonstrate that *A. fumigatus* colonization is a critical aspect of CF disease pathogenesis. A subset of these patients develops allergic broncho-pulmonary aspergillosis (ABPA), a particularly difficult disease to diagnose and treat. Individuals with CF and/or asthma are typically diagnosed with ABPA and exhibit a type 2 immune response that leads to the production of high levels of interleukin 4 (IL-4), airway eosinophilia, and increased total and *A. fumigatus*-specific IgE (6, 7). Recurrent ABPA exacerbations lead to the development of bronchiectasis, airway remodeling, and fibrosis as a long-term consequence of fungal colonization (8). Although treating ABPA patients with antifungal drugs can improve symptoms in some cases (9, 10), it is not known how or whether persistence of *A. fumigatus* in the lungs specifically contributes to ABPA disease pathogenesis.

Murine models of fungal persistence using agar beads containing *A. fumigatus* conidia successfully recapitulated long-term (21 to 28 days) colonization of fungal hyphae in the lung (11, 12); however, mice in this specific agar bead model do not develop the strong IgE/Th2 response observed in ABPA patients. Numerous other mouse models that seek to recapitulate human ABPA have been described, including utilizing *A. fumigatus* antigens (13) and repeated challenge with live conidia (14), though none of these models exhibited long-term persistence of *A. fumigatus* in the airways, a common and important feature of ABPA (5, 15, 16). Importantly, the extent of fungal growth in ABPA patients' airways is unclear, though hyphae have been identified in sputum and tissue in some patient samples (17, 18). Consequently, *in vivo* studies examining the fungal contribution to ABPA development, persistence, and disease progression are currently difficult to conduct. This is a critical question to address because it is expected to help inform when antifungal therapies may be effective in the context of ABPA.

The goal of the current study was to identify a strain of *A. fumigatus* that is capable of long-term persistence in the lung of immunocompetent mice. Using a clinical strain isolated from a sputum sample of an ABPA patient, viable *A. fumigatus* was recovered from the murine airways for up to 21 days. Animals with persistent fungal burden developed increased serum IgE, eosinophilia, airway damage, mucus production, and an increased immune response to reexposure to fungi, all common features of ABPA. Surprisingly, these symptoms developed despite little to no hyphal growth observed in the airways of animals with persistent fungal burden. Consequently, these data demonstrate that a fungal strain with resistance to leukocyte killing and relatively low virulence is capable of long-term persistence in the murine lung and initiating ABPA-like disease pathogenesis.

## RESULTS

***Aspergillus fumigatus* clinical isolate W72310 is resistant to immune cell-mediated killing and persists in the murine lung.** Previous work from our laboratory found that a clinical isolate strain, W72310, had reduced virulence compared to the commonly studied reference strain CEA10 in mice with suppressed immune systems (19). Conidia from W72310 have also been reported to germinate more slowly under a variety of conditions (20) in comparison to other *A. fumigatus* strains. We hypothesized that a slow-growing, less virulent strain may evade immune clearance and allow establishment of long-term fungal persistence in murine airways. In order to test this hypothesis, we first compared W72310 and CEA10 persistence in the immunocompetent murine lung 7 days after one fungal intranasal inoculation. Grocott-Gomori methenamine silver (GMS) staining of fixed lungs revealed that fungal conidia were still present in W72310-exposed lungs 7 days postinoculation; however, no observable conidia were found in CEA10-challenged animals (Fig. 1A). While swollen conidia could be

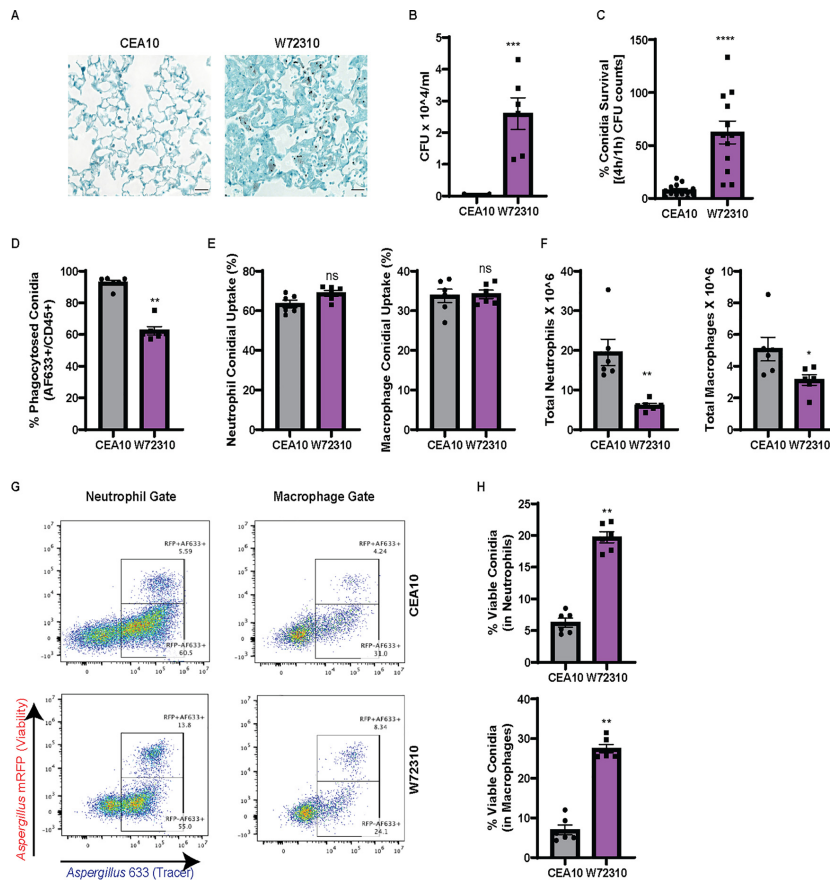


**FIG 1** *A. fumigatus* clinical isolate W72310 persists longer in the murine lung and is resistant to leukocyte-mediated death compared to the common laboratory strain CEA10. (A) C57BL/6 mice were intranasally inoculated with  $1 \times 10^7$  live CEA10 or W72310 conidia and euthanized after 7 days. Lungs were fixed in formalin and stained for fungi (GMS stain, black).  $n=6$  to 8 animals, scale bars = 100  $\mu$ m, 40 $\times$ . (B) Lungs from parallel experiments were assessed for total CFU ( $n=6$  to 8 animals). (C) CEA10 and W72310 live conidia were incubated with primary bone marrow-derived macrophages for 1 or 4 h, and CFU were quantified. Data are represented as percent survival of 4 h/1 h. Data include 3 independent experiments. C57BL/6 mice were oropharyngeally inoculated with  $3.0 \times 10^7$  AF633-stained mRFP-CEA10 or mRFP-W72310 conidia for 36 h. (D to F) Lungs were analyzed by flow cytometry for percent phagocytosis of conidia in immune cells (AF633<sup>+</sup>/CD45<sup>+</sup>) (D), percent positive conidia (AF633) in neutrophils and macrophages (E), and total neutrophils (CD45<sup>+</sup>/Ly6G<sup>+</sup>/CD11b<sup>+</sup>) and macrophages (CD45<sup>+</sup>/Ly6G<sup>-</sup>/CD11b<sup>+</sup>/CD64<sup>+</sup>) (F). (G and H) Viability of conidia phagocytosed in neutrophils and macrophages was analyzed by flow cytometry (G) and quantified (H). Representative micrographs were selected out of 6 mice per group. Mann-Whitney single comparisons were used. ns,  $P > 0.05$ ; \*,  $P \leq 0.05$ ; \*\*,  $P \leq 0.01$ ; \*\*\*,  $P \leq 0.001$ .

observed in W72310-inoculated animals, no hyphal growth was visible across multiple independent histopathology sections. In a parallel experiment, quantification of total CFU revealed viable fungi only from lungs inoculated with W72310 (Fig. 1B), indicating W72310 persists longer than CEA10 in C57BL/6J mice.

To address how W72310 conidia persist in the lung, we assayed the susceptibility of W72310 and CEA10 fungal conidia to killing by bone marrow-derived macrophages

(BMDMs) *ex vivo*. After incubation of either W72310 or CEA10 conidia with BMDMs for 4 h, W72310 conidial survival was 6-fold higher than CEA10 (Fig. 1C). In order to test this observation *in vivo*, CEA10 and W72310 that ectopically express monomeric red fluorescent protein (mRFP) were generated in order to distinguish live (mRFP<sup>+</sup>) from dead (mRFP<sup>-</sup>) conidia by flow cytometry. Given the relatively short half-life of RFP (approximately 45 min) in the phagolysosome of leukocytes, this fluorescent protein functioned as a fungal viability marker during cellular interactions with leukocytes. A fluorescent tracer dye (Alexa Fluor 633 [AF633]) was covalently attached to the surface of the mRFP-expressing strains and served as a conidial tracer (21). We utilized this assay to quantify leukocyte uptake and viability of W72310 and CEA10 conidia in the murine lung. At 36 h after inoculation with AF633-stained mRFP-CEA10 or W72310 conidia, the percentage of W72310 conidia that were phagocytosed by CD45<sup>+</sup> immune cells was 30% less than the percentage of CEA10 conidia in CD45<sup>+</sup> immune cells (Fig. 1D). However, comparison of neutrophil and macrophage conidial uptake (% positive AF633) showed no difference between CEA10 and W72310 (Fig. 1E). The reduced phagocytosis of W72310 conidia correlated with a 4-fold reduction in neutrophils and 2-fold reduction in total macrophages in the lungs of mice inoculated with W72310 compared to CEA10 (Fig. 1F). The percentage of viable W72310 conidia phagocytosed by neutrophils and macrophages significantly increased 4-fold in comparison to CEA10 (Fig. 1G and H). Taken together, these data suggest the *A. fumigatus* strain W72310 recruits fewer inflammatory cells and is killed less efficiently than the highly virulent CEA10 strain in a murine model of fungal bronchopneumonia.

**Comparison of W72310 sensitization to CEA10 sensitization in the murine lung.** Given the persistent presence of the W72310 strain in the murine lung, its increased resistance to leukocyte-mediated killing, and the altered cellular response to W72310 conidia, we next compared the overall immune responses to sensitization with CEA10 and W72310 live conidia. Animals were intranasally inoculated and sensitized to W72310 or CEA10 conidia as indicated (Fig. 2A). Compared to phosphate-buffered saline (PBS)-sensitized animals, CEA10 and W72310 animals had 6- and 8-fold-increased serum IgE, respectively (Fig. 2B). Although we observed a trend for more total IgE in animals exposed to W72310 compared to CEA10, the difference was not statistically significant. Additionally, small but detectable CFU were observed in lungs sensitized with CEA10; however, approximately 10<sup>6</sup> CFU were detected in lungs of animals sensitized with W72310 (Fig. 2C). In parallel, total RNA was extracted from whole lungs and analyzed for changes in mRNA levels of immune-related genes using NanoString nCounter technology. As expected, overall changes in mRNA levels were strikingly different in PBS-sensitized animals compared to the two fungal strains (Fig. 2D). Increased signatures in pathways related to cytokine/chemokine signaling, host-pathogen interactions, and innate and adaptive immune signaling were observed in fungal challenged animals as expected (Fig. 2E). Interestingly, the only immune-related pathways with reduced mRNA levels in fungus-exposed mice compared to PBS were transforming growth factor  $\beta$  (TGF- $\beta$ ) and inflammasome-encoding genes (Fig. 2E). Using GO-term analysis with a cutoff of  $P \leq 0.01$  to differentiate highly significant pathways in the W72310-sensitized lung compared to PBS, analysis showed prevalent eosinophil, monocyte, and lymphocyte chemotaxis, ERK1 and ERK2 signaling, interferon gamma (IFN- $\gamma$ ) response signaling, and general immune system responses (Fig. 2F). Comparison of PBS- and W72310-sensitized lungs revealed 174 increased and 38 decreased mRNA transcripts (Fig. 2G). Surprisingly, transcripts of only 9 genes were differentially abundant (2-fold or higher) between CEA10- and W72310-challenged mice. Of these, transcripts of all 9 genes were increased in W72310-sensitized animals compared to CEA10-sensitized animals (Fig. 2H). These differentially expressed transcripts are encoded by the genes *nos2*, *clec4e*, *cxcl-9*, *cxcl-10*, *ccl4*, *cxcl-11*, *klra21*, *cxcl3*, and *tnfa*, transcripts largely involved in T cell/monocyte recruitment and activation, host defense, and CXCR3 receptor activation. The lack of differences between CEA10- and W72310-challenged animals seems especially striking given the clear differences in persistent fungal burden.

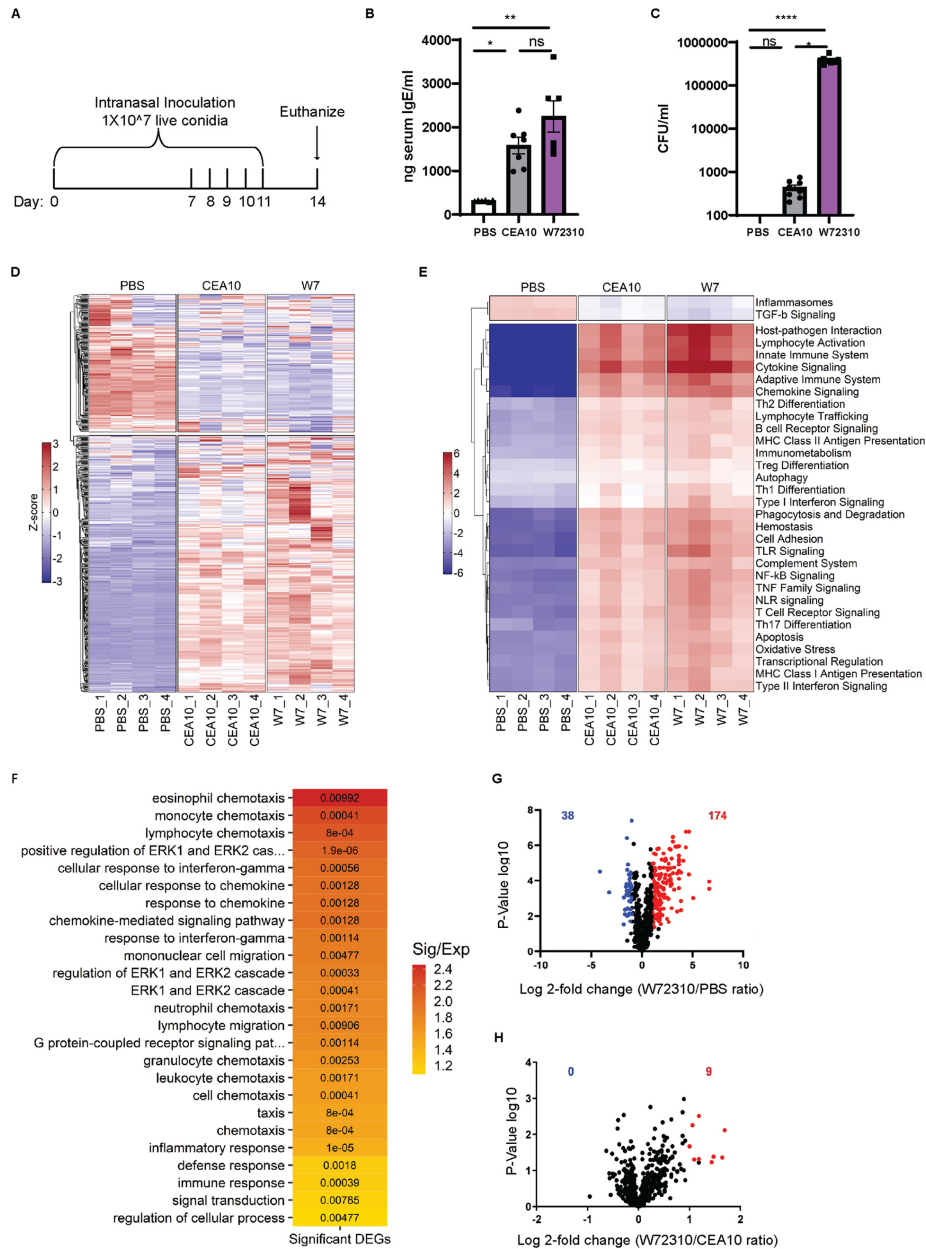


**FIG 2** W72310-induced sensitization is similar to CEA10-induced sensitization in the murine lung. (A) Mice were inoculated with either PBS or  $1 \times 10^7$  live W72310/CEA10 conidia on the indicated days and euthanized on day 14. (B) Total serum IgE was measured by ELISA on blood

(Continued on next page)



**W72310 accumulates in the murine lung during sensitization.** ABPA patients are sensitized to *A. fumigatus* antigens (22). A previous report demonstrated that fungi could persist longer in an allergen-sensitized murine lung than a control lung (23), so we next determined whether sensitization with W72310 or CEA10 increased persistence of a subsequent exposure to W72310 or CEA10 conidia. In light of the data from the immunocompetent murine model (Fig. 1), it is likely that W72310 sensitization alone would cause an accumulation of fungi in the lung, so in order to differentiate between fungi present from sensitization and fungi present due to challenge, we generated CEA10 and W72310 strains that were resistant to hygromycin. Mice were sensitized with either PBS, wild-type (WT) CEA10, or WT W72310 and challenged with either PBS, W72310-hyg, or CEA10-hyg. CFU were measured on Sabouraud dextrose agar (SAB)-containing plates (total CFU) or SAB/hygromycin-containing plates ("challenge" CFU) from the lungs of mice euthanized 7 days after challenge (Fig. 3A). Interestingly, no live conidia were detected in mice sensitized with CEA10 and challenged with PBS, demonstrating that repeated intranasal (i.n.) inoculation was not sufficient to drive CEA10 fungal conidia accumulation in the murine lung (Fig. 3B). In contrast, approximately  $1 \times 10^7$  live conidia were detected from mice sensitized with W72310 and challenged with PBS, indicating an accumulation of viable fungi in the lung from repeated W72310 i.n. sensitizations (Fig. 3B). Challenge with CEA10-hyg in W72310-sensitized mice did not facilitate persistence of CEA10; however, an almost 2-fold increase in CFU was observed in W72310-challenged mice when sensitized with W72310 but not CEA10 (Fig. 3B). Collectively, these data indicate that sensitization causes a modest increase in persistence of W72310 but not CEA10. Consequently, fungal sensitization itself is not sufficient or necessary to promote fungal persistence in the lung with all strains of *A. fumigatus*.

**Sensitization and challenge with W72310 cause increased fungal persistence in the lung in association with increased serum IgE.** To determine whether W72310 persists long-term in the mouse lung, we sensitized animals as described for Fig. 2 and subsequently "challenged" mice with another fungal dose on day 0 (Fig. 4A). As a control, animals were sensitized to PBS only and challenged with one dose of W72310 on day 0. To determine fungal persistence, CFU were chosen for quantitation despite the filamentous morphology of *A. fumigatus* because hyphal elements could not be observed in histopathology samples at any time point. Total CFU increased in the lungs of animals sensitized and challenged with W72310 at 2, 7, and 21 days postchallenge in comparison to PBS-sensitized controls (Fig. 4B). This significance was not observed in lungs 28 days postchallenge. CFU were detected 2 and 7 days postchallenge in the PBS-sensitized control group. Surprisingly, CFU were still detectable 21 and 28 days postchallenge in this group as well, although to a much lesser extent. Fixed lungs were stained for fungi (GMS) to observe the fungal presence and morphology. At 2 and 7 days postchallenge in both PBS- and W72310-sensitized mice, prominent conidia were visible (Fig. 4C). Despite the quantification of detectable CFU in PBS-sensitized mice 21 and 28 days postchallenge, conidia were not visible by GMS stain after 7 days (Fig. 4C). Conidia were strongly visible 21 days after challenge in the W72310-sensitized mice; however, they appeared to be taken up in large vacuolar phagocytes (Fig. 4C). Interestingly, multiple conidia were visible in a single host cell. Conidia were mostly

#### FIG 2 Legend (Continued)

samples collected from animals.  $n = 6$  to 7 mice. (C) Total CFU were measured in the lungs of mice.  $n = 8$  mice. Mann-Whitney test with Dunn's multiple comparison was used. \*,  $P \leq 0.05$ ; \*\*,  $P \leq 0.01$ ; \*\*\*,  $P \leq 0.001$ ; \*\*\*\*,  $P \leq 0.0001$ . (D) Total mRNA was extracted from the whole lung, and gene expression was analyzed by NanoString nCounter immunology panel. Downregulation (blue) or upregulation (red) of individual replicates was represented by heatmap;  $n = 4$  mice/group. (E) Pathway signature of mice sensitized to either PBS, CEA10, or W72310. (F) Heatmap showing the degree of enrichment and  $P$  value for each GO-term enriched in increased genes. The color of each tile indicates the  $\log_2$ -transformed degree of enrichment for a given term within each gene set. The  $P$  value is overlaid in text to show the significance of each term. The terms on the  $y$  axis are ordered according to decreasing degree of enrichment from top to bottom. (G) Volcano plot showing the distribution of fold changes in gene expression in W72310-treated mice compared to PBS: genes with absolute fold changes  $\geq 2$  and with  $P$  value  $\leq 0.05$  (Student's  $t$  test) are shown in blue, and genes with absolute fold changes  $\geq 2$  and with  $P$  value  $\leq 0.05$  (Student's  $t$  test) are shown in red. (H) Volcano plot showing the distribution of fold changes in gene expression in W72310-treated mice compared to CEA10: genes with absolute fold changes  $\geq 2$  and with  $P$  value  $\leq 0.05$  (Student's  $t$  test) are shown in red.

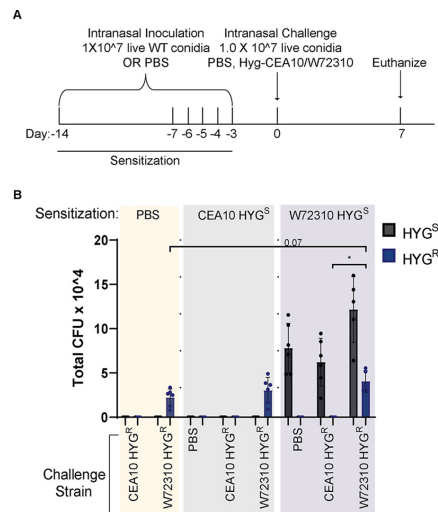


**FIG 3** W72310 accumulates in the mouse lung during sensitization. (A) C57BL/6 mice were inoculated with either PBS or  $1 \times 10^7$  live W72310/CEA10 conidia on the indicated days (sensitization) and challenged on day 0 with either PBS, Hyg-CEA10, or Hyg-W72310; animals were euthanized 7 days after challenge. (B) Lung homogenates were spread on plates containing SAB alone or SAB plus hygromycin and quantified for total CFU. "Challenge" CFU were identified as colonies grown on hygromycin plates, and "Sensitization" CFU were calculated by subtracting hygromycin CFU values from total CFU values (SAB-alone plates). HYG<sup>S</sup>, hygromycin-sensitive; HYG<sup>R</sup>, hygromycin resistant.  $n = 6$  to 12 mice per group. Mann-Whitney test with Dunn's multiple comparison was used. \*,  $P \leq 0.05$ .

nondetectable by 28 days, with a small number visible by GMS stain. Collectively, these data demonstrate that W72310 can persist in a fungus-sensitized murine lung up to 1 month after inoculation.

Blood was collected from each animal, and total serum IgE levels were measured by enzyme-linked immunosorbent assay (ELISA) to determine the overall allergic response. As expected, total IgE levels increased 2 and 7 days postchallenge in W72310-sensitized mice compared to controls (Fig. 4D); however, significant increases were not detected at 21 and 28 days. Interestingly, even in the PBS-sensitized animals, total serum IgE was increased at 21 days compared to PBS-sensitized control at 2 days. Overall, these data indicate that sensitization and challenge with strain W72310 maintain high levels of IgE.

**Sensitization and challenge with W72310 cause increased inflammation, leakage, and mucous cell metaplasia.** Eosinophilia is a hallmark of ABPA disease (24). Differential staining of airway/bronchoalveolar lavage (BAL) fluid cells revealed that eosinophils were increased 2, 7, and 21 days after sensitization and challenge with W72310 live conidia in comparison to PBS-sensitized controls (Fig. 5A). Moreover, macrophages and lymphocytes were increased at all time points (Fig. 5A). Interestingly, lymphocytes and eosinophils continued to be detectable 28 days postchallenge but at lower levels. Overall neutrophils decreased over time, but no significant differences were observed between control and experimental groups at any time points (Fig. 5A). The inflammatory response was also assessed by staining lung sections for hematoxylin and eosin (H&E). Some cellular infiltrates were observed in PBS-sensitized mice 2 and 7 days postchallenge with W72310, while robust inflammation, including eosinophils, was observed in animals sensitized and challenged with W72310 at all time points (Fig. 5B). Furthermore, animals sensitized and challenged with W72310 for all time points had detectable mucous cells in airways as shown by periodic acid-Schiff

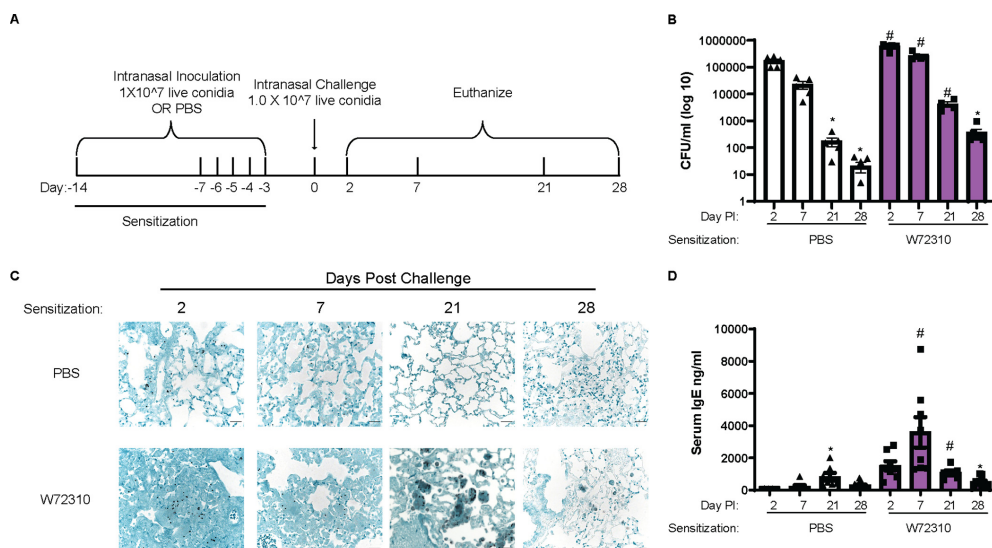


**FIG 4** Sensitization and challenge with W72310 causes increased fungal persistence in the lung in association with increased serum IgE. (A) Schematic of ABPA model protocol. C57BL/6 mice were inoculated with either PBS or  $1 \times 10^7$  live W72310 conidia on the indicated days and challenged on day 0. Animals were subsequently euthanized on days 2, 7, 21, and 28. (B) CFU were quantified from total lung homogenates at the indicated time points and represented on a log scale. (C) Paraffin-embedded fixed lungs were stained with GMS, and images were captured at 40 $\times$ ; scale bar = 100  $\mu$ m. (D) Total serum IgE was measured by ELISA on blood samples collected from animals. (B and D) Kruskal-Wallis with Dunn's comparison to 2-day time point (within same sensitization protocol): \*,  $\leq 0.05$ ; Kruskal-Wallis with Dunn's comparison to same time point (within different sensitization protocol): #,  $\leq 0.05$ . Data include 2 independent experiments and  $n = 8$  to 12 mice.

(PAS)-stained lung sections (Fig. 5B, black arrows). At early time points, 2 and 7 days after challenge, there were a large number of mucus-producing cells, which persisted at lower levels at later time points.

Total albumin in the BAL fluid was measured to evaluate the extent of vascular leakage and potential damage to the lungs in the airways. Quantification of albumin showed significant increases in animals sensitized and challenged with W72310 at 7 and 21 days compared to PBS-sensitized controls, indicating airway damage that resolved by day 28 (Fig. 5C).

**Mice recall challenged with W72310 have increased airway inflammation and damage in the lungs.** Major features of ABPA disease are periods of remission and exacerbation (25). To determine if mice with persistent W72310 in the lungs were susceptible to a recall response, mice were sensitized and challenged with either PBS or W72310 and 21 days after challenge all animals were recall challenged with either PBS or W72310 live conidia (Fig. 6A). We chose to rechallenge mice at 21 days after the initial challenge because we wanted to use a time point in which conidia had been persistent long-term but were still highly prevalent. This was in order to determine if the presence of conidia themselves could maintain an environment in the lung prone to "exacerbations." BAL fluid and lung suspension neutrophils and eosinophils were significantly increased in the W72310 recall-challenged group compared to the PBS recall-challenged group (Fig. 6B). Serum IgE levels were increased 5-fold in mice sensitized and challenged with W72310 at 21 days compared to PBS-sensitized challenged mice, as would be expected (based on results from the time course [Fig. 4D]), and BAL fluid albumin was measured in order to assess damage and leakage in the airways (Fig. 6C). Total albumin levels were increased 2-fold in the airways of mice sensitized, challenged, and recall challenged with W72310 compared to both PBS controls. Th2

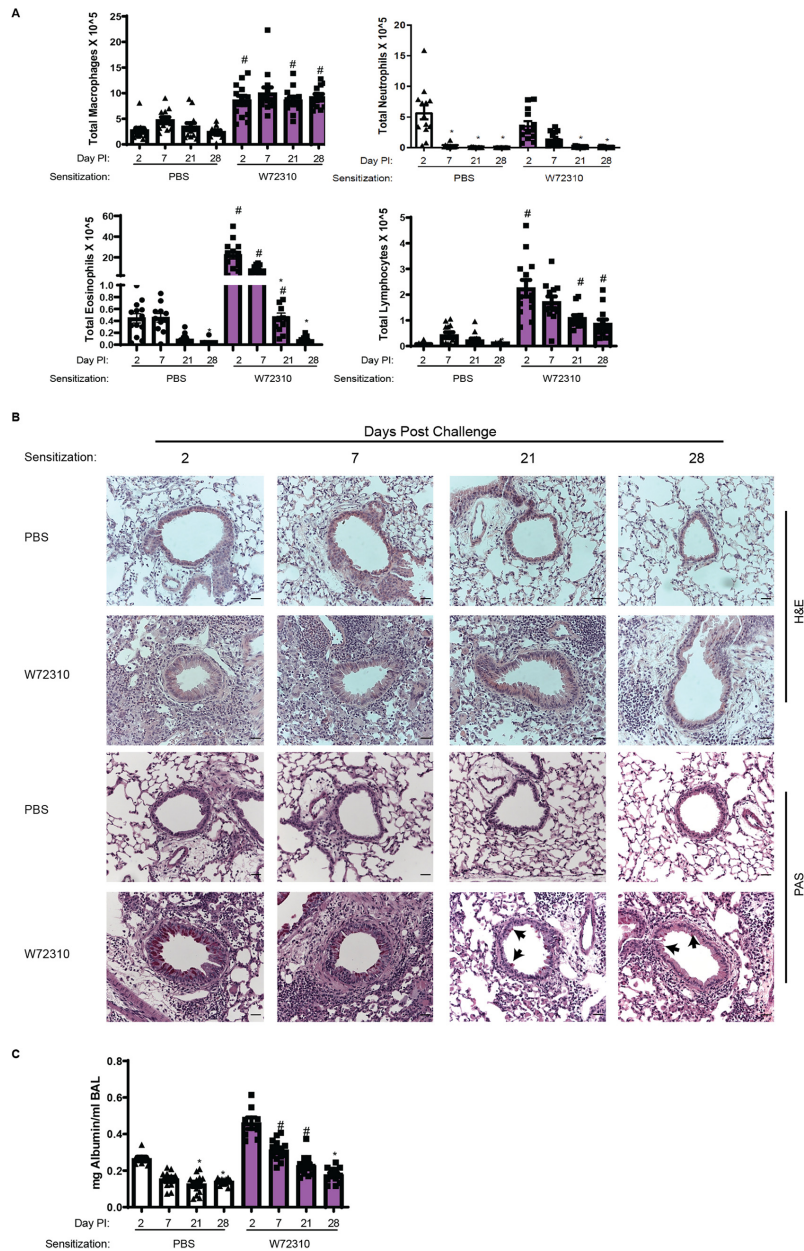


**FIG 5** Sensitization and challenge with W72310 cause increased pulmonary inflammation, leakage, and mucous cell metaplasia. (A) Total BAL fluid was quantified for individual cell populations of macrophages, neutrophils, lymphocytes, and (Continued on next page)

cytokines IL-4/IL-10 and Th1 cytokine IFN- $\gamma$  were significantly increased in BAL fluid of mice sensitized, challenged, and recall challenged with W72310 compared to PBS controls (Fig. 6D). IL-17A cytokine levels were not detectable (data not shown). Collectively, these data demonstrate that W72310 persists for several weeks in a fungus-sensitized murine lung and elicits strong inflammation, damage, mucus production, and an exacerbation-like immune response.

**Comparison of W72310 and CEA10 whole-genome sequences.** Given the clear differences in immune response to CEA10 and W72310, we wanted to address potential fungus-mediated mechanisms for these observations. As a first step toward understanding the fungal contribution to these responses, whole-genome sequencing of CEA10 and W72310 was conducted. Sequencing and variant analysis revealed a total of 56,036 variants in W72310 that differed from the AF293 reference genome, compared to only 13,014 variants identified in CEA10. These variants included 2,392 positions in W72310 and 874 variants in CEA10 for which no allele could be determined (and which possibly represent a deletion at that position compared to the AF293 reference genome). We consequently identified 49,806 variants that were exclusive to W72310 and not shared with CEA10 (18,088 excluding synonymous and intergenic variants), compared to only 8,302 variants found in CEA10 but not present in W72310 (1,922 excluding synonymous and intergenic variants). W72310 also had a greater number of missense variants with a total of 6,486, compared to only 814 in CEA10. Given the differences observed between W72310 and CEA10 in conidial viability, germination rate, and persistence in the lung, we narrowed our focus to nonsynonymous variants unique to W72310 (not present in CEA10) occurring in genes involved in oxidative stress responses, cell wall biology, melanin, and metabolism using reverse GO-term mapping. Variants were identified in 20 unique oxidative stress response genes, 6 cell wall genes, and 6 melanin genes (Table 1). Interestingly, no variants were identified in core metabolism genes. When nonsynonymous variants unique to W72310 were mapped onto putative allergen genes, 184 single nucleotide polymorphisms (SNPs) and indels in 69 unique genes, with mutation load ranging from 1 to 21 variants per gene, were found (Table 2). In order to corroborate differences observed in oxidative stress resistance, mRFP-CEA10 and mRFP-W72310 strains were assayed for susceptibility to oxidative stress-inducing agents, hydrogen peroxide and menadione. The percentage of viable CEA10 conidia (RFP<sup>+</sup>) was significantly reduced by 50% (hydrogen peroxide) and 40% (menadione), respectively. In contrast, incubation of W72310 with hydrogen peroxide and menadione decreased the percentage of viable conidia by only less than 5% (Fig. 7). Collectively, these data show that W72310 conidia are less susceptible to oxidative stress-induced death than those of CEA10 and this may contribute to its persistent phenotype in the mouse lung. The allele(s) driving this phenotype in W72310 conidia remains to be determined in future studies.

## DISCUSSION

In the current study, we characterized a unique clinical strain of *A. fumigatus* which persists in the murine lung and elicits an ABPA-like disease state. By identifying and characterizing the W72310 strain, our studies demonstrated that an *A. fumigatus* strain can be resistant to immune cell-mediated killing and that it can persist in the murine lung as viable conidia while eliciting a strong IgE/inflammatory/damage response. These data are important because they suggest *A. fumigatus* strains exist in the population that can persist in mammalian airways and induce pathological immune responses without robust fungal growth. Moreover, our data provide an opportunity to uncover

### FIG 5 Legend (Continued)

eosinophils. (B) Paraffin-embedded fixed lungs were stained with H&E and PAS, and images were captured at 20 $\times$ ; scale bar=100  $\mu$ m. (C) BAL supernatant was analyzed for total concentrations of albumin. (A and C) Kruskal-Wallis with Dunn's comparison to 2-day time point (within same sensitization protocol): \*,  $\leq 0.05$ . Kruskal-Wallis with Dunn's comparison to same time point (within different sensitization protocol): #,  $\leq 0.05$ . Data include 2 independent experiments and  $n=8$  to 12 mice.

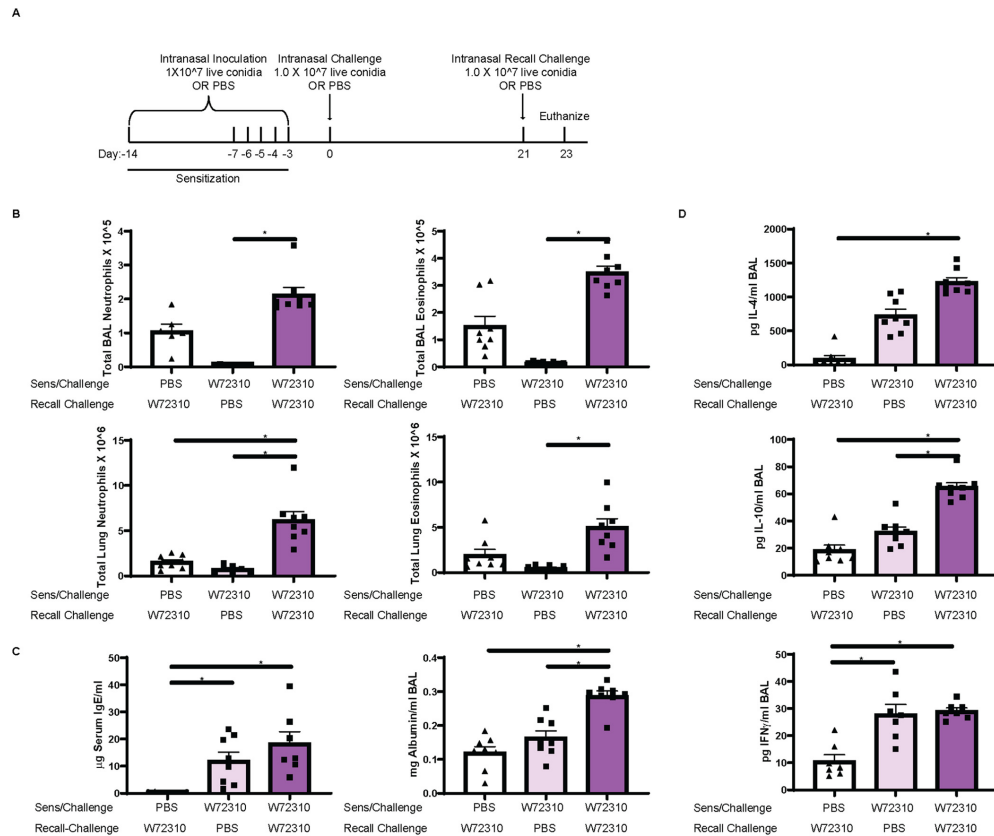


**FIG 6** Sensitization and challenge with W72310 and subsequent recall challenge cause increased tissue inflammation, damage, Th1/2, and IgE response. (A) Schematic of ABPA exacerbation protocol. C57BL/6 mice were inoculated with either PBS or  $1 \times 10^7$  live W72310 conidia on the indicated days (sensitization and challenge) and recall challenged 21 days after initial challenge. Animals were subsequently euthanized 48 h later. (B) Neutrophils (CD45<sup>+</sup>/SiglecF<sup>+</sup>/Ly6G<sup>+</sup>/CD11b<sup>+</sup>) and eosinophils (CD45<sup>+</sup>/SiglecF<sup>+</sup>/CD11c<sup>low</sup>) were quantified by flow cytometry in BAL fluid and lung suspensions. (C) Serum was isolated from mice, total IgE levels were quantified, and BAL supernatant was analyzed for total albumin. (D) BAL supernatant IL-4, IL-10, and IFN- $\gamma$  were measured. Mann-Whitney test with Dunn's multiple comparison was used. \*,  $P \leq 0.05$ .

novel fungal contributions to allergy-like diseases due to the long-term persistence of W72310 conidia in murine lungs.

We hypothesize that a key fungal mechanism for fungal persistence is enhanced oxidative stress resistance of the W72310 conidia. Reactive oxygen species (ROS) generated by NADPH-oxidases in neutrophils and macrophages are critical components in host defense against *A. fumigatus* infection (26, 27). Intriguingly, our data demonstrate that W72310 conidia are more resistant to both hydrogen peroxide- and menadione-induced death than CEA10 conidia (Fig. 7). Moreover, neutrophils and macrophages have reduced killing of W72310 conidia compared to CEA10 conidia (Fig. 1G). Genome sequencing revealed that W72310 has 20 oxidative stress response genes with high-impact SNPs (Table 1). Of particular interest, perhaps, the catalase *Afu6g03890/catA* has 6 variants in W72310 and not CEA10 (Table 1). Previous studies demonstrated that a catalase mutant generated in *A. fumigatus* was more sensitive to hydrogen peroxide. Interestingly, its conidia did not have any

**TABLE 1** Nonsynonymous variants found in W72310 relative to AF293 that are not found in CEA10 (O<sub>2</sub> stress, cell wall, and melanin genes)

	Gene ID	No. of exclusive variants	Annotation
O <sub>2</sub> stress	Afu2g01520	10	Ortholog(s) has role in ascospore formation, hyphal growth, response to oxidative stress, sporocarp development involved in sexual reproduction
	Afu3g10530	6	Putative protein serine/threonine kinase
	Afu6g03890	6	Spore-specific catalase
	Afu2g04680	5	Protein serine/threonine kinase
	Afu4g10770	5	Psi-producing oxygenase A
	Afu5g11820	5	Ortholog(s) has cytosol, nucleus localization
	Afu6g12522	5	Putative transcription factor and response regulator of a two-component signal transduction system
	Afu2g00200	4	Ortholog(s) has catalase activity
	Afu1g13600	3	Ortholog(s) has cyclin-dependent protein kinase activating kinase activity, cyclin-dependent protein serine/threonine kinase regulator activity, protein serine/threonine kinase activity
	Afu3g12670	3	Putative serine/threonine protein kinase
	Afu4g09110	3	Putative cytochrome c peroxidase
	Afu2g01700	2	Ortholog(s) has AMP-activated protein kinase activity, ARF guanyl-nucleotide exchange factor activity
	Afu3g02270	2	Mycelial catalase
	Afu4g00180	2	Fatty acid 8,11-diol synthase
	Afu7g03720	2	Ortholog(s) has RNA polymerase II carboxy-terminal domain kinase activity, cyclin-dependent protein kinase activating kinase activity, cyclin-dependent protein serine/threonine kinase activity
	Afu1g01980	1	Ortholog(s) has role in hyphal growth, response to cold, response to heat, response to oxidative stress, response to salt stress, sporocarp development involved in sexual reproduction
	Afu1g05930	1	Ortholog(s) has protein serine/threonine kinase activity
	Afu3g12120	1	Putative fatty acid oxygenase
	Afu5g08580	1	Putative alpha-1,6-mannosyltransferase that initiates the linkage of the N-glycan outer chain
	Afu5g09240	1	Cu/Zn superoxide dismutase
Cell wall	Afu1g13670	5	Conidial cell wall protein A
	Afu6g08510	5	Putative cell wall biosynthesis protein
	Afu3g07650	4	Has domain(s) with predicted pectinesterase activity, role in cell wall modification and cell wall localization
	Afu2g03120	2	Putative cell wall glucanase
	Afu4g03240	2	Putative cell wall galactomannoprotein
	Afu8g06880	2	Ortholog(s) has pectinesterase activity and role in pectin catabolic process
Melanin	Afu2g04200	9	4-Hydroxyphenylpyruvate dioxygenase involved in the L-tyrosine degradation pathway
	Afu1g16590	7	Putative C <sub>2</sub> H <sub>2</sub> transcription factor
	Afu1g15440	4	Putative alpha(1-3) glucan synthase
	Afu2g17550	1	Heptaketide hydrolyase ayg1
	Afu2g17560	1	1,3,6,8-Tetrahydroxynaphthalene reductase arp2
	Afu2g17600	1	Conidial pigment polyketide synthase alb1

difference in susceptibility to immune-cell-mediated killing and had similar pathogenicity in mouse models of aspergillosis as did wild-type controls (28–30). Since there are 20 oxidative stress response genes with variants in the W72310 strain, it seems likely that more than one gene/mechanism is involved in its defense against ROS-induced killing. However, we cannot rule out that novel alleles of genes like *catA* encode proteins with increased activity.

Another fungus-centric striking observation from our studies is that W72310 persists in the mouse lung largely as viable conidia. Based on the histology at 21 days postchallenge (Fig. 4C), we observed that the majority of conidia appear to be phagocytosed by large macrophage-like cells. Previous histological analyses of invasive aspergillosis patients have also demonstrated the presence of multiple conidia per giant cell (31); however, the viability of the fungus is not known. Case reports often show *A. fumigatus* in the lung as germlings or hyphae by GMS stain (32), but it is not known whether conidia, germlings, hyphae, or some combination contribute to ABPA and fungal allergic disease pathogenesis. Given that W72310 has previously been shown to have reduced germination rates in comparison to other strains (19, 20), another explanation for its persistence is that remaining in its conidial form does not



**TABLE 2** Nonsynonymous variants found in W72310 relative to AF293 that are not found in CEA10 (allergen genes)

Gene ID	No. of exclusive variants	Annotation
Afu1g02980	21	Putative 6-phosphogluconolactonase
Afu7g05740	10	Putative NAD-dependent malate dehydrogenase
Afu5g11320	9	Allergen Asp f 29
Afu5g04170	6	Heat shock protein
Afu1g14560	5	Putative 1,2-alpha-mannosidase
Afu2g01010	5	Putative myo-inositol-phosphate synthase
Afu2g01170	5	1,3-Beta-glucanosyltransferase with a role in elongation of 1,3-beta-glucan chains
Afu3g11690	5	Putative class II fructose-bisphosphate aldolase
Afu1g09470	4	Putative class V aminotransferase
Afu1g09670	4	Putative HLH transcription factor
Afu2g13530	4	Putative translation elongation factor EF-2 subunit
Afu3g00590	4	Asp-hemolysin
Afu4g01290	4	Glycosyl hydrolase family 75 chitosanase
Afu6g10300	4	Allergen Asp f 28
Afu1g14570	3	Putative phosphoribosyl-AMP cyclohydrolase
Afu2g03830	3	Allergen Asp f 4
Afu2g09960	3	Putative mitochondrial Hsp70 chaperone
Afu3g01110	3	Putative GMP synthase (glutamine-hydrolyzing)
Afu4g10130	3	Ortholog(s) has alpha-amylase activity and role in carbohydrate catabolic process
Afu4g11720	3	Putative phosphatidyl synthase
Afu5g09580	3	Conidial hydrophobin
Afu6g04920	3	Putative NAD-dependent formate dehydrogenase
Afu6g10660	3	Putative ATP citrate lyase subunit
Afu7g05720	3	Pyruvate dehydrogenase complex, dihydrolipoamide acetyltransferase component
Afu1g04130	2	FG-GAP repeat protein
Afu2g10100	2	Allergen Asp f 8
Afu2g11150	2	Putative secretory-pathway GDP dissociation inhibitor
Afu2g11260	2	Putative 3-isopropylmalate dehydratase with a predicted role in nitrogen metabolism
Afu2g16820	2	Putative curved DNA-binding protein
Afu3g00600	2	Ortholog of <i>Aspergillus fumigatus</i> A1163: AFUB_047840
Afu3g02270	2	Mycelial catalase
Afu3g09320	2	Serine hydroxymethyltransferase
Afu4g03240	2	Putative cell wall galactomannoprotein
Afu4g06670	2	Allergen Asp f 7
Afu4g10460	2	Homocitrate synthase, essential enzyme of the alpha-aminoadipate pathway of lysine biosynthesis
Afu5g05540	2	Putative nucleosome assembly protein
Afu5g09210	2	Autophagic (vacuolar) serine protease
Afu5g13300	2	Putative extracellular aspartic endopeptidase
Afu6g02230	2	Putative glucokinase
Afu6g02280	2	Allergen Asp f 3
Afu6g09690	2	Glutathione S-transferase gliG
Afu6g09740	2	Thioredoxin reductase gliT
Afu8g07080	2	Putative secreted metalloprotease
Afu1g02820	1	Putative NADH-quinone oxidoreductase
Afu1g06830	1	Putative 60s acidic ribosomal protein superfamily member
Afu1g07440	1	Molecular chaperone
Afu1g08980	1	UPF0160 domain protein
Afu1g10630	1	Putative S-adenosylmethionine synthetase
Afu1g11460	1	Putative 1,3-beta-glucanosyltransferase
Afu2g00690	1	Ortholog(s) has glucan 1,4-alpha-glucosidase activity, role in polysaccharide metabolic process and Golgi apparatus, endoplasmic reticulum, prospore membrane localization
Afu2g06150	1	Putative protein disulfide isomerase
Afu2g12630	1	Allergen Asp f 13
Afu2g13250	1	Putative bifunctional tryptophan synthase
Afu2g15430	1	Sorbitol/xylulose reductase
Afu3g03060	1	Allergen Asp f 34
Afu3g07430	1	Putative peptidyl-prolyl <i>cis-trans</i> isomerase
Afu3g10460	1	Putative nuclear transport factor
Afu3g11300	1	Putative proteasome component
Afu3g11400	1	Aspartic acid endopeptidase
Afu4g00610	1	Putative aryl-alcohol dehydrogenase

(Continued on next page)

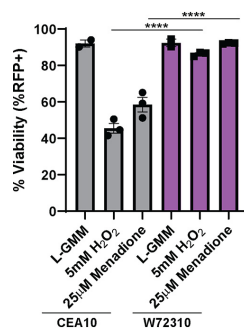


TABLE 2 (Continued)

Gene ID	No. of exclusive variants	Annotation
Afu4g07410	1	Has domain(s) with predicted catalytic activity
Afu4g07690	1	Putative phosphoribosylaminoimidazole-carboxamide formyltransferase/IMP cyclohydrolase
Afu4g08720	1	Putative secreted phospholipase B
Afu5g06390	1	Putative adenosine kinase
Afu5g10550	1	ATP synthase F1, beta subunit
Afu6g06770	1	Putative enolase
Afu6g11330	1	Ortholog(s) has thiamine phosphate phosphatase activity and role in dephosphorylation, thiamine biosynthetic process
Afu6g12930	1	Mitochondrial aconitate hydratase
Afu8g05020	1	Putative secreted <i>N</i> -acetylhexosaminidase

allow full immune recognition of the fungus. Of note, W72310 elicited less of an inflammatory response than CEA10 in an immunocompetent pulmonary challenge model (Fig. 1E). LC3-associated phagocytosis has been shown to be critical in fungal killing and is dependent on exposure of the fungal cell wall components melanin and  $\beta$ -glucan (33). Sequence analysis showed high-impact SNPs in 6 cell wall genes and 6 melanin genes which could potentially prevent full recognition and/or killing of the fungus (Table 1). Collectively, SNPs in melanin and cell wall stress genes may affect overall germination, and immune cell recognition of W72310 and SNPs in oxidative stress response genes could affect overall viability of phagocytosed W72310 conidia. Rigorous fungal genetic studies will be needed to determine specifically which gene(s) is important overall for the persistent phenotype.

Despite a similar immunological response to sensitization between W72310 and CEA10, select interferon-responsive genes were differentially expressed. CXCR3 was not differentially expressed between W72310 and CEA10 (data not shown); however, expression of its ligands, CXCL9 and CXCL10, was higher in W72310-sensitized lungs than in those sensitized to CEA10. CXCL9 and CXCL10, which have been shown to be induced in other mouse models of asthma and *A. fumigatus*-induced inflammation (34–36), activate Th1-type immune responses through CXCR3. Because CXCR3 is preferentially expressed in Th1 cells (37), this could indicate a potential role for the Th1 immune response in the overall persistence observed from W72310. Both in a mouse model of severe asthma and in humans with severe asthma, CXCL10 was shown to play a critical role in corticosteroid resistance and Th1-mediated inflammation (38).



**FIG 7** W72310 is more resistant to oxidative stress-induced death than CEA10. mRFP-CEA10 and mRFP-W72310 were incubated with either 25  $\mu$ M menadione or 5 mM H<sub>2</sub>O<sub>2</sub> for 6 h and analyzed by flow cytometry for viability (%RFP<sup>+</sup>). Data are representative of 3 independent experiments with 3 to 4 technical replicates/experiment. One-way analysis of variance (ANOVA) with Tukey's multiple comparison was used; \*\*\*\*,  $P \leq 0.0001$ .

However, differences in the immune response at this time point could be in response to either the different strains of fungi or different quantities of fungi, since we observe significantly more W72310 CFU at this time point (Fig. 2C).

The results of our present study indicate that persistent conidial colonization in the fungus-sensitized mouse lung causes many features of ABPA-like disease (Fig. 4 and 6). Diagnosis of ABPA has proven to be challenging, and it has long been postulated that ABPA rates are underrepresented due to a lack of consistency in diagnostic methods (22). Elevated total and *A. fumigatus*-specific IgE, *A. fumigatus* cutaneous reactivity, bronchial asthma, airway eosinophilia, and bronchiectasis are the major criteria utilized to diagnose ABPA. Our data show increased airway eosinophilia, serum IgE, and albumin in the BAL fluid of mice up to 21 days after challenge with *A. fumigatus*, indicating a pathogenic role for *A. fumigatus* long-term persistence. In other published mouse models of ABPA, repeated inoculation is required for these phenotypes to be maintained (34, 39). Further analysis of airway mechanics, host immunology, and changes in morphology will be needed to determine the extent of ABPA disease-like pathogenesis in animals with a longer-term W72310 infection.

Importantly, ABPA is primarily diagnosed in patients with cystic fibrosis, due to an environment in the lung prone to long-term microbial colonization. Mouse models of CF have also shown a strong role for *A. fumigatus* in CF disease pathogenesis. CF transmembrane conductance regulator (CFTR) knockout (KO) and dF508 mice develop robust inflammatory, IL-4, and IgE (specifically in CD4<sup>+</sup> T cells) responses to *A. fumigatus* hyphal extract (40). Additionally, exposure of mice to *A. fumigatus* conidia for 24 to 72 h causes increased inflammation, mucus production, and BAL fluid inflammatory cytokine production in CFTR KO compared to WT mice (41), and increased inflammasome activity was observed in CFTR KO mice in response to *A. fumigatus* conidial exposure (42). Future experiments exposing genetically engineered CF mice to W72310 could provide valuable insight into mechanisms of disease pathogenesis and therapeutic efficacy. These types of studies could be especially critical because the concept that strains of *A. fumigatus* can survive in the lung without germinating but cause ABPA-like disease would significantly affect the types of treatments a patient would receive, including antifungals. Moreover, identification of specific fungal alleles that promote long-term persistence may help diagnose chronic infections in lieu of transient colonization that would help guide antifungal deployment in these at-risk groups, such as CF patients.

## MATERIALS AND METHODS

**Animal inoculations.** Mice were housed in autoclaved cages at  $\leq 4$  mice per cage with HEPA-filtered air and water. For single-exposure studies, outbred wild-type C57BL/6 female mice 8 to 12 weeks old (Jackson Laboratories) were intranasally inoculated with  $1 \times 10^7$  live conidia (in 40  $\mu$ l PBS) per mouse. *A. fumigatus* strains CEA10 and W72310 were grown on 1% glucose minimal medium (GMM) for 3 days at 37°C, and conidia were collected in 0.01% Tween and washed 3 times in sterile PBS. Animals were inoculated with  $3 \times 10^7$  live conidia for 36 h (FLARE),  $1 \times 10^7$  live conidia 1 time in week 1 and 5 times in week 2 (sensitization), and  $1 \times 10^7$  live conidia on the first day of week 3 (challenge). Animals were monitored daily for disease symptoms, and we carried out our animal studies in strict accordance with the recommendations in the *Guide for the Care and Use of Laboratory Animals* (43). The animal experimental protocol 00002241 was approved by the Institutional Animal Care and Use Committee (IACUC) at Dartmouth College.

**Isolation of bone marrow and coculture conditions.** After euthanasia, femur and tibia were extracted from 8- to 12-week-old C57BL/6 mice and the bones were flushed with PBS to collect bone marrow-derived cells. After red blood cell lysis, cells were counted and cultured with either mRFP-CEA10 or mRFP-W72310 AF633-stained conidia as described previously (21) for 16 h at a 10:1 multiplicity of infection (MOI) with 10 ng/ml interferon gamma (IFN- $\gamma$ ) and 25 mM hydroxyurea (HU).

**In vitro conidial killing assay.** Freshly harvested murine BMDMs were dosed to  $1 \times 10^6$ /ml in medium, and 1 ml of the above culture was transferred to each well of a 24-well plate. After an overnight incubation at 37°C with 5% CO<sub>2</sub> to allow attachment, the BMDM medium was removed and replaced with 0.5 ml of fresh BMDM medium containing  $2 \times 10^6$ /ml *A. fumigatus* conidia from strains of interest (MOI = 1). After 1 h, unbound/unphagocytosed conidia were removed in all wells by aspirating the BMDM medium and gently washing with 1 ml of PBS for each well. For the 1-h group, 200  $\mu$ l 0.5% sterile SDS in distilled water was added and incubated for 10 min to lyse the macrophages and conduct serial dilutions in sterile 0.01% Tween 80 in distilled water. For the 4-h group, 0.5 ml BMDM medium was added back and incubated for another 3 h before lysing the SDS solution followed by serial dilutions as

above. All serial dilutions (from  $10^4$  to  $10^5$ ,  $100\mu\text{l}$ ) were pipetted on GMM plates via sterile plate spreaders and incubated for 2 days. Plates containing between 30 and 200 colonies were counted, and the number of viable conidia was calculated. The survival rate of 3-h BMDM killing was calculated by  $n$  (4-h group)/ $n$  (1-h group).

**Hygromycin-resistant and mRFP strain generation.** Protoplasts from strains CEA10 and W72310 were generated with *Trichoderma harzianum* (Millipore Sigma) lysing enzyme and transformed ectopically with linear constructs of the *gpdA*-driven *hph* hygromycin resistance gene or H2A-mRFP (CEA10) as previously described (44, 45).

**RNA preparation and NanoString analysis.** Animals were “sensitized” to either PBS, CEA10, or W72310 as described previously, and lungs were removed at euthanasia for mRNA analysis. Lungs were freeze-dried, homogenized with glass beads using Mini Bead Beater (BioSpec Products Inc., Bartlesville, OK), and resuspended in TRIzol (Thomas Scientific) and chloroform to extract RNA according to manufacturer’s instructions. After RNA was assessed for quality, 500 ng of RNA was used per NanoString reaction using the nCounter Mouse Immunology v1 Gene Expression Panel (NanoString). nSolver 4.0 software was used for background subtraction and normalization. nCounter Advanced Analysis 2.0 was used for quality control analysis and pathway analysis. For additional pathway analysis, accession numbers were converted to Entrez IDs via the DAVID Gene Accession Conversion Tool (46, 47). The Entrez IDs were then used to pull GO terms for each gene from the Mouse Genome Informatics’ website (<http://www.informatics.jax.org/batch>). The resulting file was reformatted to fit the TopGO package’s requirements for gene ID to GO ID conversion (gene\_ID:t GOID1;GOID2:..:GOIDX). Genes were classified as increased or decreased based on a 2-fold change cutoff and a  $P$  value of  $\leq 0.05$ . Lists of all differentially expressed genes (DEGs), increased DEGs, or decreased DEGs were inserted into separate TopGOdata objects using the gene ID to GO ID conversion file to assign all possible GO terms for each gene. A nodesize cutoff of 10 was used, and a classic Fisher test followed by a Benjamini-Hochberg correction for multiple testing was performed via the TopGO R package (48) to determine enriched GO terms within the data sets. The degree of enrichment was calculated as the number of significant genes divided by the number of genes expected by random chance. Data were plotted via the ggplot2 and ComplexHeatmap (49) packages in R version 3.6.2 (12 December 2019).

**CFU.** Whole lungs were homogenized in 1 ml sterile PBS using glass beads in a Mini Bead Beater. Serial dilutions (1:10 to 1:1,000) were then spread onto agar plates containing Sabouraud medium or Sabouraud medium containing  $175\mu\text{g/ml}$  hygromycin and incubated overnight (O/N) at  $37^\circ\text{C}$ . Plate dilutions containing 50 to 100 visible colonies were quantified and expressed as a measurement of CFU per milliliter.

**Histology: GMS, PAS, and H&E.** After euthanasia, cannulas were inserted into trachea and lungs were excised from the body cavity. Lungs were inflated with 10% buffered formalin phosphate for 24 h and stored in 70% ethanol until embedding. Paraffin-embedded sections were stained with hematoxylin and eosin (H&E), Grocott-Gomori methenamine silver (GMS), and periodic acid-Schiff (PAS). Slides were analyzed microscopically with a Zeiss Axioplan 2 imaging microscope (Carl Zeiss Microimaging, Inc., Thornwood, NY) fitted with a QImaging Retiga-SRV Fast 1394 RGB camera.

**Serum analysis.** Cardiac punctures were performed postmortem. After 1 h at room temperature, blood samples were centrifuged at  $2,000 \times g$  for 30 min, and serum was isolated. Total IgE was measured by ELISA using a kit (Invitrogen) and performed according to the manufacturer’s instructions.

**BAL analysis (inflammatory cells, albumin, ELISAs).** After euthanasia, cannulas were inserted into trachea and lungs were removed. Lungs were lavaged with 3 sequential cold PBS washes (1 ml, 0.5 ml, 0.5 ml). Broncho-alveolar lavage (BAL) fluid was centrifuged at  $300 \times g$  for 5 min, and supernatant was removed for cytokine (IL-4, IL-10, and IFN- $\gamma$  [R&D]) and albumin (Eagle Diagnostics) analysis according to manufacturer’s instructions. Remaining cells were counted and centrifuged onto slides using Rotofix Cytospin. Up to 300 cells were counted to determine percentages of macrophages, neutrophils, eosinophils, and lymphocytes. Total numbers of individual cell populations were calculated using individual percentages multiplied by total BAL cell numbers.

**Cell death assay.** Liquid GMM was inoculated with  $2.0 \times 10^6$  mRFP-CEA10 or mRFP-W72310 and incubated with either  $25\mu\text{M}$  menadione or 5 mM hydrogen peroxide for 6 h at  $37^\circ\text{C}$ . After incubation, conidia were run on a Beckman Coulter Cytoflex S flow cytometer for percent positive RFP (viability). Analysis was performed using FlowJo version 9.9.6 as previously described (26).

**Flow cytometry and Fluorescence Aspergillus REporter (FLARE) analysis.** Whole-lung single-cell suspensions were prepared as described previously (45). Briefly, lungs were minced and digested in buffer containing 2.2 mg/ml collagenase type IV (Worthington),  $100\mu\text{g/ml}$  DNase I (Zymo Research), and 5% fetal bovine serum (FBS) at  $37^\circ\text{C}$  rotating for 45 min. Digested samples were then passed through an 18-gauge needle, resuspended in red blood cell lysis buffer, diluted with PBS, passed through a  $100\text{-}\mu\text{m}$  filter, and counted. For flow cytometry analysis, cells were stained with a viability dye (eFluor 780; eBioscience), anti-CD45 (Pacific Orange; Invitrogen), anti-CD11b (PECy5 [BioLegend] for cellularity, PerCPy5.5 [BioLegend] for FLARE), anti-CD11c (phycoerythrin [PE], BioLegend), anti-Ly6G (fluorescein isothiocyanate [FITC], BioLegend), anti-CD64 (BV421; BioLegend), and anti-SiglecF (BV421; BD Bioscience). Samples were analyzed on a MACSQuant VYB flow cytometer (cellularity) or Beckman Coulter Cytoflex S (FLARE). Macrophages were identified as  $\text{CD45}^+/\text{Ly6G}^-/\text{CD11b}^+/\text{CD64}^+$ , neutrophils were identified as  $\text{CD45}^+/\text{SiglecF}^-/\text{Ly6G}^+/\text{CD11b}^+$ , and eosinophils were identified as  $\text{CD45}^+/\text{SiglecF}^+/\text{CD11c}^{\text{low}}$ . Analysis was performed with FlowJo version 9.9.6.

**Genome sequencing and variant analyses.** Mycelial cultures of *A. fumigatus* using liquid glucose minimal medium with yeast extract were inoculated in small petri dishes grown overnight (18 to 24 h) at  $37^\circ\text{C}$ . Mycelia were collected, lyophilized, and bead beaten to powder, and DNA was extracted as previously described (50). Genomic sequencing libraries of the DNA were constructed using the SeqOnce

(SeqOnce Biosciences, Pasadena, CA) with multiplexing barcodes by the Genomics Core at UC Riverside Institute for Integrative Genome Biology. The genomic libraries were sequenced as 2 × 150-bp reads on an Illumina Novaseq 6000 (Illumina, San Diego, CA) at UC San Francisco Sequencing Core to generate ~2.17 Gb of sequence. Sequence data for strain CEA10 were obtained from the Sequence Read Archive under accession no. [ERR232423](https://www.ncbi.nlm.nih.gov/bioproject/PRJEB1497) and BioProject [PRJEB1497](https://www.ncbi.nlm.nih.gov/bioproject/PRJEB1497). The sequence reads for each strain were aligned to the Af293 genome downloaded from FungiDB v.46 (51, 52) using BWA v0.7.17 (53) and converted to the BAM file format after running fixmate and sort commands in SAMtools v1.10 (54). Duplicate reads were removed, and reads were indexed using MarkDuplicates and Build BamIndex in Picard tools v2.18.3 (<http://broadinstitute.github.io/picard>). To avoid overcalling variants near alignment gaps, reads were further realigned using RealignerTargetCreator and IndelRealigner in the Genome Analysis Toolkit GATK v3.7 (55). The variants (SNPs and indels) for W72310 and CEA10 were genotyped relative to the *A. fumigatus* reference genome Af293 using the HaplotypeCaller step in GATK v4.0 (<https://doi.org/10.1101/201178>). Filtering was accomplished using GATK's SelectVariants call with the following parameters: for SNPs, -window-size = 10, -QualByDepth < 2.0, -MapQual < 40.0, -QScore < 100, -MapQualityRankSum < -12.5, -StrandOddsRatio > 3.0, -FisherStrandBias > 60.0, -ReadPosRankSum < -8.0; for indels, -window-size = 10, -QualByDepth < 2.0, -MapQualityRankSum < -12.5, -StrandOddsRatio > 4.0, -FisherStrandBias > 200.0, -ReadPosRank < -20.0, -InbreedingCoeff < -0.8. Resultant variants were annotated with snpEff (56) using the Gene File Format gene annotation for Af293 v.46 in FungiDB. Variants that overlapped transposable elements (TEs) were removed by positional mapping to locations of annotated TEs in the FungiDB v.46 release of the Af293 reference genome, using BEDtools -subtract (57). Mutations in W72310 were analyzed relative to CEA10 using a custom script implemented in the R programming environment (58). To identify mutations occurring in allergen genes, a database of genes putatively capable of eliciting an immune response was curated from the published literature ( $n=113$ ) (Table 2) and mapped against W72310 variant positions using a custom script in R. Putative allergen genes in W72310 containing variants other than synonymous or intergenic mutations were annotated in Fungi DB v.46 (52). To investigate variants unique to W72310 and occurring in genes relevant to the phenotypes of interest in this study (oxidative stress, cell wall integrity, primary metabolism, and melanin production), we used reverse GO mapping of the terms GO:0006979 (response to oxidative stress), GO:0005618 (cell wall), GO:0044238 (primary metabolic process) GO:0006582 (melanin metabolic process), and GO:0042438 (melanin biosynthetic process).

**Statistical analysis.** All statistical analyses were performed with Prism 8.3 software (GraphPad Software Inc., San Diego, CA). For *in vitro* comparison of 2 groups, Student's *t* test was used. For animal experiments, nonparametric analyses were performed (Kruskal-Wallis, Dunn's multiple comparisons; Mann-Whitney, single comparisons). All error bars represent standard errors of the means. NS,  $P > 0.05$ ; \*,  $P \leq 0.05$ ; \*\*,  $P \leq 0.01$ ; \*\*\*,  $P \leq 0.001$ ; \*\*\*\*,  $P \leq 0.0001$ .

**Data availability.** Sequence data for W72310 were deposited in the Sequence Read Archive under BioProject no. [PRJNA614926](https://www.ncbi.nlm.nih.gov/bioproject/PRJNA614926). The code and data files for variant assessment associated with this project can be accessed via GitHub in the repository stjichlab/W72310 (<https://doi.org/10.5281/zenodo.4116457>) (59).

## ACKNOWLEDGMENTS

This work was supported by the efforts of R.A.C. through funding by NIH National Institute of Allergy and Infectious Diseases (NIAID) (grant no. R01AI130128 and R01AI146121), a pilot award from the Cystic Fibrosis Foundation (CFF) Research Development Award (STANTO15RO), and a CFF research award (CRAMERGO19). C.H.K. was supported by the NIH NIAID Ruth L. Kirschstein National Research Service Award (no. F31AI138354). Core facility support provided by NIH grant P30-DK117469 and NIH grant P20-GM113132 to the Dartmouth BioMT COBRE. J.E.S. is a CIFAR fellow in the program Fungal Kingdom: Threats and Opportunities. Computational analyses were performed on the University of California-Riverside HPCC supported by grants from the National Science Foundation (MRI-1429826) and NIH (S10OD016290). T.M.H. received support from NIH grants R01 AI093808 and R01 139632 and Core Grant P30 CA008748 (to MSKCC). J.J.O. received support from NIH grant R01 AI139133.

## REFERENCES

- Pashley CH. 2014. Fungal culture and sensitisation in asthma, cystic fibrosis and chronic obstructive pulmonary disorder: what does it tell us? *Mycopathologia* 178:457–463. <https://doi.org/10.1007/s11046-014-9804-y>.
- Haase G, Skopnik H, Groten T, Kusenbach G, Posselt HG. 1991. Long-term fungal cultures from sputum of patients with cystic fibrosis: Langzeitpilzkulturen von Sputum bei Patienten mit zystischer Fibrose. *Mycoses* 34:373–376. <https://doi.org/10.1111/j.1439-0507.1991.tb00797.x>.
- Rapaka RR, Kolls JK. 2009. Pathogenesis of allergic bronchopulmonary aspergillosis in cystic fibrosis: current understanding and future directions. *Med Mycol* 47(Suppl 1):S331–S337. <https://doi.org/10.1080/1369378080266777>.
- Saunders RV, Modha DE, Claydon A, Gaillard EA. 2016. Chronic *Aspergillus fumigatus* colonization of the pediatric cystic fibrosis airway is common and may be associated with a more rapid decline in lung function. *Med Mycol* 54:537–543. <https://doi.org/10.1093/mmy/myv119>.
- Stevens DA, Moss RB, Kurup VP, Knutsen AP, Greenberger P, Judson MA, Denning DW, Cramer R, Brody AS, Light M, Skov M, Maish W, Mastella G, Participants in the Cystic Fibrosis Foundation Consensus Conference. 2003. Allergic bronchopulmonary aspergillosis in cystic fibrosis—state of the art: Cystic Fibrosis Foundation Consensus Conference. *Clin Infect Dis* 37:S225–S264. <https://doi.org/10.1086/376525>.
- King J, Brunel SF, Warris A. 2016. *Aspergillus* infections in cystic fibrosis. *J Infect* 72:S50–S55. <https://doi.org/10.1016/j.jinf.2016.04.022>.

27. Chotirmall SH, McElvaney NG. 2014. Fungi in the cystic fibrosis lung: bystanders or pathogens? *Int J Biochem Cell Biol* 52:161–173. <https://doi.org/10.1016/j.biocel.2014.03.001>.
28. Kauffman HF. 2003. Immunopathogenesis of allergic bronchopulmonary aspergillosis and airway remodeling. *Front Biosci* 8:e190–e196. <https://doi.org/10.2741/990>.
29. Hayes D, Murphy BS, Lynch JE, Feola DJ. 2010. Aerosolized amphotericin for the treatment of allergic bronchopulmonary aspergillosis. *Pediatr Pulmonol* 45:1145–1148. <https://doi.org/10.1002/ppul.21300>.
30. Wark P. 2004. Pathogenesis of allergic bronchopulmonary aspergillosis and an evidence-based review of azoles in treatment. *Respir Med* 98:915–923. <https://doi.org/10.1016/j.rmed.2004.07.002>.
31. Urb M, Snarr BD, Wojewodka G, Lehoux M, Lee MJ, Ralph B, Divangahi M, King IL, McGovern TK, Martin JG, Fraser R, Radzioch D, Sheppard DC. 2015. Evolution of the immune response to chronic airway colonization with *Aspergillus fumigatus* hyphae. *Infect Immun* 83:3590–3600. <https://doi.org/10.1128/IAI.00359-15>.
32. Nawada R, Amitani R, Tanaka E, Niimi A, Suzuki K, Murayama T, Kuze F. 1996. Murine model of invasive pulmonary aspergillosis following an earlier stage, noninvasive *Aspergillus* infection. *J Clin Microbiol* 34:1433–1439. <https://doi.org/10.1128/JCM.34.6.1433-1439.1996>.
33. Hogaboam CM, Gallinat CS, Taub DD, Strieter RM, Kunkel SL, Lukacs NW. 1999. Immunomodulatory role of C10 chemokine in a murine model of allergic bronchopulmonary aspergillosis. *J Immunol* 162:6071–6079.
34. Murdock BJ, Shreiner AB, McDonald RA, Osterholzer JJ, White ES, Toews GB, Huffnagle GB. 2011. Coevolution of  $T_H1$ ,  $T_H2$ , and  $T_H17$  responses during repeated pulmonary exposure to *Aspergillus fumigatus* conidia. *Infect Immun* 79:125–135. <https://doi.org/10.1128/IAI.00508-10>.
35. Kosmidis C, Denning DW. 2015. The clinical spectrum of pulmonary aspergillosis. *Thorax* 70:270–277. <https://doi.org/10.1136/thoraxjnl-2014-206291>.
36. Paugam A, Baixench M-T, Demazes-Dufeu N, Burgel P-R, Sauter E, Kanaan R, Dussert D, Dupouy-Camet J, Hubert D. 2010. Characteristics and consequences of airway colonization by filamentous fungi in 201 adult patients with cystic fibrosis in France. *Med Mycol* 48:532–536. <https://doi.org/10.3109/13693786.2010.503665>.
37. Chen KTK. 1993. Cytology of allergic bronchopulmonary aspergillosis. *Diagn Cytopathol* 9:82–85. <https://doi.org/10.1002/dc.2840090118>.
38. Chetty A. 2003. Pathology of allergic bronchopulmonary aspergillosis. *Front Biosci* 8:e110–e114. <https://doi.org/10.2741/945>.
39. Kowalski CH, Beattie SR, Fuller KK, McGurk EA, Tang Y-W, Hohl TM, Obar JJ, Cramer RA, Jr. 2016. Heterogeneity among isolates reveals that fitness in low oxygen correlates with *Aspergillus fumigatus* virulence. *mBio* 7:e01515-16. <https://doi.org/10.1128/mBio.01515-16>.
40. Caffrey-Carr AK, Kowalski CH, Beattie SR, Blaseg NA, Upshaw CR, Thammarahong A, Lust HE, Tang Y-W, Hohl TM, Cramer RA, Obar JJ. 2017. Interleukin 1 $\alpha$  is critical for resistance against highly virulent *Aspergillus fumigatus* isolates. *Infect Immun* 85:e00661-17. <https://doi.org/10.1128/IAI.00661-17>.
41. Jhingran A, Mar KB, Kumasaka DK, Knoblaugh SE, Ngo LY, Segal BH, Iwakura Y, Lowell CA, Hamerman JA, Lin X, Hohl TM. 2012. Tracing conidia fate and measuring host cell antifungal activity using a reporter of microbial viability in the lung. *Cell Rep* 2:1762–1773. <https://doi.org/10.1016/j.celrep.2012.10.026>.
42. Patel AR, Patel AR, Singh S, Khawaja I. 2019. Diagnosing allergic bronchopulmonary aspergillosis: a review. *Cureus* 11:e4550. <https://doi.org/10.7759/cureus.4550>.
43. Fukahori S, Matsuse H, Tsuchida T, Kawano T, Nishino T, Fukushima C, Kohno S. 2014. Clearance of *Aspergillus fumigatus* is impaired in the airway in allergic inflammation. *Ann Allergy Asthma Immunol* 113:180–186. <https://doi.org/10.1016/j.anaai.2014.05.011>.
44. Keown K, Abbott S, Kuzeljevic B, Rayment JH, Chilvers MA, Yang CL. 2019. An investigation into biomarkers for the diagnosis of ABPA and aspergillosis disease in cystic fibrosis. *Pediatr Pulmonol* 54:1787–1793. <https://doi.org/10.1002/ppul.24465>.
45. Agarwal R, Chakrabarti A, Shah A, Gupta D, Meis JF, Guleria R, Moss R, Denning DW, ABPA complicating asthma ISHAM working group. 2013. Allergic bronchopulmonary aspergillosis: review of literature and proposal of new diagnostic and classification criteria. *Clin Exp Allergy* 43:850–873. <https://doi.org/10.1111/cea.12141>.
46. Shlezinger N, Irmer H, Dhingra S, Beattie SR, Cramer RA, Braus GH, Sharon A, Hohl TM. 2017. Sterilizing immunity in the lung relies on targeting fungal apoptosis-like programmed cell death. *Science* 357:1037–1041. <https://doi.org/10.1126/science.aan0365>.
47. Boyle KB, Stephens LR, Hawkins PT. 2012. Activation of the neutrophil NADPH oxidase by *Aspergillus fumigatus*. *Ann N Y Acad Sci* 1273:68–73. <https://doi.org/10.1111/j.1749-6632.2012.06821.x>.
48. Paris S, Wysong D, Debeaupuis JP, Shibuya K, Philippe B, Diamond RD, Latgé JP. 2003. Catalases of *Aspergillus fumigatus*. *Infect Immun* 71:3551–3562. <https://doi.org/10.1128/IAI.71.6.3551-3562.2003>.
49. Calera JA, Paris S, Monod M, Hamilton AJ, Debeaupuis JP, Diaquin M, López-Medrano R, Leal F, Latgé JP. 1997. Cloning and disruption of the antigenic catalase gene of *Aspergillus fumigatus*. *Infect Immun* 65:4718–4724. <https://doi.org/10.1128/IAI.65.11.4718-4724.1997>.
50. Lessing F, Knemeyer O, Wozniok I, Loeffler J, Kurzai O, Haertl A, Brakhage AA. 2007. The *Aspergillus fumigatus* transcriptional regulator AfYap1 represents the major regulator for defense against reactive oxygen intermediates but is dispensable for pathogenicity in an intranasal mouse infection model. *Eukaryot Cell* 6:2290–2302. <https://doi.org/10.1128/EC.00267-07>.
51. Milroy CM, Blanshard JD, Lucas S, Michaels L. 1989. Aspergillosis of the nose and paranasal sinuses. *J Clin Pathol* 42:123–127. <https://doi.org/10.1136/jcp.42.2.123>.
52. Pokharel S, Ylagan L, Cheney R. 2014. Allergic bronchopulmonary aspergillosis: a diagnostic challenge. *J Cytol Histol* 54:2. <https://doi.org/10.4172/2157-7099.54-021>.
53. Akoumianaki T, Kymizi I, Valsecchi I, Gresnigt MS, Samonis G, Drakos E, Boumpas D, Muszkieta L, Prevost MC, Kontoyiannis DP, Chavakis T, Netea MG, Van De Veerdonk FL, Brakhage AA, El-Benna J, Beauvais A, Latgé JP, Chamli G. 2016. *Aspergillus* cell wall melanin blocks LC3-associated phagocytosis to promote pathogenicity. *Cell Host Microbe* 19:79–90. <https://doi.org/10.1016/j.chom.2015.12.002>.
54. Ramaprakash H, Shibata T, Duffy KE, Ismailoglu UB, Bredernitz RM, Moreira AP, Coelho AL, Das AM, Fursov N, Chupp GL, Hogaboam CM. 2011. Targeting ST2L potentiates CpG-mediated therapeutic effects in a chronic fungal asthma model. *Am J Pathol* 179:104–115. <https://doi.org/10.1016/j.ajpath.2011.03.032>.
55. Schuh JM, Blease K, Hogaboam CM. 2002. CXCR2 is necessary for the development and persistence of chronic fungal asthma in mice. *J Immunol* 168:1447–1456. <https://doi.org/10.4049/jimmunol.168.3.1447>.
56. Su Y-C, Rolph MS, Hansbro NG, Mackay CR, Sewell WA. 2008. Granulocyte-macrophage colony-stimulating factor is required for bronchial eosinophilia in a murine model of allergic airway inflammation. *J Immunol* 180:2600–2607. <https://doi.org/10.4049/jimmunol.180.4.2600>.
57. Bonecchi R, Bianchi G, Bordignon PP, D'Ambrosio D, Lang R, Borsatti A, Sozzani S, Allavena P, Gray PA, Mantovani A, Sinigaglia F. 1998. Differential expression of chemokine receptors and chemotactic responsiveness of type 1 T helper cells (Th1s) and Th2s. *J Exp Med* 187:129–134. <https://doi.org/10.1084/jem.187.1.129>.
58. Gauthier M, Chakraborty K, Oriss TB, Raundhal M, Das S, Chen J, Huff R, Sinha A, Fajt M, Ray P, Wenzel SE, Ray A. 2017. Severe asthma in humans and mouse model suggests a CXCL10 signature underlies corticosteroid-resistant Th1 bias. *JCI Insight* 2:e94580. <https://doi.org/10.1172/jci.insight.94580>.
59. Hogaboam CM, Blease K, Mehrad B, Steinhauser ML, Standiford TJ, Kunkel SL, Lukacs NW. 2000. Animal model: chronic airway hyperreactivity, goblet cell hyperplasia, and peribronchial fibrosis during allergic airway disease induced by *Aspergillus fumigatus*. *Am J Pathol* 156:723–732. [https://doi.org/10.1016/S0002-9440\(10\)64775-X](https://doi.org/10.1016/S0002-9440(10)64775-X).
60. Allard JB, Poynter ME, Marr KA, Cohn L, Rincon M, Whittaker LA. 2006. *Aspergillus fumigatus* generates an enhanced Th2-biased immune response in mice with defective cystic fibrosis transmembrane conductance regulator. *J Immunol* 177:5186–5194. <https://doi.org/10.4049/jimmunol.177.8.5186>.
61. Chaudhary N, Datta K, Askin FB, Staab JF, Marr KA. 2012. Cystic fibrosis transmembrane conductance regulator regulates epithelial cell response to *Aspergillus* and resultant pulmonary inflammation. *Am J Respir Crit Care Med* 185:301–310. <https://doi.org/10.1164/rccm.201106-1027OC>.
62. Iannitti RG, Napolioni V, Oikonomou V, De Luca A, Galosi C, Pariano M, Massi-Benedetti C, Borghi M, Puccetti M, Lucidi V, Colombo C, Ficarelli E, Lass-Flörl C, Majo F, Cariani L, Russo M, Porcaro L, Ricciotti G, Ellemunter H, Ratcliff L, De Benedictis FM, Tases VN, Dinarello CA, van de Veerdonk FL, Romani L. 2016. IL-1 receptor antagonist ameliorates inflammasome-dependent inflammation in murine and human cystic fibrosis. *Nat Commun* 7:10791. <https://doi.org/10.1038/ncomms10791>.
63. National Research Council. 2011. Guide for the care and use of laboratory animals, 8th ed. National Academies Press, Washington, DC.
64. Grahl N, Puttkamonkul S, Macdonald JM, Gamcsik MP, Ngo LY, Hohl TM, Cramer RA. 2011. In vivo hypoxia and a fungal alcohol dehydrogenase

- influence the pathogenesis of invasive pulmonary aspergillosis. *PLoS Pathog* 7:e1002145. <https://doi.org/10.1371/journal.ppat.1002145>.
45. Kowalski CH, Kerkaert JD, Liu K-W, Bond MC, Hartmann R, Nadell CD, Stajich JE, Cramer RA. 2019. Fungal biofilm morphology impacts hypoxia fitness and disease progression. *Nat Microbiol* 4:2430–2412. <https://doi.org/10.1038/s41564-019-0558-7>.
46. Huang DW, Sherman BT, Lempicki RA. 2009. Bioinformatics enrichment tools: paths toward the comprehensive functional analysis of large gene lists. *Nucleic Acids Res* 37:1–13. <https://doi.org/10.1093/nar/gkn923>.
47. Huang DW, Sherman BT, Tan Q, Kir J, Liu D, Bryant D, Guo Y, Stephens R, Baseler MW, Lane HC, Lempicki RA. 2007. DAVID Bioinformatics Resources: expanded annotation database and novel algorithms to better extract biology from large gene lists. *Nucleic Acids Res* 35(Web Server issue): W169–W175. <https://doi.org/10.1093/nar/gkm415>.
48. Alexa A, Rahnenführer J, Lengauer T. 2006. Improved scoring of functional groups from gene expression data by decorrelating GO graph structure. *Bioinformatics* 22:1600–1607. <https://doi.org/10.1093/bioinformatics/btl140>.
49. Gu Z, Eils R, Schlesner M. 2016. Complex heatmaps reveal patterns and correlations in multidimensional genomic data. *Bioinformatics* 32:2847–2849. <https://doi.org/10.1093/bioinformatics/btw313>.
50. Griffiths LJ, Anyim M, Doffman SR, Wilks M, Millar MR, Agrawal SG. 2006. Comparison of DNA extraction methods for *Aspergillus fumigatus* using real-time PCR. *J Med Microbiol* 55:1187–1191. <https://doi.org/10.1099/jmm.0.46510-0>.
51. Stajich JE, Harris T, Brunk BP, Brestelli J, Fischer S, Harb OS, Kissinger JC, Li W, Nayak V, Pinney DF, Stoeckert CJ, Roos DS. 2012. FungiDB: an integrated functional genomics database for fungi. *Nucleic Acids Res* 40(Database issue):D675–D681. <https://doi.org/10.1093/nar/gkr918>.
52. Basenko EY, Pulman JA, Shanmugasundram A, Harb OS, Crouch K, Starns D, Warrenfeltz S, Aurrecoechea C, Stoeckert CJ, Kissinger JC, Roos DS, Hertz-Fowler C. 2018. FungiDB: an integrated bioinformatic resource for fungi and oomycetes. *J Fungi* 4:39. <https://doi.org/10.3390/jof4010039>.
53. Li H, Wren J. 2014. Toward better understanding of artifacts in variant calling from high-coverage samples. *Bioinformatics* 30:2843–2851. <https://doi.org/10.1093/bioinformatics/btu356>.
54. Li H, Handsaker B, Wysoker A, Fennell T, Ruan J, Homer N, Marth G, Abecasis G, Durbin R, 1000 Genome Project Data Processing Subgroup. 2009. The Sequence Alignment/Map format and SAMtools. *Bioinformatics* 25:2078–2079. <https://doi.org/10.1093/bioinformatics/btp352>.
55. Van der Auwera GA, Carneiro MO, Hartl C, Poplin R, Del Angel G, Levy-Moonshine A, Jordan T, Shakir K, Roazen D, Thibault J, Banks E, Garimella KV, Altshuler D, Gabriel S, DePristo MA. 2013. From FastQ data to high confidence variant calls: the Genome Analysis Toolkit best practices pipeline. *Curr Protoc Bioinformatics* 43:11.10.1–11.10.33. <https://doi.org/10.1002/0471250953.bi1110s43>.
56. Cingolani P, Platts A, Wang LL, Coon M, Nguyen T, Wang L, Land SJ, Lu X, Ruden DM. 2012. A program for annotating and predicting the effects of single nucleotide polymorphisms, SnpEff: SNPs in the genome of *Drosophila melanogaster* strain w1118; iso-2; iso-3. *Fly (Austin)* 6:80–92. <https://doi.org/10.4161/fly.19695>.
57. Quinlan AR, Hall IM. 2010. BEDTools: a flexible suite of utilities for comparing genomic features. *Bioinformatics* 26:841–842. <https://doi.org/10.1093/bioinformatics/btq033>.
58. R Development Core Team. 2013. R: a language and environment for statistical computing. R Foundation for Statistical Computing, Vienna, Austria.
59. Stajich JE, Lofgren LA. 2020. stajichlab/W72310: W72310 variant pipeline. <https://zenodo.org/record/4116457#.X8k75KpKgWo>.

## Appendix IV

### Fungal Biofilm Morphology Impacts Hypoxia Fitness and Disease Progression

Caitlin H. Kowalski, Joshua D. Kerkaert, Ko-Wei Liu, Matthew C. Bond, Raimo Hartmann,  
Carey D. Nadell, Jason E. Stajich & Robert A. Cramer

KWL designed and performed the experiments, and analyzed the results in Figure 6J and  
6K

# Fungal biofilm morphology impacts hypoxia fitness and disease progression

Caitlin H. Kowalski<sup>1</sup>, Joshua D. Kerkaert<sup>1</sup>, Ko-Wei Liu<sup>1</sup>, Matthew C. Bond<sup>2</sup>, Raimo Hartmann<sup>4</sup>, Carey D. Nadell<sup>3</sup>, Jason E. Stajich<sup>3</sup> and Robert A. Cramer<sup>1\*</sup>

**Microbial populations form intricate macroscopic colonies with diverse morphologies whose functions remain to be fully understood. Despite fungal colonies isolated from environmental and clinical samples revealing abundant intraspecies morphological diversity, it is unclear how this diversity affects fungal fitness and disease progression. Here we observe a notable effect of oxygen tension on the macroscopic and biofilm morphotypes of the human fungal pathogen *Aspergillus fumigatus*. A hypoxia-typical morphotype is generated through the expression of a subtelomeric gene cluster containing genes that alter the hyphal surface and perturb interhyphal interactions to disrupt in vivo biofilm and infection site morphologies. Consequently, this morphotype leads to increased host inflammation, rapid disease progression and mortality in a murine model of invasive aspergillosis. Taken together, these data suggest that filamentous fungal biofilm morphology affects fungal-host interactions and should be taken into consideration when assessing virulence and host disease progression of an isolated strain.**

Surface-dwelling microorganisms organize into macroscopic colonies of intricately structured populations that have intrigued scientists for decades<sup>1,2</sup>. For bacteria and yeast, the inter- and intraspecies heterogeneity of these macroscopic morphologies in vitro are well-understood<sup>3,4</sup>; and microbial colony morphology (CM) variants are observed in clinical samples<sup>5,6</sup>. The challenge remains to determine how CM diversity reflects physiological variation and contributes to environmental fitness. CM is associated with changes in extracellular matrix<sup>7</sup>, stress resistance<sup>8</sup>, reproduction<sup>9</sup> and metabolism<sup>10</sup>; but it remains unclear, particularly for filamentous fungi, how CM affects pathogenesis and what genetic factors play a role in fungal CM diversification.

Intraspecies CM variation can arise through accumulated genetic changes or through transcriptional rewiring resulting in phenotypic switching<sup>11,12</sup>. The human pathogenic mould *Aspergillus fumigatus* shows phenotypic plasticity at 0.2% O<sub>2</sub>, where CM differs compared to that at 21% O<sub>2</sub> and is variable across strains<sup>13</sup>. Physiological changes and genetic mechanisms facilitating stable morphotype variants in *A. fumigatus* and other human pathogenic filamentous fungi are not well-characterized, nor is their effect on pathogenesis and disease progression. Progress in understanding fungal CM and phenotypic variability has been limited partly by the underlying genetic complexity. Given the intraspecies CM variation found in *A. fumigatus* isolates and the effect of oxygen on CM, we sought to assess how a low-oxygen CM variant affects *A. fumigatus* pathogenesis and invasive aspergillosis disease progression and to identify genetic factors involved in CM variation.

## Results

**Oxygen tension significantly influences fungal CM and biofilm architecture.** *A. fumigatus* CM is heterogeneous in response to oxygen tension<sup>13</sup>. A screen of 58 isolates at 0.2% O<sub>2</sub> for two morphological features—colony furrowing and percentage vegetative mycelia (white, non-conidiating mycelia; PVM)—revealed abundant furrowing (mean, 5.30) and a high PVM (mean, 70.4%) (Fig. 1a and

Supplementary Fig. 1a). Colonies at 21% O<sub>2</sub> have significantly fewer furrows (mean, 1.85;  $P < 0.0001$ ) and significantly reduced PVM (mean, 32%;  $P < 0.0001$ ) (Fig. 1b). Oxygen tension is a significant source of variation for both colony furrowing (31.67%,  $P < 0.0001$ ) and PVM (55.77%,  $P < 0.0001$ ) (Fig. 1c,d). Most isolates screened have low furrowing and low PVM at normal oxygen (N-MORPH) and increased furrowing and PVM at low oxygen (hypoxia; H-MORPH; Fig. 1e). We consider a strain to be H-MORPH if furrows are greater than three and PVM is greater than 40% when grown in our culture conditions. A subset of clinical strains adopt H-MORPH even at 21% O<sub>2</sub> (filled circles, Fig. 1b–d,f). Three such strains—CDC20.2, F11698 and F16311—have significantly increased low oxygen fitness (H/N) relative to the N-MORPH reference AF293 (Fig. 1f and Supplementary Fig. 1b).

H-MORPH submerged fungal biofilms have altered biofilm architecture compared to AF293 (Fig. 1g). AF293 biofilms have a mat of filaments at the base perpendicular to the vertical axis. Above ~50 µm, filaments grow polarized toward the air-liquid interface with little deviation from the vertical axis (Fig. 1h and Supplementary Video 1). Clinical H-MORPH strains are similar in the first ~50 µm but the remaining volume contains filaments that deviate from the vertical axis (Fig. 1h and Supplementary Fig. 2). This pattern of altered architecture is similar to AF293 cultured at 0.2% O<sub>2</sub> (Supplementary Video 2) and in the AF293 hypoxia-evolved H-MORPH strain EVOL20 independent of oxygen tension (Supplementary Videos 3 and 4, Fig. 1i,j and Supplementary Figs. 1c and 2). These data suggest that CM is an indicator of microscopic biofilm architecture affected by oxygen.

**H-MORPH occurs throughout genetically diverse strains of *A. fumigatus*.** H-MORPH is not segregated by clade in the *A. fumigatus* phylogeny (Supplementary Fig. 3). Two H-MORPH clinical strains—F11698/NCPF-7816 and F13611—represent the abundant *A. fumigatus* genetic diversity with one present in each of the two major clades (Supplementary Fig. 3). Genetically similar,

<sup>1</sup>Department of Microbiology and Immunology, Geisel School of Medicine at Dartmouth, Hanover, NH, USA. <sup>2</sup>Department of Biological Science, Dartmouth College, Hanover, NH, USA. <sup>3</sup>Department of Microbiology and Plant Pathology and Institute for Integrative Genome Biology, University of California-Riverside, Riverside, CA, USA. <sup>4</sup>Unaffiliated: Raimo Hartmann. \*e-mail: Robert.A.Cramer@Dartmouth.edu



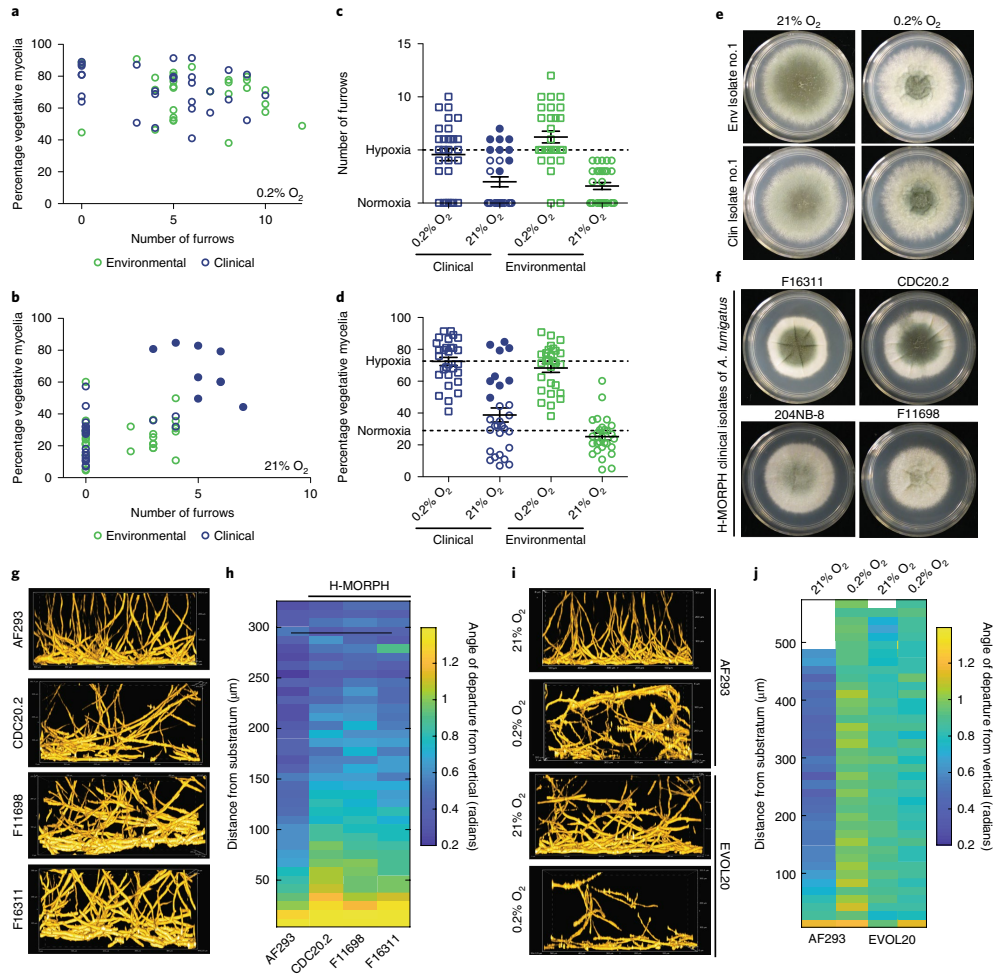


**Fig. 1 | Macroscopic morphotypes and biofilm architecture of *A. fumigatus* are influenced by oxygen tension.** **a, b**, Environmental ( $n = 29$  biologically independent samples) and clinical ( $n = 29$  biologically independent samples) isolates of *A. fumigatus* strains plotted for morphotype characteristics (furrowing and percentage vegetative mycelia) when grown at 0.2% O<sub>2</sub> (**a**) or 21% O<sub>2</sub> (**b**). **c, d**, Two-way ANOVA shows oxygen tension significantly contributes to the variation of colony furrowing (31.67%,  $P < 0.0001$ ) (**c**) and PVM (55.77%,  $P < 0.0001$ ) (**d**) in clinical ( $n = 29$  biologically independent samples) and environmental ( $n = 29$  biologically independent samples) strains. Dashed lines indicated the mean values per condition; error bars indicate s.e.m. (centre). **e**, Representative isolates with an increased PVM (white) and furrowing when cultured at 0.2% O<sub>2</sub> versus 21% O<sub>2</sub>. Images are representative of three biologically independent experiments. **f**, Example clinical strains that adopt H-MORPH during growth at 21% O<sub>2</sub> (closed blue circles in **b**, **c** and **d**). Images are representative of three biologically independent replicates. **g**, Representative side-view slices of submerged fungal biofilms from *A. fumigatus* H-MORPH clinical isolates in **f**. **h**, Quantification of vertical alignment of filaments as a function of biofilm depth. **i, j**, Representative side-view slices of submerged fungal biofilms of AF293 and the H-MORPH EVOL20 at 21% O<sub>2</sub> (24 h) and 0.2% O<sub>2</sub> (36 h) (**i**) with vertical alignment quantification (**j**). For **h** and **j** each lane is a representative alignment from a minimum of three independent biological replicates. Biofilm images are sample volumes of approximately 300 μm (height) × 500 μm (length) × 200 μm (width) and represent a minimum of three biologically independent experiments.

co-isolated, clinical strains, IFM 59356-3 and IFM 59356-1, have H-MORPH and N-MORPH respectively (Supplementary Fig. 4a). Consistent with H-MORPH (Fig. 1g, h), IFM 59356-3 has a biofilm

with greater filament deviation from the vertical relative to its N-MORPH counterpart IFM 59356-1 (Supplementary Fig. 4b, c). The lack of clustering of H-MORPH in the phylogeny and the

ability to generate this CM suggest multiple genetic mechanisms probably exist through which *A. fumigatus* evolves these morphological features.

**A subtelomeric gene *hrmA* allele is sufficient to generate H-MORPH.** An in vitro experimental evolution approach with AF293 in 0.2% O<sub>2</sub> generated the strain EVOL20 that adopts H-MORPH independent of oxygen tension (Supplementary Fig. 1c,d)<sup>13</sup>. Whole-genome sequence analysis of EVOL20 revealed three non-synonymous mutations compared to AF293 (Supplementary Table 1), including a missense mutation in an uncharacterized hypothetical protein Afu5g14900. This single nucleotide polymorphism (D304G) was only identified in H-MORPH EVOL20 from the passed population (Supplementary Fig. 1f). RNA sequencing indicates that Afu5g14900 transcript is significantly increased in EVOL20 relative to AF293 in both normal ( $P=0.0002$ ) and low-oxygen conditions ( $P<0.0001$ ; Supplementary Fig. 1e). Due to the generation of H-MORPH in EVOL20, the gene Afu5g14900 is named hypoxia-responsive morphology factor A, *hrmA*.

In AF293, *hrmA* loss ( $\Delta hrmA^{\Delta F}$ ) does not alter in vitro CM in terms of furrowing and PVM, however, reconstitution of  $\Delta hrmA^{\Delta F}$  with the EVOL20 allele of *hrmA* (*hrmA*<sup>R-EV</sup>) is sufficient to generate H-MORPH independent of oxygen tension (Fig. 2a,b). Allele *hrmA*<sup>R-EV</sup> has hypoxia fitness equivalent to EVOL20 (Fig. 2c). Conversely, *hrmA* loss in EVOL20 ( $\Delta hrmA^{EV}$ ) results in a loss of H-MORPH during growth at 21% O<sub>2</sub> (Fig. 2a,b) and a reduction in hypoxia fitness (Fig. 2c). Similar to H-MORPH locked clinical isolates (Fig. 1g) and EVOL20, *hrmA*<sup>R-EV</sup> generates a biofilm with vertically misaligned filaments above the first ~50  $\mu$ m (Fig. 2d,e). Loss of *hrmA* in EVOL20 restores AF293-like biofilm architecture (Fig. 2f,g). Thus, the hypoxia-evolved allele of *hrmA* is sufficient and necessary to generate H-MORPH in AF293 and EVOL20, respectively.

**H-MORPH coincides with the initiation of the hypoxia transcriptional response at ambient oxygen tensions.** RNA sequencing was used to visualize broad consequences of H-MORPH at normal- and low-oxygen tensions. Hierarchical clustering of the transcriptomes reveals H-MORPHs *hrmA*<sup>R-EV</sup> and *hrmA*<sup>OE</sup> (overexpression of the AF293 allele in AF293) cluster independently from N-MORPHs AF293 and  $\Delta hrmA^{\Delta F}$  (Supplementary Fig. 5). Of the differentially expressed transcripts between *hrmA*<sup>R-EV</sup> and AF293 in 21% and 0.2% O<sub>2</sub>, 58% are oxygen-responsive genes in AF293 (Fig. 3a and Supplementary Table 3). The gene ontology functional categories GO:0016491 oxidoreductase activity (32/904) and GO:0005506 iron ion binding (7/142) are significantly enriched in the differentially expressed genes between *hrmA*<sup>R-EV</sup> and AF293 (Supplementary Table 2); two categories shown previously to be enriched during the hypoxia response<sup>14</sup>.

Transcripts with an increase or decrease of at least fourfold between AF293 and *hrmA*<sup>R-EV</sup> were categorized as 'hypoxia-induced genes' ( $H/N > 4$ ), 'hypoxia-reduced genes' ( $H/N < -4$ ) or 'hypoxia non-responsive genes' ( $4 > H/N > -4$ ) (Supplementary Table 4). At 21% O<sub>2</sub>, 51% of the transcripts increased in *hrmA*<sup>R-EV</sup> compared to AF293 are hypoxia-induced genes; conversely, 45% of the transcripts reduced in *hrmA*<sup>R-EV</sup> compared to AF293 are hypoxia-reduced genes (Fig. 3b). Thus, H-MORPH strains, mediated by *hrmA*, activate the transcriptional hypoxic response despite oxygen replete conditions. At 0.2% O<sub>2</sub> where *hrmA*<sup>R-EV</sup> is more fit than AF293, 71.8% of increased transcripts are hypoxia-reduced transcripts, further supporting an altered physiological response to hypoxic stress in H-MORPH strains (Fig. 3b). The inverted hypoxia response of *hrmA*<sup>R-EV</sup> coincides with reduced fungal biomass at 21% O<sub>2</sub> and increased biomass at 0.2% O<sub>2</sub> (Fig. 3c). However, following a shift from ambient oxygen to low oxygen the H-MORPH *hrmA*<sup>R-EV</sup> has increased growth rate compared to the N-MORPH AF293 (Fig. 3d).

**HrmA is induced during murine pulmonary aspergillosis and facilitates the expression of a subtelomeric gene cluster.** Previous reports suggest increased *hrmA* expression in vivo in a triamcinolone murine model of invasive aspergillosis<sup>15</sup>. In that model, *hrmA* transcript levels significantly increase from 24 to 72 h after fungal inoculation (Fig. 4a). An increase in *hrmA* transcript in *hrmA*<sup>R-EV</sup> (at the native locus) is also observed (Fig. 4b). The allele *hrmA* is a member of a subtelomeric gene cluster that responds to nitrogen starvation, a laboratory condition that transcriptionally correlates with a host-adaptation transcriptional response<sup>16</sup>. Consistent with the assignment of *hrmA* to a subtelomeric gene cluster, we observe an influence of *hrmA* on transcript levels of genes surrounding its native locus, termed here the *hrmA*-associated cluster (HAC). In  $\Delta hrmA^{EV}$ , the messenger RNA levels of three surrounding genes (Afu5g14880, Afu5g14890 and Afu5g14910) are significantly reduced compared to EVOL20 (Fig. 4c). Ectopic overexpression of the AF293 allele of *hrmA* (*hrmA*<sup>OE</sup>) acts in trans to facilitate an increase in transcripts of four HAC genes (Afu5g14880, Afu5g14890, Afu4g14910 and Afu5g14920; Fig. 4d).

Analysis of co-regulated transcripts from RNA sequencing predicts that HAC extends from Afu5g14865 to Afu5g14920 and includes a putative unannotated ORF 3' to Afu5g14910 (Supplementary Fig. 6a,c). The average gene size and percentage GC content of HAC is not different from the AF293 genomic average (Supplementary Fig. 6b)<sup>17</sup>; but in the hypoxia-fit strain A1163 (ref. <sup>13</sup>), there is a subtelomeric HAC that is syntenic to AF293 HAC and two additional putative homologous clusters that are not present in AF293 (Supplementary Fig. 6c). The presence of these potential homologous clusters in a distantly related *A. fumigatus* strain suggests intragenomic movement of this genomic region. The clusters share certain genic components including genes encoding a MyB/SANT domain, a kinase domain, a DUF2841 domain and putative *hrmA* paralogs (*hrmB*, AFUB\_044390; *hrmC*, AFUB\_096600). Analysis of HAC across sequenced strains indicates heterogeneous abundance of the original and homologous gene clusters (Supplementary Fig. 3, alignment: [https://github.com/stajichlab/Afum\\_hrmA\\_cluster\\_evolution](https://github.com/stajichlab/Afum_hrmA_cluster_evolution); <https://doi.org/10.5281/zenodo.3257606>), potentially highlighting a role for these homologous clusters in H-MORPH generation where HAC is absent. Other Ascomycetes encode genes similar to *hrmA*, including the human fungal pathogens *Histoplasma capsulatum* and *Coccidioides immitis* (Supplementary Table 7; [https://github.com/stajichlab/Afum\\_hrmA\\_cluster\\_evolution](https://github.com/stajichlab/Afum_hrmA_cluster_evolution)).

**HrmA nuclear localization is necessary for the induction of HAC.** The HrmA protein sequence reveals a predicted N-terminal bipartite nuclear localization signal (<http://nls-mapper.iab.keio.ac.jp/>) and a weakly predicted RNA recognition motif domain ( $E$ -value, 0.01) (Supplementary Fig. 7a). Overexpression of the parental allele of *hrmA* with a C-terminal green fluorescent protein (GFP) tag in AF293 generates oxygen-independent H-MORPH (Fig. 4e,f). In contrast, overexpression of *hrmA* with a disrupted nuclear localization signal is unable to generate H-MORPH (Fig. 4e,f) despite increased levels of *hrmA* transcript (Fig. 4i). Confocal imaging reveals GFP signal enriched in the same location as the nuclear DAPI stain for the WT (wild type, AF293) allele but a lack of this enrichment for the nuclear localization signal mutant (Fig. 4g,h). Without localization to the nucleus or nuclear region, HrmA is unable to facilitate HAC induction as shown by the cluster gene *cgmA* (Afu5g14910) (Fig. 4i).

Despite low sequence similarity in the alignment to the RNA recognition motif domain in HrmA, there are two conserved phenylalanine residues in this domain that are also present in *hrmB* and *hrmC* in strain A1163. When these conserved phenylalanine residues are each mutated to alanine, overexpression of this allele cannot generate H-MORPH despite observing *hrmA* nuclear region

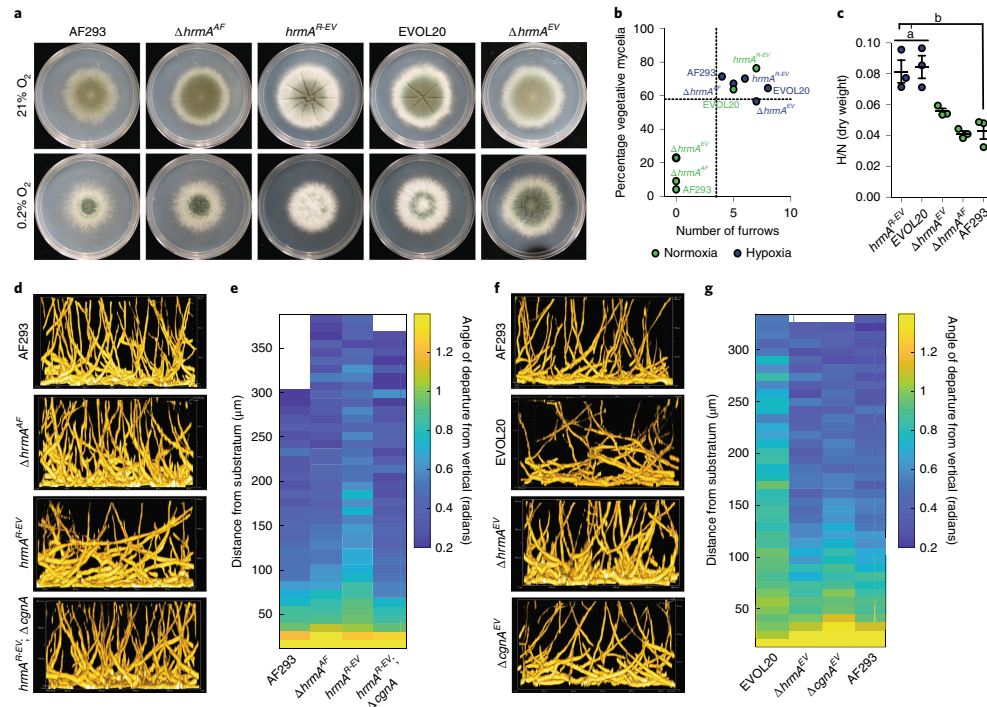


**Fig. 2 | The hypoxia-evolved allele of the subtelomeric gene *hrmA* is sufficient to generate H-MORPH and collapse biofilm architecture.** **a**, A hypoxia-evolved allele of *hrmA*, from the hypoxia-evolved strain EVOL20, is sufficient to generate H-MORPH in AF293 (*hrmA*<sup>R-EV</sup>) and necessary for H-MORPH in EVOL20. Images are representative of three biologically independent experiments. **b**, Morphotype quantification indicates that *hrmA*<sup>R-EV</sup> and EVOL20 are above the mean (dashed lines) for furrowing and PVM, regardless of oxygen tension but dependent on *hrmA*/*cgnA*. **c**, Allele *hrmA*<sup>R-EV</sup> (*n* = 3 biologically independent samples per group) has increased fitness (*a*, *P* = 0.9942; *b*, *P* = 0.0033 by one-way ANOVA with Tukey's multiple comparison test) in low oxygen as determined by dry weight. Error bars indicate s.e.m. (centre). **d, e**, Representative side-view slices of submerged fungal biofilms reveal that altered biofilm architecture in *hrmA*<sup>R-EV</sup> is dependent on *cgnA* as shown in **d** and quantified in **e**. **f, g**, Representative side-view slices of submerged fungal biofilms revealing that *hrmA* and *cgnA* are necessary for the collapse in biofilm architecture observed with EVOL20 as shown in **f** and quantified in **g**. Colony and biofilm analysis are representative of three biological replicates. Biofilm images are sample volumes of approximately 300 μm (height) × 500 μm (length) × 200 μm (width).

localization (Supplementary Fig. 7b–d). Aromatic residues are critical in many RNA recognition motif protein structures for direct interaction with nucleic acids<sup>18</sup>. Further studies are needed to determine the molecular function of *hrmA* in fungi.

**H-MORPH is generated through HrmA-mediated induction of HAC.** Loss of HAC induction abolishes H-MORPH indicating that HAC is necessary for this morphotype and increased hypoxia fitness (Fig. 5 and Supplementary Fig. 7). Expression of the HAC gene Afu5g14910, *cgnA*, is an indicator of HrmA downstream effects and encodes a predicted collagen-like protein, a class of proteins present but unstudied in other fungi (Supplementary Table 5). In *A. fumigatus*, CgnA has a tripeptide G-X-Y repeat of G-Q-I and G-Q-S and lacks a canonical secretion signal. Despite induction of *cgnA* greater than 100-fold relative to AF293 in *hrmA*<sup>OE</sup> (Fig. 4d; morphology Supplementary Fig. 8e), comparative levels of *cgnA* overexpression in the absence of increased *hrmA*

(*cgnA*<sup>OE</sup>) does not induce H-MORPH nor alter the hypoxic growth of AF293 (Supplementary Fig. 8). Loss of *cgnA* in the context of increased HAC abolishes H-MORPH, indicating a role for *cgnA* and possibly other HAC genes, in the generation of H-MORPH (Fig. 5a,b and Supplementary Fig. 8e). Loss of *cgnA* in HAC-induced strains EVOL20 and *hrmA*<sup>R-EV</sup> reduces the hypoxia fitness of these strains (Fig. 5c and Supplementary Fig. 8f) and restores the N-MORPH biofilm architecture and filament alignment to that of AF293 (Fig. 2).

To further characterize the role of *cgnA* and HAC in the generation of H-MORPH, we assessed features of the hyphal surface, as surface alteration and adhesion are associated with other microbial collagen-like proteins<sup>19–21</sup>. Loss of *cgnA* and regeneration of N-MORPH increases surface adherence of H-MORPH strains (Fig. 5d), probably the consequence of extracellular matrix detachment from the H-MORPH strains (Supplementary Fig. 8g and Fig. 5e) that is dependent on *cgnA*. In the clinical strains IFM 59356-1

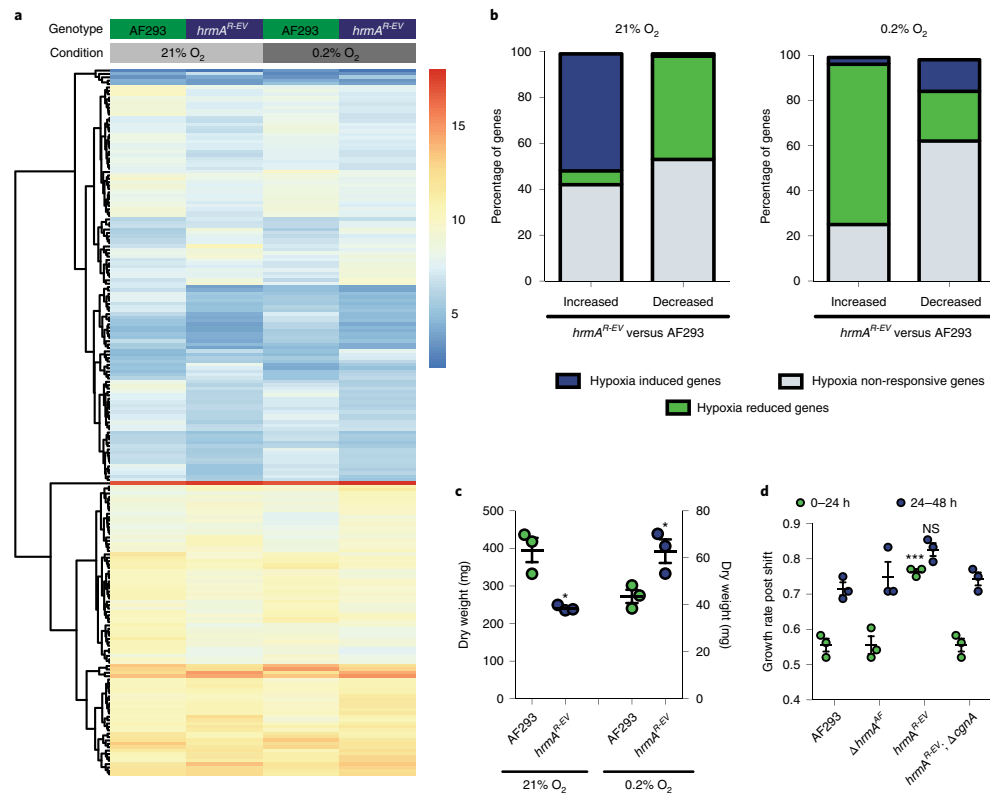


**Fig. 3 | Transcriptional rewiring of the hypoxia response is dependent on the hypoxia-evolved allele of *hrmA* and primes for improved growth in low oxygen.** **a**, A heat map of collapsed biological replicates showing top genes with  $P < 0.05$  (two-sided) and  $\log_2$  differential expression  $> 1$  with a minimum FPKM of 5. Significance was determined with DESeq2 which uses the Wald test for differential expression and adjustments for multiple comparisons using Benjamini and Hochberg procedures. In this subset, *hrmA*<sup>R-EV</sup> versus AF293 reveals large-scale changes in both 21% and 0.2% O<sub>2</sub> as a result of the hypoxia-evolved *hrmA* allele. **b**, Classification of all genes increased or decreased twofold in *hrmA*<sup>R-EV</sup>/AF293 at 21% O<sub>2</sub> or 0.2% O<sub>2</sub> reveals activation of the hypoxia transcriptional response at ambient oxygen and reduction in this response at low oxygen in *hrmA*<sup>R-EV</sup>. **c**, The growth advantage of *hrmA*<sup>R-EV</sup> at 0.2% O<sub>2</sub> ( $*P = 0.0282$ ) coincides with a significant ( $*P = 0.0088$ ) reduction in fungal growth at 21% O<sub>2</sub>. Two-tailed unpaired *t*-test performed on  $n = 3$  independent biological replicates with error bars showing s.e.m. (centred). **d**, A transition from 48 h of growth at 21% O<sub>2</sub> to growth at 0.2% O<sub>2</sub> shows an initial increase ( $***P < 0.0001$ ) in growth rate during the first 24 h at 0.2% O<sub>2</sub> for *hrmA*<sup>R-EV</sup> that is not present (NS,  $P = 0.0789$ ) 24–48 h after shift to 0.2% O<sub>2</sub>. One-way ANOVA with Tukey's multiple comparison test was performed on  $n = 3$  biologically independent samples. Error bars indicate s.e.m. (centre); NS, not significant.

(N-MORPH) and IFM 59356-3 (H-MORPH), matrix detachment and reduced surface adherence is observed in H-MORPH relative to the N-MORPH (Supplementary Fig. 4d,e). Matrix detachment from the H-MORPH filaments is not a defect in extracellular matrix production as it is still visibly secreted into the biofilms (Fig. 5e). A significant component of the extracellular matrix is galactosaminogalactan (GAG) and loss of GAG through deletion of the UDP-glucose-4-epimerase *uge3* abolishes surface adherence<sup>22,23</sup>. Chemical modifications of GAG also prevents attachment of matrix to the hyphae<sup>23</sup>, so we investigated the ability of secreted GAG from *hrmA*<sup>OE</sup> to complement the adherence defect of the GAG-deficient strain  $\Delta uge3^{\Delta F}$ . Culture supernatants containing secreted GAG from AF293 and *hrmA*<sup>OE</sup> were both able to significantly increase adherence of  $\Delta uge3^{\Delta F}$  (Fig. 5f). These data suggest

that HAC/*cgnA* modifies the hyphal surface mediating matrix/GAG detachment. To determine if GAG secretion was necessary for H-MORPH, we generated *uge3* deletions in *hrmA*<sup>OE</sup> and EVOL20; as a result, CM did not change but surface adherence was abolished (Supplementary Fig. 9a,b). Loss of GAG production in AF293 does not affect hypoxia fitness nor the biofilm architecture (Supplementary Fig. 9d,e).

H-MORPHs *hrmA*<sup>R-EV</sup> and EVOL20 have significantly thinner cell walls than the N-MORPH AF293 and in EVOL20 this is dependent on *cgnA* (Fig. 5g and Supplementary Fig. 10). To determine if the cell wall architecture is altered, we imaged cell wall components through the use of calcofluor white (CFW) stain for chitin detection and soluble Dectin-1 for  $\beta$ -glucan detection<sup>24</sup>. H-MORPH *hrmA*<sup>R-EV</sup> has reduced total chitin that is dependent on the induction

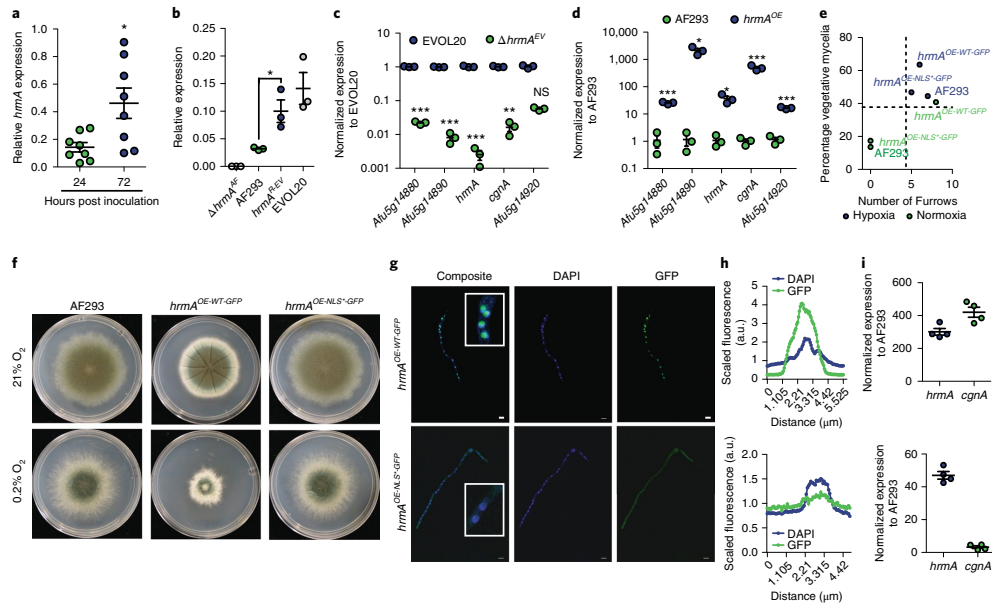


**Fig. 4 | HrmA localizes to the nucleus where it facilitates induction of a subtelomeric gene cluster.** **a**, Allele *hrmA* transcripts are detected in vivo during murine invasive disease with WT *A. fumigatus* and increase in abundance from 24 to 72 h after inoculation ( $n=8$  biologically independent animals, unpaired two-tailed Student's  $t$ -test,  $^{*}P=0.0151$ ). **b**, Introduction of the evolved allele of *hrmA* (*hrmA<sup>EV</sup>*) is sufficient to induce significantly increased mRNA levels of *hrmA* compared to AF293 ( $^{*}P=0.0290$ ) and similar to EVOL20 ( $P=0.3066$ ) ( $n=3$  biologically independent samples). Students unpaired two-tailed  $t$ -test performed, error bars indicate s.e.m. (centre). **c**, In the hypoxia-evolved EVOL20, loss of *hrmA* leads to a significant reduction in mRNA for the gene cluster surrounding the *hrmA* native locus (HAC) ( $n=3$  biologically independent samples). Unpaired Student's two-tailed  $t$ -test performed between EVOL20 and  $\Delta$ *hrmA<sup>EV</sup>* with error bars representing s.e.m. (centre) (Afu5g14880,  $^{***}P<0.0001$ ; Afu5g14890,  $^{***}P<0.0001$ ; *hrmA*,  $^{***}P<0.0001$ ; *cgnA*,  $^{**}P=0.0017$ ; Afu5g14920, (NS)  $P=0.0604$ ). **d**, Ectopic integration of a constitutively overexpression WT allele of *hrmA* in AF293 acts in trans to significantly increase mRNA levels HAC ( $n=3$  biologically independent samples). Unpaired Student's two-tailed  $t$ -test performed between AF293 and *hrmA<sup>OE</sup>* with error bars representing s.e.m. (centre) (Afu5g14880,  $^{***}P=0.0002$ ; Afu5g14890,  $^{*}P=0.0184$ ; *hrmA*,  $^{*}P=0.0371$ ; *cgnA*,  $^{***}P=0.0009$ ; Afu5g14920,  $^{***}P<0.0001$ ). **e–h**, In a minimum of three independent experiments, overexpression of *hrmA* (*hrmA<sup>OE-WT-GFP</sup>*) generates H-MORPH independent of oxygen tension (**e**) but dependent on an N-terminal nuclear localization signal (**f**) and nuclear localization of HrmA (a.u., arbitrary units) (**g,h**). Scale bars, 5  $\mu$ m. **i**, Localization to the nucleus is necessary for the induction of the HAC gene *cgnA* (Afu5g14900) ( $n=3$  biologically independent samples). Error bars indicate s.e.m. (centre).

of *cgnA* (Fig. 5h and Supplementary Fig. 11a). In contrast, *hrmA<sup>R-EV</sup>* has significantly increased *cgnA*-dependent  $\beta$ -glucan exposure (Fig. 5i and Supplementary Fig. 11b). Allele *hrmA<sup>R-EV</sup>* is also more sensitive to growth on CFW in both normal and low oxygen compared to AF293,  $\Delta$ *hrmA<sup>AF</sup>* and *hrmA<sup>R-EV</sup>*;  $\Delta$ *cgnA* (Supplementary Fig. 11c). No difference in sensitivity to the  $\beta$ -glucan synthase inhibitor caspofungin was observed (Supplementary Fig. 11d). We propose that these surface changes alter matrix attachment and inter-hyphal interactions in the developing biofilms resulting in a loss of vertically aligned polarized growing filaments.

**H-MORPH altered biofilm architecture occurs in vivo.** We next sought to determine if the altered filament surface influences the inter-filament interactions in vivo. We adopted the miPACT/PACT tissue-clearing methods (microbial identification after passive clarity technique) to visualize in vivo fungal lesions in three dimensions using fluorescently labelled fungi (we term this technique funPACT: fungal imaging after passive clarity technique)<sup>25–27</sup>. At 4 days post inoculation (d.p.i.) and 5 d.p.i. large inflammatory foci

with fungal elements are observed in the airways of animals challenged with AF293 or EVOL20. At both time points, AF293 lesions are dense at the centre with filaments radiating from the foci of infection, becoming less dense away from the centre (Fig. 6a and Supplementary Video 5). There is a high degree of connectivity between filaments in AF293 lesions but not in EVOL20 lesions. At 4 d.p.i. and 5 d.p.i. the EVOL20 lesions are visibly more diffuse than those of AF293 (Fig. 6a,b and Supplementary Fig. 13). There are no dense foci in the EVOL20 lesions and single filaments can be observed dispersed in distinct locations in the mass of host immune infiltrate (Fig. 6b and Supplementary Video 6).

To quantify differences in lesion architecture, we performed Gömöri methenamine silver stain and applied a nearest-neighbour algorithm to quantify the 'compactness' of fungal lesions in the large airways. The more compact a fungal lesion is, the shorter the distance between each filament and its nearest neighbours; while more diffuse lesions have larger average distances between filaments. Qualitative analysis of the histopathology between N-MORPH AF293 and H-MORPH EVOL20 supported the hypothesis that



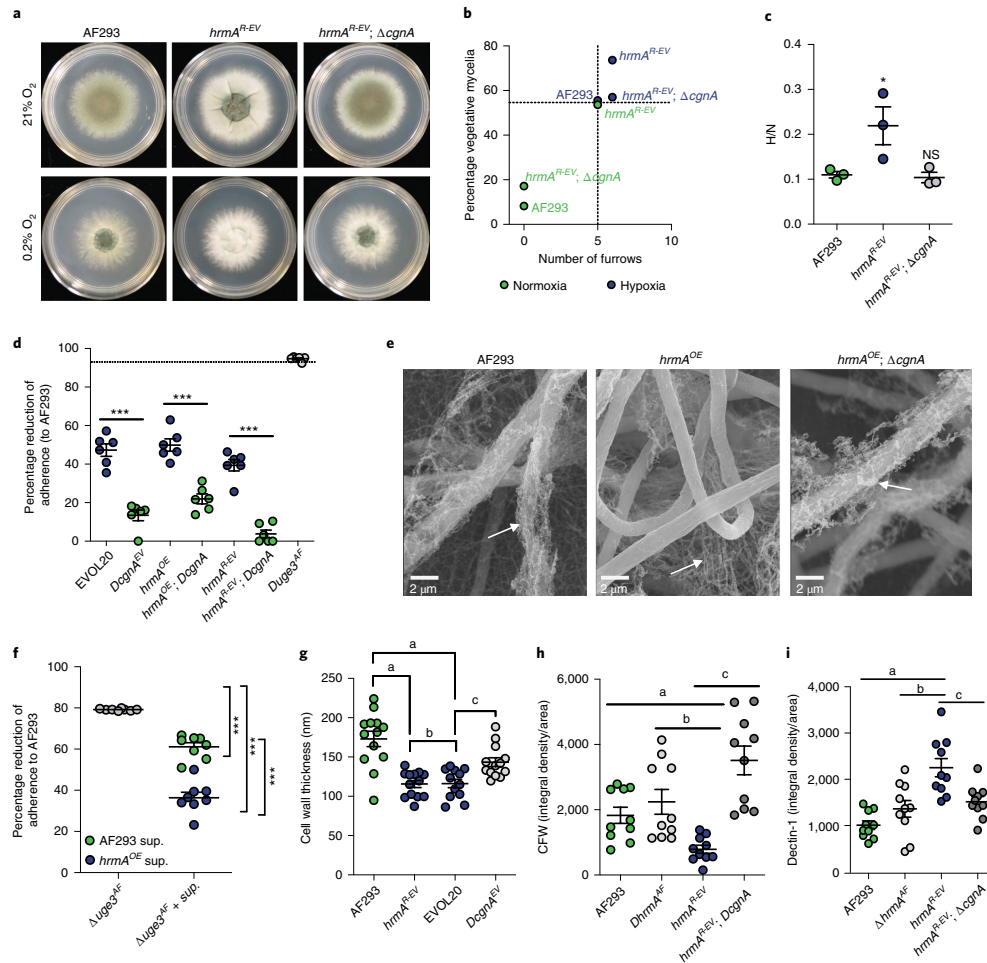


**Fig. 5 | HrmA-facilitated induction of the surrounding subtelomeric gene cluster leads to increased hypoxia fitness and a modified hyphal surface.** **a, b.** In a minimum of three independent experiments, loss of *cgnA* in *hrmA*<sup>R-EV</sup> abolishes H-MORPH (**a**) generating a AF293-like oxygen-responsive morphotype in regards to furrows and PVM (**b**). **c.** Representative HAC gene *cgnA* is necessary for the increased hypoxia fitness of *hrmA*<sup>R-EV</sup> ( $n=3$  biological independent samples, one-way ANOVA with Dunnett's multiple comparison test,  $*P=0.0433$  and NS  $P=0.9847$ ). **d.** Adherence to plastic is reduced in response to HAC induction (EVOL20, *hrmA*<sup>OE</sup>, *hrmA*<sup>R-EV</sup>) and is dependent on *cgnA*. Biologically independent biological samples ( $n=6$ ) are from two independent experimental repetitions. One-way ANOVA with Sidak's multiple comparison test performed,  $***P<0.0001$ . Error bars indicate s.e.m. (centre). **e.** SEM of 24 h submerged fungal biofilms reveal detachment of extracellular matrix from *hrmA*<sup>OE</sup> hyphae that is dependent on *cgnA*. White arrows indicate extracellular matrix. Images are representative of three replicates. **f.** Addition of culture supernatants with secreted extracellular matrix to the non-adherent strain *Dug3*<sup>ΔF</sup> significantly ( $***P<0.0001$ ) rescues adherence. Biologically independent samples ( $n=8$ ) with one-way ANOVA with Tukey's multiple comparison test. Error bars indicate s.e.m. (centre). **g.** The cell walls of *hrmA*<sup>R-EV</sup> and EVOL20 are significantly (a,  $P<0.001$ ; b,  $P>0.9999$ ; c,  $P=0.0334$ ) thinner than those of AF293 or *ΔcgnA*<sup>EV</sup>. Independent biological samples ( $n=13$ ) with one-way ANOVA and Tukey's multiple comparisons test. Error bars indicate s.e.m. (centre). **h, i.** *hrmA*<sup>R-EV</sup> has reduced total chitin staining by CFW fluorescence ( $n=10$  independent biological samples; a,  $P=0.0492$ ; b,  $P=0.0049$ ; c,  $P<0.0001$ ) (**h**) and increased  $\beta$ -glucan staining by Dectin-1 ( $n=10$  independent biological samples; a,  $P<0.0001$ ; b,  $P=0.0006$ ; c,  $P=0.0044$ ) (**i**). One-way ANOVA with Sidak's multiple comparison test for significance; error bars indicate s.e.m. (centre); NS, not significant (**f** and **g**).

H-MORPH fungal lesions are more diffuse and quantification reveals significantly less compact lesions with EVOL20 than AF293 (Fig. 6c). Expansion of this algorithm to lesions of N-MORPHS

$\Delta$ *hrmA*<sup>AF</sup> and *hrmA*<sup>R-EV</sup>;  $\Delta$ *cgnA* and H-MORPH *hrmA*<sup>R-EV</sup> reveal significantly reduced compactness of *hrmA*<sup>R-EV</sup> compared to the N-MORPH strains (Fig. 6c and Supplementary Figs. 12 and 13c).

The diffuse nature of the *hrmA*<sup>R-EV</sup> lesion is dependent on *cgnA* and only coincides with H-MORPH.

**H-MORPH facilitate disease progression.** H-MORPH F11698 (Supplementary Fig. 4h) ( $n=7$ ) is significantly increased in murine virulence relative to AF293 ( $n=5$ ;  $P=0.0096$ ; Supplementary Fig. 4i). However, these are non-isogenic strains with an estimated 35,759 single nucleotide polymorphisms between them that could contribute to differences in virulence and morphology. A second comparison between closely related clinical isolates N-MORPH IFM 59356-1 and H-MORPH IFM 59356-3 reveals a 40% increase in survival at 14 d.p.i. and a 5-d delay before the first mortality event in N-MORPH inoculated animals. By quantitative real-time polymerase chain reaction (qRT-PCR) no significant difference in mRNA levels of *hrmA* or the HAC gene *cgnA* is observed between these two strains that contain 51 non-synonymous single nucleotide polymorphisms between them (Supplementary Fig. 4g).

Loss of *hrmA* in AF293 does not affect murine mortality, however introduction of the hypoxia-evolved allele of *hrmA* (*hrmA*<sup>R-EV</sup>) and generation of H-MORPH significantly augments virulence in a *cgnA*-dependent manner (Fig. 6d). Loss of *hrmA* or *cgnA* in the H-MORPH EVOL20 significantly attenuates EVOL20 virulence (Fig. 6e). Despite the H-MORPH strains increased virulence, there is no significant difference in fungal burden between AF293, *hrmA*<sup>R-EV</sup>,  $\Delta$ *hrmA*<sup>AF</sup> and *hrmA*<sup>R-EV</sup>;  $\Delta$ *cgnA* at 4 d.p.i. (Fig. 6f). Increased  $\beta$ -glucan exposure in the cell wall of H-MORPH strains is consistent with observed increases in inflammation at 4 d.p.i. (Fig. 6g and Supplementary Fig. 1h,i). The airways where H-MORPH *hrmA*<sup>R-EV</sup> is growing are full of immune cell infiltrate that is reduced around lesions of N-MORPH strains (Fig. 6g).

Host cell damage measured through lactate dehydrogenase (LDH) release in bronchoalveolar lavage fluid (BALF) after inoculation with *hrmA*<sup>R-EV</sup> indicates a significant increase in host cell damage (Fig. 6h). In both the airways and lung tissue, H-MORPH inoculum is associated with a significant increase in total cells (Supplementary Fig. 14a,e) and CD45<sup>+</sup> leucocytes (Supplementary Fig. 14b,f). A significant increase in the neutrophil chemoattractant KC from BALF is detected (Fig. 6i) and corresponds with an increase in airway neutrophils (Fig. 6j). The elevated host response to inoculation with H-MORPH *hrmA*<sup>R-EV</sup> is dependent on HAC/*cgnA*, as loss of *cgnA* does not reduce *hrmA* transcripts (Supplementary Fig. 14h). These data indicate that localized pulmonary inflammation is increased following inoculation with H-MORPH; but in addition, systemic inflammation, as measured by spleen weight, is significantly increased 60 h after fungal inoculation with *hrmA*<sup>R-EV</sup> compared to AF293,  $\Delta$ *hrmA*<sup>AF</sup> and *hrmA*<sup>R-EV</sup>;  $\Delta$ *cgnA* (Fig. 6k). Together, these data suggest H-MORPH occurs in vivo and significantly affects disease progression in part through an increase in immunopathogenesis.

## Discussion

While morphological heterogeneity has been reported among filamentous fungi<sup>6,13,28,29</sup>, there is an existing gap in knowledge that links CM with specific genetic determinants and disease outcomes. Here we discover an oxygen-mediated mechanism of *A. fumigatus* CM that is associated with increased disease progression and fungal virulence. H-MORPH CM leads to increased hypoxia fitness and enhanced virulence through alterations in fungal biofilm architecture that promote increased host inflammation. It remains an open question how H-MORPH confers a fitness benefit during low-oxygen growth on a population scale and, on the microscale, how the coinciding altered biofilms affect oxygen metabolism of individual filaments. Colony wrinkling or rugose CM has been characterized in a number of microorganisms, including *Candida albicans*, where increased oxygen penetration is observed in wrinkles<sup>30</sup>. Further investigation is necessary to address how the morphotype variant H-MORPH confers increased hypoxia fitness.

Our studies identified a subtelomeric gene cluster probably regulated by the gene *hrmA* that is sufficient to drive H-MORPH when expressed (Supplementary Fig. 15). This cluster of genes is interesting independent of its facilitation of H-MORPH for more reasons including: (1) its location in the subtelomeric region<sup>16</sup>, (2) its mysterious origin and strain-dependent putative duplications (Supplementary Fig. 6), (3) its strain-specific occurrence across the *A. fumigatus* phylogeny (Supplementary Fig. 3) and (4) its genetic content (Supplementary Fig. 6). Genetic variation in the cluster genes (Afu5g14865 and Afu5g14920) has also been observed in clinical strains<sup>38</sup>. The evolutionary history of HAC and the putative homologous gene clusters and their molecular functions remains an intriguing area of future study. However, the isogenic set of morphotype variants generated here will serve as tools to continue to interrogate the physiological consequences of CM on *A. fumigatus* pathogenesis. Understanding how fungal macroscopic morphotypes reflect in vivo phenotypic changes in human fungal pathogens may allow for morphotype indicators of disease progression and advancement of patient care.

## Methods

**Strains and growth conditions.** *A. fumigatus* AF293 was used in the published experimental evolution approach that generated EVOL20 (ref. 13). Mutant strains were generated in AF293, the uracil/uridine auxotroph AF293.1 or EVOL20 (Supplementary Table 6). IFM 59356-1 and IFM 59356-3 were provided by D. Hagiwara<sup>4</sup>. Strains were cultured as described on 1% glucose minimal media (GMM)<sup>31</sup> and collected for experimentation as previously described<sup>31</sup>.

**Strain construction.** Strain genotypes are provided in Supplementary Table 6. Gene replacement mutants were generated as previously described using overlap extension PCR<sup>32</sup>. The *hrmA*-GFP alleles were constructed through overlap extension PCR to tag *HrmA* at the C terminus. Site-directed mutation of *hrmA* was carried out using QuikChange Site-Directed Mutagenesis (Agilent).

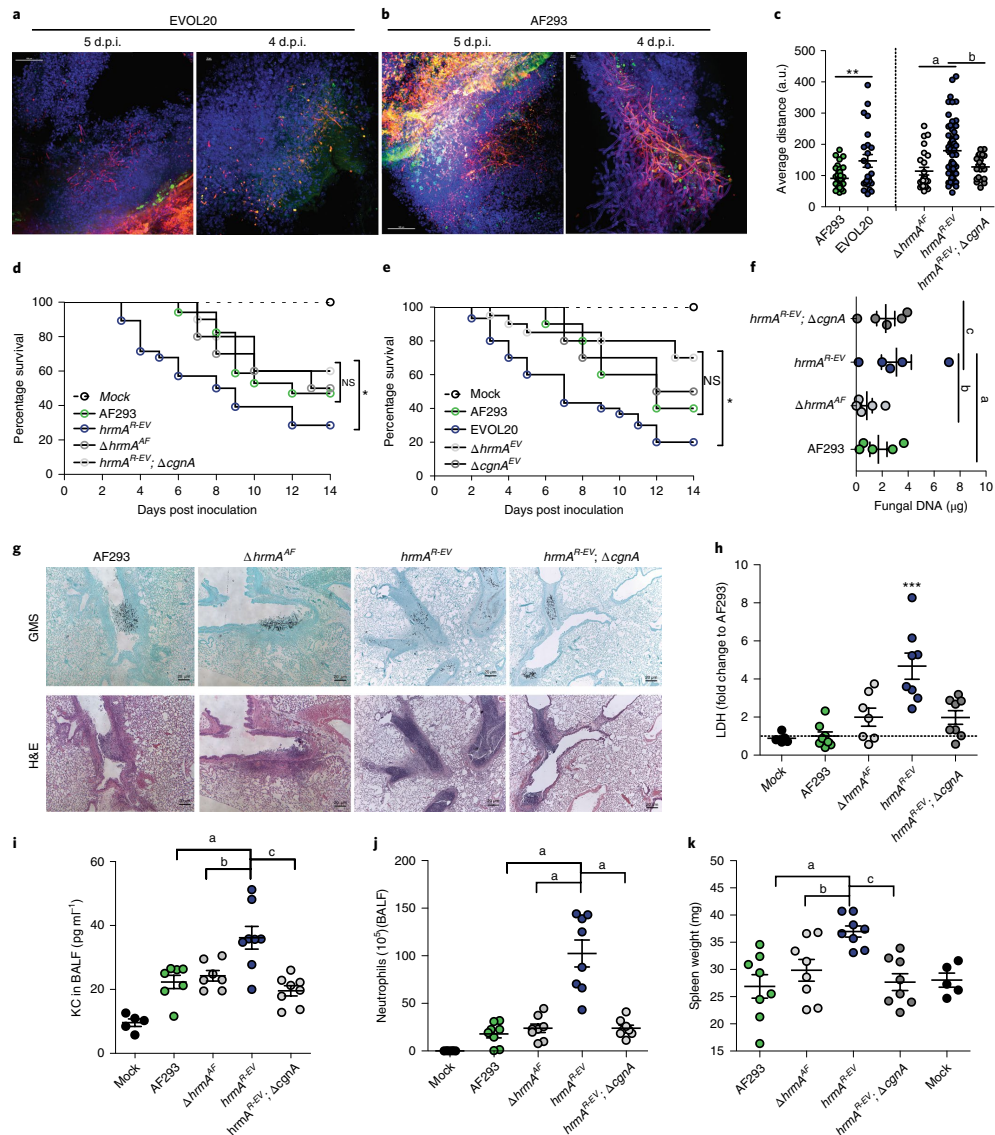
**Fig. 6 | H-MORPH contributes to increased virulence through increased inflammation and diffuse lesion morphology.** **a,b**, EVOL20<sup>tdomato</sup> (**a**) or AF293<sup>tdomato</sup> (**b**) murine lesions stained with DAPI and FITC-soy bean agglutinin. Scale bars: 4 d.p.i., 10  $\mu$ m; 5 d.p.i., 100  $\mu$ m. Results represent five independent animals from two independent preparations. **c**, Nearest-neighbour algorithm shows significantly increased distances between intralesion filaments in AF293 and EVOL20 (\*\* $P=0.0052$ ) and *hrmA*<sup>R-EV</sup> (**a**,  $P=0.0003$ ; **b**,  $P=0.0068$ ) (AF293  $n=45$ , EVOL20  $n=24$ , *hrmA*<sup>R-EV</sup>  $n=25$ , *hrmA*<sup>R-EV</sup>;  $\Delta$ *cgnA*  $n=22$  biologically independent samples). One-way ANOVA with Sidak's multiple comparison test. **d**, *hrmA*<sup>R-EV</sup> ( $n=28$  independent animals) is significantly more virulent ( $P=0.0346$  by Gehan-Breslow-Wilcoxon test, GBW) than AF293 ( $n=16$  independent animals) and *hrmA*<sup>R-EV</sup>;  $\Delta$ *cgnA* ( $n=10$  independent animals,  $P=0.0417$  by GBW). AF293 and *hrmA*<sup>R-EV</sup>;  $\Delta$ *cgnA* do not differ in virulence (NS:  $P=0.2087$  by GBW). **e**, EVOL20 ( $n=30$  independent animals) is significantly more virulent than *hrmA*<sup>R-EV</sup> ( $n=20$  independent animals,  $P=0.0008$  by GBW),  $\Delta$ *cgnA*<sup>EV</sup> ( $n=10$  independent animals,  $P=0.0353$  by GBW) and AF293 ( $n=10$  independent animals,  $P=0.0465$  by GBW). AF293,  $\Delta$ *hrmA*<sup>EV</sup> ( $P=0.1731$  by GBW) nor  $\Delta$ *cgnA*<sup>EV</sup> ( $P=0.7812$  by GBW) differ in virulence. **f**, *hrmA*<sup>R-EV</sup> does not increase fungal burden (**a**,  $P=0.4669$ ; **b**,  $P=0.1322$ ; **c**,  $P=0.7960$ , one-way ANOVA with Dunnett's multiple comparison test,  $n=5$  independent animals each). **g**, Histopathology ( $n=6$  independent animals each from two separate preparations) at 4 d.p.i. indicate a *cgnA*-dependent increase in cellular infiltrate in *hrmA*<sup>R-EV</sup> lesions (scale bar, 20  $\mu$ m). **h-k**, Mice inoculated with *hrmA*<sup>R-EV</sup> ( $n=8$  independent animals per group) at 60 h after inoculation show increased LDH (**a**,  $P<0.0001$ ; **b**,  $P=0.0013$ ; **c**,  $P=0.0009$ ) (**h**), chemoattractant KC (**a**,  $P=0.0013$ ; **b**,  $P=0.0052$ ; **c**,  $P=0.0001$ ) (**i**), BALF neutrophils (**a**,  $P<0.0001$ ) (**j**) and spleen weight (**a**,  $P=0.0009$ ; **b**,  $P=0.0191$ ; **c**,  $P=0.0021$ ) (**k**). One-way ANOVA with Dunnett's multiple comparisons test for **h-k**. All error bars indicate s.e.m.

Overexpression strains used the *A. nidulans* *gpdA* promoter for constitutive expression and this was introduced ectopically. Fluorescent strains expressing tdTomato were transformed with linear constructs of *gpdA*-driven tdTomato. Protoplasting was done with *Trichoderma harzianum* (Sigma) lysing enzyme<sup>13,34</sup>. Strains were confirmed by Southern blotting as described previously<sup>13,34</sup>.

**Growth and CM assays.** Growth assays were performed as previously described<sup>13</sup>. Macroscopic morphology was quantified on GMM. A total 1,000 spores were spotted at the centre of the plates and grown for 72–96 h at 21% O<sub>2</sub> or 0.2% O<sub>2</sub>.

Representative images are of three biological replicates. Statistics were performed with one-way analysis of variance (ANOVA) with Tukey post test for multiple comparisons or two-tailed Student's *t*-test. Error bars indicate s.e.m. centred at the mean. For shift experiments, cultures were started as described at 21% O<sub>2</sub> for 48 h, then shifted to 0.2% O<sub>2</sub> for 48 h.

**Macroscopic morphology quantification.** Colonies were imaged with a Canon PowerShot SX40 HS. In Fiji (ImageJ), images were converted to 8-bit. Colony perimeter was selected and a colour threshold was set to quantify percentage of the





colony that was 'white'. Furrows were counted by selecting only those that radiated away from the point of inoculation. A 'branched' furrow counted as a single furrow (Supplementary Fig. 1). The influence of oxygen on morphology was measured with a two-way ANOVA (GraphPad Prism).

**RNA extraction and qrtPCR.** Mycelia from liquid shaking cultures were flash frozen (~50 mg) and bead beaten for 1 min with 2.3 mm beads in 200 µl of Trisure (Bioline Reagents). Homogenate was brought to a total volume of 1 ml of Trisure and RNA was extracted as previously described<sup>31</sup>. For RNA sequencing and qrtPCR, 50 ml cultures of  $10^6$  spores ml<sup>-1</sup> were grown in normoxia (21% O<sub>2</sub>) at 37 °C at 200 r.p.m. for 18 h before being shifted to low oxygen (0.2% O<sub>2</sub>). When necessary, 25 ml culture was collected at 18 h for the normoxia samples. For qrtPCR and RNA sequencing, 5 µg of RNA was DNase treated with Ambion Turbo DNase (Life Technologies) according to the manufacturer's instruction. For qrtPCR DNase-treated RNA was processed as previously described<sup>31</sup>. The mRNA levels were normalized to *actA* and *tub2* for all qrtPCR analyses. Statistical analysis for  $n > 2$  was performed with one-way ANOVA with Dunnett post test for multiple comparisons. Error bars indicate s.e.m. The qrtPCR data were collected on a CFX Connect Real-Time PCR Detection System (Bio-Rad) with CFX Maestro Software (Bio-Rad) and primer sequences are provided in Supplementary Table 9.

**RNA sequencing and analysis.** RNA sequencing and RNA library preparation were carried out by SeqMatic LLC. Briefly, DNase-treated RNA (400–600 ng l<sup>-1</sup>) were sent for QC using RNA Screen Tape Analysis (Agilent) and RNA library preparation using an Illumina TruSeq Standard mRNA library<sup>32</sup> preparation kit with poly-A mRNA enrichment. RNA sequencing was performed as Illumina NextSeq High Output Run with single end reads at 1 × 75 base pairs (bp). Analysis of RNA-Seq was performed by aligning sequence reads to the annotated genome of *A. fumigatus* strain Af293 obtained from FungiDB (release 35)<sup>36</sup> with GSNAP (2 December 2018) with splice-aware, single-ended mode<sup>37</sup>. The alignments were processed with Picard (v.2.14.1) to clean, sort and assign read groups (tools CleanSam, AddOrReplaceReadGroups) (<http://broadinstitute.github.io/picard/>). Sequence read counts overlapping genes were computed with featureCount tool in the Subread package (v.1.6.2; ref. <sup>38</sup>). The read count table was processed in R using the DESeq2 (v.3.8) to identify differentially regulated genes and generate heat maps. Pipeline BASH scripts for the alignment, read count pipeline and R analysis are available in the github repository ([https://github.com/stajichlab/Afum\\_RNASeq\\_hrmA](https://github.com/stajichlab/Afum_RNASeq_hrmA); BioProject PRJNA551460). Heat map in Fig. 4 was drawn using collapsed replicates showing top DESeq2 with a  $P < 0.05$  and log of differential expression  $> 1$  and a minimum FPKM (fragments per kilobase of transcript per million mapped reads) of 5. Heat map in Fig. 4 was drawn using collapsed replicates showing transcripts with computed expression value difference with an adjusted  $P < 0.05$  and log of differential expression  $> 1$  and a minimum FPKM of 5. Heat map in Supplementary Fig. 5 was drawn showing all replicates and a  $P$ -value cutoff of 0.05 for genotype as an explaining variable for expression differences.

**Surface attachment assays.** Briefly,  $10^4$  spores seeded per well in a round-bottom 96-well polystyrene plate were incubated for 24 h at 37 °C at ambient oxygen in 1% GMM. Wells were washed twice with water and stained for 10 min with 0.1% (wt/vol) crystal violet. Following two washes with water, remaining crystal violet was dissolved in 100% ethanol and absorbance was quantified at 600 nm. For matrix complementation experiments, matrix donating strains were cultured in RPMI 1640 (Gibco) at  $5 \times 10^7$  spores ml<sup>-1</sup> in 100 ml for 24 h at 37 °C at ambient oxygen. Cultures were filtered through Miracloth to remove fungus and supernatants were further filtered through a 0.22 µm PVDF sterile filter syringe. Filtered supernatants containing secreted GAG were diluted to 40% in fresh RPMI 1640 and used to perform the adherence assay with the attachment-deficient strain  $\Delta uge3$ .

**Murine virulence assays.** *Survival.* Female CD-1 outbred mice (Charles River Laboratory), 20–24 g were immune-suppressed with a single dose of triamcinolone acetonide (Kenalog-10, Bristol-Myer Squibb) at 40 mg kg<sup>-1</sup> 24 h before inoculation. Mice were inoculated with  $10^7$  spores per 40 µl of sterile PBS buffer as previously described<sup>33,34</sup> and monitored for end-point criteria. Kaplan–Meier curves were generated and log-rank Mantel–Cox tests and Gehan–Breslow–Wilcoxon tests were performed.

**Histopathology, fungal burden and nearest-neighbour calculation.** Lungs from mice immune-suppressed as described were harvested 4 d.p.i. Lungs were prepared for Gömöri methenamine silver and hematoxylin and eosin staining or fungal burden quantification as described<sup>31</sup>. A nearest-neighbour calculation was applied to Gömöri methenamine silver images<sup>39</sup>. In Matlab (MathWorks), binary images were generated and filaments defined as objects. Lesions in airways were analysed blindly. Mean distances between each object in a lesion and its 30 nearest neighbours was calculated. For nearest-neighbour calculations four murine lungs were processed per experimental group with two histopathology slides prepared per animal. For fungal burden four to five animals were used per group.

**FunPACT sample preparation.** Lungs from mice immune-suppressed as described above were harvested on days 4 and 5 after inoculation. Lungs were harvested

and perfused with 1% paraformaldehyde and fixed for 24 h at room temperature. Following fixation, lobes of fixed lungs were separated with one lobe per 1.75 ml microcentrifuge tube. Lobes were washed with PBS and embedded in 4% (vol/vol) 29:1 acrylamide:bis-acrylamide (Bio-Rad) and 0.25% (wt/vol) VA-044 (Wako) in PBS<sup>40</sup>. To facilitate polymerization, tubes were left open at 0.2% O<sub>2</sub> at 37 °C for 1 h and then closed and incubated at 37 °C in a water bath for 4 h. Embedded lobes were maintained at 4 °C or were processed for PACT tissue clearing. To clear the lobes, embedded lobes were trimmed of excess polymer and cut into 1 mm cubes using a stereomicroscope. Cubes were incubated in 20 ml of 8% (wt/vol) sodium dodecyl sulfate in PBS shaking at 150 r.p.m. at 37 °C for 6–8 weeks in the dark. When cubes became transparent, they were processed for staining and imaging.

After clearing, the cubes were washed three times with PBS for 1 h each. A subset of cubes was then transferred to a 1.75 ml microcentrifuge tube and stained for 48 h with FITC-soy bean agglutinin at 20 µg ml<sup>-1</sup> (Vector Labs). Lectin-labelled cubes were washed in PBS for 24 h to remove excess lectin and cubes were placed in a refractive index matching solution (40 g HistoDenz; Sigma, in 30 ml of PBS<sup>41</sup>) with DAPI (10 µg ml<sup>-1</sup>). Stained cubes in refractive index matching solution + DAPI were mounted on standard 24 × 40 × 1.5 glass slides with a press-to-seal silicone isolator (Invitrogen; P24744).

**Cellularity and immunological studies.** Mice were immune-suppressed and inoculated as described above with eight mice per group. At 60 h after fungal inoculation, animals were killed using a lethal dose of pentobarbital and bronchoalveolar lavage was performed, then BALF and cells, lungs and spleens were collected. Cells from bronchoalveolar lavage and lungs were prepared for staining. Lung tissue was minced and digested with 2.2 mg ml<sup>-1</sup> collagenase IV (Worthington), 1 U ml<sup>-1</sup> DNaseI (Zymo Research) and 5% PBS at 37 °C for 45 min. BALF was centrifuged to isolate cells and suspended in red blood cell lysis buffer. Re-suspended cells from lung homogenate were also treated for red blood cell lysis. Cell numbers were enumerated with Trypan Blue staining. For cellularity analysis, the cells were stained with fixable viability dye (eFluor 780, eBioscience), anti-CD45 (Pacific orange, Invitrogen), anti-CD11b (PECy5, BioLegend), anti-Ly6G (FITC, BioLegend) and anti-SiglecF (BV421, BD bioscience), and then analysed on a MacsQuant VYB cytometer. The neutrophils were identified as CD45<sup>+</sup>SiglecF<sup>+</sup>CD11b<sup>dim</sup> cells. Methods were adapted from Misharin et al.<sup>42</sup>. Samples were run on a MacsQuant VYB cytometer and analysed with FlowJo v9.9.6. The gating strategy is provided in Supplementary Fig. 16. BALF was used to quantify host cell damage and chemoattractant KC through the use of LDH-cytotoxicity colorimetric assay (BioVision no. K311) and Mouse CXCL1/KC DuoSet ELISA (R&D Systems no. DY453), respectively.

**Fungal biofilm sample preparation.** Biofilms for imaging were cultured in MatTek dishes (MatTek no. P35G-1.0-14-C) by seeding  $10^7$  spores ml<sup>-1</sup> of GMM with 2 ml per dish for 24 h at 37 °C with 5% CO<sub>2</sub> at 21% O<sub>2</sub> or 0.2% O<sub>2</sub>. CFW stain (Sigma) was used to visualize the hyphae at a final concentration of 25 µg ml<sup>-1</sup> for 15 min.

**Fluorescent microscopy.** Fluorescent confocal microscopy was performed on an Andor W1 Spinning Disk Confocal with a Nikon Eclipse Ti inverted microscope stand with Perfect Focus, a Zeiss LSM880 with two multi-alkali photomultiplier tubes, GaAsP detector and a transmitted light detector or a Zeiss LSM800 AxioObserver.

**HrmA localization studies.** Fungi were cultured on coverslips in GMM at 30 °C for 18 h until short hyphae, were washed, ultraviolet fixed, stained with 5 µg ml<sup>-1</sup> DAPI (Life Technologies) and mounted on slides. Images were acquired with a ×100 oil-immersion objective at 488 nm (GFP) and 405 nm (DAPI) on the Andor W1 Spinning Disk Confocal. Z-stacks were assembled in Fiji (ImageJ) with sum intensity projections. Images are representative of at least ten images. Quantification was performed as previously described<sup>43</sup>.

**Fungal biofilm imaging and quantification.** Biofilms were imaged in MatTek dishes with a ×20 multi-immersion objective (Nikon) or ×10 multi-immersion objective (Zeiss, C-Apochromat ×10/0.45 W M27) using water. CFW biofilms were imaged at 405 nm and tdtomato biofilms were imaged at 561 nm at depths from 300 to 500 nm. Three-dimensional projections were generated in Nikon NIS-Elements Viewer (Nikon) or Zeiss Blue (Zeiss). For quantification of biofilm architecture strains expressed tdtomato and were imaged on the Zeiss LSM880 AxioObserver with the exception of IFM 59356-1 and IFM 59356-3 which were stained with CFW (25 µg ml<sup>-1</sup>). To quantify the branch length and branch density distribution of the hyphae network image stacks were processed in BiofilmQ (<https://drescherlab.org/data/biofilmQ/>) as follows. First, noise and background fluorescence where removed by local averaging, that is Tophat-filtering, respectively. Second, the hyphae structure was binarized by thresholding using Otsu's method<sup>44</sup>. Third, the obtained data were skeletonized with a custom BiofilmQ analysis module and all branches above a threshold length were considered for further investigation. Visualization of branch features was performed in BiofilmQ.

**FunPACT imaging.** Mounted samples for funPACT were imaged on the Andor W1 Spinning Disk Confocal with a  $\times 20$  multi-immersion objective lens used with oil or a  $\times 40$  oil-immersion objective. Areas of fungal growth were identified by manual scanning at 561 nm. Lesions were imaged at 405, 488 and 561 nm at various depths. Images were processed in Nikon NIS-Elements Viewer for deconvolution and three-dimensions rendering.

**Cell wall staining.** Hyphae were generated as described for localization studies. Filaments were stained with  $25 \mu\text{g ml}^{-1}$  CFW (Fluorescent Brightener 28, Sigma) for 15 min or soluble Dectin-1 as described previously<sup>44</sup>. Ten hyphae images were processed per strain.

**Scanning and transmission electron microscopy.** Fungal biofilms for scanning and transmission electron microscopy were grown on 12 mm sterile glass coverslips in six-well plates for 24 h at 37 °C at 21% O<sub>2</sub> with  $10^6$  spores ml<sup>-1</sup> in RPMI 1640 (Gibco). Two coverslips were generated per sample. Samples were processed for SEM (scanning electron microscopy) through a critical point drying method. Briefly, media were removed and replaced with fixative (2% GTA/2% PF in 0.05 M sodium cacodylate at pH 7.4) for 15 min at room temperature. Fresh fixative was then added for 24 h. Coverslips were then washed three times (0.05 M sodium cacodylate at pH 7.4 for 5 min) and then incubated for 1 h at room temperature in 1% OsO<sub>4</sub> in 0.05 M sodium cacodylate before three washings as before. Samples were then ethanol dehydrated for 10 min in each 30%, 50%, 70% and 85% ethanol and were then washed three times in 100% ethanol. Coverslips were then transferred to a critical point drying holder and incubated in 100% hexamethyldisilazane twice for 10 min each. Samples were then mounted on SEM stubs and coated with osmium plasma coater (4 nm) and were stored in a desiccator before imaging. SEM images were acquired on an FEI (Thermo Fisher Scientific) Scios2 LoVac dual beam FEG/FIB scanning electron microscope with a Schottky emitter source. Images were acquired at 15.0 kV with 3 nm spot size.

**Transmission electron microscopy and cell wall measurements.** For transmission electron microscopy fungal biofilms were fixed in 5 ml of 2 $\times$  fixative (2% GTA/2% PF in 0.05 M sodium cacodylate pH 7.4) for 1 h and then replaced with fresh fixative. Biofilms were scraped from coverslips and hyphae were pelleted and excess fixative removed. Hyphae were transferred to 100  $\mu\text{l}$  of 2% molten agar and solidified. Agar drops were trimmed to removed excess agar and transferred to 1 ml of fresh fixative and rotated for 3 h at room temperature then 48 h at 4 °C. Pellet was rinsed in 0.1 M sodium cacodylate/0.1 M sucrose to remove GTA and then postfix treated with 2% OsO<sub>4</sub> in 0.1 M sodium cacodylate/0.07 M sucrose for 2 h. Soft agar pellet was then rinsed twice with dH<sub>2</sub>O and then transferred to En-bloc stain with 1% uranyl acetate for 2 h at room temperature in the dark. Pellet was then dehydrated through ethanol series at room temperature with 30%, 50%, 70% for 30 min each, then on a rotator for 2 d, followed by further dehydration with 85% then 95% ethanol for 30 min and then 100% ethanol for six rinses over 6 h. Samples were then left at 4 °C for 48 h. Samples were then incubated twice in propylene oxide for 30 min each, then immersed in 1:1 LX112 (LADD):PO for 1 h at room temperature and then in 1.5:1 LX112:PO for 18 h. LX112 from LADD epoxy solution was used in 6A:4B for medium hard block. Excess fluid was removed and samples were placed in vacuum desiccator for 24 h before being transferred to BEEM capsules with fresh LX112, centrifuged for 30 min at 1500 r.p.m. and returned to vacuum desiccator for 12 h. Samples were polymerized at 45 °C for 24 h, 60 °C for 24 h and then cooled and thin sectioned and placed in 2% UA<sub>MeOH</sub> for 10 min followed by 3% Reynolds lead citrate for 2–3 min. Protocol was based on Burghardt & Droleskey<sup>45</sup>. Samples were imaged on JEOL JEM 1010 transmission electron microscope at 100.0 kV. To determine cell wall size, ImageJ was used to open images files and for each cross-section of a filament ten measurements of cell wall thickness, disregarding the electron-dense extracellular matrix, were averaged per filament.

**Statistics and reproducibility.** All statistical analysis was performed in GraphPad Prism 5, GraphPad Prism 8 and R. Unless otherwise noted, all statistical analyses were performed with a minimum of three biologically independent samples. All images are representative of a minimum of three biologically independent samples that represent a minimum of three independent experimentations unless otherwise noted. The funPact images are representative of five independent animals but to reduce the use of animals, samples for funPact images were generated from two independent sample preparations. For comparisons between two groups two-tailed unpaired *t*-tests were performed. For comparisons between more than two groups one-way ANOVA with Tukey, Sidak or Dunnett post tests for multiple comparisons were performed. All error bars indicate s.e.m. centred around the mean.

**Ethics statement.** The National Research Council Guide for the Care and Use of Laboratory Animals was strictly followed for all animal experiments. The animal experiment protocol was approved by Institutional Animal Care and Use Committee at Dartmouth College (protocol: cram.ra.1)

**Reporting Summary.** Further information on research design is available in the Nature Research Reporting Summary linked to this article.

## Data availability

RNA sequencing data that support the findings of this study have been deposited under NCBI Gene Expression Omnibus with the identifier GSE133440 under the BioProject PRJNA551460. The genomic sequencing data for EVOL20 and reference AF293 have been deposited under BioProject identifier PRJNA417720. All strains and any other data used to support these findings will be made available upon reasonable request to the corresponding author.

## Code availability

The custom scripts that were used in this study are available at [https://github.com/stajichlab/Afum\\_RNASeq\\_hrmA](https://github.com/stajichlab/Afum_RNASeq_hrmA), [https://github.com/stajichlab/Afum\\_hrmA\\_cluster\\_evolution](https://github.com/stajichlab/Afum_hrmA_cluster_evolution), [https://github.com/stajichlab/Afum\\_popgenome](https://github.com/stajichlab/Afum_popgenome) and [https://github.com/stajichlab/Afum\\_EVOL20](https://github.com/stajichlab/Afum_EVOL20). The BiofilmQ software is available for public download at <https://drescherlab.org/data/biofilmQ/>. Other data that support the findings presented here are available upon request from the corresponding author.

Received: 19 December 2018; Accepted: 9 August 2019;

Published online: 23 September 2019

## References

- Slutsky, B., Buffo, J. & Soll, D. R. High-frequency switching of colony morphology in *Candida albicans*. *Science* **230**, 666–669 (1985).
- Simpson, L. M., White, V. K., Zane, S. F. & Oliver, J. D. Correlation between virulence and colony morphology in *Vibrio vulnificus*. *Infect. Immun.* **55**, 269–272 (1987).
- Kuthan, M. et al. Domestication of wild *Saccharomyces cerevisiae* is accompanied by changes in gene expression and colony morphology. *Mol. Microbiol.* **47**, 745–754 (2003).
- Workentine, M. L. et al. Phenotypic heterogeneity of *Pseudomonas aeruginosa* populations in a cystic fibrosis patient. *PLoS ONE* **8**, e60225 (2013).
- Haussler, S. et al. Highly adherent small-colony variants of *Pseudomonas aeruginosa* in cystic fibrosis lung infection. *J. Med. Microbiol.* **52**, 295–301 (2003).
- Hagiwara, D. et al. Whole-genome comparison of *Aspergillus fumigatus* strains serially isolated from patients with aspergillosis. *J. Clin. Microbiol.* **52**, 4202–4209 (2014).
- Fong, J. C. & Yildiz, F. H. The *rbmBCDEF* gene cluster modulates development of rugose colony morphology and biofilm formation in *Vibrio cholerae*. *J. Bacteriol.* **189**, 2319–2330 (2007).
- Drenkard, E. & Ausubel, F. M. *Pseudomonas* biofilm formation and antibiotic resistance are linked to phenotypic variation. *Nature* **416**, 740–743 (2002).
- Miller, M. G. & Johnson, A. D. White-opaque switching in *Candida albicans* is controlled by mating-type locus homeodomain proteins and allows efficient mating. *Cell* **110**, 293–302 (2002).
- Workentine, M. L. et al. Phenotypic and metabolic profiling of colony morphology variants evolved from *Pseudomonas fluorescens* biofilms. *Environ. Microbiol.* **12**, 1565–1577 (2010).
- Jain, N., Guerrero, A. & Fries, B. C. Phenotypic switching and its implications for the pathogenesis of *Cryptococcus neoformans*. *FEMS Yeast Res.* **6**, 480–488 (2006).
- Jain, N., Hasan, F. & Fries, B. C. Phenotypic switching in fungi. *Curr. Fungal Infect. Rep.* **2**, 180–188 (2008).
- Kowalski, C. H. et al. Heterogeneity among isolates reveals that fitness in low oxygen correlates with *Aspergillus fumigatus* virulence. *MBio* **7**, e01515-16 (2016).
- Barker, B. M. et al. Transcriptomic and proteomic analyses of the *Aspergillus fumigatus* hypoxia response using an oxygen-controlled fermenter. *BMC Genom.* **13**, 62 (2012).
- Kale, S. D. et al. Modulation of immune signaling and metabolism highlights host and fungal transcriptional responses in mouse models of invasive pulmonary aspergillosis. *Sci. Rep.* **7**, 17096 (2017).
- McDonagh, A. et al. Sub-telomere directed gene expression during initiation of invasive aspergillosis. *PLoS Pathog.* **4**, e1000154 (2008).
- Fedorova, N. D. et al. Genomic islands in the pathogenic filamentous fungus *Aspergillus fumigatus*. *PLoS Genet.* **4**, e1000046 (2008).
- Law, M. J., Chambers, E. J., Katsamba, P. S., Haworth, I. S. & Laird-Offringa, I. A. Kinetic analysis of the role of the tyrosine 13, phenylalanine 56 and glutamine 54 network in the U1A/U1 hairpin II interaction. *Nucleic Acids Res.* **33**, 2917–2928 (2005).
- Abdel-Nour, M. et al. The *Legionella pneumophila* collagen-like protein mediates sedimentation, autoaggregation, and pathogen-phagocyte interactions. *Appl. Environ. Microbiol.* **80**, 1441–1454 (2014).
- Chen, S. M. et al. Streptococcal collagen-like surface protein 1 promotes adhesion to the respiratory epithelial cell. *BMC Microbiol.* **10**, 320 (2010).
- Wang, C. & St Leger, R. J. A collagenous protective coat enables *Metarhizium anisopliae* to evade insect immune responses. *Proc. Natl Acad. Sci. USA* **103**, 6647–6652 (2006).

22. Gravelat, F. N. et al. *Aspergillus* galactosaminogalactan mediates adherence to host constituents and conceals hyphal beta-glucan from the immune system. *PLoS Pathog.* **9**, e1003575 (2013).
23. Lee, M. J. et al. Deacetylation of fungal exopolysaccharide mediates adhesion and biofilm formation. *mBio* **7**, e00252–00216 (2016).
24. Brown, G. D. & Gordon, S. Immune recognition: a new receptor for beta-glucans. *Nature* **413**, 36–37 (2001).
25. DePas, W. H. et al. Exposing the three-dimensional biogeography and metabolic states of pathogens in cystic fibrosis sputum via hydrogel embedding, clearing, and rRNA labeling. *mBio* **7**, e00796–16 (2016).
26. Yang, B. et al. Single-cell phenotyping within transparent intact tissue through whole-body clearing. *Cell* **158**, 945–958 (2014).
27. Chung, K. et al. Structural and molecular interrogation of intact biological systems. *Nature* **497**, 332–337 (2013).
28. Ballard, E. et al. In-host microevolution of *Aspergillus fumigatus*: a phenotypic and genotypic analysis. *Fungal Genet. Biol.* **113**, 1–13 (2018).
29. Gago, S., Denning, D. W. & Bowyer, P. Pathophysiological aspects of *Aspergillus* colonization in disease. *Med. Mycol.* **57**, S219–S227 (2018).
30. Morales, D. K. et al. Control of *Candida albicans* metabolism and biofilm formation by *Pseudomonas aeruginosa* phenazines. *mBio* **4**, e00526–00512 (2013).
31. Beattie, S. R. et al. Filamentous fungal carbon catabolite repression supports metabolic plasticity and stress responses essential for disease progression. *PLoS Pathog.* **13**, e1006340 (2017).
32. Szewczyk, E. et al. Fusion PCR and gene targeting in *Aspergillus nidulans*. *Nat. Protoc.* **1**, 3111–3120 (2006).
33. Grah, N. et al. In vivo hypoxia and a fungal alcohol dehydrogenase influence the pathogenesis of invasive pulmonary aspergillosis. *PLoS Pathog.* **7**, e1002145 (2011).
34. Willger, S. D. et al. A sterol-regulatory element binding protein is required for cell polarity, hypoxia adaptation, azole drug resistance, and virulence in *Aspergillus fumigatus*. *PLoS Pathog.* **4**, e1000200 (2008).
35. Love, M. I., Huber, W. & Anders, S. Moderated estimation of fold change and dispersion for RNA-seq data with DESeq2. *Genome Biol.* **15**, 550 (2014).
36. Basenko, E. Y. et al. FungiDB: an integrated bioinformatic resource for fungi and oomycetes. *J. Fungi (Basel)* **4**, 39 (2018).
37. Wu, T. D., Reeder, J., Lawrence, M., Becker, G. & Brauer, M. J. GMAP and GSNAP for genomic sequence alignment: enhancements to speed, accuracy, and functionality. *Methods Mol. Biol.* **1418**, 283–334 (2016).
38. Liao, Y., Smyth, G. K. & Shi, W. featureCounts: an efficient general purpose program for assigning sequence reads to genomic features. *Bioinformatics* **30**, 923–930 (2014).
39. Friedman, J. H., Bentley, J. & Finkel, R. A. An algorithm for finding best matches in logarithmic expected time. *ACM Trans. Math. Softw.* **3**, 209–226 (1977).
40. Treweek, J. B. et al. Whole-body tissue stabilization and selective extractions via tissue-hydrogel hybrids for high-resolution intact circuit mapping and phenotyping. *Nat. Protoc.* **10**, 1860–1896 (2015).
41. Misharin, A. V., Morales-Nebreda, L., Mutlu, G. M., Budinger, G. R. & Perlman, H. Flow cytometric analysis of macrophages and dendritic cell subsets in the mouse lung. *Am. J. Respir. Cell Mol. Biol.* **49**, 503–510 (2013).
42. Danhof, H. A. & Lorenz, M. C. The *Candida albicans* ATO gene family promotes neutralization of the macrophage phagolysosome. *Infect. Immun.* **83**, 4416–4426 (2015).
43. Liao, P. S., Chew, T. S. & Chung, P. C. A fast algorithm for multilevel thresholding. *J. Inf. Sci. Eng.* **17**, 713–727 (2001).
44. Shephardson, K. M. et al. Hypoxia enhances innate immune activation to *Aspergillus fumigatus* through cell wall modulation. *Microbes Infect.* **15**, 259–269 (2013).
45. Burghardt, R. C. & Droleskey, R. Transmission electron microscopy. *Curr. Protoc. Microbiol.* **3**, 1–39 (2006).

## Acknowledgements

We thank J. Obar (Dartmouth) for his helpful comments, A. Lavanway and L. Howard (Dartmouth) for their microscopy expertise, T. J. Smith for graphical model design and construction, D. Limoli for funPACT assistance, S. Dhingra for tool development (plasmids), D. Carter-House for assistance with DNA extraction for whole genome sequencing and S. Lockhart, S. Howard, and D. Hagiwara for sharing *A. fumigatus* isolates. This work was supported by the efforts of R.A.C. through funding by NIH National Institute of Allergy and Infectious Diseases (NIAID) (grant nos. R01AI130128 and 2R01AI081838). R.A.C. holds an Investigators in Pathogenesis of Infectious Diseases Award from the Burroughs Wellcome Fund. C.H.K. was supported by the Molecular and Cellular Biology Training Grant at Dartmouth (no. 5T32 GM 8704–20, principal investigator: D. Compton) from the National Institute of General Medical Sciences from July 2016 to June 2018 and the NIH NIAID Ruth L. Kirschstein National Research Service Award (no. F31AI138354) from July 2018. C.D.N. is supported by the National Science Foundation (grant no. MCB 1817342), a Burke Award from Dartmouth College, a pilot award from the Cystic Fibrosis Foundation (grant no. STANTO15RO) and NIH grant no. P20-GM113132 to the Dartmouth BioMT COBRE. Data analyses were performed on the UC Riverside High-Performance Computational Cluster supported by grant nos. NSF DBI-1429826 and NIH S10-OD016290.

## Author contributions

C.H.K. designed, performed and analysed most of the experiments and wrote the manuscript. J.D.K. performed the histopathology quantification and assisted with funPact analysis. K.L. performed the cellularity analysis. M.C.B. assisted with fluorescent microscopy analysis. R.H. generated software for biofilm analysis. C.D.N. generated software for biofilm analysis and performed the biofilm analysis. J.E.S. performed analysis on genomic and RNA sequencing and phylogenetic analysis. R.A.C. designed experiments, supervised the study and edited the manuscript. All authors reviewed and approved the manuscript.

## Competing interests

The authors declare no competing interests.

## Additional information

**Supplementary information** is available for this paper at <https://doi.org/10.1038/s41564-019-0558-7>.

**Reprints and permissions information** is available at [www.nature.com/reprints](http://www.nature.com/reprints).

**Correspondence and requests for materials** should be addressed to R.A.C.

**Publisher's note** Springer Nature remains neutral with regard to jurisdictional claims in published maps and institutional affiliations.

© The Author(s), under exclusive licence to Springer Nature Limited 2019

## Reporting Summary

Nature Research wishes to improve the reproducibility of the work that we publish. This form provides structure for consistency and transparency in reporting. For further information on Nature Research policies, see [Authors & Referees](#) and the [Editorial Policy Checklist](#).

### Statistics

For all statistical analyses, confirm that the following items are present in the figure legend, table legend, main text, or Methods section.

n/a Confirmed

- ☐ ☒ The exact sample size ( $n$ ) for each experimental group/condition, given as a discrete number and unit of measurement
- ☐ ☒ A statement on whether measurements were taken from distinct samples or whether the same sample was measured repeatedly
- ☐ ☒ The statistical test(s) used AND whether they are one- or two-sided  
*Only common tests should be described solely by name; describe more complex techniques in the Methods section.*
- ☐ ☒ A description of all covariates tested
- ☐ ☒ A description of any assumptions or corrections, such as tests of normality and adjustment for multiple comparisons
- ☐ ☒ A full description of the statistical parameters including central tendency (e.g. means) or other basic estimates (e.g. regression coefficient) AND variation (e.g. standard deviation) or associated estimates of uncertainty (e.g. confidence intervals)
- ☐ ☒ For null hypothesis testing, the test statistic (e.g.  $F$ ,  $t$ ,  $r$ ) with confidence intervals, effect sizes, degrees of freedom and  $P$  value noted  
*Give  $P$  values as exact values whenever suitable.*
- ☐ ☒ For Bayesian analysis, information on the choice of priors and Markov chain Monte Carlo settings
- ☐ ☒ For hierarchical and complex designs, identification of the appropriate level for tests and full reporting of outcomes
- ☐ ☒ Estimates of effect sizes (e.g. Cohen's  $d$ , Pearson's  $r$ ), indicating how they were calculated

Our web collection on [statistics for biologists](#) contains articles on many of the points above.

### Software and code

Policy information about [availability of computer code](#)

Data collection

Nikon NIS-Elements Viewer (Nikon) software, Bio-Rad CFX Maestro, Zeiss Black, MACSQuant VYB

Data analysis

Nikon NIS-Elements Viewer, FIJI (ImageJ), GraphPad Prism 5, MatLab, R, BiofilmQ, Zeiss Blue, FlowJo version 9.9.6

For manuscripts utilizing custom algorithms or software that are central to the research but not yet described in published literature, software must be made available to editors/reviewers. We strongly encourage code deposition in a community repository (e.g. GitHub). See the Nature Research [guidelines for submitting code & software](#) for further information.

### Data

Policy information about [availability of data](#)

All manuscripts must include a [data availability statement](#). This statement should provide the following information, where applicable:

- Accession codes, unique identifiers, or web links for publicly available datasets
- A list of figures that have associated raw data
- A description of any restrictions on data availability

The following figures have associated raw data: Figure S4, Figure S1, Figure 4, Figure 1. Following the final draft of the manuscript accession numbers to the raw data will be uploaded with accession numbers and doi addresses provided. These data include genome sequencing and RNA-sequencing.

### Field-specific reporting

Please select the one below that is the best fit for your research. If you are not sure, read the appropriate sections before making your selection.

- ☒ Life sciences      ☐ Behavioural & social sciences      ☐ Ecological, evolutionary & environmental sciences

For a reference copy of the document with all sections, see [nature.com/documents/nr-reporting-summary-flat.pdf](https://www.nature.com/documents/nr-reporting-summary-flat.pdf)

## Life sciences study design

All studies must disclose on these points even when the disclosure is negative.

Sample size	Power analysis was performed to determine sample size for animal experiments (survival etc.)
Data exclusions	Data were excluded from animal studies when mice were sacrificed due to symptoms of central nervous system (CNS) infection. These exclusions were based on the pre-established criteria that mice suffering from CNS infection present different pathologies than those with pulmonary infections. A replicate for hrMAR-EV in hypoxia for the RNA-sequencing was excluded due to poor RNA quality and PCA plot indicating that this sample did not cluster with the other replicates.
Replication	All attempts at replication were successful. FunPACT was not replicated with these exact samples because of the use of animal lives and the 10-12 week period of sample processing, however n=5 were utilized for each experimental group and were accumulated from two separate sample preparations/processings.
Randomization	For animal studies, mice were randomly sorted (by groups of 4 or 5) into experimental or mock groups. For in vitro fungal assays no randomization was performed.
Blinding	Blinding was used in the replication of all animal studies and in the analysis of histopathology samples and fluorescent fungal biofilms. Blinding was not used in other in vitro fungal assays.

## Reporting for specific materials, systems and methods

We require information from authors about some types of materials, experimental systems and methods used in many studies. Here, indicate whether each material, system or method listed is relevant to your study. If you are not sure if a list item applies to your research, read the appropriate section before selecting a response.

Materials & experimental systems	Methods
n/a	n/a
Included in the study	Included in the study
<input type="checkbox"/> Antibodies	<input checked="" type="checkbox"/> ChIP-seq
<input checked="" type="checkbox"/> Eukaryotic cell lines	<input type="checkbox"/> Flow cytometry
<input checked="" type="checkbox"/> Palaeontology	<input checked="" type="checkbox"/> MRI-based neuroimaging
<input type="checkbox"/> Animals and other organisms	
<input checked="" type="checkbox"/> Human research participants	
<input checked="" type="checkbox"/> Clinical data	

### Antibodies

Antibodies used	The antibodies used in the paper were bought from eBioscience, Invitrogen, Biolegend and BD bioscience: Fixable Viability Dye (eFluor™ 780, eBioscience, 65-0865-14) anti-CD45 (Pacific orange, Invitrogen, Clone 30-F11, MCD4530) anti-CD11b (PECy5, BioLegend, Clone M1/70, 101209) anti-Ly6G (FITC, BioLegend, Clone 1A8, 127605) anti-SiglecF (BV421, BD bioscience, Clone E50-2440, 562681)
Validation	The antibodies were validated based on the datasheet provided by the manufacturers.

### Animals and other organisms

Policy information about [studies involving animals](#); [ARRIVE guidelines](#) recommended for reporting animal research

Laboratory animals	Charles River CD-1 outbred female mice 6-8 weeks (20-24 grams).
Wild animals	The study did not involve wild animals
Field-collected samples	The study did not involve field-collected samples. Clinical samples were published previously and provided by those laboratories.
Ethics oversight	The National Research Council Guide for the Care and Use of Laboratory Animals was strictly followed for all animal experiments. The animal experiment protocol was approved by Institutional Animal Care and Use Committee (IACUC) at Dartmouth College (protocol: cram.ra.1).

Note that full information on the approval of the study protocol must also be provided in the manuscript.

## Flow Cytometry

### Plots

Confirm that:

- ☒ The axis labels state the marker and fluorochrome used (e.g. CD4-FITC).
- ☒ The axis scales are clearly visible. Include numbers along axes only for bottom left plot of group (a 'group' is an analysis of identical markers).
- ☒ All plots are contour plots with outliers or pseudocolor plots.
- ☒ A numerical value for number of cells or percentage (with statistics) is provided.

### Methodology

Sample preparation	The lungs were minced in the digestion buffer containing PBS, 2.2 mg/ml Collagenase IV (Worthington), 1U/ml DNaseI (Zymo research) and 5% FBS and were incubated in 37 °C for 45 minutes. The suspended cells from BAL and lungs were treated with RBC lysis buffer and enumerated with Trypan blue staining.
Instrument	MacsQuant VYB cytometer
Software	FlowJo version 9.9.6
Cell population abundance	The isolated cells from BAL and lung were sufficient for antibody staining and data analysis.
Gating strategy	The gating strategies were the same as the supplementary figure.

- ☒ Tick this box to confirm that a figure exemplifying the gating strategy is provided in the Supplementary Information.

## Appendix V

MDA5 is an essential sensor of a pathogen-associated molecular pattern associated with vitality that is necessary for host resistance against *Aspergillus fumigatus*

Xi Wang, Alayna K Caffrey-Carr, Ko-Wei Liu, Vanessa Espinosa, Walburga Croteau, Sourabh Dhingra, Amariliz Rivera, Robert A Cramer, Joshua J Obar

KWL designed and performed the experiments, and analyzed the results in Figure 9



# HHS Public Access

Author manuscript

*J Immunol.* Author manuscript; available in PMC 2021 December 01.

Published in final edited form as:

*J Immunol.* 2020 December 01; 205(11): 3058–3070. doi:10.4049/jimmunol.2000802.

## MDA5 is an essential vita-PAMP sensor necessary for host resistance against *Aspergillus fumigatus*

Xi Wang<sup>\*,§</sup>, Alayna K. Caffrey-Carr<sup>\*,†,2,§</sup>, Ko-wei Liu<sup>\*</sup>, Vanessa Espinosa<sup>‡</sup>, Walburga Croteau<sup>\*</sup>, Sourabh Dhingra<sup>\*,3</sup>, Amariliz Rivera<sup>‡</sup>, Robert A. Cramer<sup>\*</sup>, Joshua J. Obar<sup>\*,#</sup>

<sup>\*</sup>Geisel School of Medicine at Dartmouth, Department of Microbiology & Immunology, Lebanon, NH 03756, United States

<sup>†</sup>Montana State University, Department of Microbiology & Immunology, Bozeman, MT 59718, United States

<sup>‡</sup>Center for Immunity & Inflammation, Rutgers - New Jersey Medical School, Newark, NJ, 07103, United States

### Abstract

RIG-I like receptors (RLR) are cytosolic RNA sensors that signal through the MAVS adaptor to activate interferon responses against viruses. Whether the RLR family has broader effects on host immunity against other pathogen families remains to be fully explored. Herein we demonstrate that MDA5/MAVS signaling was essential for host resistance against pulmonary *Aspergillus fumigatus* challenge through the regulation of antifungal leukocyte responses in mice. Activation of MDA5/MAVS signaling was driven by dsRNA from live *A. fumigatus* serving as a key vitality-sensing pattern-recognition receptor. Interestingly, induction of type I interferons after *A. fumigatus* challenge was only partially dependent on MDA5/MAVS signaling, whereas type III interferon expression was entirely dependent on MDA5/MAVS signaling. Ultimately, type I and III interferon signaling drove the expression of CXCL10. Furthermore, the MDA5/MAVS-dependent interferon response was critical for the induction of optimal antifungal neutrophil killing of *A. fumigatus* spores. In conclusion, our data broaden the role of the RLR family to include a role in regulating antifungal immunity against *A. fumigatus*.

### INTRODUCTION

*Aspergillus fumigatus* is a ubiquitous environmental mold that humans inhale on a daily basis. Multiple environmental surveys have demonstrated a range of several hundred to

<sup>#</sup>Corresponding author: Joshua J. Obar, Geisel School of Medicine at Dartmouth, Department of Microbiology & Immunology, 1 Medical Center Drive, Lebanon, NH 03756, Fax: +1 (603) 650-6223, Telephone: +1 (603) 650-6858, joshua.j.obar@dartmouth.edu.

<sup>2</sup>Current Address: Loxo Oncology, Boulder, CO 80301

<sup>3</sup>Current Address: Clemson University, Biological Sciences Department, Clemson, SC, 29634

#### AUTHOR CONTRIBUTIONS

Conceived and designed the experiments: XW, AKC, AR, RC, JJO. Performed the experiments: XW, AKC, VE, KL, WC, SD.

Analyzed the data: XW, AKC, VE, KL, WC, AR, JJO. Wrote the paper: XW, JJO.

XW and AKC are co-first authors: AKC initiated these studies before graduating, while XW picked up and completed these studies and helped write the manuscript, which warranted listing XW first.

<sup>§</sup>These authors contributed equally to this work

**Conflict of Interests:** The authors have declared that no conflict of interest exists.



thousands of *A. fumigatus* conidia can be inhaled daily (1–3). Individuals with normal immune systems readily clear *A. fumigatus* conidia from their airways without problems. However, immunocompromised individuals are at significantly greater risk of developing invasive pulmonary aspergillosis (IPA)<sup>4</sup>. IPA is a life-threatening disease with over 300,000 cases globally and a high mortality rate of 30% – 50% (4). Patients at increased risk of developing IPA include those receiving chemotherapy treatments for cancer and patients receiving immunosuppressive regimens to prevent graft-versus-host disease (GVHD) following hematopoietic stem cell transplants or solid organ transplants (5–9). Furthermore, epidemiology studies predict a steady increase of IPA cases in the future due to the projected continual increase of immune compromised patients (10). Additionally, individuals with single nucleotide polymorphisms (SNPs) or primary immunodeficiencies in key antifungal signaling or effector pathways, such as CARD9 (11), pentraxin 3 (12, 13), or NADPH oxidase (14, 15) are highly susceptible to IPA. Thus, these clinical observations demonstrate that host innate immune responses are imperative in deactivating viable fungal conidia to avoid fungal establishment in the lung, and failure of such processes result in fungal germination and fungal growth and dissemination, ultimately culminating in IPA.

If the physical barriers of the lungs are bypassed by the inhaled *A. fumigatus* conidia, airway epithelial cells and lung-resident macrophages comprise the first line of defense against inhaled conidia. It is well established that lung resident macrophages, including alveolar macrophages (16, 17) and CCR2<sup>+</sup> monocytes (18, 19) are critical for initiating the early inflammatory milieu necessary for the recruitment of innate immune cells to the respiratory tract to mediate host resistance against invasive disease. These innate immune effector cells include neutrophils (20, 21), inflammatory monocytes (18, 19), NKT cells (22), and plasmacytoid dendritic cells (23–25). The cytokine/chemokine signaling networks necessary to regulate the recruitment of inflammatory cells to the respiratory tract are rapidly emerging, but still much remains to be learnt.

Recently, it has become well appreciated that the host inflammatory response induced by *A. fumigatus* is tightly tuned to the virulence of the individual strain under study (26–30). Being able to recognize pathogenic traits of microbes is key to appropriately responding to infection (31), one such trait is being able to resist killing and remain viable (32). Two crucial inflammatory pathways in signaling bacterial vitality are inflammasome-dependent secretion of IL-1 $\beta$  and induction of the interferon response, which both can be driven by bacterial RNA (33, 34). We and others have previously demonstrated that inflammasomes are essential for IL-1 $\beta$  production after *A. fumigatus* challenge (35–38). Interestingly, Kanneganti and colleagues have shown that the NLRP3 and AIM2 inflammasomes could be activated by fungal RNA and DNA, respectively (35). Moreover, both type I and type III interferons have been shown to be essential for host resistance against pulmonary *A. fumigatus* challenge (39), but the fungal PAMP and host pattern-recognition pathways

<sup>4</sup>Abbreviations: RLR, RIG-I like receptors; IPA, invasive pulmonary aspergillosis; GVHD, graft-versus-host disease; SNP, single nucleotide polymorphism; GMM, glucose minimal medium; PBS, phosphate buffered saline; i.t., intratracheal; BALF, bronchoalveolar lavage fluid; GMS, Grocott-Gomori methenamine silver; FLARE, fluorescent *Aspergillus* reporter; vita-PAMP, vitality pathogen-associated molecular pattern

leading to type I and type III interferon expression following *A. fumigatus* challenge have not been well elucidated.

Type I and type III interferon responses are best understood in the context of virus infections. Following virus infections, Toll-like receptors (including TLR3, TLR7/8, TLR9), cGAS/STING, and RIG-I-like receptors (RIG-I and MDA5) are known to be critical in the induction of type I and type III interferons (review by (40–42)). However, during fungal infections much less is currently known. Both TLR3 and TLR9 are known to be involved in the antifungal defenses against *A. fumigatus* (43–46), but only their role in the induction of type I interferons has been explored (45, 47). Following *Candida albicans* infection TLR7 is known to be involved in the induction of type I interferons (48, 49). Moreover, a Dectin-1/Syk/Irf5 signaling network has been shown to be critical in the induction of type I interferons following *C. albicans* challenge (50). Finally, Dectin-1 has been shown to be partially involved in the induction of type I and III interferons following respiratory *A. fumigatus* challenge (51). However, the role of cytosolic sensing pattern-recognition receptors systems in the antifungal interferon response has not been well studied.

Our data demonstrate that MDA5/MAVS-dependent signaling is necessary for host resistance against *A. fumigatus* infection through the accumulation and activation of antifungal effector functions of neutrophils in the fungal challenged airways. MAVS signaling drove expression of both type I and type III interferon, which ultimately drove the expression of the interferon inducible chemokines CXCL9 and CXCL10. Overall, our study reveals a critical role for MDA5 in host anti-fungal immunity, which supports a broader role of MDA5 in monitoring the health of the host cytosol.

## MATERIALS AND METHODS

### Mice.

C57BL/6J (Jackson Laboratory, Stock #000664), *Mavs*<sup>−/−</sup> (Jackson Laboratory, Stock #008634), and *Ifih1*<sup>−/−</sup> (Jackson Laboratory, Stock # 015812) were all originally purchased from Jackson Laboratories and sequentially bred in-house at Geisel School of Medicine at Dartmouth. *Ifnar*<sup>−/−</sup>, *Ifnlr*<sup>−/−</sup>, and *Ifnar*<sup>−/−</sup> *Ifnlr*<sup>−/−</sup> DKO were kindly provided by Dr. Sergei Kotenko and Dr. Joan Durbin (52) and bred in-house at Rutgers – New Jersey Medical School. Wild-type B6.129F2 (Jackson Laboratory, Stock #101045) mice, used as controls for the *Mavs*<sup>−/−</sup> mice, were purchased directly from Jackson Laboratories. All mice were 8–16 weeks of age at the time of challenge. Both male and female mice were used for these experiments. All animal experiments were approved by either the Rutgers – New Jersey Medical School Institutional Animal Care and Use Committee or Dartmouth College Institutional Animal Care and Use Committee.

### Preparation of *Aspergillus fumigatus* conidia.

*A. fumigatus* CEA10 and Af293 strains were used for this study. Each strain was grown on glucose minimal media (GMM) agar plates for 3 days at 37°C. Conidia were harvested by adding 0.01% Tween 80 to plates and gently scraping conidia from the plates using a cell

scraper. Conidia were then filtered through sterile Miracloth, were washed, and resuspended in phosphate buffered saline (PBS), and counted on a hemocytometer.

#### Preparation of swollen conidia and heat-killing.

*A. fumigatus* CEA10 conidia were collected, as described above. To generate a homogenous population of swollen conidia, conidia were resuspended at  $5 \times 10^6$  conidia per ml in RPMI containing  $0.5 \mu\text{g/ml}$  of voriconazole (Sigma-Aldrich) and incubated at  $37^\circ\text{C}$  for 15 h, as previously done (53). Conidia were then washed twice and adjusted to  $4 \times 10^8$  conidia per ml in PBS-Tween 80. To heat-kill the swollen conidia, the conidial suspension was incubated in a  $100^\circ\text{C}$  water bath for 30 minutes. The conidial concentration and efficiency of heat-killing was verified by plating on GMM agar.

#### *Aspergillus fumigatus* pulmonary challenge model.

Mice were challenged with *A. fumigatus* conidia by the intratracheal (i.t.) route. Mice were anesthetized by inhalation of isoflurane; subsequently, mice were challenged i.t. with  $\sim 4 \times 10^7$  *A. fumigatus* conidia in a volume of  $100 \mu\text{l}$  PBS. At the indicated time after *A. fumigatus* challenge, mice were euthanized using a lethal overdose of pentobarbital. Bronchoalveolar lavage fluid (BALF) was collected by washing the lungs with 2 ml of PBS containing  $0.05\text{M}$  EDTA. BALF was clarified by centrifugation and stored at  $-20^\circ\text{C}$  until analysis. After centrifugation, the cellular component of the BALF was resuspended in  $200 \mu\text{l}$  of PBS and total BAL cells were determined by hemocytometer count. BALF cells were subsequently spun onto glass slides using a Cytospin4 cytocentrifuge (Thermo Scientific) and stained with Diff-Quik (Siemens) or Hema 3™ Stat Pack (Fisher Scientific) stain sets for differential counting. For histological analysis lungs were filled with and stored in 10% buffered formalin phosphate for at least 24 hours. Lungs were then embedded in paraffin and sectioned into 5-micron sections. Sections were stained with Grocott-Gomori methenamine silver (GMS) using standard histological techniques to assess lung inflammatory infiltrates and fungal germination, respectively. Representative pictures of lung sections were taken using either the 20X or 40X objectives on an Olympus IX73 with a Zeiss Azicam 208 color camera.

#### Luminex assay for cytokine and chemokine secretion from experimental murine models of invasive aspergillosis.

BALF and lung homogenates from B6/129F2 mice and *Mavs*<sup>-/-</sup> mice challenged with *A. fumigatus* 12 or 48 h prior were analyzed for cytokines and chemokines using Milliplex Mouse Cytokine & Chemokine 32-plex (Millipore). Plates were read using a BioPlex 200 (Bio-Rad) in the Immune Monitoring and Flow Cytometry Core Facility at Dartmouth College.

#### Quantitative RT-PCR analysis.

Total RNA from lungs was extracted with Trizol (Invitrogen). One microgram of total RNA was reverse transcribed using High Capacity cDNA Reverse Transcription Kit (Applied Biosystems). TaqMan Fast Universal Master Mix (2X) No AmpErase UNG and TaqMan probes (Applied Biosystems, Catalog #4331182) for *Ifna2* (Mm00833961\_s1), *Ifnb1*

(Mm00439552\_s1), *Ifnl2/3* (Mm0404158\_gH), *Ifng* (Mm01168134\_m1), *Cxcl9* (Mm00434946\_m1), and *Cxcl10* (Mm00445235\_m1) were used and normalized to *Gapdh* (Mm99999915\_g1). Gene expression was calculated using  $\Delta\Delta CT$  method relative to naïve sample.

#### Western blot analysis.

Total protein from whole lungs was extracted using RIPA buffer. Total protein was quantified using a DC™ Protein Assay (Bio-Rad). For Western Blot analysis, 40µg of total protein was loaded per well. Gels were run at 100V for ~1 hour at room temperature and then transferred to PVDF membranes at 100V for ~1 hour at 4°C. After transfer, the membranes were blocked with TBST + 5% milk for 1 hour at room temperature. Following blocking, blots were rinsed twice with TBST buffer. Staining with primary antibodies was done in TBST with 5% BSA at 4°C for overnight on a roller. Primary antibodies used for these studies were rabbit anti-STAT1 (Cell Signaling, #9172S, 1/1000), rabbit anti-pSTAT1 (Cell Signaling, #7649P, 1/1000 dilution), and rabbit anti-β-actin (Abcam, ab75186, 1/40,000). After primary antibody staining blots were washed four times with TBST. Blots were then stained with a donkey anti-rabbit IgG conjugated to HRP (Cell Signaling, #7074P2, 1/4000 dilution) in TBST + 5% milk for 1 hour at room temperature with gentle shaking. After secondary antibody staining blots were washed four times with TBST. Blots were developed using ECL Clarity (Bio-Rad) for 5 minutes, then analyzed using an Alpha Innotech FluorChem Q imager.

#### Generation of a Fluorescent *Aspergillus fumigatus* reporter (FLARE) strain in the CEA10 background.

CEA10:H2A.X<sup>A. nidulans::ptrA</sup> was constructed in two steps. First, *gpdA*(p) was amplified from DNA isolated from strain *A. nidulans* A4 (Source: FGSC) using primers RAC2888 and RAC2799. Histone variant H2A.X (AN3468) was amplified (without stop codon) from A4 DNA using primers RAC4582 and RAC4583. mRFP fragment was amplified from plasmid pXDRFP4 (Source: FGSC) using primers RAC2600 and RAC4575 and terminator for *A. nidulans trpC* gene was amplified using primers RAC2536 and RAC2537. The four fragments were then fused together with primers RAC1981 and RAC4134 using fusion PCR resulting in H2A.X first round fragment as described earlier (54). All primers are listed in Supplemental Table 1.

Secondly, we targeted integration of the H2A.X::rfp to the intergenic locus between AFUB\_023460 and AFUB\_023470. For this, left homology arm was amplified from CEA10 genomic DNA using primers RAC3873 and RAC3874. Right homology arm was amplified with primers RAC3875 and RAC3876. Dominant selection marker gene *ptrA* conferring resistance to pyrithiamine hydrobromide was amplified from plasmid pSD51.1 with primers RAC2055 and RAC2056. The four fragments were then fused together with primers RAC3877 and RAC3878 using fusion PCR as described earlier (54). After the construct generation, polyethylene glycol mediated transformation of protoplast was performed as described earlier (54). Transformants were screened by PCR (data not shown) and confirmed with southern blot analysis as described earlier (55). mRFP fluorescence was confirmed with FACS (Fluorescence activated cell sorting) analysis.

### Fluorescent *Aspergillus fumigatus* reporter (FLARE) assay.

To measure both conidial uptake and viability in distinct immune cell populations we used fluorescent *Aspergillus* reporter (FLARE). The CEA10-based FLARE was labelled with AlexaFluor 633 membrane labeling, as described elsewhere (56). Bronchoalveolar lavage (BAL) and lung cell suspensions were prepared as described elsewhere (56) and stained with anti-Ly6G (1A8), anti-CD11b (M1/70), anti-CD11c (HL3), anti-CD45 (30-F11), anti-CD206 (C068C2) and a fixable viability dye (eBioscience; Catalog #65-0865-14). Neutrophils were identified as CD45<sup>+</sup>CD11b<sup>+</sup>Ly6G<sup>+</sup>, alveolar macrophages as CD45<sup>+</sup>CD11b<sup>+</sup>Ly6G<sup>-</sup>CD206<sup>dim</sup>, interstitial macrophages as CD45<sup>+</sup>CD11b<sup>+</sup>Ly6G<sup>-</sup>CD206<sup>-</sup>, and monocytes as CD45<sup>+</sup>CD11b<sup>dim</sup>Ly6G<sup>-</sup>CD206<sup>+</sup> cells, as previously defined (57, 58). Flow cytometric data were collected on a CytoFLEX (Beckman Coulter). All data was analyzed using FlowJo software.

### Primary murine fibroblast cultures.

Ears from 6–12 week-old C57BL/6J and *Ifih1*<sup>-/-</sup> mice were collected, washed in 70% EtOH, then PBS, and finally minced using scissors. For each ear, 500  $\mu$ l of 1000 U/ml collagenase (Gibco, REF 17101-015) in HBSS was used to digest them at 37°C for 25 minutes. The tissues were then centrifuged at 500  $\times$  g for 3 minutes and then washed once with HBSS. Ears were subsequently digested with 500  $\mu$ l of 0.05% trypsin in HBSS for a further 20 minutes in 37°C. The tissues were then centrifuged again at 500  $\times$  g for 3 minutes, and the trypsin was discarded and replaced by 0.5ml fibroblast media [10% FCS, 1% MEM Non-essential amino acids, 1% penicillin-streptomycin in DMEM]. The tissues were then pushed through a sterile 40  $\mu$ m cell strainer via the plunger of a 3ml syringe to obtain single cell suspensions. For every ear, 25ml of fibroblast media was used to initiate the murine fibroblast culture in tissue culture flasks and a media change was conducted every two days. The fibroblasts were usually confluent and harvested on day 6 by 0.25% trypsin digest for 5min in 37°C and then collected with fresh fibroblast media.

### Isolation of total RNA from *Aspergillus fumigatus*.

*A. fumigatus* conidia was harvested from GMM plates and inoculated at  $1 \times 10^6$  per ml in liquid GMM. Cultures were grown for 24h in 37°C with shaking at 250 rpm in an orbital shaker. Mycelia were then filtered and wrapped in sterile Miracloth, dried by repeated paper towel absorption, and weighed. For every 50 mg of mycelium, 1 ml of Trisure (Bioline) was added and mixed. The Trisure-mycelium mixture was frozen by liquid nitrogen to release cellular content and then homogenized using a mortar and pestle. For every 1 ml of Trisure used, 0.2 ml chloroform was added and vortexed, and the solution was centrifuged for 15 min at 12000  $\times$  g at 4°C. The aqueous phase was then transferred to a new tube and 0.5 ml of isopropanol was added, vortexed, and centrifuged for 10 min at 12000  $\times$  g at 4°C. The supernatant was then removed, and the pellet was washed by 1 ml 75% ethanol via vortexing followed with centrifuging for 5 min at 7500  $\times$  g at 4°C. The 75% ethanol was then removed to allow a complete air dry of the RNA, followed by dissolving in molecular biology grade water and stored in -80°C.

### Stimulation of murine fibroblasts with fungal RNA.

Freshly harvested murine fibroblasts were dosed at  $5 \times 10^4$ /ml in fibroblast media and transferred to 24-well tissue culture treated plates with 0.5 ml per well. The plate was incubated for one day to allow the attachment of murine fibroblasts. Fibroblasts were then transfected via LyoVec™ (InvivoGen)/RNA complexes. For every 200  $\mu$ l of LyoVec™, 2  $\mu$ g of either poly-IC (InvivoGen), 5'-ppp RNA (InvivoGen), or *A. fumigatus* RNA was diluted in 80  $\mu$ l molecular biology grade water, mixed, and incubated in room temperature for 30 minutes to assemble the liposome. The assembled liposome complexes were then added to 5 ml of fibroblast medium and 0.5 ml of the above transfection media was transferred to each well of 24-well plates after removal of the original medium. Twenty-four hours after transfection the supernatant was collected for subsequent ELISA analysis.

### ELISA analysis for cytokine and chemokine secretion.

Cell culture supernatants from fibroblast stimulated with *A. fumigatus* RNA were analyzed by ELISA for CXCL10 (R&D Systems, Cat. DY466) and Interferon alpha (Invitrogen, Cat. BMS6027TWO). Plates were read using an Epoch BioTek Gen5 microplate reader at 450nm, and the background was subtracted at 570nm.

### Statistical analysis.

Statistical significance for *in vitro* and *ex vivo* data was determined by a Mann-Whitney U test, one-way ANOVA using a Tukey's or Dunn's post-test, or two-way ANOVA with Tukey's post-test through the GraphPad Prism 7 software as outlined in the figure legends. Mouse survival data were analyzed with the Mantel-Cox log rank test using GraphPad Prism.

## RESULTS

### Induction of an optimal interferon response by *Aspergillus fumigatus* is dependent on viable conidia.

The polysaccharide-rich cell wall is a major driver of the inflammatory response against *A. fumigatus* and other fungi. Following *C. albicans* challenge the Dectin-1 (*Clec7a*) receptor is critical in the induction of type I interferons following (50). Dectin-1 is only partially responsible for induction of the type I and type III interferon response induced by *A. fumigatus* (51). To test whether the fungal cell wall was essential for driving the type I and type III interferon response, we stimulated C57BL/6J mice with  $4 \times 10^7$  live or heat-killed swollen conidia of the CEA10 strain of *A. fumigatus*. Forty hours post-challenge with live swollen conidia there was an induction of IL-28 (IFN- $\lambda$ ), CXCL10, and TNF $\alpha$  secretion (Figure 1). In contrast, when challenged with heat-killed swollen conidia secretion of both IL-28 (IFN- $\lambda$ ) and CXCL10 was markedly reduced, while TNF $\alpha$  was still induced (Figure 1). These findings demonstrate that while cell carbohydrates in heat-killed swollen conidia still drove robust inflammatory cytokines (such as TNF $\alpha$ ), as has previously been demonstrated (53, 59), there is an alternative pattern-recognition receptor pathway which is largely responsible for the interferon response induced by live *A. fumigatus* conidia.

### dsRNA from *Aspergillus fumigatus* drives an MDA5-dependent interferon response.

Vitality sensing during bacterial infection through recognition of bacterial RNA has been shown to be critical for the induction of protective immune responses through the secretion of both IL-1 $\beta$  and type I interferons (33). Thus, we next wanted to test whether *A. fumigatus* RNA could drive interferon release. To test this hypothesis, primary murine fibroblasts from C57BL/6J mice were stimulated with naked or liposome packaged total RNA from the Af293 strain of *A. fumigatus*. As expected, untreated fibroblast or empty liposome treated did not drive significant secretion of IFN $\alpha$  or CXCL10, while liposome packaged polyI:C drove significant secretion of both (Figure 2A). Liposome-packaged Af293 RNA drove secretion of both IFN $\alpha$  and CXCL10, while naked Af293 could not drive their production (Figure 2A). Taken together, these data demonstrate that intracellular sensing of *A. fumigatus* RNA can drive an interferon-dependent inflammatory response.

Intracellular sensing of RNA is mediated by the RIG-I-like receptor family, composed of RIG-I and MDA5, for the induction of interferons. Both RIG-I and MDA5 recognize distinct structures in foreign RNA (60, 61). To test whether ssRNA or dsRNA from *A. fumigatus* was required to drive type I IFN secretion, we extended these *in vitro* fibroblast stimulation studies by pre-treating the *A. fumigatus* RNA pool with either RNase S1 or RNase III, which will selectively cleave ssRNA and dsRNA, respectively, prior to liposome packaging. We also treated the fungal RNA pool with DNase I as a control. Similar to our previous result, total *A. fumigatus* RNA packaged in liposomes was able to induce IFN $\alpha$  secretion from murine fibroblast (Figure 2B). Pre-treatment of the *A. fumigatus* RNA with either RNase S1 or DNase I had no impact on the secretion of IFN $\alpha$  (Figure 2B). In contrast, pre-treatment of the *A. fumigatus* RNA with RNase III completely ablated the secretion of IFN $\alpha$  from primary murine fibroblasts (Figure 2B). These data suggest that recognition of double-stranded fungal RNA in the cytosol is necessary for the interferon response induced by *A. fumigatus*.

To date the most well characterized intracellular receptor for dsRNA is MDA5 (60). To test whether *A. fumigatus* RNA initiates an interferon response in a MDA5-dependent manner we treated primary murine fibroblasts isolated from C57BL/6J or *Ifih1*<sup>-/-</sup> mice liposome packaged fungal RNA. As positive controls, we utilized high molecular weight polyI:C, a known MDA5 ligand, and 5'ppp-RNA, a known RIG-I ligand. Eighteen hours after stimulation cell culture supernatants were collected for ELISA analysis to assess IFN $\alpha$  secretion. Unstimulated or LyoVec<sup>TM</sup> only stimulated fibroblast did not secrete any IFN $\alpha$  (Figure 2B). As positive controls, 5'ppp-RNA stimulated equivalent secretion of IFN $\alpha$  from both wild-type and *Ifih1*-deficient fibroblasts; while high molecular weight polyI:C stimulated robust IFN $\alpha$  secretion from wild-type fibroblast, which was significantly reduced in *Ifih1*-deficient fibroblasts (Figure 2B). The induction of IFN $\alpha$  secretion by *A. fumigatus* RNA was partially dependent on MDA5, like what we also observed with high molecular weight polyI:C (Figure 2B). Interestingly, RNase III treatment ablated both the MDA5-dependent and -independent IFN- $\alpha$  response (Figure 2B), which suggests there is another dsRNA receptor that contributes to the IFN- $\alpha$  response in response to encapsulated fungal RNA.

### MAVS-dependent signaling is required for interferon expression after *Aspergillus fumigatus* challenge

During viral infections RLR family members are critical in initiating both the type I and type III interferon responses (62). Moreover, stimulation of *Ifih1*-deficient murine macrophages with *C. albicans* resulted in a slight decrease in *Ifnb* mRNA expression, which did not reach significance (63). However, the specific role of MDA5/MAVS in initiating the induction of a broad range of interferons to other fungal pathogens has not been explored. To test the role of MAVS signaling in the induction of interferons after respiratory challenge with *A. fumigatus*, we challenged B6.129F2 mice and *Mavs*<sup>-/-</sup> mice with 4×10<sup>7</sup> conidia of CEA10. We collected lungs from the *A. fumigatus* challenged mice at 3 and 48 h post-inoculation for quantitative RT-PCR analysis to assess interferon expression patterns. Similar to previous observations with C57BL/6J mice (39), wild-type B6.129F2 mice expressed high levels of type I interferons, *Ifna4* (Figure 3A) and *Ifnb* (Figure 3B), at 3 h post-inoculation that waned with time. Both type II interferon (*Ifng*) (Figure 3D) and type III interferon (*Ifnl2/3*) (Figure 3C) were expressed at higher levels at 48 h post-inoculation in wild-type B6.129F2 mice. Interestingly, in the *Mavs*-deficient mice type I interferon levels were only decreased by approximately 50% (Figure 3A–B), whereas the expression of type II and type III interferons were nearly completely ablated in the absence of MAVS (Figure 3C–D). Thus, MAVS-dependent signaling is essential for the late expression of type III interferon and only partially responsible for early expression of type I interferons.

To confirm that the expression of interferons resulted in down-stream IFN signaling, we next examined the phosphorylation of STAT1. STAT1 phosphorylation is essential for the signaling of all interferon classes. Lungs from C57BL/6J mice challenged 6, 24, or 48 h prior with either the CEA10 or Af293 strains were collected, and total proteins were extracted for Western blot analysis. Both the CEA10 and Af293 strains induced a bi-phasic induction of STAT1 phosphorylation (Figure 4A). Specifically, significant STAT1 phosphorylation was observed at 6 and 48 h after challenge, but minimal phosphorylation was observed at 24 h (Figure 4A). These data fit with our earlier observation that type I interferons are produced by 3 h post-challenge, while type II and type III interferons are highly expressed at later times (Figure 3). We next examined the phosphorylation of STAT1 in the lungs of B6.129F2 and *Mavs*<sup>-/-</sup> mice challenged with the CEA10 strain of *A. fumigatus* at 6 and 48 h after challenge, times when we saw high levels of STAT1 phosphorylation. Like C57BL/6J mice, wild-type B6.129F2 mice induced robust phosphorylation of STAT1 at both 6 and 48 h (Figure 4B). Interestingly, at 6 h after challenge with *A. fumigatus* the phosphorylation of STAT1 in the *Mavs*<sup>-/-</sup> mice was not significantly different, although there was a slight but reproducible reduction (Figure 4B–C), which fits with our earlier observation that type I interferon mRNA levels were only mildly reduced at 3 h post-challenge with *A. fumigatus* (Figure 3A–B). In contrast, phosphorylation of STAT1 in the *Mavs*<sup>-/-</sup> mice was significantly decreased at 48 h post-challenge with *A. fumigatus* (Figure 4B–C), which corresponds with the significant decrease in type III interferon mRNA levels we observed at this time (Figure 3C). Taken together, these results strongly support the conclusion that MAVS signaling is critical for the late expression of type III interferons in response to *A. fumigatus* instillation and initiation of the interferon response that is necessary for host resistance against *A. fumigatus* infection.



### Alteration of the airway inflammatory milieu after *Aspergillus fumigatus* challenge in the absence of MAVS-dependent signaling

While our data demonstrates that all the classes of interferons are decreased to vary degrees after pulmonary *A. fumigatus* challenged, we next wanted to more broadly understand the cytokine and chemokine response in the airways of *Mavs*<sup>-/-</sup> mice. To achieve this, we challenged B6.129F2 and *Mavs*<sup>-/-</sup> mice with  $4 \times 10^7$  conidia of *A. fumigatus*. At 12 and 48 h after challenge with *A. fumigatus*, the BALF was analyzed using a 32-plex Milliplex cytokine assay. Numerous cytokines and chemokines—TNF $\alpha$ , IL-17A, CCL2, and CCL4—were expressed in a manner that was completely independent of MAVS signaling (Figure 5). Interestingly, IL-1 $\alpha$ , IL-1 $\beta$ , CXCL1, and CXCL2 secretion were significantly greater in the absence of MAVS signaling (Figure 5). In contrast, IL-12p70, CXCL9, and CXCL10 secretion was significantly impaired in the absence of MAVS signaling, particularly at 48 h post-challenge despite the large increase in fungal burden (Figure 5). These data suggest that MAVS-dependent signaling is critical for induction and/or maintenance of these cytokines.

### *Cxcl9* and *Cxcl10* mRNA expression after pulmonary *Aspergillus fumigatus* challenge requires both type I and type III interferons

The marked decrease in CXCL9 and CXCL10 expression in the absence of MAVS following *A. fumigatus* challenge was quite striking, because both CXCL9 and CXCL10 are interferon-inducible chemokines (64). To test the role of type I and type III interferons in the induction of CXCL9 and CXCL10 expression, we challenged C57BL/6, *Ifnar*<sup>-/-</sup>, *Ifnlr*<sup>-/-</sup>, and *Ifnar*<sup>-/-</sup> *Ifnlr*<sup>-/-</sup> (DKO) mice with  $4 \times 10^7$  conidia of *A. fumigatus*. Forty-eight hours later, lungs were collected for quantitative RT-PCR analysis to assess *Cxcl9* and *Cxcl10* mRNA expression patterns. Both *Ifnar*- and *Ifnlr*-deficient mice had a significant decrease in their expression of both *Cxcl9* (Figure 6A) and *Cxcl10* (Figure 6B). In general, the defect in *Cxcl9* and *Cxcl10* mRNA expression was greater in the absence of type III interferon signaling, particularly regarding *Cxcl9* expression. Importantly, the *Ifnar*<sup>-/-</sup> *Ifnlr*<sup>-/-</sup> (DKO) mice had the most severe defect in *Cxcl9* and *Cxcl10* expression (Figure 6). Overall, these data demonstrate that type I and type III interferon signaling are essential for the expression of both *Cxcl9* and *Cxcl10*.

### MDA5/MAVS-dependent signaling is required for host resistance against *Aspergillus fumigatus* infection

These previous data suggest that MDA5 can sense *A. fumigatus* RNA to drive an interferon response, which could be critical in vitality sensing following an *in vivo* challenge with *A. fumigatus*. Thus, we wanted to test the role of MDA5/MAVS signaling in host resistance against respiratory challenge with the human fungal pathogen, *A. fumigatus*. To globally assess the role of the RLR family in antifungal immunity, we initially challenged B6.129F2 mice and *Mavs*<sup>-/-</sup> mice with  $4 \times 10^7$  conidia of the CEA10 strain, since MAVS is the central signaling adaptor for both RIG-I and MDA5-mediated responses (65–68). We monitored the survival of the *A. fumigatus* challenged mice over the next two weeks. *Mavs*-deficient mice were more susceptible to pulmonary challenge with *A. fumigatus* than wild-type, B6.129F2 mice (Figure 7A; Mantel-Cox log rank test,  $p = 0.0001$ ). Additionally, susceptibility of the *Mavs*<sup>-/-</sup> mice to *A. fumigatus* challenge is not dependent on the strain of *A. fumigatus* used

because *Mavs*<sup>-/-</sup> mice challenged with the Af293 strain were also highly susceptible to infection (Supplemental Figure 1; Mantel-Cox log rank test,  $p < 0.0001$ ).

It is widely acknowledged that neutrophils and macrophages are critical antifungal effector cells for clearing *A. fumigatus* from the lungs. Thus, we assessed inflammatory cell accumulation in the airways via differential microscopic counting of cytopins stained with Diff-Quik from the BALF. The increased susceptibility of *Mavs*-deficient mice to *A. fumigatus* challenge was associated with decreased accumulation of macrophages and neutrophils in the airways compared with B6.129F2 mice at 40 h post-challenge (Figure 7B). Next, we assessed fungal growth and tissue invasion in the lung by histological analysis at 40 h after conidial instillation. Strikingly, GMS staining of lung tissue from *Mavs*-deficient mice revealed the presence of germinating *A. fumigatus* conidia at 40 h that was not observed to the same extent in B6.129F2 mice (Figure 7C). When the presence of germinating *A. fumigatus* conidia was quantified, wild-type B6.129F2 mice displayed low levels of fungal germination ( $17.6\% \pm 2.9$ ) compared with *Mavs*<sup>-/-</sup> mice in which most of the fungal material had germinated ( $73.8\% \pm 7.6$ ) by 40 h post-challenge (Figure 7C). B6.129F2 mice had very few areas of fungal material throughout their lungs, but it was associated with robust cellular infiltration and tissue destruction (Figure 7C).

To specifically address which RLR sensor is involved in regulating the innate anti-fungal immune response against *A. fumigatus* we chose to assess the role of MDA5 because of its role in the *in vitro* sensing of *A. fumigatus* RNA (Figure 2). Specifically, we challenged C57BL/6J and *Ifih1*<sup>-/-</sup> mice with  $4 \times 10^7$  conidia of *A. fumigatus*. We monitored the survival of the *A. fumigatus* challenged mice over the next ten days. Like the *Mavs*-deficient mice, *Ifih1*-deficient mice were more susceptible to pulmonary challenge with *A. fumigatus* than wild-type C57BL/6J mice (Figure 8A; Mantel-Cox log rank test,  $p = 0.0004$ ). Analogous to what we observed in the *Mavs*-deficient mice, the increased susceptibility of *Ifih1*-deficient mice to *A. fumigatus* challenge was associated with decreased accumulation of neutrophils in the airways compared with C57BL/6J mice at 40 h post-challenge (Figure 8B). GMS staining of lung tissue from *Ifih1*-deficient mice revealed the presence of germinating *A. fumigatus* conidia at 42 h that was not observed to the same extent in C57BL/6J mice (Figure 8C) similar to our observation in the *Mavs*-deficient mice.

While immune competent animal models have provided important insights into the host immune pathways necessary for antifungal control (11, 13, 56, 69–71), we wanted to assess the importance of MDA5/MAVS signaling in a clinically relevant immune compromised model of IPA. For this we utilized the triamcinolone model of IPA (72). Briefly, C57BL/6J and *Ifih1*<sup>-/-</sup> mice were immunosuppressed with triamcinolone and then subjected to challenge with  $10^6$  conidia of the Af293 strain of *A. fumigatus*. At 72 h post-inoculation lungs were collected for histological analysis for fungal growth. Interestingly, *Ifih1*<sup>-/-</sup> mice had a significantly greater number of fungal lesions per lung section than C57BL/6J mice (Supplemental Figure 2A). Moreover, the fungal lesions appear to be larger and contain more fungi (Supplemental Figure 2A). Additionally, the BALF from *Ifih1*<sup>-/-</sup> challenged mice had higher levels of LDH activity (Supplemental Figure 2B) and albumin (Supplemental Figure 2C), which are indicators of lung damage and leakage, respectively, than C57BL/6J challenged mice. Taken together, these results strongly support the

conclusion that MDA5/MAVS signaling is critical for host resistance against *A. fumigatus* in an immune competent murine model and critical for disease progression in a corticosteroid immune compromised murine model.

#### Neutrophil antifungal effector functions are decreased in the absence of MDA5.

To determine whether MDA5/MAVS signaling regulates antifungal effector cell functions, we used FLARE conidia challenge of C57BL/6 or *Ifih1*<sup>-/-</sup> mice to assess neutrophil-mediated conidial uptake and killing. FLARE conidia encode a fungal viability indicator (DsRed) and contain a tracer fluorophore (Alexa Fluor 633) (56). For this study we generated a novel FLARE strain in the CEA10 strain background (Supplemental Figure 3). FLARE conidia emit two fluorescence signals (DsRed and Alexa Fluor 633) when the conidia are alive, but only emit a single fluorescence signal (Alexa Fluor 633) when the conidia are dead. This approach allows us to determine the frequency of conidia-engaged immune cells that contain either live or dead fungal cells in the BAL and lungs. The frequency of conidia-engaged neutrophils was similar between the C57BL/6 and *Ifih1*<sup>-/-</sup> mice (Figure 9A). However, the frequency of conidia-engaged neutrophils that contain live conidia was increased among *Ifih1*<sup>-/-</sup> mice compared with C57BL/6J mice, indicating a defect in conidial killing (Figure 8B). Specifically, the frequency of neutrophils that contain live conidia was 1.9-fold and 2.1-fold higher for BAL and lung fluid of *Ifih1*<sup>-/-</sup> mice compared with their C57BL/6J counterparts (Figure 9B). Thus, these data indicate that neutrophil-mediated antifungal killing of *A. fumigatus* conidia requires MDA5/MAVS activation and signaling.

## DISCUSSION

It is now well appreciated that the host inflammatory response induced by *A. fumigatus* is tightly tuned to the virulence of the individual strain under study (26–30). One key determinant for sensing the threat posed by filamentous fungi is changes in fungal cell wall composition. Specifically, detection of  $\beta$ -1,3-glucan linked polysaccharides by Dectin-1 (*Clec7a*) occurs only upon conidial swelling and germling formation, which are the earliest steps of fungal growth (53, 59). Interestingly, our data demonstrate that while heat-killed swollen conidia of *A. fumigatus* can induce the secretion of pro-inflammatory cytokines, such as TNF $\alpha$ , they do not drive the secretion of IFN $\alpha$  and CXCL10 (Figure 1). These data suggest that heat sensitive fungal factors other than cell wall polysaccharides are responsible for driving the interferon response following respiratory *A. fumigatus* challenge. Consistent with this observation, individual polysaccharides commonly found in the *A. fumigatus* cell wall are not sufficient to induce an interferon response (73). Thus, other less studied fungal traits, that appear to require live fungi, are needed to induce a protective interferon response.

Intriguingly, during bacterial infections one key virulence trait sensed by the host immune system to tune the inflammatory response is the ability of the bacteria to resist killing and remain viable. Two crucial inflammatory pathways that signal bacterial vitality to the host are inflammasome secretion of IL-1 $\beta$  and an interferon response through TRIF and cGAS/STING signaling (33, 34, 74). Following respiratory challenge with *A. fumigatus* both IL-1 $\beta$  and type I/III interferons have been shown to be critical for antifungal immunity (35, 39).

While we and others have previously demonstrated that inflammasomes are essential for the IL-1 $\beta$  response after respiratory challenge with *A. fumigatus* (35–38), the innate pattern-recognition receptor(s) leading to type I/III interferon expression have not been elucidated. Moreover, fungal molecules that signal vitality to the host are not yet defined.

In bacteria one critical PAMP associated with vitality (vita-PAMP) is RNA. Using an *E. coli* infection model, bacterial RNA was shown to be sufficient to drive both inflammasome-dependent IL-1 $\beta$  secretion and TRIF-dependent IFN $\beta$  secretion (33). Heat-killing of *E. coli* drove the loss of RNA and its subsequent inflammatory response (33). Several innate RNA sensors have been identified in mammalian hosts, including TLR3 (75), TLR7 (76), MDA5 (77), and RIG-I (78). TLR3 and TLR7 signal through TRIF (79), while MDA5 and RIG-I signal through MAVS (65–68) to drive the interferon response. In our study, RNase III treatment of total RNA isolated from *A. fumigatus* demonstrates that dsRNA from *A. fumigatus* is sufficient to drive an interferon response (Figure 2B). TLR3 and MDA5 are both receptors for dsRNA (60, 75, 78). Importantly, mice lacking *Mavs* displayed a markedly reduced type III interferon (IL-28/IFN $\lambda$ ), CXCL9, and CXCL10 secretion, but only a moderate defect in type I interferons (Figure 4). In contrast, the expression of *Ifna1* and *Ifnb1* are regulated by both TRIF (46) and TLR3 (45). Interestingly, the role of TRIF appears to be restricted to the non-hematopoietic compartment (46), likely epithelial cells (80). Taken together these data suggest the type I interferon response following live *A. fumigatus* challenge is primarily driven by TLR3/TRIF-dependent signaling, while the type III interferon response is primarily driven by MDA5/MAVS-dependent signaling.

Our data raises an interesting conundrum of how RNA from live *A. fumigatus* enters host cell cytoplasm to drive MDA5/MAVS activation. One potential mechanism for the translocation of RNA from the phagosome to the cytosol is damage to the phagosomal membrane and the leakage of phagosomal contents to cytosol. In their original work describing vita-PAMPs Blander and colleagues found that phagosomes containing *E. coli* exhibited intrinsic leakiness, which enabled RNA from the live *E. coli* to enter the cytosol and activate cytosolic PRRs (33). However, phagosome leakiness is not unique to these bacterial systems as this has been previously described for particles such as beads and crystals that induce phagosome destabilization (81, 82). Interestingly, fungal pathogens can also drive phagosome destabilization and rupture leading to the activation of inflammasomes and pyroptosis (26, 83). In contrast to the passive nature of phagosomal leakage, SIDT2 has been shown to actively transport of dsRNA from the endosome to the cytosol for detection by RLRs, which was necessary for the IFN response to Poly(I:C), ECMV, and HSV-1 (84). Another alternative pathway may be extracellular vesicles. Fungal extracellular vesicles contain a variety of cargos including RNA, polysaccharides, and enzymes (85). Since extracellular vesicles possess the lipid bilayer structure like liposomes, they could deliver their contents to the cytosol via membrane fusion. Interestingly, extracellular vesicles from *Mycobacterium tuberculosis* have been shown to be sufficient for the activation of RIG-I (86, 87). Studies examining how *A. fumigatus* RNA found in the phagosomal compartment gains access to the cytoplasm to mediate the activation of cytosolic PRRs to drive the enhanced vita-PAMP response are on-going.

The purpose of vitality sensing is to drive robust inflammation that is in line with the threat posed by the invading pathogen. Neutrophils are well known to be critical antifungal effector cells needed for the prevention of fungal germination and clearance of *A. fumigatus* from the lungs (20). Our results demonstrate that MDA5/MAVS-dependent signaling is necessary for both the optimal accumulation (Figures 7 and 8) and activation of neutrophils in *Aspergillus* challenged murine airways (Figure 9). Following pulmonary challenge with *A. fumigatus* it has been established that both type I and type III interferons are essential for host resistance through enhancing neutrophil ROS production and antifungal effector functions (39). Our FLARE data support these previous observations as neutrophils in both the lungs and airways of *Ifih1*-deficient mice are significantly impaired in their antifungal killing capacity at 48 h after challenge (Figure 9), which corresponds with a time when type III interferons are nearly absent in mice lacking MDA5/MAVS signaling. Decreased accumulation of neutrophils in the *Mavs*- and *Ifih1*-deficient mice did not correlate with classical neutrophil chemoattractants, such as CXCR2 ligands, that are required to maintain host resistance against *A. fumigatus* (36, 70, 88). Rather, in the absence of *Mavs* and *Ifih1* there was a marked decrease in CXCL9 and CXCL10, which are both ligands for CXCR3. Recently, CXCR3 has been suggested to be a potential chemoattractant for neutrophils in certain systems (89, 90). However, *Cxcr3*-deficient mice appear to recruit normal numbers of neutrophils following *A. fumigatus* challenge (25). Thus, why *Mavs*- and *Ifih1*-deficient mice accumulate few neutrophils in their lungs following challenge warrants further research.

Type I interferon response can have both beneficial and detrimental effects to the host. For example, during LCMV Armstrong infection type I interferons drive host resistance (91), but excessive type I interferon levels found following LCMV Clone 13 infection promote virus persistence and immunopathology (92–94). Thus, the optimal tuning of the magnitude of the type I interferon response can dictate disease outcome following viral infection. The role of type I interferons during fungal infections has now been studied in several model systems, demonstrating a similar dichotomy. Following *A. fumigatus* challenge both type I and type III interferons are essential for host resistance against invasive aspergillosis through enhancing neutrophil ROS production and antifungal effector functions (24, 39). Moreover, augmentation of the type I interferon in X-CGD mice with invasive aspergillosis following treatment with Poly(I:C) improved disease outcomes (95). Similarly, during *Cryptococcus neoformans* treatment with Poly(I:C) drove type I interferon expression and iron limitation which corresponded with improved disease outcomes (96, 97). However, opposing roles of type I interferon signaling in T cell polarization following *C. neoformans* challenge have been observed, either promoting protective Th1 cells (98) or non-protective Th2 cells (99). After *Histoplasma capsulatum* challenge type I interferon signaling is essential for host resistance (100). The role of type I interferons during *Candida* spp. infections appear to be more complex. During *Candida glabrata* infection type I interferons promote fungal persistence through dampening nutritional immunity (101–103). Following *C. albicans* challenge, type I interferons either promote host resistance (49, 50, 104) or promote immunopathological immune responses which enhance disease (105). Thus, much remains to be learned about how interferons regulate infection outcomes during fungal infections. In this regard, how the detection of cell wall PAMPs, like  $\beta$ -1,3-glucans, by Dectin-1 (47, 50,

51) and fungal RNA, through TLRs (47, 48, 100, 103) and RLRs (63), coordinate the type I and type III interferon responses needed to be further explored. vita-PAMPs appear to be essential for the optimal induction the RNA driven interferon responses.

While the role of RLRs in host immunity was originally associated with antiviral innate immune responses (reviewed by (42)), recent studies have begun to expand the role of RLRs in immunity to other pathogens, including *C. albicans*, *Listeria monocytogenes*, *Mycobacterium tuberculosis*, and *Plasmodium falciparum* (40, 63, 86, 106–109). Our study adds *A. fumigatus* to the list of non-viral pathogens which can activate the RLR family. Further studies aiming to decipher the cellular and molecular mechanisms by which *A. fumigatus* enhances antifungal immunity through MDA5 activation are expected to inform us how the host uses these vita-PAMPs to sense the threat posed by fungal pathogens. Understanding how best to alter the host to the treat a pathogen poses will enable us to develop strategies to harness the inflammatory response for prophylactic or therapeutic gain in vulnerable populations. Interestingly, exogenous Poly(I:C) treatment prophylactically improves outcomes of invasive aspergillosis in *gp91<sup>phox</sup>*-deficient mice, particularly when challenged with resting conidia rather than germlings (95). Our previous work has highlighted that germlings induced a highly inflammatory response dependent on IL-1 $\alpha$  (26) and LTB<sub>4</sub> (27); thus, understanding the interplay and activation of the type I/III interferon, IL-1 $\alpha$ , and LTB<sub>4</sub> inflammatory response necessary to control both the conidial and hyphal forms will essential for completely understanding host resistance and therapeutic options against *A. fumigatus*. Finally, our study raises the possibility that MDA5/MAVS and type I/III interferon signaling in critical for preventing invasive aspergillosis in vulnerable human patient populations.

## Supplementary Material

Refer to Web version on PubMed Central for supplementary material.

## ACKNOWLEDGEMENTS

Thank you to Dr. Brent Berwin (Geisel School of Medicine at Dartmouth), Dr. David Leib (Geisel School of Medicine at Dartmouth), and Dr. Tobias Hohl (Memorial Sloan Kettering Cancer Center) for helpful discussion on this project and manuscript. Thank you to Stacy Ceron for assistance in generation of the primary murine fibroblast cultures.

Research in this study was supported in part by institutional startup funds to JJO in part through the Dartmouth Lung Biology Center for Molecular, Cellular, and Translational Research grant P30 GM106394 (PI: Bruce A. Stanton) and Center for Molecular, Cellular and Translational Immunological Research grant P30 GM103415 (PI: William R. Green). JJO was partially supported by a Munck-Pfefferkorn Award from Dartmouth College and NIH R01 AI139133 grant. Work by AR was partially funded by NIH R01 AI114647 grant. AR and RAC are Investigators in the Pathogenesis of Infectious Diseases supported by the Burroughs Wellcome Fund. The funders had no role in the preparation or publication of the manuscript.

## REFERENCES

1. Chazalet V, Debeaupuis JP, Sarfati J, Lortholary J, Ribaud P, Shah P, Cornet M, Vu Thien H, Gluckman E, Brucker G, and Latge JP. 1998 Molecular typing of environmental and patient isolates of *Aspergillus fumigatus* from various hospital settings. *J Clin Microbiol* 36: 1494–1500. [PubMed: 9620367]

2. Goodley JM, Clayton YM, and Hay RJ. 1994 Environmental sampling for aspergilli during building construction on a hospital site. *J Hosp Infect* 26: 27–35. [PubMed: 7910180]
3. Hospenthal DR, Kwon-Chung KJ, and Bennett JE. 1998 Concentrations of airborne *Aspergillus* compared to the incidence of invasive aspergillosis: lack of correlation. *Med Mycol* 36: 165–168. [PubMed: 9776829]
4. Brown GD, Denning DW, Gow NA, Levitz SM, Netea MG, and White TC. 2012 Hidden killers: human fungal infections. *Sci Transl Med* 4: 165rv113.
5. Baddley JW, Andes DR, Marr KA, Kontoyiannis DP, Alexander BD, Kauffman CA, Oster RA, Anaissie EJ, Walsh TJ, Schuster MG, Wingard JR, Patterson TF, Ito JI, Williams OD, Chiller T, and Pappas PG. 2010 Factors associated with mortality in transplant patients with invasive aspergillosis. *Clin Infect Dis* 50: 1559–1567. [PubMed: 20450350]
6. Steinbach WJ, Marr KA, Anaissie EJ, Azie N, Quan SP, Meier-Kriesche HU, Apewokin S, and Horn DL. 2012 Clinical epidemiology of 960 patients with invasive aspergillosis from the PATH Alliance registry. *J Infect* 65: 453–464. [PubMed: 22898389]
7. Garcia-Vidal C, Upton A, Kirby KA, and Marr KA. 2008 Epidemiology of invasive mold infections in allogeneic stem cell transplant recipients: biological risk factors for infection according to time after transplantation. *Clin Infect Dis* 47: 1041–1050. [PubMed: 18781877]
8. Upton A, Kirby KA, Carpenter P, Boeckh M, and Marr KA. 2007 Invasive aspergillosis following hematopoietic cell transplantation: outcomes and prognostic factors associated with mortality. *Clin Infect Dis* 44: 531–540. [PubMed: 17243056]
9. Thompson GR 3rd and Patterson TF. 2008 Pulmonary aspergillosis. *Semin Respir Crit Care Med* 29: 103–110. [PubMed: 18365992]
10. Bongomin F, Gago S, Oladele RO, and Denning DW. 2017 Global and Multi-National Prevalence of Fungal Diseases-Estimate Precision. *J Fungi (Basel)* 3: 67.
11. Rieber N, Gazendam RP, Freeman AF, Hsu AP, Collar AL, Sugui JA, Drummond RA, Rongkavitt C, Hoffman K, Henderson C, Clark L, Mezger M, Swamydas M, Engeholm M, Schule R, Neumayer B, Ebel F, Mikelis CM, Pittaluga S, Prasad VK, Singh A, Milner JD, Williams KW, Lim JK, Kwon-Chung KJ, Holland SM, Hartl D, Kuijpers TW, and Lionakis MS. 2016 Extrapulmonary *Aspergillus* infection in patients with CARD9 deficiency. *JCI Insight* 1: e89890. [PubMed: 27777981]
12. Fisher CE, Hohl TM, Fan W, Storer BE, Levine DM, Zhao LP, Martin PJ, Warren EH, Boeckh M, and Hansen JA. 2017 Validation of single nucleotide polymorphisms in invasive aspergillosis following hematopoietic cell transplantation. *Blood* 129: 2693–2701. [PubMed: 28270451]
13. Cunha C, Aversa F, Lacerda JF, Busca A, Kurzai O, Grube M, Löffler J, Maertens JA, Bell AS, Inforzato A, Barbat E, Almeida B, Santos e Sousa P, Barbui A, Potenza L, Caira M, Rodrigues F, Salvatori G, Pagano L, Luppi M, Mantovani A, Velardi A, Romani L, and Carvalho A. 2014 Genetic PTX3 deficiency and aspergillosis in stem-cell transplantation. *N Engl J Med* 370: 421–432. [PubMed: 24476432]
14. Morgenstern DE, Gifford MA, Li LL, Doerschuk CM, and Dinuer MC. 1997 Absence of respiratory burst in X-linked chronic granulomatous disease mice leads to abnormalities in both host defense and inflammatory response to *Aspergillus fumigatus*. *J Exp Med* 185: 207–218. [PubMed: 9016870]
15. Pollock JD, Williams DA, Gifford MA, Li LL, Du X, Fisherman J, Orkin SH, Doerschuk CM, and Dinuer MC. 1995 Mouse model of X-linked chronic granulomatous disease, an inherited defect in phagocyte superoxide production. *Nat Genet* 9: 202–209. [PubMed: 7719350]
16. Grimm MJ, Vethanayagam RR, Almyroudis NG, Dennis CG, Khan AN, D'Auria AC, Singel KL, Davidson BA, Knight PR, Blackwell TS, Hohl TM, Mansour MK, Vyas JM, Rohm M, Urban CF, Kelkka T, Holmdahl R, and Segal BH. 2013 Monocyte- and macrophage-targeted NADPH oxidase mediates antifungal host defense and regulation of acute inflammation in mice. *J Immunol* 190: 4175–4184. [PubMed: 23509361]
17. Bhatia S, Fei M, Yarlagadda M, Qi Z, Akira S, Saijo S, Iwakura Y, van Rooijen N, Gibson GA, St Croix CM, Ray A, and Ray P. 2011 Rapid host defense against *Aspergillus fumigatus* involves alveolar macrophages with a predominance of alternatively activated phenotype. *PLoS One* 6: e15943. [PubMed: 21246055]

18. Espinosa V, Jhingran A, Dutta O, Kasahara S, Donnelly R, Du P, Rosenfeld J, Leiner I, Chen CC, Ron Y, Hohl TM, and Rivera A. 2014 Inflammatory monocytes orchestrate innate antifungal immunity in the lung. *PLoS Pathog* 10: e1003940. [PubMed: 24586155]
19. Hohl TM, Rivera A, Lipuma L, Gallegos A, Shi C, Mack M, and Pamer EG. 2009 Inflammatory monocytes facilitate adaptive CD4 T cell responses during respiratory fungal infection. *Cell Host Microbe* 6: 470–481. [PubMed: 19917501]
20. Mircescu MM, Lipuma L, van Rooijen N, Pamer EG, and Hohl TM. 2009 Essential role for neutrophils but not alveolar macrophages at early time points following *Aspergillus fumigatus* infection. *J Infect Dis* 200: 647–656. [PubMed: 19591573]
21. Bonnett CR, Cornish EJ, Harmsen AG, and Burritt JB. 2006 Early neutrophil recruitment and aggregation in the murine lung inhibit germination of *Aspergillus fumigatus* Conidia. *Infect Immun* 74: 6528–6539. [PubMed: 16920786]
22. Cohen NR, Tatituri RV, Rivera A, Watts GF, Kim EY, Chiba A, Fuchs BB, Mylonakis E, Besra GS, Levitz SM, Brigl M, and Brenner MB. 2011 Innate recognition of cell wall beta-glucans drives invariant natural killer T cell responses against fungi. *Cell Host Microbe* 10: 437–450. [PubMed: 22100160]
23. Loures FV, Rohm M, Lee CK, Santos E, Wang JP, Specht CA, Calich VL, Urban CF, and Levitz SM. 2015 Recognition of *Aspergillus fumigatus* hyphae by human plasmacytoid dendritic cells is mediated by dectin-2 and results in formation of extracellular traps. *PLoS Pathog* 11: e1004643. [PubMed: 25659141]
24. Ramirez-Ortiz ZG, Lee CK, Wang JP, Boon L, Specht CA, and Levitz SM. 2011 A nonredundant role for plasmacytoid dendritic cells in host defense against the human fungal pathogen *Aspergillus fumigatus*. *Cell Host Microbe* 9: 415–424. [PubMed: 21575912]
25. Guo Y, Kasahara S, Jhingran A, Tosini NL, Zhai B, Aufiero MA, Mills KAM, Gjonbalaj M, Espinosa V, Rivera A, Luster AD, and Hohl TM. 2020 During *Aspergillus* Infection, Monocyte-Derived DCs, Neutrophils, and Plasmacytoid DCs Enhance Innate Immune Defense through CXCR3-Dependent Crosstalk. *Cell Host Microbe* doi: 10.1016/j.chom.2020.1005.1002.
26. Caffrey-Carr AK, Kowalski CH, Beattie SR, Blaseg NA, Upshaw CR, Thammahong A, Lust HE, Tang YW, Hohl TM, Cramer RA, and Obar JJ. 2017 IL-1alpha is Critical for Resistance Against Highly Virulent *Aspergillus fumigatus* Isolates. *Infect Immun* 85: e00661–00617. [PubMed: 28947643]
27. Caffrey-Carr AK, Hilmer KM, Kowalski CH, Shepardson KM, Temple RM, Cramer RA, and Obar JJ. 2018 Host-Derived Leukotriene B4 Is Critical for Resistance against Invasive Pulmonary Aspergillosis. *Front Immunol* 8: 1984. [PubMed: 29375586]
28. Caffrey AK and Obar JJ. 2016 Alarmin(g) the innate immune system to invasive fungal infections. *Curr Opin Microbiol* 32: 135–143. [PubMed: 27351354]
29. Rizzetto L, Giovannini G, Bromley M, Bowyer P, Romani L, and Cavalieri D. 2013 Strain dependent variation of immune responses to *A. fumigatus*: definition of pathogenic species. *PLoS One* 8: e56651. [PubMed: 23441211]
30. Rosowski EE, Raffa N, Knox BP, Golenberg N, Keller NP, and Huttenlocher A. 2018 Macrophages inhibit *Aspergillus fumigatus* germination and neutrophil-mediated fungal killing. *PLoS Pathog* 14: e1007229. [PubMed: 30071103]
31. Vance RE, Isberg RR, and Portnoy DA. 2009 Patterns of pathogenesis: discrimination of pathogenic and nonpathogenic microbes by the innate immune system. *Cell Host Microbe* 6: 10–21. [PubMed: 19616762]
32. Blander JM and Sander LE. 2012 Beyond pattern recognition: five immune checkpoints for scaling the microbial threat. *Nat Rev Immunol* 12: 215–225. [PubMed: 22362354]
33. Sander LE, Davis MJ, Boekschoten MV, Amsen D, Dascher CC, Ryffel B, Swanson JA, Muller M, and Blander JM. 2011 Detection of prokaryotic mRNA signifies microbial viability and promotes immunity. *Nature* 474: 385–389. [PubMed: 21602824]
34. Barbet G, Sander LE, Geswell M, Leonardi I, Cerutti A, Iliev I, and Blander JM. 2018 Sensing Microbial Viability through Bacterial RNA Augments T Follicular Helper Cell and Antibody Responses. *Immunity* 48: 584–598. [PubMed: 29548673]



35. Karki R, Man SM, Malireddi RK, Gurung P, Vogel P, Lamkanfi M, and Kanneganti TD. 2015 Concerted activation of the AIM2 and NLRP3 inflammasomes orchestrates host protection against *Aspergillus* infection. *Cell Host Microbe* 17: 357–368. [PubMed: 25704009]
36. Caffrey AK, Lehmann MM, Zickovich JM, Espinosa V, Shepardson KM, Watschke CP, Hilmer KM, Thammarahong A, Barker BM, Rivera A, Cramer RA, and Obar JJ. 2015 IL-1 $\alpha$  signaling is critical for leukocyte recruitment after pulmonary *Aspergillus fumigatus* challenge. *PLoS Pathog* 11: e1004625. [PubMed: 25629406]
37. Said-Sadier N, Padilla E, Langsley G, and Ojcius DM. 2010 *Aspergillus fumigatus* stimulates the NLRP3 inflammasome through a pathway requiring ROS production and the Syk tyrosine kinase. *PLoS One* 5: e10008. [PubMed: 20368800]
38. Moretti S, Bozza S, Oikonomou V, Renga G, Casagrande A, Iannitti RG, Puccetti M, Garlanda C, Kim S, Li S, van de Veerdonk FL, Dinarello CA, and Romani L. 2014 IL-37 inhibits inflammasome activation and disease severity in murine aspergillosis. *PLoS Pathog* 10: e1004462. [PubMed: 25375146]
39. Espinosa V, Dutta O, McElrath C, Du P, Chang YJ, Cicciarelli B, Pitler A, Whitehead I, Obar JJ, Durbin JE, Kotenko SV, and Rivera A. 2017 Type III interferon is a critical regulator of innate antifungal immunity. *Science Immunology* 2: eaan5357. [PubMed: 28986419]
40. Wu J, Tian L, Yu X, Pattaradilokrat S, Li J, Wang M, Yu W, Qi Y, Zeituni AE, Nair SC, Crampton SP, Orandle MS, Bolland SM, Qi CF, Long CA, Myers TG, Coligan JE, Wang R, and Su XZ. 2014 Strain-specific innate immune signaling pathways determine malaria parasitemia dynamics and host mortality. *Proc Natl Acad Sci U S A* 111: E511–520. [PubMed: 24474800]
41. Lazear HM, Schoggins JW, and Diamond MS. 2019 Shared and Distinct Functions of Type I and Type III Interferons. *Immunity* 50: 907–923. [PubMed: 30995506]
42. Dixit E and Kagan JC. 2013 Intracellular pathogen detection by RIG-I-like receptors. *Adv Immunol* 117: 99–125. [PubMed: 23611287]
43. Herbst S, Shah A, Mazon Moya M, Marzola V, Jensen B, Reed A, Birrell MA, Saijo S, Mostowy S, Shaunak S, and Armstrong-James D. 2015 Phagocytosis-dependent activation of a TLR9-BTK-calcineurin-NFAT pathway co-ordinates innate immunity to *Aspergillus fumigatus*. *EMBO Mol Med* 7: 240–258. [PubMed: 25637383]
44. Ramaprakash H, Ito T, Standiford TJ, Kunkel SL, and Hogaboam CM. 2009 Toll-like receptor 9 modulates immune responses to *Aspergillus fumigatus* conidia in immunodeficient and allergic mice. *Infect Immun* 77: 108–119. [PubMed: 18936185]
45. Carvalho A, De Luca A, Bozza S, Cunha C, D'Angelo C, Moretti S, Perruccio K, Iannitti RG, Fallarino F, Pierini A, Latge JP, Velardi A, Aversa F, and Romani L. 2012 TLR3 essentially promotes protective class I-restricted memory CD8(+) T-cell responses to *Aspergillus fumigatus* in hematopoietic transplanted patients. *Blood* 119: 967–977. [PubMed: 22147891]
46. de Luca A, Bozza S, Zelante T, Zagarella S, D'Angelo C, Perruccio K, Vacca C, Carvalho A, Cunha C, Aversa F, and Romani L. 2010 Non-hematopoietic cells contribute to protective tolerance to *Aspergillus fumigatus* via a TRIF pathway converging on IDO. *Cell Mol Immunol* 7: 459–470. [PubMed: 20835271]
47. Khan NS, Kasperkovitz PV, Timmons AK, Mansour MK, Tam JM, Seward MW, Reedy JL, Puranam S, Feliu M, and Vyas JM. 2016 Dectin-1 Controls TLR9 Trafficking to Phagosomes Containing beta-1,3 Glucan. *J Immunol* 196: 2249–2261. [PubMed: 26829985]
48. Biondo C, Malara A, Costa A, Signorino G, Cardile F, Midiri A, Galbo R, Papasergi S, Domina M, Pugliese M, Teti G, Mancuso G, and Beninati C. 2012 Recognition of fungal RNA by TLR7 has a nonredundant role in host defense against experimental candidiasis. *Eur J Immunol* 42: 2632–2643. [PubMed: 22777843]
49. Biondo C, Signorino G, Costa A, Midiri A, Gerace E, Galbo R, Bellantoni A, Malara A, Beninati C, Teti G, and Mancuso G. 2011 Recognition of yeast nucleic acids triggers a host-protective type I interferon response. *Eur J Immunol* 41: 1969–1979. [PubMed: 21480215]
50. del Fresno C, Soulat D, Roth S, Blazek K, Udalova I, Sancho D, Ruland J, and Ardavin C. 2013 Interferon-beta production via Dectin-1-Syk-IRF5 signaling in dendritic cells is crucial for immunity to *C. albicans*. *Immunity* 38: 1176–1186. [PubMed: 23770228]

51. Dutta O, Espinosa V, Wang K, Avina S, and Rivera A. 2020 Dectin-1 Promotes Type I and III Interferon Expression to Support Optimal Antifungal Immunity in the Lung. *Front Cell Infect Microbiol* 10: 321. [PubMed: 32733815]
52. Lin JD, Feng N, Sen A, Balan M, Tseng HC, McElrath C, Smirnov SV, Peng J, Yasukawa LL, Durbin RK, Durbin JE, Greenberg HB, and Kolenko SV. 2016 Distinct Roles of Type I and Type III Interferons in Intestinal Immunity to Homologous and Heterologous Rotavirus Infections. *PLoS Pathog* 12: e1005600. [PubMed: 27128797]
53. Hohl TM, Van Epps HL, Rivera A, Morgan LA, Chen PL, Feldmesser M, and Pamer EG. 2005 *Aspergillus fumigatus* triggers inflammatory responses by stage-specific beta-glucan display. *PLoS Pathog* 1: e30. [PubMed: 16304610]
54. Szewczyk E, Nayak T, Oakley CE, Edgerton H, Xiong Y, Taheri-Talesh N, Osmani SA, and Oakley BR. 2006 Fusion PCR and gene targeting in *Aspergillus nidulans*. *Nat Protoc* 1: 3111–3120. [PubMed: 17406574]
55. Willger SD, Puttikamonkul S, Kim KH, Burritt JB, Grahl N, Metzler LJ, Barbuch R, Bard M, Lawrence CB, and Cramer RA Jr. 2008 A sterol-regulatory element binding protein is required for cell polarity, hypoxia adaptation, azole drug resistance, and virulence in *Aspergillus fumigatus*. *PLoS Pathog* 4: e1000200. [PubMed: 18989462]
56. Jhingran A, Mar KB, Kumasaka DK, Knoblauch SE, Ngo LY, Segal BH, Iwakura Y, Lowell CA, Hamerman JA, Lin X, and Hohl TM. 2012 Tracing conidial fate and measuring host cell antifungal activity using a reporter of microbial viability in the lung. *Cell Rep* 2: 1762–1773. [PubMed: 23200858]
57. Schyns J, Bureau F, and Marichal T. 2018 Lung Interstitial Macrophages: Past, Present, and Future. *J Immunol Res* 2018: 5160794. [PubMed: 29854841]
58. Misharin AV, Morales-Nebreda L, Mutlu GM, Budinger GR, and Perlman H. 2013 Flow cytometric analysis of macrophages and dendritic cell subsets in the mouse lung. *Am J Respir Cell Mol Biol* 49: 503–510. [PubMed: 23672262]
59. Steele C, Rapaka RR, Metz A, Pop SM, Williams DL, Gordon S, Kolls JK, and Brown GD. 2005 The beta-glucan receptor dectin-1 recognizes specific morphologies of *Aspergillus fumigatus*. *PLoS Pathog* 1: e42. [PubMed: 16344862]
60. Pichlmair A, Schulz O, Tan CP, Rehwinkel J, Kato H, Takeuchi O, Akira S, Way M, Schiavo G, and Reis e Sousa C. 2009 Activation of MDA5 requires higher-order RNA structures generated during virus infection. *J Virol* 83: 10761–10769. [PubMed: 19656871]
61. Pichlmair A, Schulz O, Tan CP, Naslund TI, Liljestrom P, Weber F, and Reis e Sousa C. 2006 RIG-I-mediated antiviral responses to single-stranded RNA bearing 5'-phosphates. *Science* 314: 997–1001. [PubMed: 17038589]
62. Odendall C, Dixit E, Stavru F, Bierre H, Franz KM, Durbin AF, Boulant S, Gehrke L, Cossart P, and Kagan JC. 2014 Diverse intracellular pathogens activate type III interferon expression from peroxisomes. *Nat Immunol* 15: 717–726. [PubMed: 24952503]
63. Jaeger M, van der Lee R, Cheng SC, Johnson MD, Kumar V, Ng A, Plantinga TS, Smeekens SP, Oosting M, Wang X, Barchet W, Fitzgerald K, Joosten LA, Perfect JR, Wijmenga C, van de Veerdonk FL, Huynen MA, Xavier RJ, Kullberg BJ, and Netea MG. 2015 The RIG-I-like helicase receptor MDA5 (IFIH1) is involved in the host defense against *Candida* infections. *Eur J Clin Microbiol Infect Dis* 34: 963–974. [PubMed: 25579795]
64. Groom JR and Luster AD. 2011 CXCR3 ligands: redundant, collaborative and antagonistic functions. *Immunol Cell Biol* 89: 207–215. [PubMed: 21221121]
65. Seth RB, Sun L, Ea CK, and Chen ZJ. 2005 Identification and characterization of MAVS, a mitochondrial antiviral signaling protein that activates NF-kappaB and IRF 3. *Cell* 122: 669–682. [PubMed: 16125763]
66. Kawai T, Takahashi K, Sato S, Coban C, Kumar H, Kato H, Ishii KJ, Takeuchi O, and Akira S. 2005 IPS-1, an adaptor triggering RIG-I- and Mda5-mediated type I interferon induction. *Nat Immunol* 6: 981–988. [PubMed: 16127453]
67. Xu LG, Wang YY, Han KJ, Li LY, Zhai Z, and Shu HB. 2005 VISA is an adapter protein required for virus-triggered IFN-beta signaling. *Mol Cell* 19: 727–740. [PubMed: 16153868]

68. Meylan E, Curran J, Hofmann K, Moradpour D, Binder M, Bartenschlager R, and Tschopp J. 2005 Cardif is an adaptor protein in the RIG-I antiviral pathway and is targeted by hepatitis C virus. *Nature* 437: 1167–1172. [PubMed: 16177806]
69. Garlanda C, Hirsch E, Bozza S, Salustri A, De Acetis M, Nota R, Maccagno A, Riva F, Bottazzi B, Peri G, Doni A, Vago L, Botto M, De Santis R, Carminati P, Siracusa G, Altruda F, Vecchi A, Romani L, and Mantovani A. 2002 Non-redundant role of the long pentraxin PTX3 in anti-fungal innate immune response. *Nature* 420: 182–186. [PubMed: 12432394]
70. Jhingran A, Kasahara S, Shepardson KM, Junecko BA, Heung LJ, Kumasaka DK, Knoblaugh SE, Lin X, Kazmierczak BI, Reinhart TA, Cramer RA, and Hohl TM. 2015 Compartment-specific and sequential role of MyD88 and CARD9 in chemokine induction and innate defense during respiratory fungal infection. *PLoS Pathog* 11: e1004589. [PubMed: 25621893]
71. Drummond RA, Collar AL, Swamydas M, Rodriguez CA, Lim JK, Mendez LM, Fink DL, Hsu AP, Zhai B, Karauzum H, Mikelis CM, Rose SR, Ferre EM, Yockey L, Lemberg K, Kuehn HS, Rosenzweig SD, Lin X, Chittiboina P, Datta SK, Belhorn TH, Weimer ET, Hernandez ML, Hohl TM, Kuhns DB, and Lionakis MS. 2015 CARD9-Dependent Neutrophil Recruitment Protects against Fungal Invasion of the Central Nervous System. *PLoS Pathog* 11: e1005293. [PubMed: 26679537]
72. Kowalski CH, Beattie SR, Fuller KK, McGurk EA, Tang YW, Hohl TM, Obar JJ, and Cramer RA Jr. 2016 Heterogeneity among Isolates Reveals that Fitness in Low Oxygen Correlates with *Aspergillus fumigatus* Virulence. *mBio* 7: e01515–01516. [PubMed: 27651366]
73. Fermanitt CS, Sano K, Liu Z, Ishii N, Seino J, Dobbs N, Suzuki T, Fu YX, Lehrman MA, Matsuo I, and Yan N. 2019 A bioactive mammalian disaccharide associated with autoimmunity activates STING-TBK1-dependent immune response. *Nat Commun* 10: 2377. [PubMed: 31147550]
74. Moretti J, Roy S, Bozec D, Martinez J, Chapman JR, Ueberheide B, Lamming DW, Chen ZJ, Horng T, Yeretsian G, Green DR, and Blander JM. 2017 STING Senses Microbial Viability to Orchestrate Stress-Mediated Autophagy of the Endoplasmic Reticulum. *Cell* 171: 809–823. [PubMed: 29056340]
75. Alexopoulou L, Holt AC, Medzhitov R, and Flavell RA. 2001 Recognition of double-stranded RNA and activation of NF-kappaB by Toll-like receptor 3. *Nature* 413: 732–738. [PubMed: 11607032]
76. Lund JM, Alexopoulou L, Sato A, Karow M, Adams NC, Gale NW, Iwasaki A, and Flavell RA. 2004 Recognition of single-stranded RNA viruses by Toll-like receptor 7. *Proc Natl Acad Sci U S A* 101: 5598–5603. [PubMed: 15034168]
77. Gitlin L, Barchet W, Gilfillan S, Cella M, Beutler B, Flavell RA, Diamond MS, and Colonna M. 2006 Essential role of mda-5 in type I IFN responses to polyriboinosinic:polyribocytidylic acid and encephalomyocarditis picornavirus. *Proc Natl Acad Sci U S A* 103: 8459–8464. [PubMed: 16714379]
78. Kato H, Takeuchi O, Sato S, Yoneyama M, Yamamoto M, Matsui K, Uematsu S, Jung A, Kawai T, Ishii KJ, Yamaguchi O, Otsu K, Tsujimura T, Koh CS, Reis e Sousa C, Matsuura Y, Fujita T, and Akira S. 2006 Differential roles of MDA5 and RIG-I helicases in the recognition of RNA viruses. *Nature* 441: 101–105. [PubMed: 16625202]
79. Yamamoto M, Sato S, Mori K, Hoshino K, Takeuchi O, Takeda K, and Akira S. 2002 Cutting edge: a novel Toll/IL-1 receptor domain-containing adapter that preferentially activates the IFN-beta promoter in the Toll-like receptor signaling. *J Immunol* 169: 6668–6672. [PubMed: 12471095]
80. Beisswenger C, Hess C, and Bals R. 2012 *Aspergillus fumigatus* conidia induce interferon-beta signalling in respiratory epithelial cells. *Eur Respir J* 39: 411–418. [PubMed: 21778165]
81. Davis MJ and Swanson JA. 2010 Technical advance: Caspase-1 activation and IL-1beta release correlate with the degree of lysosome damage, as illustrated by a novel imaging method to quantify phagolysosome damage. *J Leukoc Biol* 88: 813–822. [PubMed: 20587739]
82. Hornung V, Bauernfeind F, Halle A, Samstad EO, Kono H, Rock KL, Fitzgerald KA, and Latz E. 2008 Silica crystals and aluminum salts activate the NALP3 inflammasome through phagosomal destabilization. *Nat Immunol* 9: 847–856. [PubMed: 18604214]
83. Wellington M, Koselny K, and Krysan DJ. 2012 *Candida albicans* morphogenesis is not required for macrophage interleukin 1beta production. *mBio* 4: e00433–00412. [PubMed: 23269828]

84. Nguyen TA, Smith BRC, Tate MD, Belz GT, Barrios MH, Elgass KD, Weisman AS, Baker PJ, Preston SP, Whitehead L, Garnham A, Lundie RJ, Smyth GK, Pellegrini M, O'Keeffe M, Wicks IP, Masters SL, Hunter CP, and Pang KC. 2017 SIDT2 Transports Extracellular dsRNA into the Cytoplasm for Innate Immune Recognition. *Immunity* 47: 498–509 e496. [PubMed: 28916264]
85. Joffe LS, Nimrichter L, Rodrigues ML, and Del Poeta M. 2016 Potential Roles of Fungal Extracellular Vesicles during Infection. *mSphere* 1:
86. Cheng Y and Schorey JS. 2019 Extracellular vesicles deliver Mycobacterium RNA to promote host immunity and bacterial killing. *EMBO Rep* 20:
87. Singh PP, Li L, and Schorey JS. 2015 Exosomal RNA from Mycobacterium tuberculosis-Infected Cells Is Functional in Recipient Macrophages. *Traffic* 16: 555–571. [PubMed: 25753779]
88. Mehrad B, Strieter RM, Moore TA, Tsai WC, Lira SA, and Standiford TJ. 1999 CXCR chemokine receptor-2 ligands are necessary components of neutrophil-mediated host defense in invasive pulmonary aspergillosis. *J Immunol* 163: 6086–6094. [PubMed: 10570298]
89. Lang S, Li L, Wang X, Sun J, Xue X, Xiao Y, Zhang M, Ao T, and Wang J. 2017 CXCL10/IP-10 Neutralization Can Ameliorate Lipopolysaccharide-Induced Acute Respiratory Distress Syndrome in Rats. *PLoS One* 12: e0169100. [PubMed: 28046003]
90. Ichikawa A, Kuba K, Morita M, Chida S, Tezuka H, Hara H, Sasaki T, Ohteki T, Ranieri VM, dos Santos CC, Kawaoka Y, Akira S, Luster AD, Lu B, Penninger JM, Uhlig S, Slutsky AS, and Imai Y. 2013 CXCL10-CXCR3 enhances the development of neutrophil-mediated fulminant lung injury of viral and nonviral origin. *Am J Respir Crit Care Med* 187: 65–77. [PubMed: 23144331]
91. Muller U, Steinhoff U, Reis LF, Hemmi S, Pavlovic J, Zinkernagel RM, and Aguet M. 1994 Functional role of type I and type II interferons in antiviral defense. *Science* 264: 1918–1921. [PubMed: 8009221]
92. Ng CT, Sullivan BM, Teijaro JR, Lee AM, Welch M, Rice S, Sheehan KC, Schreiber RD, and Oldstone MB. 2015 Blockade of interferon Beta, but not interferon alpha, signaling controls persistent viral infection. *Cell Host Microbe* 17: 653–661. [PubMed: 25974304]
93. Teijaro JR, Ng C, Lee AM, Sullivan BM, Sheehan KC, Welch M, Schreiber RD, de la Torre JC, and Oldstone MB. 2013 Persistent LCMV infection is controlled by blockade of type I interferon signaling. *Science* 340: 207–211. [PubMed: 23580529]
94. Wilson EB, Yamada DH, Elsaesser H, Herskovitz J, Deng J, Cheng G, Aronow BJ, Karp CL, and Brooks DG. 2013 Blockade of chronic type I interferon signaling to control persistent LCMV infection. *Science* 340: 202–207. [PubMed: 23580528]
95. Seyedmousavi S, Davis MJ, Sugui JA, Pinkhasov T, Moyer S, Salazar AM, Chang YC, and Kwon-Chung KJ. 2018 Exogenous Stimulation of Type I Interferon Protects Mice with Chronic Granulomatous Disease from Aspergillosis through Early Recruitment of Host-Protective Neutrophils into the Lung. *mBio* 9:
96. Sionov E, Mayer-Barber KD, Chang YC, Kauffman KD, Eckhaus MA, Salazar AM, Barber DL, and Kwon-Chung KJ. 2015 Type I IFN Induction via Poly-ICLC Protects Mice against Cryptococcosis. *PLoS Pathog* 11: e1005040. [PubMed: 26252005]
97. Davis MJ, Moyer S, Hoke ES, Sionov E, Mayer-Barber KD, Barber DL, Cai H, Jenkins L, Walter PJ, Chang YC, and Kwon-Chung KJ. 2019 Pulmonary Iron Limitation Induced by Exogenous Type I IFN Protects Mice from *Cryptococcus gattii* Independently of T Cells. *mBio* 10:
98. Biondo C, Midiri A, Gambuzza M, Gerace E, Falduto M, Galbo R, Bellantoni A, Beninati C, Teti G, Leanderson T, and Mancuso G. 2008 IFN-alpha/beta signaling is required for polarization of cytokine responses toward a protective type I pattern during experimental cryptococcosis. *J Immunol* 181: 566–573. [PubMed: 18566423]
99. Sato K, Yamamoto H, Nomura T, Matsumoto I, Miyasaka T, Zong T, Kanno E, Uno K, Ishii K, and Kawakami K. 2015 *Cryptococcus neoformans* Infection in Mice Lacking Type I Interferon Signaling Leads to Increased Fungal Clearance and IL-4-Dependent Mucin Production in the Lungs. *PLoS One* 10: e0138291. [PubMed: 26384031]
100. Van Prooyen N, Henderson CA, Hocking Murray D, and Sil A. 2016 CD103+ Conventional Dendritic Cells Are Critical for TLR7/9-Dependent Host Defense against *Histoplasma capsulatum*, an Endemic Fungal Pathogen of Humans. *PLoS Pathog* 12: e1005749. [PubMed: 27459510]

101. Riedelberger M, Penninger P, Tscherner M, Seifert M, Jenull S, Brunnhofer C, Scheidl B, Tsymala I, Bourgeois C, Petryshyn A, Glaser W, Limbeck A, Strobl B, Weiss G, and Kuchler K. 2020 Type I Interferon Response Dysregulates Host Iron Homeostasis and Enhances *Candida glabrata* Infection. *Cell Host Microbe* 27: 454–466 e458. [PubMed: 32075740]
102. Riedelberger M, Penninger P, Tscherner M, Hadriga B, Brunnhofer C, Jenull S, Stoiber A, Bourgeois C, Petryshyn A, Glaser W, Limbeck A, Lynes MA, Schabbauer G, Weiss G, and Kuchler K. 2020 Type I Interferons Ameliorate Zinc Intoxication of *Candida glabrata* by Macrophages and Promote Fungal Immune Evasion. *iScience* 23: 101121. [PubMed: 32428860]
103. Bourgeois C, Majer O, Frohner IE, Lesiak-Markowicz I, Hildering KS, Glaser W, Stockinger S, Decker T, Akira S, Muller M, and Kuchler K. 2011 Conventional dendritic cells mount a type I IFN response against *Candida* spp. requiring novel phagosomal TLR7-mediated IFN- $\beta$  signaling. *J Immunol* 186: 3104–3112. [PubMed: 21282509]
104. Smeekens SP, Ng A, Kumar V, Johnson MD, Plantinga TS, van Diemen C, Arts P, Verwiel ET, Gresnigt MS, Fransen K, van Sommeren S, Oosting M, Cheng SC, Joosten LA, Hoischen A, Kullberg BJ, Scott WK, Perfect JR, van der Meer JW, Wijmenga C, Netea MG, and Xavier RJ. 2013 Functional genomics identifies type I interferon pathway as central for host defense against *Candida albicans*. *Nat Commun* 4: 1342. [PubMed: 23299892]
105. Majer O, Bourgeois C, Zwolanek F, Lassnig C, Kerjaschki D, Mack M, Muller M, and Kuchler K. 2012 Type I interferons promote fatal immunopathology by regulating inflammatory monocytes and neutrophils during *Candida* infections. *PLoS Pathog* 8: e1002811. [PubMed: 22911155]
106. Hagmann CA, Herzner AM, Abdullah Z, Zillinger T, Jakobs C, Schuberth C, Coch C, Higgins PG, Wisplinghoff H, Barchet W, Hornung V, Hartmann G, and Schlee M. 2013 RIG-I detects triphosphorylated RNA of *Listeria monocytogenes* during infection in non-immune cells. *PLoS One* 8: e62872. [PubMed: 23653683]
107. Abdullah Z, Schlee M, Roth S, Mraheil MA, Barchet W, Bottcher J, Hain T, Geiger S, Hayakawa Y, Fritz JH, Civril F, Hopfner KP, Kurts C, Ruland J, Hartmann G, Chakraborty T, and Knolle PA. 2012 RIG-I detects infection with live *Listeria* by sensing secreted bacterial nucleic acids. *EMBO J* 31: 4153–4164. [PubMed: 23064150]
108. Liehl P, Zuzarte-Luis V, Chan J, Zillinger T, Baptista F, Carapau D, Konert M, Hanson KK, Carret C, Lassnig C, Muller M, Kalinke U, Saeed M, Chora AF, Golenbock DT, Strobl B, Prudencio M, Coelho LP, Kappe SH, Superti-Furga G, Pichlmair A, Vigario AM, Rice CM, Fitzgerald KA, Barchet W, and Mota MM. 2014 Host-cell sensors for *Plasmodium* activate innate immunity against liver-stage infection. *Nat Med* 20: 47–53. [PubMed: 24362933]
109. Cheng Y and Schorey JS. 2018 *Mycobacterium tuberculosis*-induced IFN- $\beta$  production requires cytosolic DNA and RNA sensing pathways. *J Exp Med* 215: 2919–2935. [PubMed: 30337468]

**KEY POINTS:**

- MDA5 is essential for maintaining host resistance against *Aspergillus fumigatus*
- MDA5 serves as a critical vitality sensor after fungal challenge
- MDA5 is essential for IFN $\lambda$  expression and anti-fungal neutrophil killing

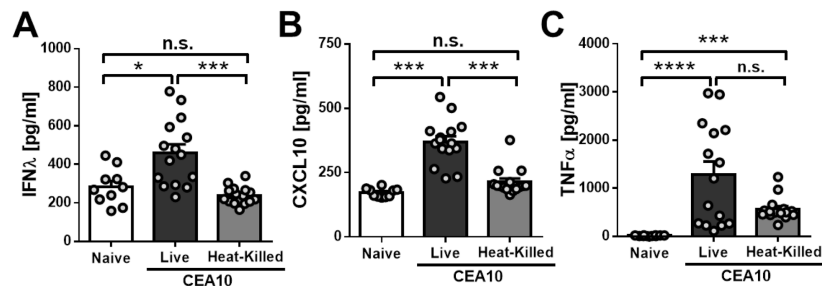


**Figure 1. Heat-killed swollen conidia have a decreased ability to induce CXCL10.** C57BL/6J mice were challenged i.t. with  $4 \times 10^7$  CEA10 live or heat-killed swollen conidia. Forty hours later BALF was collected and IL-28/IFN- $\lambda$  (A), CXCL10 (B), and TNF $\alpha$  (C) levels were determined by ELISA. Data are pooled from 2 independent experiments with 10–15 total mice per group. Statistical significance was determined using a one-way ANOVA with Dunn's post-test (\* $p < 0.05$ ; \*\* $p < 0.01$ ).

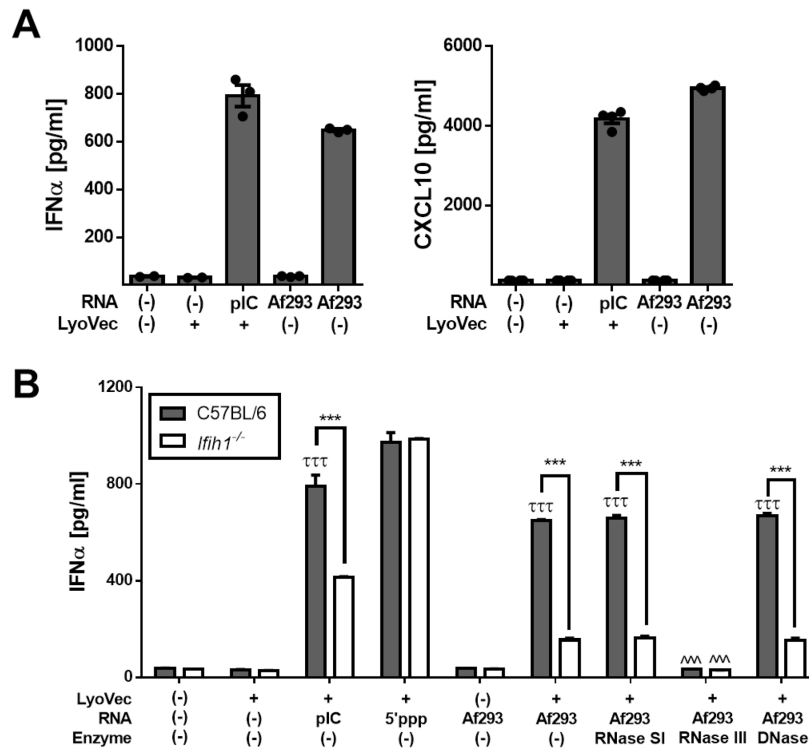


**Figure 2. *Aspergillus fumigatus* RNA induces an interferon response in a partially MDA5-dependent manner.**

(A) Primary murine fibroblasts from C57BL/6J mice were stimulated with LyoVec™ encapsulated polyI:C (pIC) or total RNA isolated from Af293 for 18 h. After stimulation cell supernatants were collected and analyzed for IFNα (left) and CXCL10 (right) by ELISA. Data from 2 independent experiments with 3 samples per group. (B) Primary murine fibroblasts from C57BL/6J and *Ifih1*<sup>-/-</sup> mice were stimulated with LyoVec™ encapsulated polyI:C (pIC) (MDA5 agonist), 5'-ppp (RIG-I agonist), or total RNA isolated from Af293 for 18 h. The total RNA pool isolated from Af293 was also treated with either RNase S1, RNase III, or DNase to degrade ssRNA, dsRNA, or DNA, respectively prior to encapsulation in LyoVec™. After stimulation cell supernatants were collected and analyzed for IFNα by ELISA. Data from 2 independent experiments with 3 samples per group. Statistical significance was determined by a two-way ANOVA with a Tukey's post-test (\*\*\* p<0.001 – LyoVec™ only vs. experimental group; \*\*\* p<0.001 – B6 vs. *Ifih1*<sup>-/-</sup>; ^^^ p<0.001 – enzyme treated vs. Af293).



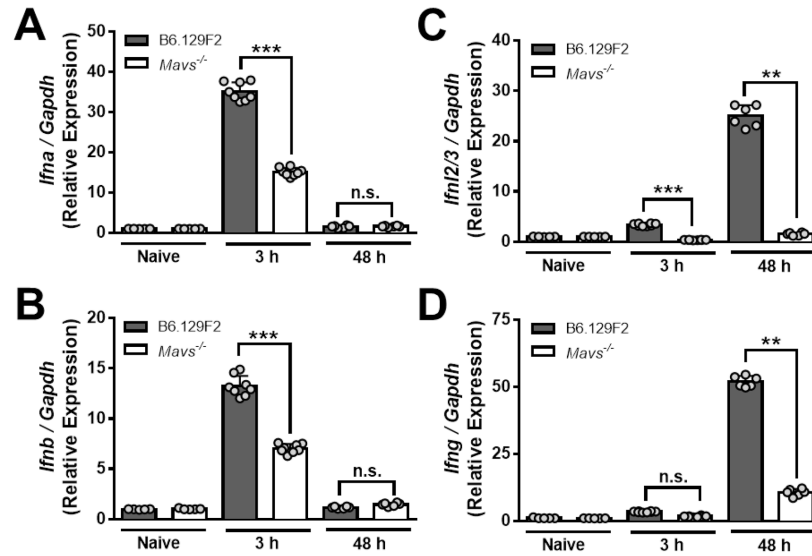


**Figure 3. *Mavs*<sup>-/-</sup> mice have decreased interferon mRNA levels after *Aspergillus fumigatus* challenge particularly at later times.**

B6.129F2 and *Mavs*<sup>-/-</sup> mice were challenged with  $4 \times 10^7$  conidia of CEA10. Lungs were collected 3 or 48h post-inoculation. Total RNA was extracted from whole lungs. Gene expression as determined by quantitative reverse transcription polymerase chain reaction (qRT-PCR) using TaqMan probes for *Ifna* (A), *Ifnb* (B), *Ifnl2/3* (C), and *Ifng* (D), which were normalized to *Gapdh* expression. Bars represent data means  $\pm$  SEM with each dot representing individual mice. Data are representative of results from at least 2 independent experiments with at least 3 mice per group. Data were analyzed using a Mann-Whitney U-test (\*\* p < 0.01; \*\*\* p < 0.0001).

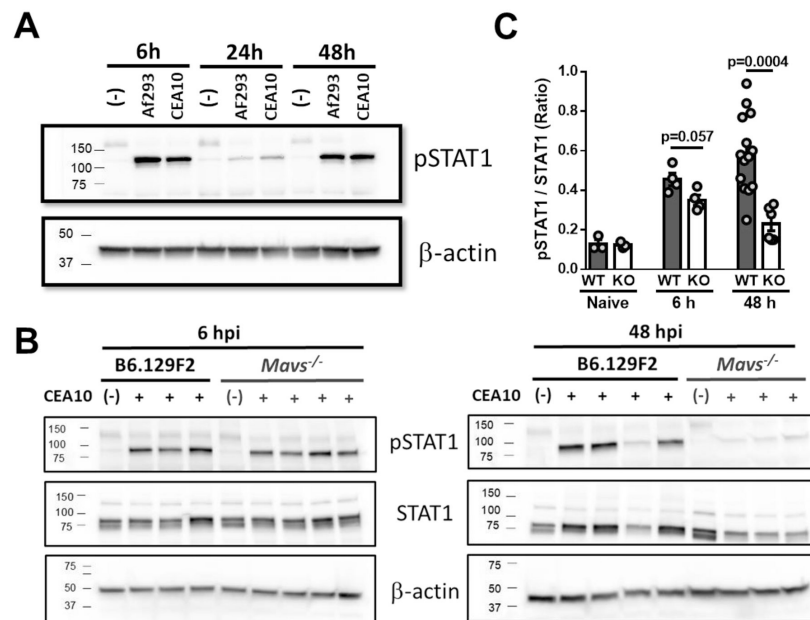


**Figure 4. *Mavs*<sup>-/-</sup> mice have decreased STAT1 phosphorylation after *Aspergillus fumigatus* challenge at later times.**

(A) C57BL/6J mice were challenged with  $4 \times 10^7$  conidia of CEA10 or Af293. Lungs were collected at 6, 24, and 48 hours post-inoculation and total protein was extracted from whole lungs. Protein expression and phosphorylation was determined by Western blot analysis. (B) B6.129F2 and *Mavs*<sup>-/-</sup> mice were challenged with  $4 \times 10^7$  conidia of CEA10. Lungs were collected at 6- or 48-hours post-inoculation and total protein was extracted from whole lungs. Protein expression and phosphorylation was determined by Western blot analysis. (C) Western blots from panel B were quantified by densitometry. Bars represent data means  $\pm$  SEM with each dot representing individual mice. Data are representative of results from at least 2 independent experiments with at least 3 mice per group. Data were analyzed using a Mann-Whitney U-test.

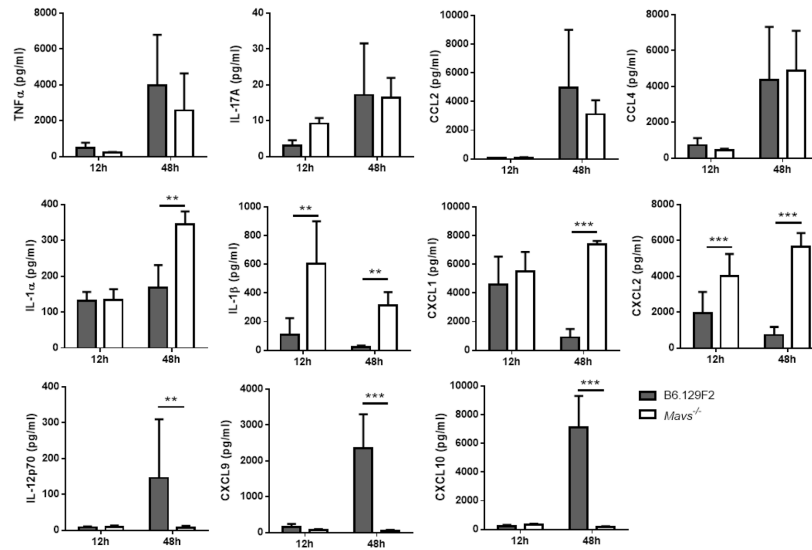


**Figure 5. *Mavs*<sup>-/-</sup> mice have an altered inflammatory milieu after *Aspergillus fumigatus* challenge in the airways.**

B6.129F2 and *Mavs*<sup>-/-</sup> mice were challenged with  $4 \times 10^7$  conidia of CEA10. Bronchoalveolar lavage fluid (BALF) was collected 12 or 48h post-inoculation. Cytokine and chemokine levels were determined using a Milliplex Mouse Cytokine & Chemokine 32-plex (Millipore). Bars represent data means  $\pm$  SEM. Data are representative of results 2 independent experiments with 4–6 mice per group. Data were analyzed using a Mann-Whitney U-test (\* p < 0.05; \*\* p < 0.01; \*\*\* p < 0.001).

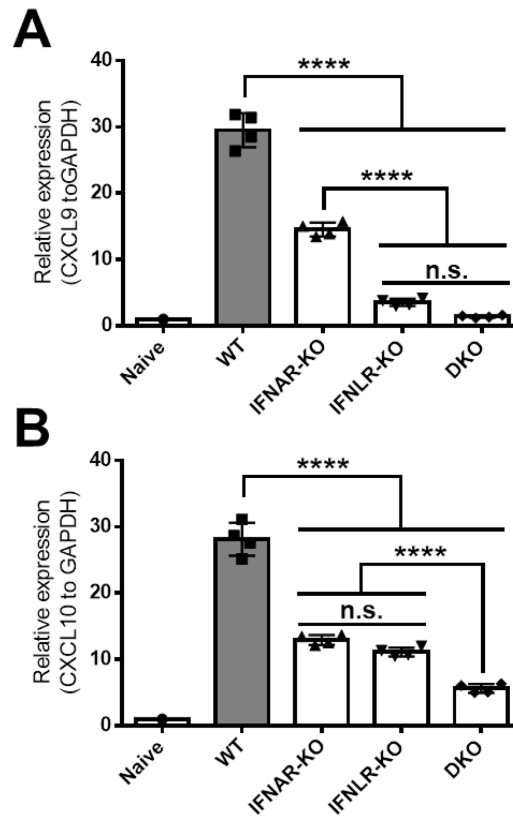


**Figure 6. Expression of *Cxcl9* and *Cxcl10* are dependent on IFN signaling.** C57BL/6J, *Ifnar*<sup>-/-</sup>, *Ifnlr*<sup>-/-</sup>, and *Ifnar*<sup>-/-</sup>*Ifnlr*<sup>-/-</sup> (DKO) mice were challenged with 4×10<sup>7</sup> conidia of CEA10. Lungs were collected 48h post-inoculation and total RNA was extracted. Gene expression as determined by quantitative reverse transcription polymerase chain reaction (qRT-PCR) using TaqMan probes for *Cxcl9* (A) and *Cxcl10*, which were normalized to *Gapdh* expression. Bars represent data means ± SEM with each symbol representing individual mice. Data are representative of results from at least 2 independent experiments with at least 4 mice per infected group. Data were analyzed using a Mann-Whitney U-test (n.s. = not significant; \*\*\*\* p < 0.0001).

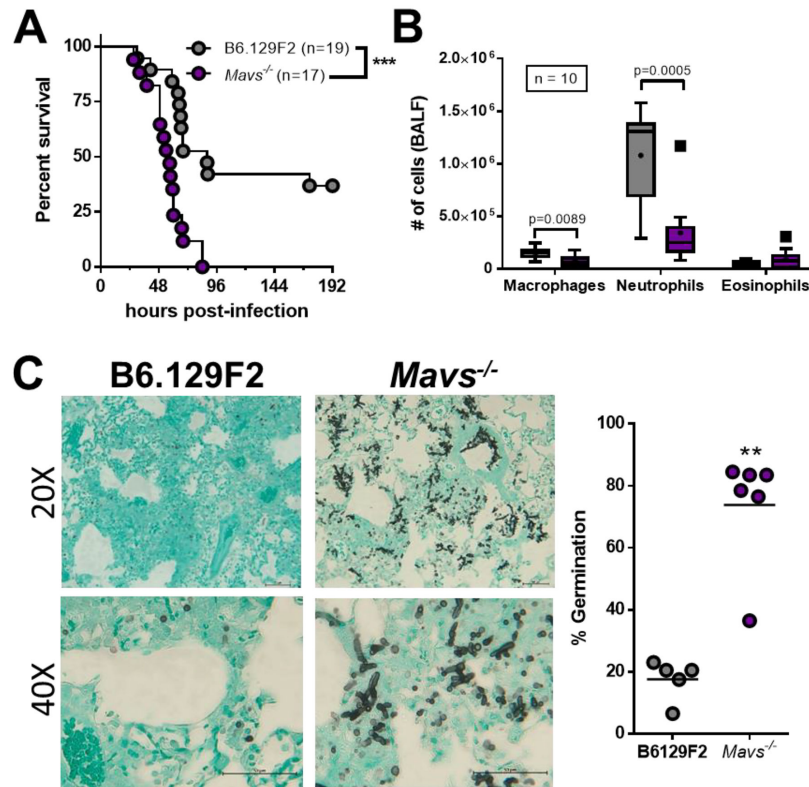


**Figure 7. *Mavs*<sup>-/-</sup> mice are highly susceptible to *Aspergillus fumigatus*.** B6.129F2 and *Mavs*<sup>-/-</sup> mice were challenged with  $4 \times 10^7$  conidia of CEA10. (A) Survival analysis in immune-competent wild-type and knock-out mice were tracked over the first days. Statistical significance was assessed using a Mantel-Cox log rank test (\*\*p = 0.0001). (B) At 36 hpi, mice were euthanized and BALF collected for quantification of macrophage and neutrophil recruitment to the airways. Data are pooled from 2 independent experiments for a total of 10 mice per group. Data are presented as box-and-whisker plots with Tukey whiskers and outliers displayed as dots. Statistical significance was determined using a Mann-Whitney U test. (C) At 40 hpi mice were euthanized and lungs saved for histological analysis. Formalin-fixed lungs were paraffin embedded, sectioned, and stained with GMS for analysis by microscopy. Representative lung sections from are shown to the left using the 20x and 40x objective. *A. fumigatus* germination rates were determined by microscopically counting both the number of conidia and number of germings in GMS-stained sections.

Data from 2 independent experiments with 4–6 mice per group. Statistical significance was determined using a Mann-Whitney U test (\*\*p < 0.01).

Author Manuscript

Author Manuscript

Author Manuscript

Author Manuscript

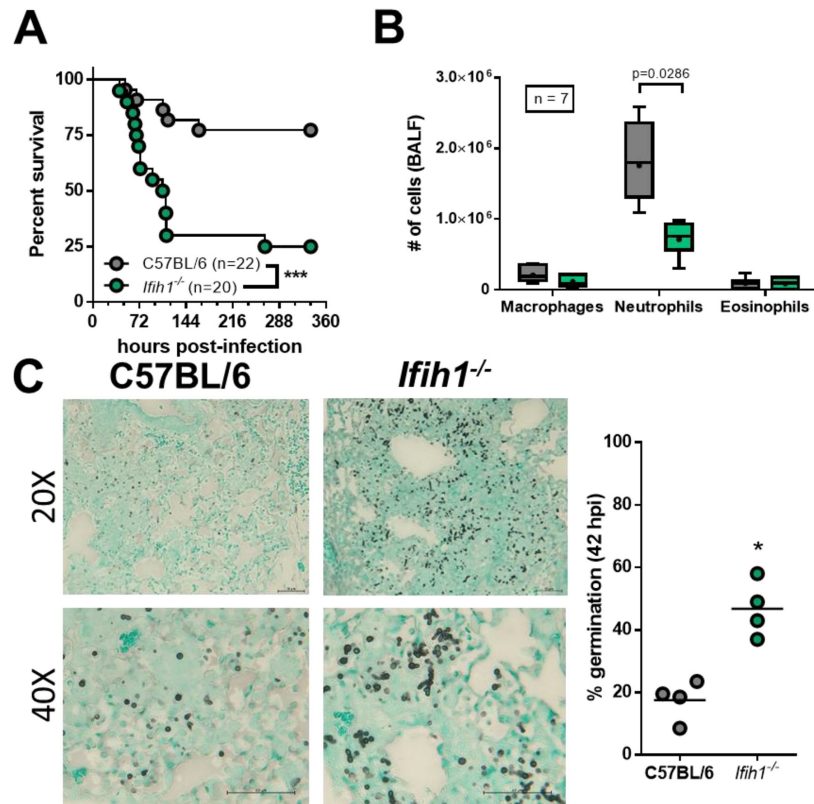


**Figure 8. *Ifih1*<sup>-/-</sup> mice are highly susceptible to *Aspergillus fumigatus*.** C57BL/6J and *Ifih1*<sup>-/-</sup> mice were challenged with  $4 \times 10^7$  conidia of CEA10. **(A)** Survival analysis in immune-competent wild-type and knock-out mice were tracked over the first 15 days. Statistical significance was assessed using a Mantel-Cox log rank test (\*\*\*p = 0.0004). **(B & E)** At 36 hpi, mice were euthanized and BALF collected for quantification of macrophage and neutrophil recruitment to the airways. Data from 2 independent experiments for a total of 7 mice per group. Data are presented as box-and-whisker plots with Tukey whiskers and outliers displayed as dots. Statistical significance was determined using a Mann-Whitney U test. **(C & F)** At 42 hpi mice were euthanized and lungs saved for histological analysis. Formalin-fixed lungs were paraffin embedded, sectioned, and stained with GMS for analysis by microscopy. Representative lung sections from are shown to the right using the 20x and 40x objective. *A. fumigatus* germination rates were determined by microscopically counting both the number of conidia and number of germings in GMS-

stained sections. Data from 2 independent experiments with 4–6 mice per group. Statistical significance was determined using a Mann-Whitney U test (\* $p < 0.05$ ; \*\* $p < 0.01$ ).

Author Manuscript

Author Manuscript

Author Manuscript

Author Manuscript



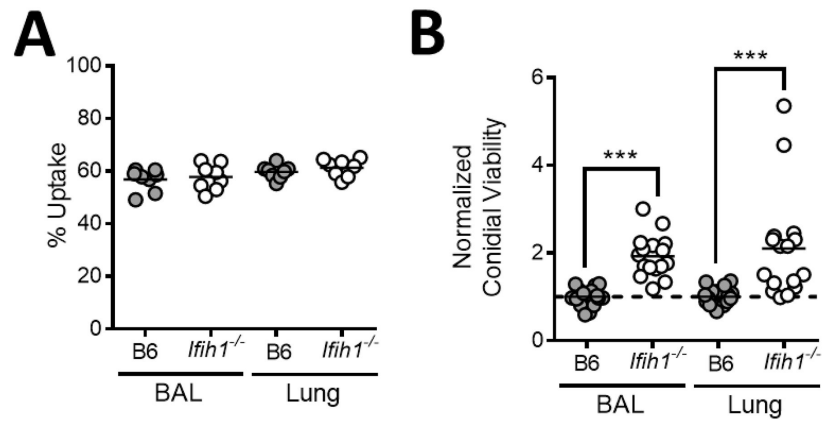


**Figure 9. *Ifih1*<sup>-/-</sup> mice have decrease antifungal killing by neutrophils *in vivo*.** C57BL/6J and *Ifih1*<sup>-/-</sup> mice were challenged with  $3 \times 10^7$  conidia of CEA10 fluorescent *Aspergillus* reporter (FLARE). Bronchoalveolar lavage (BAL) fluid and lungs were harvested at 48 hours after infection and fungal uptake and viability were analyzed with flow cytometry. Fungal uptake (**A**) and viability (**B**) in neutrophils were measured. Data pooled from 2 independent experiments with 7–9 mice per group. Statistical significance was determined using a Mann-Whitney U test (\*\**p* < 0.01).

